Laser Powder Bed Fusion of Ti-6Al-4V: A Round Robin Analysis of Powder Reuse and Process By-Products

Alexander Montelione

A dissertation

submitted in partial fulfillment of the

requirements for the degree of

Doctor of Philosophy

University of Washington

2026

Reading Committee:

Dwayne D. Arola, Chair

Ramulu Mamidala, Chair

Navid Zobeiry

Program Authorized to Offer Degree:

Materials Science and Engineering

University of Washington

Abstract

Laser Powder Bed Fusion of Ti-6Al-4V: A Round Robin Analysis of Powder Reuse and Process By-Products

Alexander Montelione

Chair(s) of the Supervisory Committee:
Dwayne D. Arola
Department of Materials Science and Engineering
Ramulu Mamidala
Department of Mechanical Engineering

Metal Additive Manufacturing (AM) provides immense value as a manufacturing method to produce high complexity parts for stress-critical applications. Metal AM though Powder Bed Fusion (PBF) technologies can produce fully dense metal parts with mechanical properties on par with wrought counterparts, and with geometries unachievable with conventional manufacturing methods. Widespread adoption of this technology requires thorough understanding of the contributors to part variability, and robust machine and part qualification.

This dissertation evaluates the effects of powder reuse in L-PBF over the course of ten builds, split into two phases. The study presents a novel approach to powder reuse through a "round robin" style study involving six independent participants following the same operational procedure and, importantly, starting with the same lot of plasma-atomized grade 5 Ti-6Al-4V metal powder.

Important metrics of powder quality are monitored throughout the study and compared to mechanical properties of the metal produced over time and between participants. Several categories of variability are considered, including intra-build (referring to variability that arises within individual builds), inter-build (variability that arises from one build to another on the same machine), and inter-machine (variability that arises between different machines run under the same nominal conditions). Byproducts of the L-PBF process, including spatter and metal vapor condensate, are investigated and characterized as important components of variability in powder quality.

Phase I of the study involved six builds performed by six participants. Samples of powder were taken prior to each build and analyzed to characterize the particle size distribution, morphology, bulk chemistry, and flowability. The mean particle size of the powder as well as its flowability increased slightly with reuse at all sites, whereas the powder chemistry did not change appreciably over the six builds conducted. Quasi-static mechanical properties of the metal produced from the reused powder were found to correlate with carbon and aluminum content, but not with reuse number.

In Phase II of the study, three of the original six participants continued with an additional four builds. Powder was again collected, analyzed, and compared between partners and against Phase I. Extended reuse was found to not intensify the trends observed in Phase I, and instead many of the measured properties stayed at, or returned to, nominal values. Powder chemistry did not change over Phase I or Phase II, although variability was observed between partners. The mean particle size of the powder samples, which had increased in Phase I, decreased back to nominal values.

Spatter and metal vapor condensate were collected in-situ and ex-situ to explore their properties and their distribution throughout the L-PBF system. Factors of size, chemistry, and deposition were measured as a foundation of understanding these materials as potential contaminants and contributors to metal variability. These results form the basis for motivating and designing further studies to investigate and mitigate the effects of these process byproducts.

Overall, these results highlight the potential variability in quality of reused powder and differences in its rate of “aging” in L-PBF, even when the machine model and starting powder lot is highly controlled. Results from this study are the first to evaluate changes in powder quality occurring at different manufacturing locations using the same initial powder lot over multiple builds, which provides valuable insight into the mechanisms of powder degradation with reuse.

Table of Contents

List of Figures

Acknowledgements

The work presented in this dissertation would not have been possible without the tremendous support of those around me, and I have many thanks to give. To my friends and family for providing endless encouragement through the many years of work. To my advisors, Dr. Arola and Dr. Mamidala, for their guidance and instruction. To my lab colleagues and collaborators, for their contributions and discussions. To all of you who have supported myself and this work, you have my heartfelt thanks.

This work was partially accomplished using facilities funded by the Joint Center for Deployment and Research in Earth Abundant Materials (JCDREAM) in Washington State. Support was provided in part from the Joint Center for Aerospace Technology Innovation (JCATI). The authors also gratefully acknowledge financial support from The Boeing Company through the Boeing Advanced Research Center and the Federal Aviation Administration through the Center of Excellence for Advanced Materials in Transport Aircraft Structures (AMTAS). Additionally, this research used statistical consulting resources provided by the Center for Statistics and the Social Sciences, University of Washington.

Part of this work was conducted at the Molecular Analysis Facility, a National Nanotechnology Coordinated Infrastructure (NNCI) site at the University of Washington, which is supported in part by funds from the National Science Foundation (awards NNCI-2025489, NNCI-1542101). This material is based in part upon work supported by the state of Washington through the University of Washington Clean Energy Institute and the Molecular Engineering & Sciences Institute

Chapter 1 Introduction and Background

1.1 Metal Additive Manufacturing

Additive Manufacturing (AM), colloquially known as 3D printing, is a term that refers to the creation of a functional element or "part" though the consolidation of precursor material. AM processes are defined as the joining of material, usually layer-by-layer, according to digital 3D model data [1,2]. The ISO-ASTM 52900 standard categorizes AM processes into seven categories: vat photopolymerization, material jetting, powder bed fusion, directed energy deposition, material extrusion, binder jetting, and sheet lamination [1]. These processes are considered fundamentally different from subtractive manufacturing (e.g. milling, turning, EDM) and formative manufacturing methodologies (e.g. forging casting, injection molding) broadly referred to as conventional manufacturing (CM) [1,2]. The specific application and material platforms available for AM technologies vary across the categories, but the concept of building a solid part from a digital model through the addition of material is shared across all AM technologies.

AM technologies began commercialization in the late 1980s, with much of the early technology being focused on rapid prototyping of designs for the automotive industry [2–4]. Early stereolithography techniques used photopolymerization to fuse layers o liquid polymers into solid parts. The process allowed quick development of prototypes for design testing and development, as well as for visualization of complex 3D geometries. However, the materials available at the time were generally brittle and weak, making them unsuitable for use in finished parts [2]. As the technology developed, additional applications for AM were found in rapid development of tooling for CM processes. Over the decades since the inception of AM, material advancements and process improvements have paved the way for direct production of application-ready parts, although a large part of the AM market still focuses on the development of tooling, jigs, and fixtures for CM applications [2]. Today, the interest in AM technologies stems from the unique design freedom that the technology offers in comparison to CM. Generally, the advantages that AM part production has over CM can be summarized in three parts, namely (i) increased design complexity, (ii) consolidation of parts or reduced assembly part count, and (iii) efficiency of material usage.

1.1.1 Design complexity

While it is often claimed that AM parts can be produced with virtually any shape, process constraints do place limitations on the geometries that can realistically be produced with any given AM technique. For example, closed hollow geometries, which can be produced by rotational molding, cannot be produced with powder bed fusion AM methods without an escape hole to free the entrapped powder. Still, the difference in the limitations between CM and AM technologies allows production of parts by AM, which would be exceedingly difficult or impossible by CM methods [2,5]. The layer-by-layer addition of material allows for material to be placed only where it is needed, either for the function of the part or as support for material on subsequent layers. Internal geometries, like those demonstrated in Figure 1.1, can be formed without having to provide access for a forming tool. Complicated geometries like lattices or honeycombs can also be built using AM without significantly increasing manufacturing cost or time, unlike in CM.

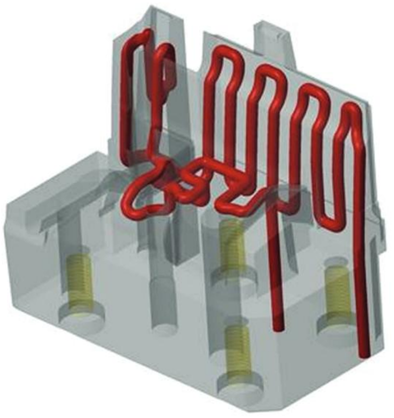

Figure 1.1: Example of an internal geometry: internal conformal cooling channel in an injection molding tool produced by AM. Reproduced from ASM handbook Vol. 24 [2].

1.1.2 *Consolidation of parts*

Another advantage of AM over CM is the ability to consolidate multi-part assemblies into a single part, which can save significant production cost by eliminating assembly costs. Furthermore, AM uniquely offers the capability of producing geometries like pipes, channels, and flanges, without needing to produce these geometries separately and the joining them together. Figure 1.2 shows an example of a 16-part assembly of CM parts consolidated into a single AM part.

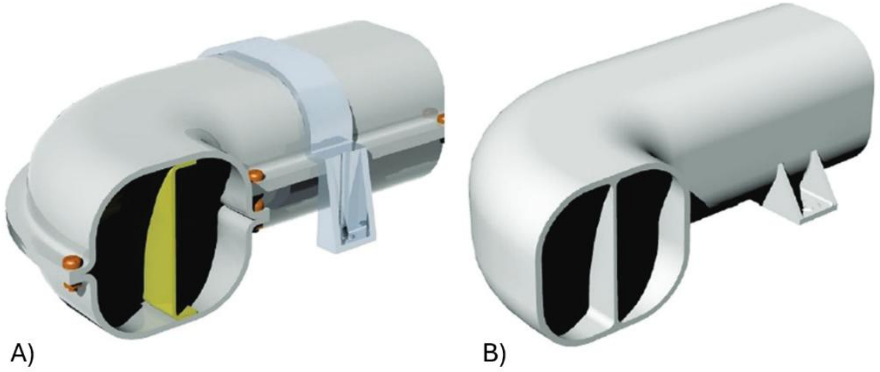

Figure 1.2: Example of a 16-part assembly (A) reduced to a single part (B) that could be manufactured using AM. Reproduced from ASM handbook Vol. 24 [2].

1.1.3 Efficiency of material usage (buy-to-fly, shape optimization)

The ability to add complexity to a part without increasing manufacturing cost opens the design space to optimization of parts for stiffness and weight. Aerospace industries often consider the "buy-to-fly ratio" of a component, which is the ratio of mass of starting material (e.g. a billet for machining) to the mass of the final component [6–8]. The CM methods used to produce parts for aerospace applications often have buy-to-fly ratios as high as 10:1, meaning only 10% of the initial material input remains in the final part and the remainder reduces to chips or scrap that needs to be recycled. Higher complexity parts generally result in higher buy-to-fly ratios as more material is removed to create the complex geometries. In comparison, most AM methods can place material where necessary, and without residual waste. While buy-to-fly ratios of 1:1 are not likely to be achievable even with AM due to the need for support structures, post-process machining, and material degradation, the ability to create near net shape components is highly desirable for the aerospace industry, particularly for materials with high cost.

In addition to efficiency in material use, AM supports complex designs by eliminating the concern for part machinability. Coupled with advances in computational power, this advantage enables computational shape optimization and topographic optimization. These techniques use analysis software to eliminate non-load bearing material in a design, or to place material in a strategic way to optimally carry loads [9]. An example of a topology-optimized design is shown in Figure 1.3.

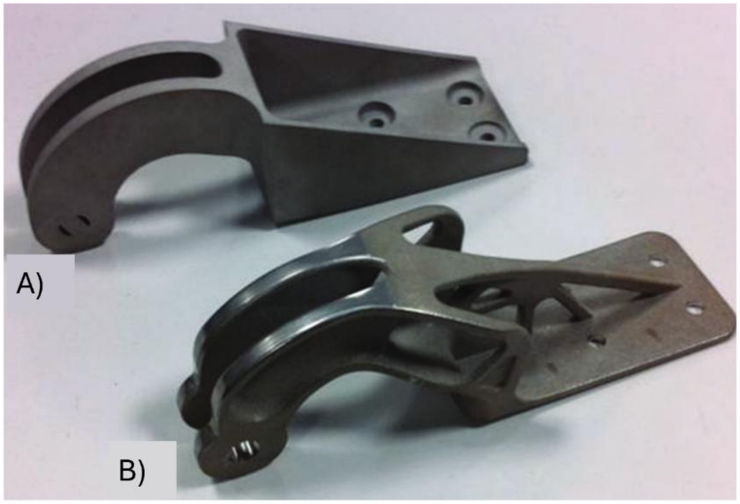

Figure 1.3: Example of a standard (A) and topology-optimized (B) Nacelle hinge bracket for Airbus A320. Reproduced from ASM handbook Vol. 24 [2].

1.1.4 Additive Manufacturing Classifications

AM methodologies can be broadly classified into single-step and multi-step processes, by the ISO/ASTM classification tree shown in Figure 1.4 [1]. In single-step AM processes, the parts are fabricated in a single operation where the basic geometric shape and material properties of the intended product are achieved simultaneously [1]. Classifications of single step AM processes are shown in Figure 1.5. These processes usually involve consolidation by fusion of similar materials in a thermal or chemical process. In contrast, multi-step processes utilize two or more operations to form the desired part geometry. Typically, the first process provides the basic geometric shape, and the following process consolidates that part, giving it the intended functional properties [1]. It is common for additional steps to be performed after the fundamental forming to fine tune the material and mechanical properties of the parts. These additional steps can include machining, heat-treatment, surface treatments, or even secondary CM processes.

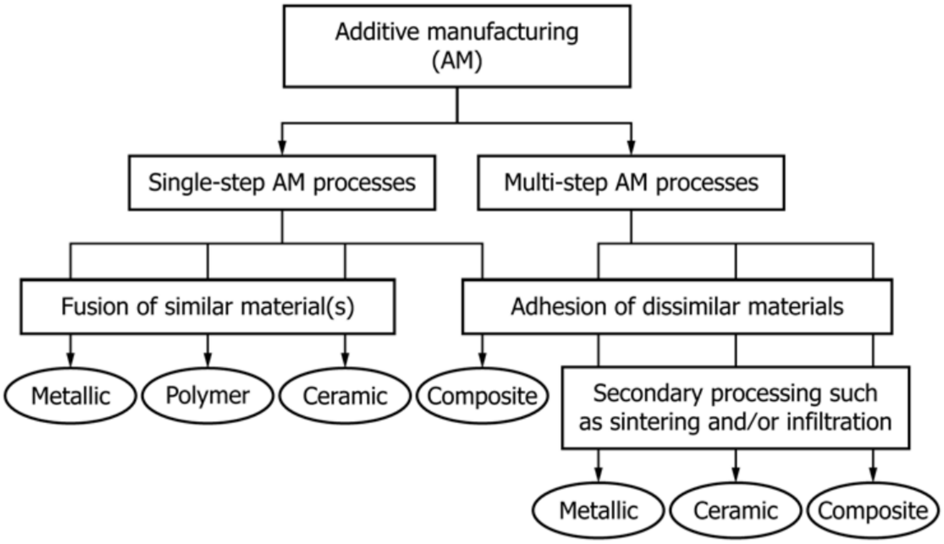

Figure 1.4: Single-step and Multi-step AM process principles, as defined by ISO / ASTM. Reproduced from ISO/ASTM 52900:2015(E) [1].

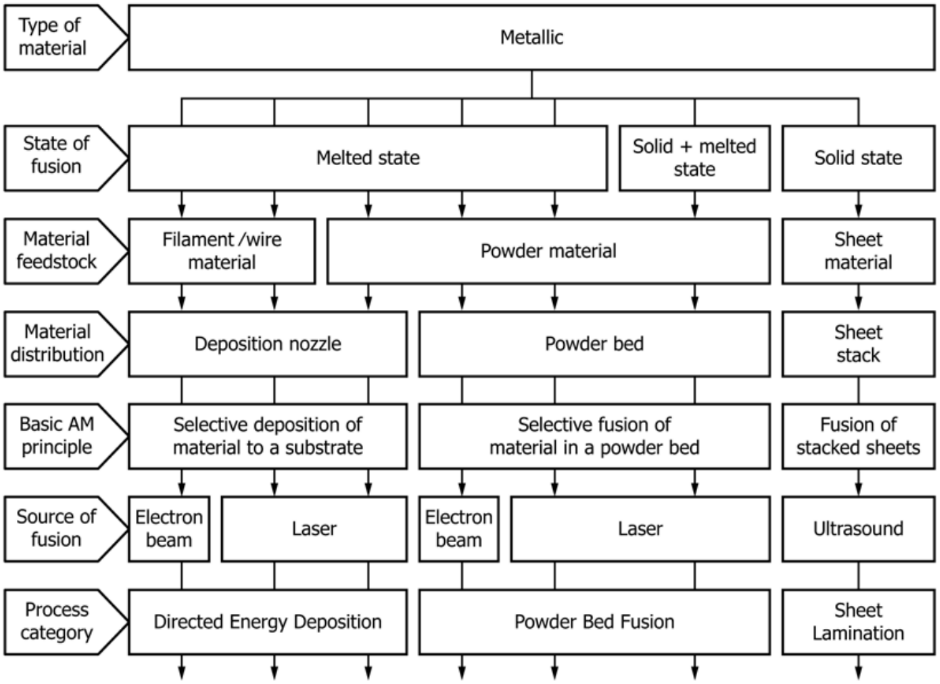

Figure 1.5: Overview of single-step AM processing principles for metallic materials, as defined by ISO / ASTM. Reproduced from ISO/ASTM 52900:2015(E) [1].

1.2 Laser and Electron Beam Powder Bed Fusion

Powder bed fusion (PBF) is a single-step AM technique that is well suited for a variety of material systems, including metals, polymers, ceramics, and even multi-material composites. The differentiating feature of PBF technologies from other AM technologies is the use of a powder bed as a material feedstock reservoir, and occasionally as structural support for the printed parts [10]. During the printing process, a thin layer of loose powder is spread uniformly across the build area. An energy source (usually a laser or electron beam) is focused on to the surface of the powder bed to heat the powder to the point of melting [11,12]. The molten metal quickly solidifies and fuses with the underlying layer, consolidating it into a part. After the powder bed is exposed, the entire bed is lowered the desired layer thickness and new powder is spread, repeating the cycle.

PBF technologies largely fall into one of two categories, either Laser PBF (L-PBF) or Electron beam PBF (E-PBF). A schematic of the AM PBF system using a laser heat source is shown in Figure 1.6. The main distinction between the two is their source of directed energy for melting the powder at the powder bed, however differences in their operation lead to each technology having specific advantages and disadvantages.

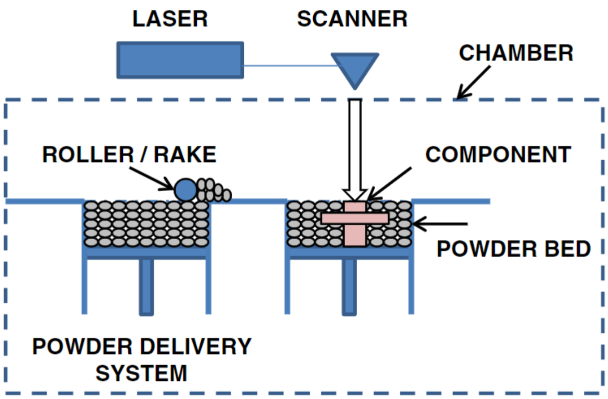

Figure 1.6: General schematic of an AM powder bed system, reproduced from [12].

1.2.1 Laser Powder Bed Fusion

First invented by Carl Deckard in 1986 [2], L-PBF emerged as a novel AM technique in the late 1980s to the early 1990s [3,13]. This technology uses a laser in the range of 20 W to 1 kW to melt sequential layers of powder, typical in the range of 20 - 100μm [11]. Early L-PBF techniques focused on sintering metal powder into a green body for subsequent consolidation into solid parts, rather than fully melting the powder directly into fully solid parts. Modern L-PBF machines can produce fully dense metallic parts with mechanical properties rivaling those of wrought metals [14]. L-PBF processes are performed at ambient temperatures and pressures under an inert gas atmosphere, to prevent rapid oxidation of the molten metal. Typically, inert gas is continuously pumped through the chamber to help clear smoke and debris that are generated during the lasing process. Due to the rapid solidification and cooling of the metal from the liquid phase to near room temperature, residual stresses develop in the parts during printing. To counter-act these stresses, support structures are designed to attach the part firmly to the build plate [11]. They also function to transfer and dissipate heat, and as platforms onto which horizontal or overhanging structures can be built.

1.2.2 Electron Beam Powder Bed Fusion

E-PBF uses a focused electron beam to deliver the energy required to melt the powder. The electron beam is generated in an electron gun, before being accelerated by an electric field, typically of around 60 kV. Electromagnetic lenses focus the beam to a narrow spot, which is moved around the build area by magnetic scan coils [11]. Due to the use of an electron beam, the system requires a high-vacuum environment to operate and can only be used on conductive materials. Consequently, E-PBF is limited primarily to metal and metal alloy systems. To increase conductivity of the powder bed, a defocused electron beam is used to heat the powder bed to elevated temperatures, on the order of 700°C for titanium alloys. This causes the powder to sinter and fuse together, increasing the electrical and thermal conductivity of the bed. As a side effect, the elevated temperatures achieve low-temperature annealing of the metal, removing residual stresses that develop from the rapid cooling of the melt pool. The stress-relief process, coupled by the increased rigidity of the powder bed due to the sintering, reduces the need for support material on the printed parts. In fact, it is possible to print parts fully detached from the build plate, supported only by the sintered powder block. The heat cycling also effects the powder, changing its properties much quicker than in L-PBF systems [15].

The L-PBF and E-PBF processes enable AM of metal powders and the development of metal components with almost unlimited geometry. Essentially any metal can be printed using these PBF technologies, provided it can be produced in a suitable powder form. Alloys can be used as well, either directly in powdered form or alloyed in-situ from corresponding amounts of pure metal powders. Due to the high cost of production, however, industrial use of PBF has mainly focused on high value commercial metals, such as aluminum and titanium. Both are metals widely used in medical and aerospace industries, due to their high strength to weight ratios and biocompatibility. Medical and aerospace fields also tend to have requirements of high part complexity.

1.3 Titanium Metallurgy

Due to a combination of excellent strength to weight ratio, biocompatibility, and corrosion resistance, titanium alloys are widely used in the aerospace and medical device industries [11,16]. Titanium alloys are also a major focus for PBF AM, both for E-PBF [14,17,18] and L-PBF [14,17,19].

Elemental titanium has two distinct crystal phases, a low temperature “α” phase where the atoms adopt a hexagonal close-packed (HCP) structure, and a high temperature “β” phase with a body-centered cubic (BCC) structure [16]. Elemental, or “commercially-pure”, titanium adopts the HCP α phase at room temperature, and transitions into the β phase only when brought above 880°C. Many elements readily alloy with titanium, and the addition of these atoms to the crystal system can affect the thermodynamic equilibrium of the system. Some alloying elements push the system towards β-phase stability, while others encourage α-phase stability [16]. Oxygen, an α-stabilizer, increases the high temperature stability of the α phase, as shown by the Ti-O phase diagram shown in Figure 1.7. Above about 12.5 wt% O, the β titanium phase is fully unstable at all temperatures. A list of other common alloying elements and their effect on the structure of titanium is provided in Table 1.1. Depending on the mix of alloying elements, the alloy may be classified as an α alloy, an α-β alloy, or a β alloy. The naming convention reflects the predominant phase present in the microstructure, with α alloys showing predominantly or entirely alpha phase, and beta phase correspondingly for β alloys. Alloys in between these are classified as α-β alloys and may contain both phases in a meta-stable equilibrium in their structure [16]. Alloys high in α-phase tend to have better chemical and corrosion resistance, while beta alloys have inherent strength from their metastable structure which readily produces precipitates and other strengthening structures [16]. By contrast, α-β alloys tend to have an excellent combination of strength and ductility, which gives them wide applicability to many industrial uses [20].

Table 1.1: Typical alloying elements of titanium and their effect on the material's structure

Element	Effect on Structure
Al, Sn, O, C , N	α-phase stabilizer
H, V, Mo, Cr, Cu	β-phase stabilizer
Zr	α and β strengthening
Si	Improved creep resistance

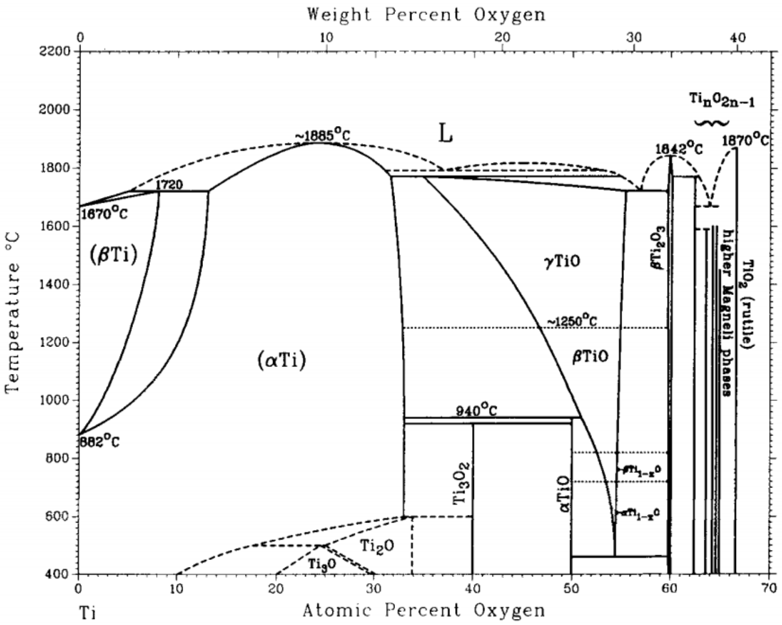

Figure 1.7: Ti-O phase diagram. Adapted from Murray & Wriedt (1987) [21]

In metal AM in general L-PBF in particular, rapid solidification of the melt pool results in epitaxial β phase grain growth from the underlying solid metal. The β phase preferentially grows in the ⟨ 1 0 0 ⟩ direction, resulting in columnar grains aligned roughly with the build direction [13]. As the metal promptly cools, the β phase becomes unstable, and rapidly decomposes into more stable forms. The transformation of the β phase can occur though a martensitic process (diffusionless) or through the nucleation and growth (diffusional) of primary α phase grains [20,22]. In the latter process, the α phase grains grow preferentially along the (110) family of crystallographic planes of the β phase, resulting in a “basket weave” or Widmanstätten structure of plate-like or needle-like alpha phase grains, termed “laths”[13,22]. Images of this type of structure in L-PBF Ti-6Al-4V are shown in Figure 1.8**.** A relationship exists between the crystallographic orientations of the parent beta grains and the resulting alpha laths, as given by the Burgers relations in equations 1.1 and 1.2 [13].

This relation can be used to group α laths to their parent β grain orientation if the orientation of the individual laths is known, often determined by electron back scatter diffraction [13].

$$(1\ 1\ 0)_{\beta} \leftrightarrow (0\ 0\ 0\ 1)_{\alpha} \qquad \text{Eq. 1.1}$$

$$\langle 1\ \bar{1}\ 1\rangle_{\beta} \leftrightarrow \langle 1\ 1\ \bar{2}\ 0\rangle_{\alpha} \qquad \text{Eq. 1.2}$$

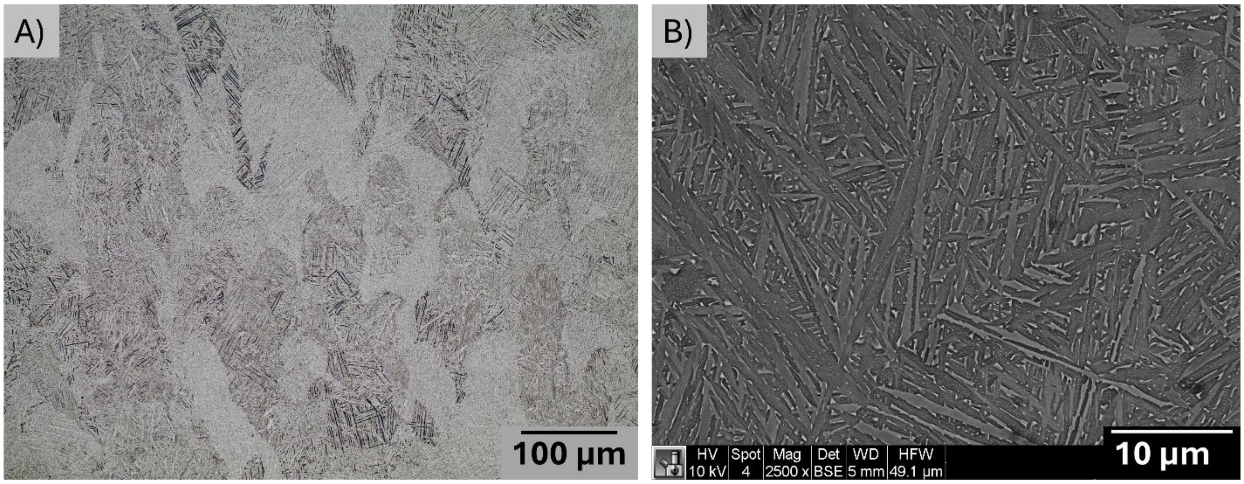

Figure 1.8: Micrographs showing typical microstructure for Ti-6Al-4V after a stress relief heat treatment. (A) an optical micrograph at low magnification showing prior beta grains. (B) an SEM microgrpah at higher magnification showing alpha laths in a Widmanstätten structure.

In metal AM of Ti-6Al-4V, energy is transferred into the metal rapidly and directionally. The molten metal initially solidifies into β phase grains, referred to as prior-β grains, which decompose into alpha phase upon further cooling. Elongation of the prior-β grains occurs due to heat conduction towards the build plate and epitaxial crystal growth [5,13]. Fast cooling rates of the beta phase metal results in the formation of a fine α` martensite structure [4,5,13].

In the as-built condition, L-PBF parts consist of an α′ phase and exhibit relatively high yield and ultimate tensile strength, but have low ductility as compared to annealed or wrought Ti-6Al-4V [13]. To improve the ductility of parts manufactured by L-PBF, stress relieving and annealing heat treatments are typically utilized. These heat treatments causes the α′ structure to decompose into α and β phases. The decomposition occurs as fine precipitates of α nucleate heterogeneously in the martensite and grow and coarsen over time [13,20].

In E-PBF, the elevated temperature of the build chamber during operation (typically in the range of 700ºC) mimics standard post processing heat treatments of L-PBF, resulting in a transformation of the α` martensite into α and β phases, with the α phase consisting of fine acicular grains [13]. The longer heating times of E-PBF further coarsen the alpha grains into thick lamellar plates, resulting in the characteristically thick alpha lathes typical of E-PBF.

1.4 Powder Reuse

1.4.1 Reuse Strategies

While many advantages of AM were discussed previously, there are also disadvantages. The the largest disadvantages of PBF AM technologies are typically the cost of the equipment, the cost of feedstock materials and the special precautions required for material handling. For metal PBF, fine metal powders are used as the precursor material. These powders are expensive and energy intensive to produce. The high cost of the powder is one of the biggest obstacles in the widespread adoption of PBF technologies [12,23]. As such, AM is generally only favored over CM for near-net shape manufacturing in cases with small production lots, where the higher cost of the AM specific raw materials is outweighed by the fixed startup costs of CM [12]. For AM to be commercially viable at a larger scale, the high cost of the raw materials needs to be addressed. Powder reuse, where the unmelted powder from a build is collected and re-used in a subsequent build, is an oft-cited strategy for increasing the energy and cost efficiency of AM [6].

The most basic form of powder reuse is performed without maintaining the overall powder volume. Specifically, the unused powder from a build is collected, possibly sieved and mixed, and returned to the machine to be used again, without any additional material being added to compensate for the loss in the previous build. This process is shown schematically in Figure 1.9(A). The advantage of this reuse strategy is traceability, as all the powder in each build is uniform in age and quality, being from the same original batch. However, the obvious disadvantage with this strategy is that the quantity of powder available decreases over time, as powder is consumed in each build. The reduction in powder volume with each build is a distinct disadvantage for PBF, where a minimum volume of powder is required to fill a build volume regardless of the quantity of metal being printed. As such, this strategy very quickly leads to not having sufficient powder to run a complete build.

The second reuse strategy, which is more common, is to replenish consumed powder with virgin powder after each build [24]. Figure 1.9(B) provides a schematic of this approach, which can maintain sufficient volume of powder to run builds indefinitely. However, the mixing of powders of different ages can result in a powder batch with a wide range of qualities and properties. Depending on the proportions of powder added and the number of reuse cycles, a small portion of powder may reach a very high cycle-age. Here, “age” refers to the number of reuse cycles a particular portion of powder has experienced, and generally the amount of accumulated degradation the powder has experienced. The small portion of highly aged and therefor low-quality powder could negatively impact the quality of the part, even when the average powder quality does not reflect that; it makes the powder batch less uniform and more variable [15].

A third reuse strategy involves treating a large body of powder as a single batch. Multiple builds are performed on the starting batch of powder without reuse, and then the recovered powder from each of those builds is combined into a new batch, with all the powder having consistent age and quality. The new batch is then used to print multiple builds, and the process repeated, as shown in Figure 1.9(C). Clearly, this process has the same advantage as the simple reuse process, but with enough powder to perform the required number of builds without running out of powder. Nevertheless, the number of builds is limited, as eventually the powder will be consumed to the point of not having sufficient powder to perform a full build.

A fourth reuse strategy is shown in Figure 1.9(D), however it requires a specific machine setup. Specifically, it requires a machine with gravity-fed dispenser hoppers, where the powder is loaded in at the top, and is dispensed from the bottom. In these machines, unused powder can be left in the hopper after a build, and the recovered powder can be added back, on top of the unused powder. In the next build, the lowest cycle-age powder is used first, followed by the next highest cycles-age, and so on. The advantage of this reuse strategy is that the youngest powder is always used first, so all the powder stays relatively consistent in age and quality. However, it is not possible to use this strategy in trough style machines, where powder is loaded into a piston controlled hopper, and then is dispensed back out the same side.

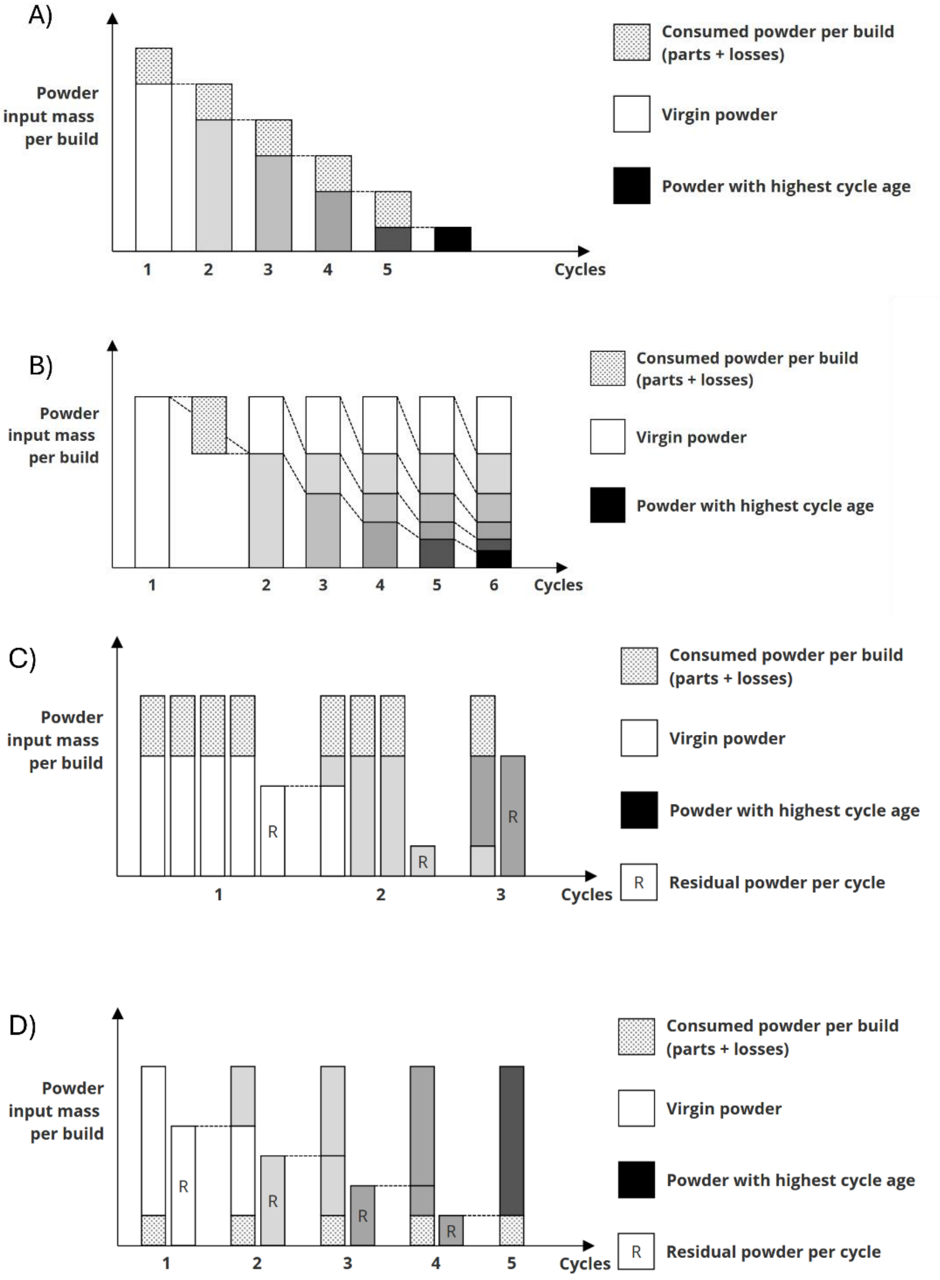

Figure 1.9: Common methods of powder reuse in PBF AM. A) Simple reuse where powder is consumed without replacement. B) Powder reuse with replacement. C) Powder batch reuse strategy. D) Continuous feed reuse strategy in top loading hoppers Adapted from [24].

Regardless of the reuse strategy, powder degradation accumulates over time. Degradation can occur through repeated heating cycles, which thermally age the powder, through accumulated mechanical deformation of the powder particles, and through contamination of the powder from foreign materials. The most common form of powder degradation is oxygen contamination, where oxygen from the external environment is incorporated into the powder particles [15].

1.4.2 Effects of Powder Reuse

Powder reuse has been studied extensively in relation to AM systems. While its effects on powder quality are relatively well understood, some areas remain less developed [25]. Average particle size has been shown to increase with powder reuse, albeit often slightly [26–33]. The size of the powder particles used in PBF AM has a significant influence on the quality of the metal produced, and is one of the most important factors of powder layer quality [10,34,35]. Packing density of the powder in each layer depends on the distribution of particle sizes and morphologies, which influences how the powder will flow when distributed across the build area. Powder reuse is often associated with improved flowability [30,31,36–42]. In addition, there is evidence that oxygen content increases gradually with reuse [7,27,28,30,31,36,37,40,42,43], which can be detrimental to the mechanical properties of parts produce from some alloys [44,45].

Powder recycling has been studied extensively in E-PBF, with most studies reporting increased surface roughness of the particles, decreased sphericity, increased flowability, and increasing levels of oxygen with reuse [46–49]. Ghods et al. showed that oxygen content in powder increased steadily when reused in an E-PBF system [50]. Notably, E-PBF systems typically hold the build chamber at high temperatures, often exceeding 700°C, to partially sinter the powder in the chamber to create a conductive path through the unmelted powder. High temperature leads to changes in the microstructure of the particles, but more importantly it enables surface oxides to diffuse into the particles [15]. In contrast to E-PBF, L-PBF does not require a high temperature build environment, so changes in powder chemistry are generally much slower to accumulate [25].

Despite the large body of literature exploring the effects of reuse on powder quality, most reported studies employ a single machine and powder producer. That approach cannot reflect the extent of variability in rate of powder “aging” between manufacturers. Even when comparing two builds performed in identical machines, slight differences in the local environment, or how the powder is stored, transported, and handled, could influence its exposure to oxygen and moisture, and how the powder ages. To the author’s knowledge, no comprehensive study has been reported that evaluates the changes in powder quality in titanium alloys with reuse across multiple machines. That limitation serves as motivation for the present investigation.

1.5 Metal Condensate, Spatter, and Ejecta

Metal AM by L-PBF is a complicated process of melting of the metal powder used and its resolidification with nearest neighbors. Due to the low laser absorptivity and high melting point of many of the metals often used in PBF, a significant energy input is required to melt and consolidate the powder bed [51]. Rapid and intense heating during laser interaction with the powder results in a plume of vaporized metal caused by the melt pool surface reaching its boiling point [52]. This process, combined with melt-pool dynamics, leads to the generation of metal vapor, spattering of molten metal, and ejection of loose powder particles and molten metal [52–55], in a manner shown schematically in Figure 1.10. Recoil pressure from this rapid expulsion of material creates instabilities in the melt pool, which can lead to droplets of molten metal (spatter) and loose powder being ejected from the adjacent area [51–53,56,57]. The metal vapor is ejected rapidly from the melt pool, reaching speeds potentially exceeding 1000 m/s [56]. Images of a metal vapor plume expanding from the melt pool are shown in Figure 1.11. Above the surface of the powder, the metal vapor rapidly cools and condenses into a cloud of airborne nanoscopic particles, which are carried out of the build chamber by the flow of inert gas over the powder bed. Gas outflow is subsequently captured and passed through a series of filters before being recirculated back through the build chamber.

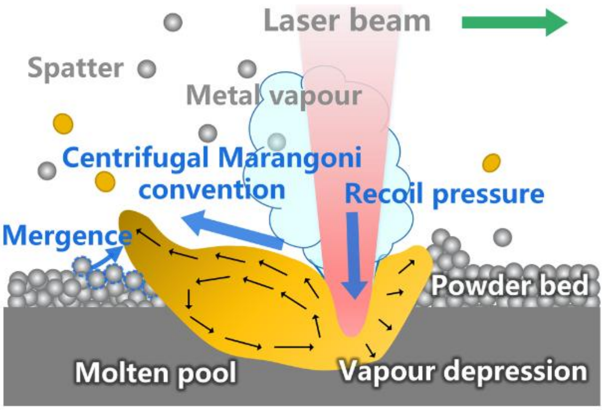

Figure 1.10: Diagram of the interactions at the laser melt pool interface Adapted from [57].

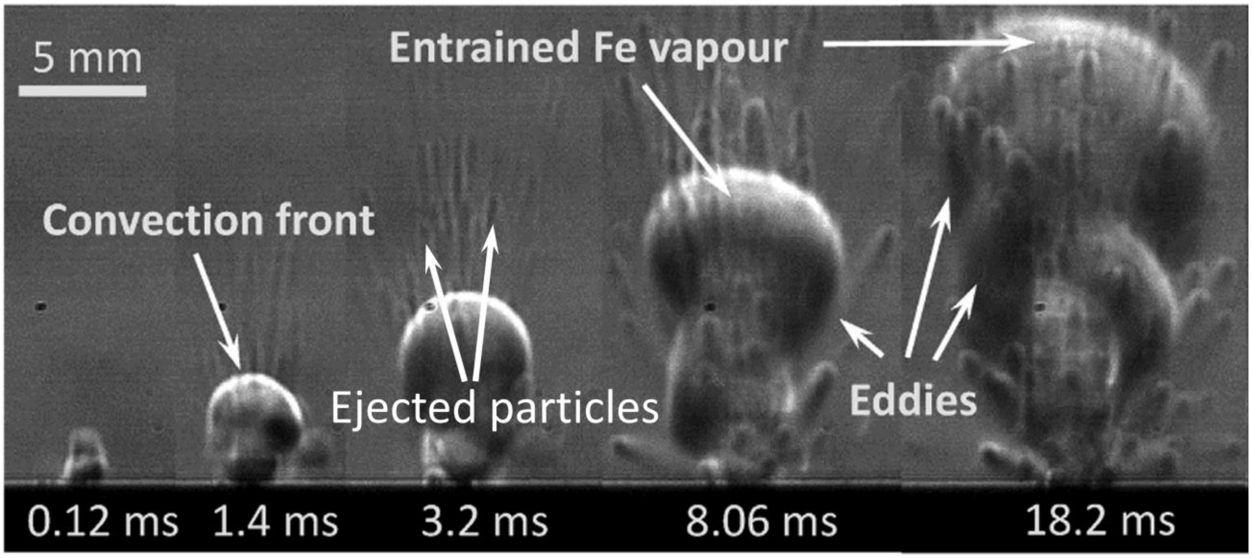

Figure 1.11: Vaporization plume by schlieren imaging showing ejected metal particles traveling through a metal vapor plume. Adapted from [56].

The character of the smoke that develops from the metal vapor is an area of active interest. Several studies on L-PBF systems have suggested that a major constituent of the recondensed vapor plume is a nano-particulate material referred to as condensate or Metal Vapor Condensate (MVC) [5,52–54,56,58]. Keaveney et al. published images of MVC formed from laser melting of Ti-6Al-4V showing morphologies of aggregated nanoparticles [59]. Likewise, Noskov et al. and Sutton et al. published images of MVC formed during L-PBF of stainless steel powders [53,54]. Images from these publications are presented in Figure 1.12 to show the typical morphology of this material.

The particles produced by the laser melting process are similar in morphology and formation to the nano-material produced by the Inert-Gas Consolidation (IGC) process described by Simchi et al. [60]. IGC involves the intentional vaporization, condensation, and collection of MVC as a method of generating nanopowder particles of various metals. The mechanism of formation of the nanoparticles in IGC is a homogeneous nucleation of metal nanoparticles from the vapor phase as a result of the loss of energy (cooling) of the metal atoms through collisions with gas atoms [60]. The resulting size of the nanoparticles is related to the normalized pressure (the ratio of the chamber pressure to the metal vapor pressure) and the normalized temperature (the ratio of the peak evaporation temperature to the boiling point of the metal). The similarities between the IGC process and the melt pool dynamics in L-PBF imply that the formation of MVC in L-PBF likely occurs through a similar pathway.

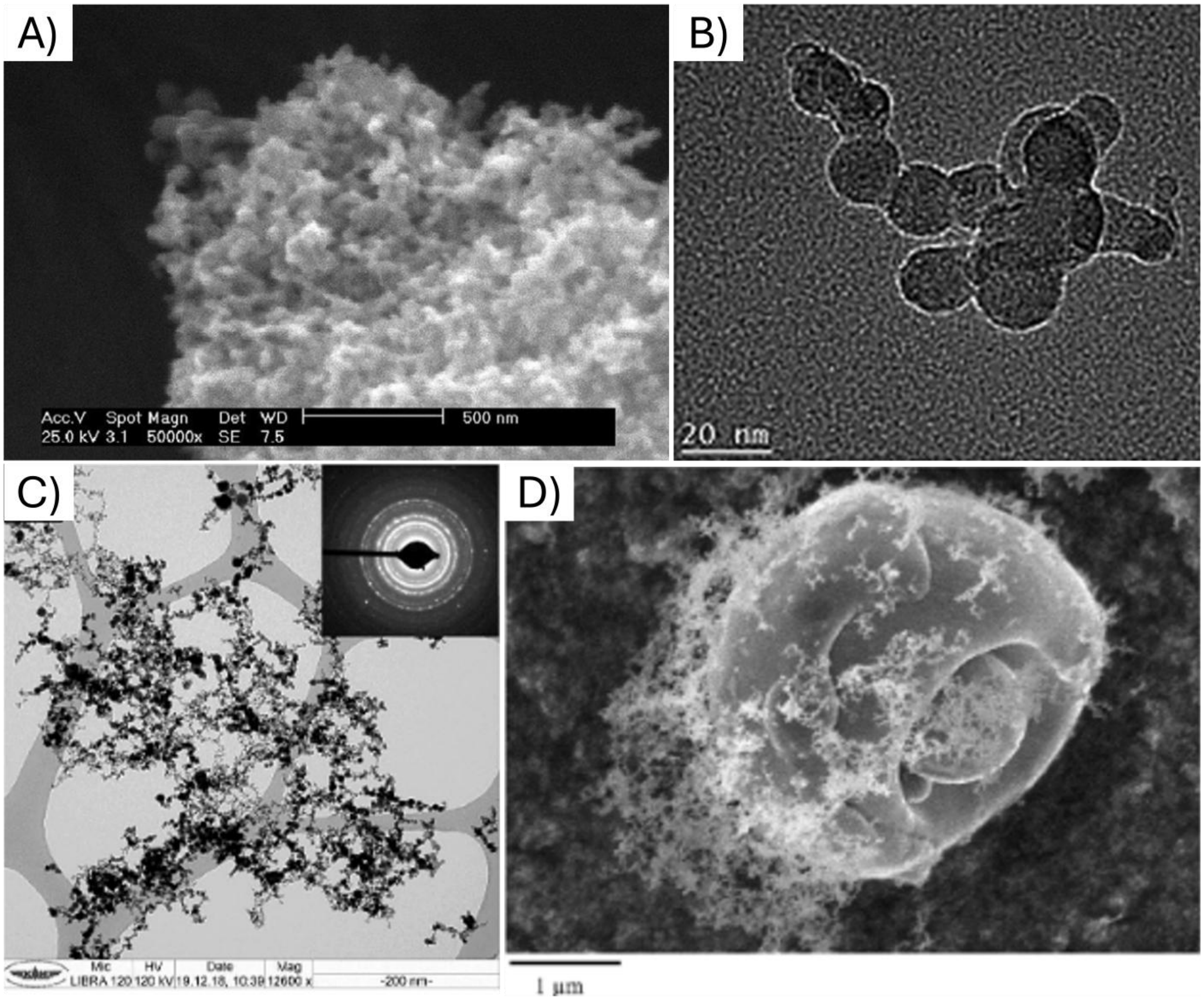

Figure 1.12: SEM images showing examples of MVC observed from (A) IGC by Simchi et al. [60], (B) L-PBF of titanium powder by Keaveney et al. [59], (C) L-PBF of stainless steel powder by Noskov et al. [54], (D) L-PBF of 304L stainless steel powder by Sutton et al. [53]. Images reproduced from sources.

The development and dispersion of MVC in the build chamber can lead to detrimental effects to the parts being built, including contamination of previously melted surfaces [5,52] and the development of pores [53,58,61]. Agius et al. discuss the role of condensate and spatter on defect generation in the context of their interference with the laser spot [5]. Ladewig et al. show how redeposition of spatter can create process irregularities in the melt layers [52]. Degradation in metal quality due to MVC has been observed in L-PBF of many metals and their alloys, including stainless steels [53,54,61], aluminum alloys [61], Inconel [52], and titanium alloys [59,61].

The high surface-area-to-volume ratio of the MVC structures make the material highly reactive and prone to rapid oxidation, which can lead to overheating and ignition of the material when present in large quantities [62]. Additionally, studies have demonstrated that the typical process involved with PBF leads to exposure of the operators to respiratory hazards in the form of ultrafine metal particles [63]. Due to the hazards associated with handling the condensate material it is not considered to be recyclable, and instead industry efforts focus on the safe containment and disposal of the material.

1.6 Objective

Enabled by a round-robin investigation focused on variability in metal quality, this dissertation evaluates the effects of powder reuse in L-PBF on powder variability over the course of ten builds, split into two phases. The study presents a novel approach to powder reuse through a similar "round robin" style study involving six independent participants following the same operational procedure and a single lot of plasma-atomized grade 5 Ti-6Al-4V metal powder. Important metrics of powder quality are monitored throughout the study and compared to mechanical properties of the metal produced over time and between participants. Several categories of variability are considered, including intra-build (referring to variability that arises within individual builds), inter-build (variability that arises from one build to another on the same machine), and inter-machine (variability that arises between different machines run under the same nominal conditions). Byproducts of the L-PBF process, including spatter and metal vapor condensate, are investigated and characterized as important components of variability in powder quality. Specifically, this dissertation aims to address the following objectives:

Aim 1: Quantify changes in powder quality for a six-build reuse program between six partners operating identical make and model of L-PBF machines using the same powder source.

Aim 2: Extend the powder reuse results for an additional four builds from three of the contributing partners.

Aim 3: Characterize the properties and behavior of the metal vapor condensate produced during L-PBF AM.

Aim 4: Evaluate the behavior of spatter in the build chamber during the printing process.

Chapter 2 Round Robin Project

2.1 Background

The content of this dissertation develops on results of a larger investigation concerning the variability in properties of AM metal by L-PBF. The parent investigation, designated as the Round Robin (RR) study, involved a cooperative effort between the University of Washington (UW) and five industry partners to build and characterize metal produced by L-PBF AM. To minimize sources of variability, all partners were required to perform their prints on the same make and model of L-PBF machine, namely the M290 produced by EOS (EOS GmbH, Germany). Details of the machine, material, and study design are described below.

2.2 Machine

The EOS M290 is a piston-fed L-PBF machine with a build volume of 250 x 250 x 325 mm. The M290 design involves a dispenser hopper and a collection hopper. A schematic of the build chamber of the M290 is shown in Figure 2.1. Powder is loaded into the dispenser hopper before the start of the build. Powder is swept across the build plate layer-by-layer through the action of a fixed recoater blade. The depth of the powder layer is controlled by the precise downward index of the build plate to obtain consistent layer heights. Excess powder is carried off the build plate to the collection or overflow hopper on the left side of the machine. A 1060-1100 nm Yt-fiber laser is focused to a spot and rastered across the power bed by the high precision optics system. The heat from the laser selectively melts areas of the powder bed to produce a solid part layer-by-layer. Solidification of the molten metal occurs nearly instantaneously after laser exposure. Once the laser rastering is complete, the build platform is lowered and a new layer of powder is swept across.

Throughout the build process, argon is pumped through the build chamber to keep the environment under an inert atmosphere. The gas enters the chamber through vents in the top and rear of the chamber, passes over the build area, and exits the machine though a nozzle assembly in the front of the chamber. The argon then flows through a series of filters before being recirculated back through the build chamber. The filtration steps remove airborne particulate that gets carried out of the build chamber by the gas flow.

After the printing cycle is complete, the excess loose powder is extracted from the build chamber using a vacuum system. The collected powder is then sieved using metal mesh sieve to remove larger particles and spatter, and then reused in later builds. Once cleaned of loose powder, the build plate with attached parts is removed from the build chamber. The printed parts are fused to the build plate and can be separated using a band saw or by electric discharge machining.

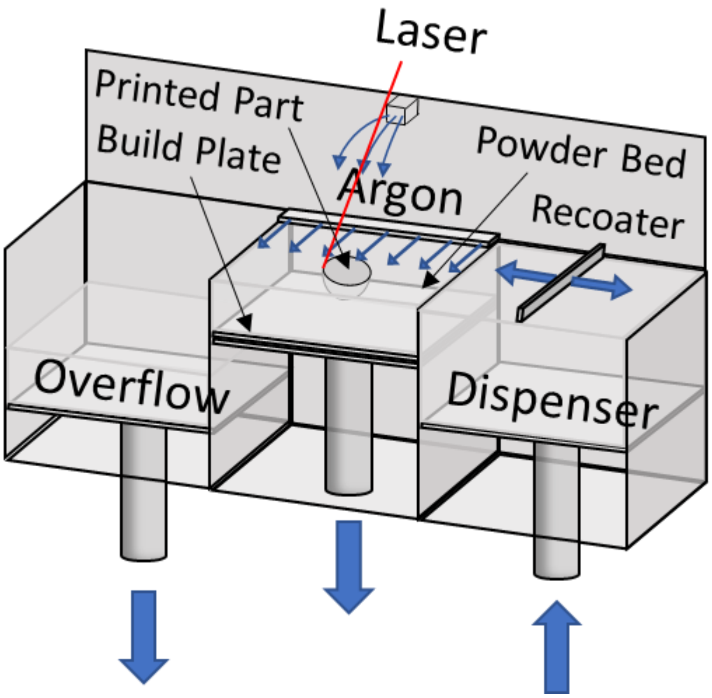

\

Figure 2.1: A schematic of the build chamber of the EOS M290 [64]

2.3 Powder

To best accomplish the goal of isolating inter-machine variability in the RR study, it was vital that all partners started with as close to identical parameters as possible. As such, a single lot of plasma atomized Grade 5 Ti-6Al-4V powder, EOS lot A 482001, was obtained from EOS solely for use in the RR study. Ideally, this single lot of powder would be used for the entire duration of the study, however due to administrative complications a second lot of powder was introduced for the second portion of the study to satisfy the volume of material needed to complete the study. The second lot of powder, EOS lot A 242001, was produced by the same manufacturer and selected to have qualities that conformed to those of the original lot. The particle size distribution characteristics and the chemical composition of both powder lots are given in Table 2.1. Additional powder characteristics can be found in the supplied Certificates of Analysis in Appendix A.

Powder reuse followed the replacement strategy described in 0. Following each build, the mass of powder consumed was replaced with an equal amount of virgin powder. The powder was then thoroughly mixed to homogenize the mass before proceeding with the next build. Samples of powder were taken prior to each build for later analysis.

Table 2.1: The particle size distribution metrics and composition of the powders used in the RR study, from the Certificates of Analysis of the powder lots

Powder Lot	**D10**	**D50**	**D90**	**Wt % Ti**	**Wt % Al**	**Wt % V**	**Wt % Fe**	**Wt % O**
A 482001	30 µm	41 µm	57 µm	Bal.	6.32	4.02	0.21	0.15
A 242001	29 µm	40 µm	57 µm	Bal.	6.38	3.94	0.21	0.13

2.4 Study Design

The goal of the RR study was to quantify the extent of variability in industrial L-PBF AM production of Grade 5 Ti-6Al-4V and to identify contributing causes. Three categories of variability were assessed, including: intra-machine, relating to the spatial variation in metal quality within a single build performed on a single machine; inter-build, relating to temporal variability in metal quality between sequential prints performed on the same machine; and inter-machine, relating to variability in in metal quality between parts produced by different machines following the same procedure. These three categories of variability necessitated a comprehensive and collaborative effort between multiple institutions. To effectively evaluate the spatial variation in metal quality that occurs within a build, the build volume was segmented into two vertical levels, designated A and B, and five horizontal zones, labeled 0-4, as shown in Figure 2.2. This spatial discretization was used consistently in all RR study builds.

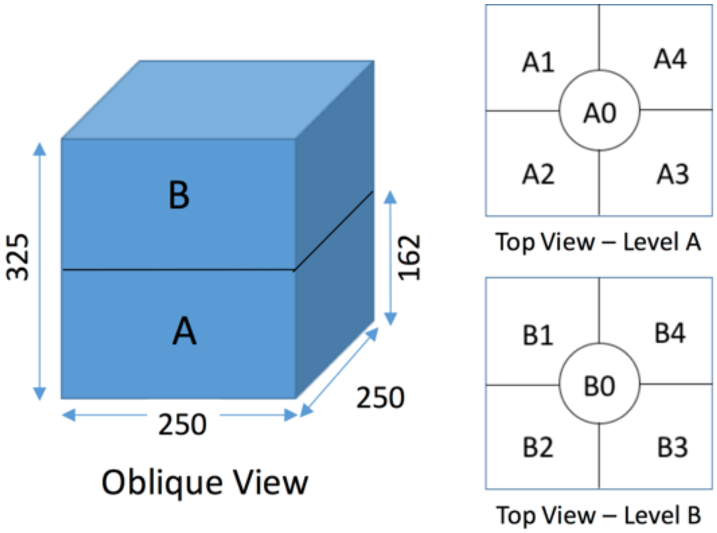

Figure 2.2: Build space discretization used in the RR study builds. The build volume was segmented into two vertical levels and 5 zones in each level.

Inter-build variability describes the extent of property variation that results from small build-to-build differences in material or operation. This variability was evaluated by printing the same build multiple times on the same machine while monitoring changes in powder quality, machine operation, and resulting metal quality. Details of the builds used in each portion of the RR study are detailed later in this section.

Inter-machine variability considers how two or more nominally similar machines may behave differently due to local environmental and procedural variables. Each portion of the RR study leveraged multiple industry participants operating the same L-PBF system (EOS M290) at different locations around the world. Each participant was given the same sequence of builds to perform. To minimize variability arising from different procedures or materials, a Process Control Document (PCD) was developed to standardize as many factors as possible between participants. This document outlined the machine make, model, and pedigree, process parameters including print speed, laser power, and melting strategy, and powder reuse methods. The full PCD is included in Appendix B.

The RR study consisted of several stages, or phases, each intending to evaluate variability in a particular measure of metal performance. Phase I evaluated porosity and tensile properties under quasi-static loading. Phase II extended the results to fatigue performance, considering both a stress relief heat treatment and hot-isostatic pressing. Additional phases may be added in the future to evaluate other properties, such as damage tolerance. The specifics of the build design for these phases is discussed next.

2.5 UWRR Phase I: Static Properties

In Phase I, the tensile properties of AM metal were evaluated under quasi-static loading. The tensile coupon design followed the ASTM E8 subsize specimen dimensions, with extra material allowance to account for post-process milling. The dimensions of the coupons in the as-built and machined conditions are shown in Figure 2.3. After printing, the coupons were sectioned from the build plate and heat treated to relieve residual stress from the printing process. The heat treatment consisted of a 1 hour ramp to 745°C followed by a 2 hour hold and furnace cooling to room temperature. Heat treatments were performed either under argon atmospheres or vacuum to minimize oxidation. Following heat treatment, the coupons were machined to remove the as-built surface texture using a CNC mill at the University of Washington.

Each of the five build zones contained ten vertical and nine horizontal coupons arranged in blocks, as can be seen in Figure 2.4 The nine horizontal coupons were arranged in three rows of three coupons each, with the vertical coupons arranged in groups of five on either side. The vertical coupons were numbered 1-10. Arranged as such, vertical coupons numbered 1-5 were located farther to the back of the machine, while vertical coupons numbered 6-10 were located closer to the front.

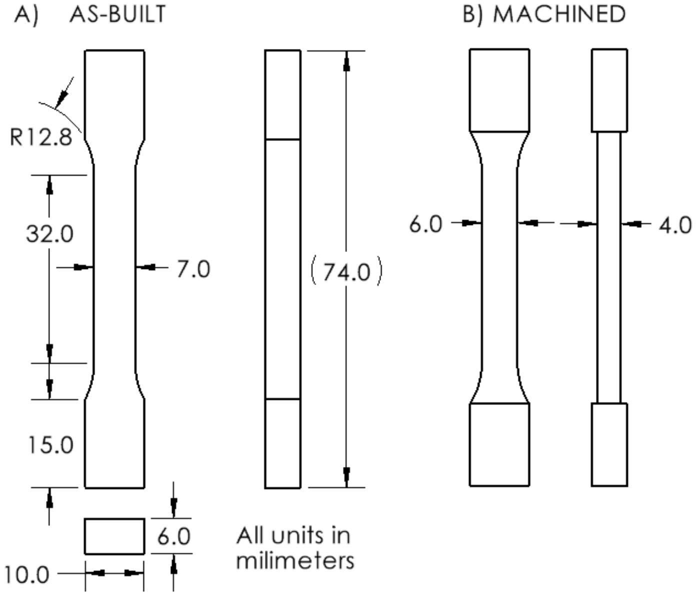

Figure 2.3: Dimensions of the tensile coupons used in Phase I in the (A) as-built and (B) machined conditions.

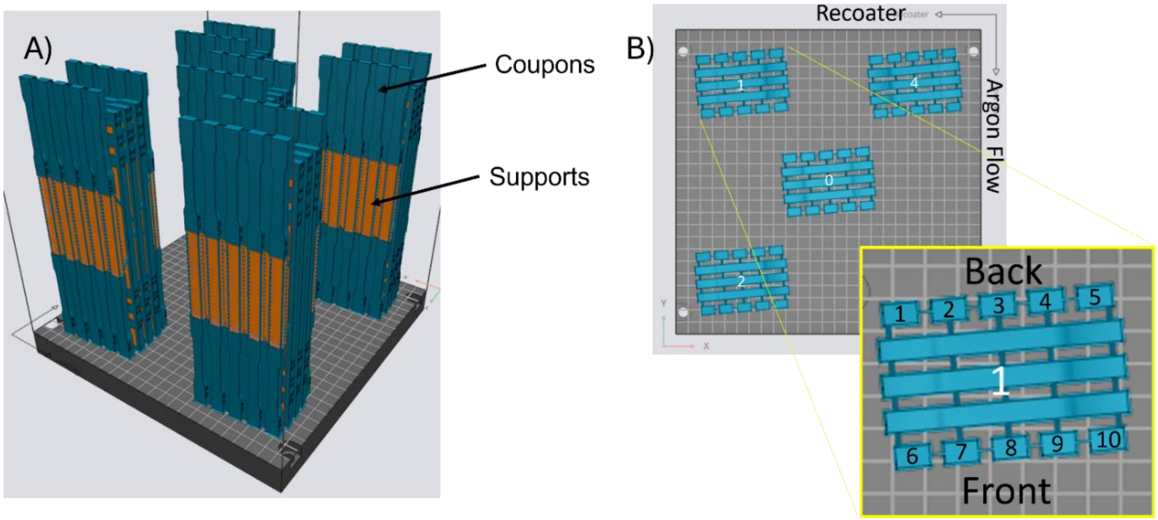

Figure 2.4: A) an oblique view of the full build design used in the Round Robin project. B) Top down view of the build showing zones 0-4. The inset shows a magnified view of zone 1, showing the numbering of the vertical coupons.

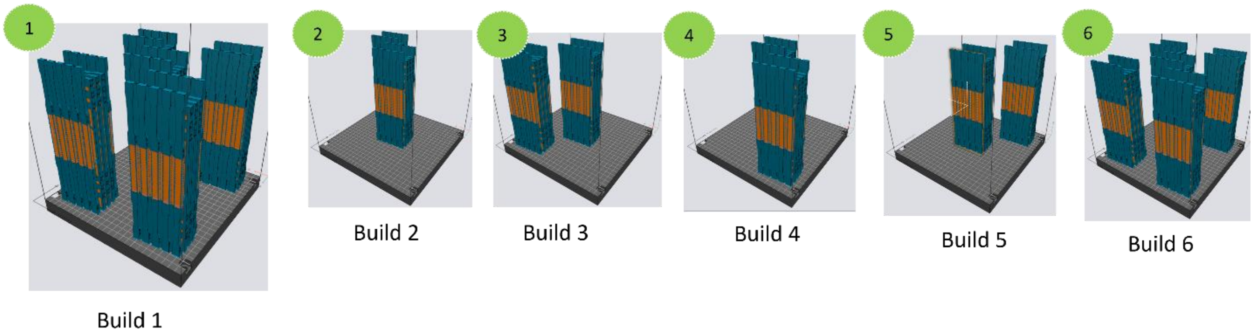

Build 1 Build 2 Build 3 Build 4 Build 5 Build 6

Figure 2.5: Oblique views of the build configurations for the sequence of six builds performed by all partners in the Round Robin study.

Each partner in Phase I of the RR study performed six builds, following the sequence of arrangements shown in Figure 2.5. Builds 1 and 6 consisted of the full complement of 5 zones, while Builds 2-5 each consisted of a reduced build design composed of the center zone (Zone 0) and one of the four corners, rotating from Zone 1 to Zone 4 for each subsequent build. The reduced design allowed for more builds to be conducted using the same quantity of power, which extended the cycle-age of the powder while still allowing for the properties of the powder and metal to be compared build-to-build. Furthermore, since all partners started with the same powder and followed the same build routine, direct comparisons could be made for the same builds across partners to evaluate the inter-machine variability.

Prior to each build, the partners were requested to collect 300 g of powder for later analysis to monitor the quality of the powder throughout the study. After each build, the coupons were sectioned from the build plate and shipped to the UW for post-processing and testing. In total, 4,102 tensile coupons were printed between all six partners.

2.6 UWRR Phase II: Cyclic Fatigue

The build design for Phase II followed the same build space discretization described for Phase I, as shown in Figure 2.2. The finalized design for Phase II is shown in Figure 2.6. Each group consists of 10 vertically oriented and 8 horizontally oriented hexagonal bars. The hex bar geometry of the coupons was selected to account for post-build machining, such that the final geometry of the coupons conformed to the ASTM E466 dimensions for circular cross-section specimens. The machined coupon dimensions are shown in Figure 2.7, and consisted of a test section diameter of 5.5 mm and a test section length of 11 mm. The grip sections were 10.5 mm in diameter and 20 mm in length. The test section was blended to the grip section by a fillet with a radius of 30 mm. The total length of the machined coupons was 75 mm, with an additional 25 mm provided below the coupon to accommodate the chuck for machining.

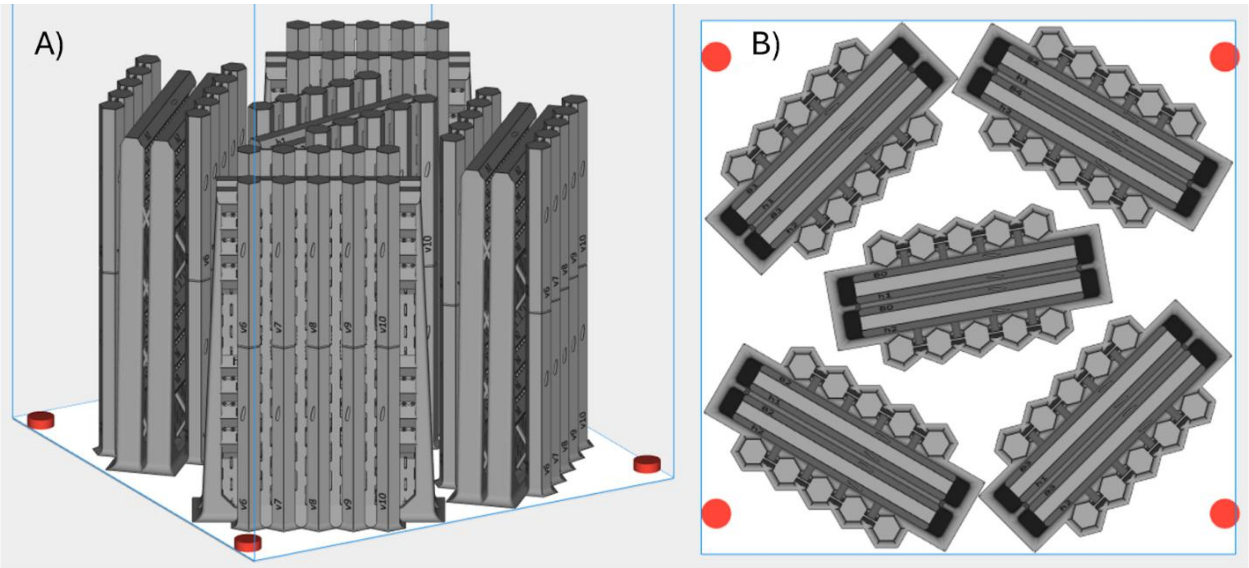

Figure 2.6: Oblique (A) and top (B) views of the final build design used for UW Build 4 and Builds 1-4 for all other partners.

The coupons were numbered following the naming convention of the static properties portion of the study, with each coupon identified by level (A or B), Zone (0-4), orientation (v or h), and number. The numbering of the coupons is shown in Figure 2.8. Labels were debossed on the face of each coupon segment to assist in tracking. The total number of coupons in the fatigue configuration was (10 vertical + 8 horizontal) * 5 zones * 2 levels =180. The total number of coupons printed per participant was (4*180) = 720. To mitigate powder consumption in Phase II and minimize the cost of entry and testing, the total number of builds was reduced to four. Build number was determined to have a limited effect on the static properties of the metal and the quality of the powder. As such the build repetition was de-prioritized as a factor in Phase II.

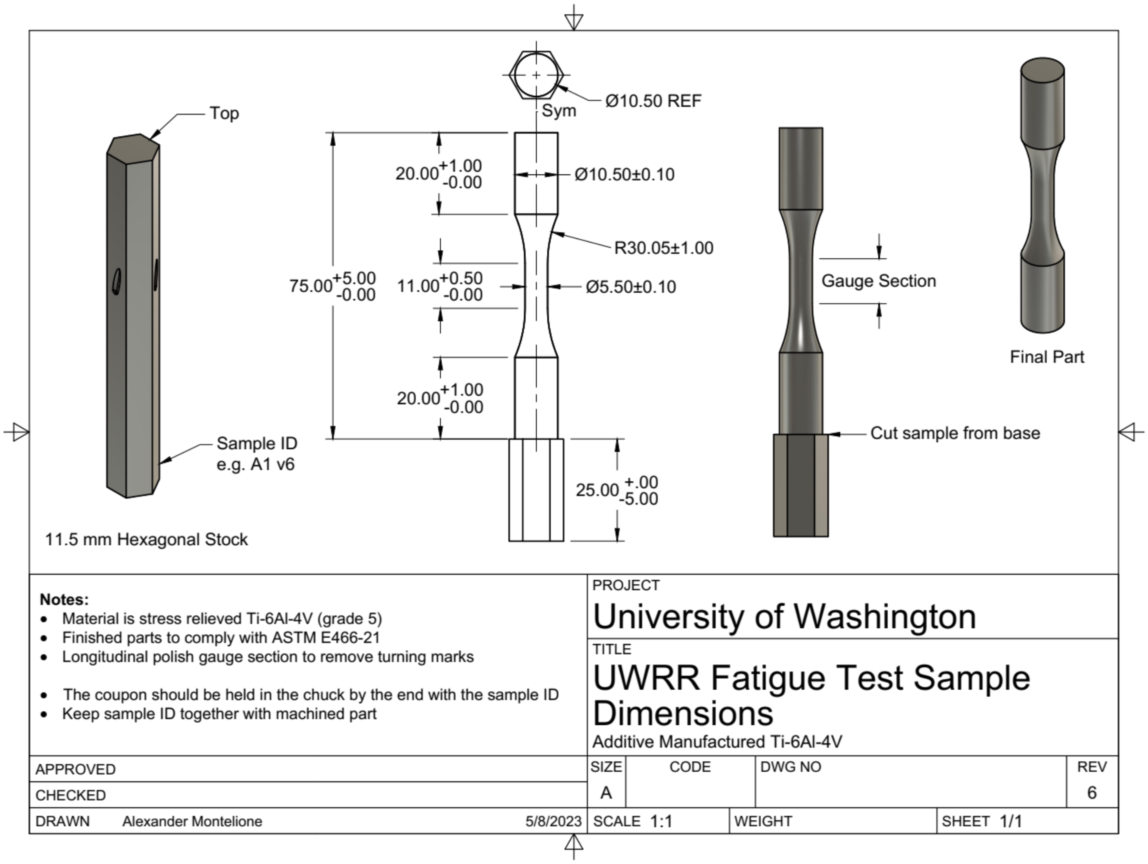

Notes:
- Material is stress relieved Ti-6Al-4V (grade 5)
- Finished parts to comply with ASTM E466-21
- Longitudinal polish gauge section to remove turning marks

- The coupon should be held in the chuck by the end with the sample ID
- Keep sample ID together with machined part

PROJECT	University of Washington			
TITLE	UWRR Fatigue Test Sample Dimensions Additive Manufactured Ti-6Al-4V			
APPROVED	SIZE A	CODE	DWG NO	REV 6
CHECKED				
DRAWN Alexander Montelione 5/8/2023	SCALE 1:1	WEIGHT	SHEET 1/1	

Figure 2.7: Machine drawing for acquiring the fatigue coupons from the printed hex bars.

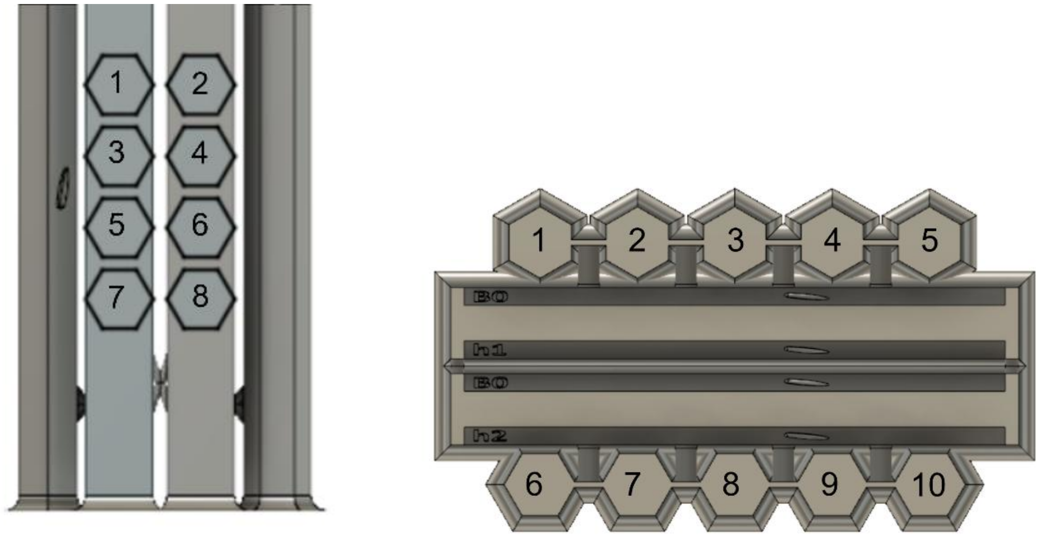

Figure 2.8: Numbering of horizontal and vertical coupons in each zone.

2.7 Design Evolution

While it was intended for all four partners to build the same set of four identical builds, challenges imposed by the design of the build forced changes to be made to the design during the study. As a result, the initial three builds printed by the UW differed slightly in their support design and coupon arrangement. Importantly, neither the design of the coupons nor the build space discretization scheme were affected by these changes.

2.7.1 UW builds 1 & 2

The initial build design followed the overall layout from Phase I, with the horizontal coupons oriented along the X-axis of the build. In Phase I, the coupon clusters were rotated by 5° around Z to avoid the recoater impacting against the flat faces of the coupon clusters. The initial Phase II design had the coupon clusters rotated 10° around Z to accommodate the longer coupons. Figure 2.9 shows the oblique and top-down views of a rendering of this initial build design. But this design presented a challenge due to the length of the coupons and support frame. As seen in Figure 2.9(B), the support frames of Zones 1 and 2 overlapped with those in Zones 3 and 4. Slight overlap also existed between the vertical coupons in Zone 0 with those in Zones 2 and 4. These overlaps would have caused those areas to be exposed twice during the print, which may have led to overheating, swelling and ultimately build issues or failure.

Several options were considered to avoid this overlap, but ultimately it was decided to merge the model bodies of the five zones into a single entity. This solution addressed the double exposure, but significantly increased the build time for the print, due to the scanning strategy employed by the EOS M290. In an effort to decrease the print time, the zones were split at a Z-height of 10 mm. The bases of the zones were merged into a single part that would print without overlap issues, and the top portions of the zones were printed as individual parts to speed up the printing process. A rendering of the merged bases is shown in Figure 2.10 for clarification. Although the UW was able to print this build design twice without issue, when the print file was sent to Boeing for printing, an issue arose that led to a recoater crash and build failure. Upon investigation, it was determined that a flaw in the build design was responsible for the crash. Separating the zones into two parts caused the EOSprint software to apply upskin laser parameters to the top two layers of the bottom part, and downskin laser parameters to the bottom two layers of the top parts, as shown in Figure 2.11(A). Cracks were observed in the failed print approximately 10 mm from the build plate in Zone 4, corresponding to the layers where the upskin and downskin laser parameters were applied. It was concluded that the different laser parameters at these layers caused weak layer bonding, resulting in delamination at these layers which precipitated the build failure.

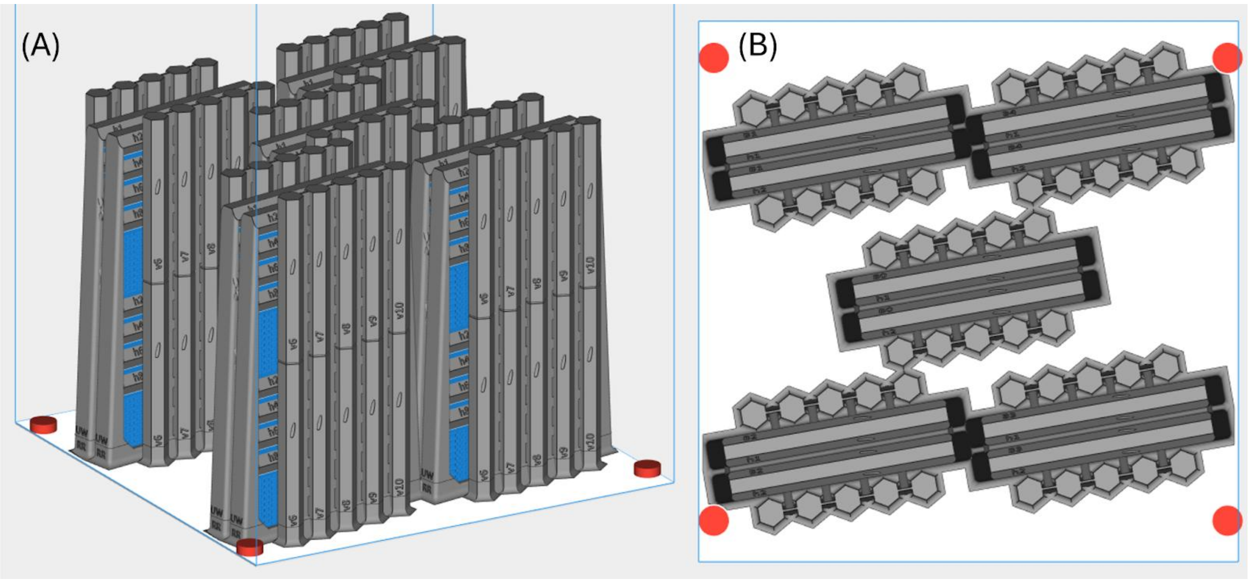

Figure 2.9: Oblique (A) and top (B) views of the initial build design used for UW builds 1 and 2.

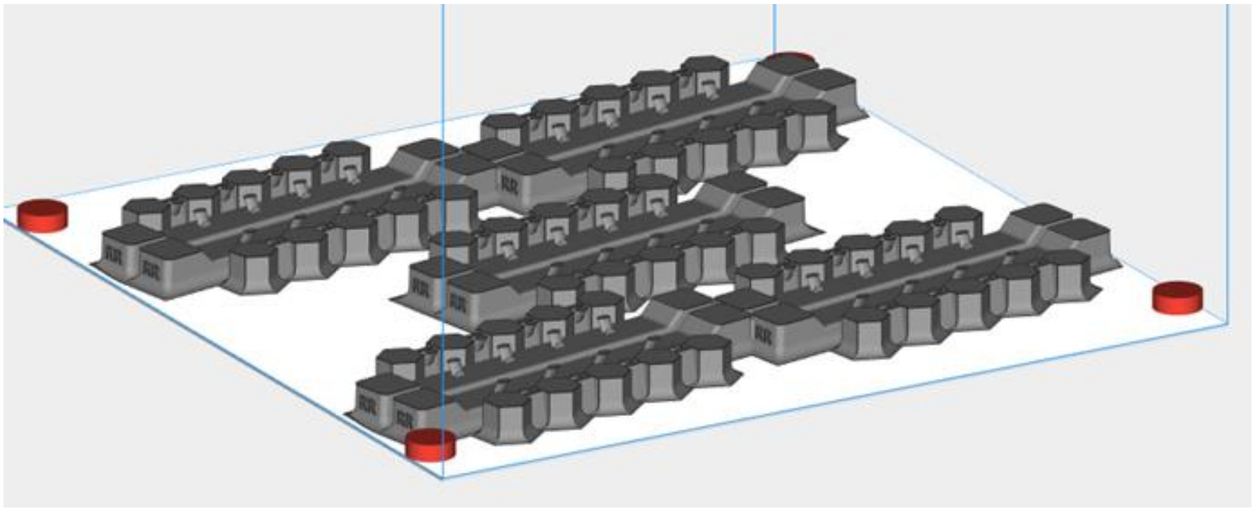

Figure 2.10: Oblique view of the merged bases of the five zones, printed as a single part

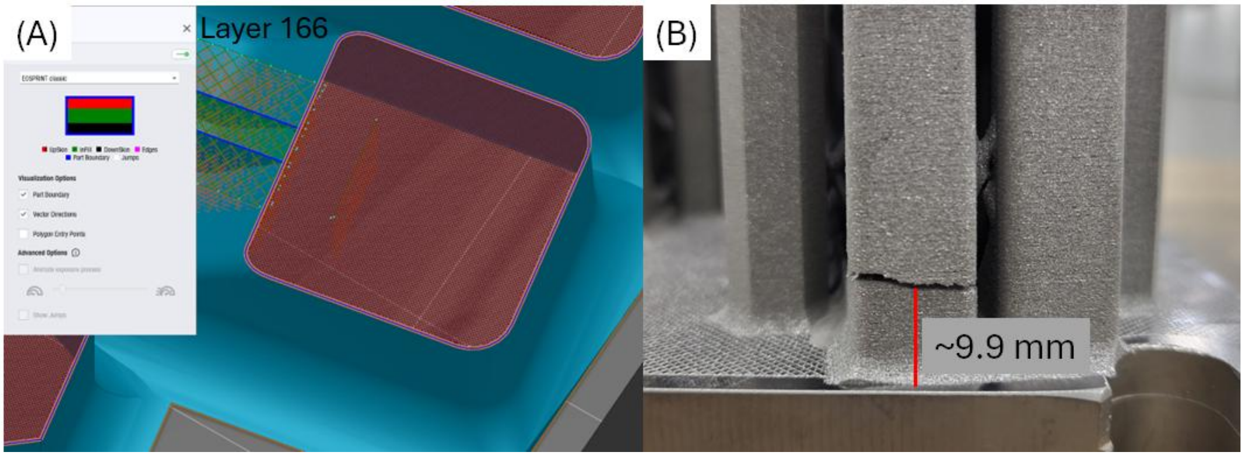

Figure 2.11: Print failure of the Phase II build design. (A) EOSprint screenshot of layer 166 showing upskin parameter laser vectors in red, and (B) crack observed in failed print at approximately 10mm.

2.7.2 UW Build 3

To address the flaw in the initial design, but keep the overall configuration of the build, an alternative segmentation process was attempted, as shown in Figure 2.12. In this intermediate build design, the zones were kept as separate parts, but were split from each other using a plane defined at the junction point of the zones, shown in Figure 2.13(A). While the build was successful (UW Build 3), cracks were observed at the junctions between Zones 1 and 4, and Zones 2 and 3, such as the one shown in Figure 2.13(B). This cracking was attributed to the laser offset parameter in the EOSprint software, which offsets the laser vectors from the outside edge of the part by approximately half the laser spot diameter, resulting in a gap between the laser vectors in adjacent parts, as can be seen in Figure 2.13(C). Due to this offset parameter, a weak junction developed between the two sides of the split, which allowed the formation and propagation of a crack.

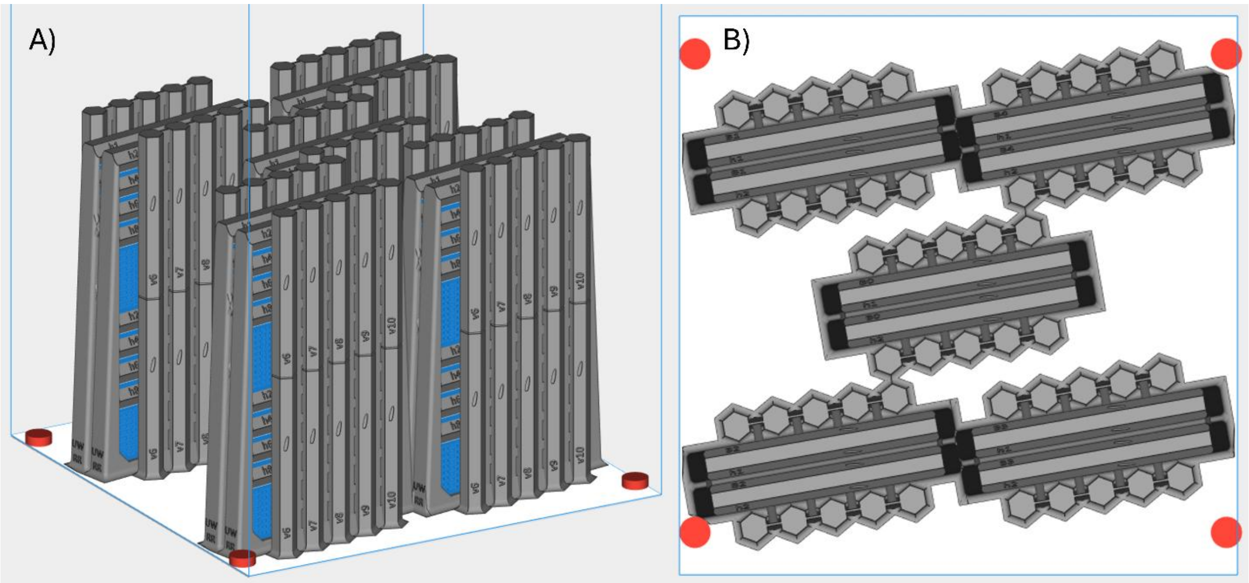

Figure 2.12: Oblique (A) and top (B) views of the intermediate build design used for UW Build 3.

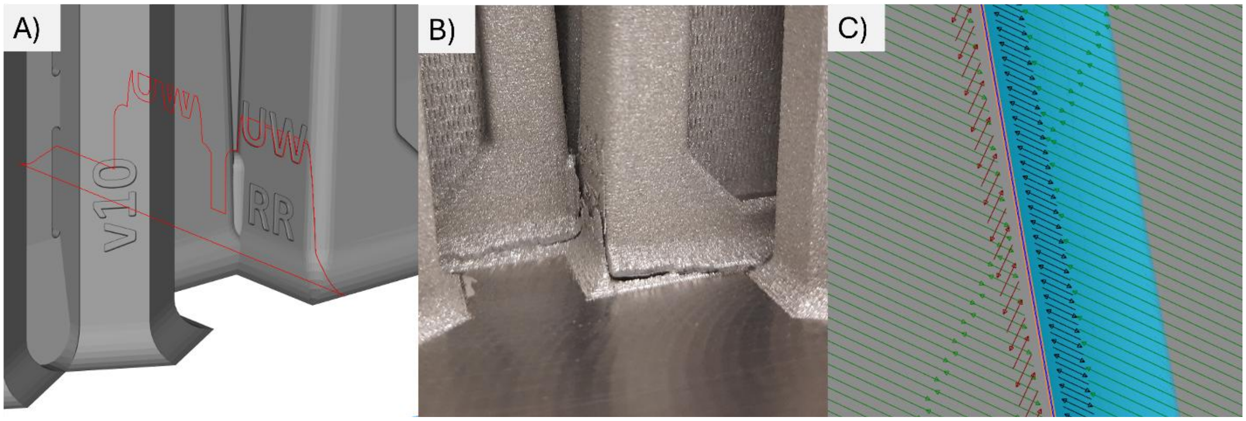

Figure 2.13: (A) A detailed view of the junction between zones 2 and 3 in the intermediate build design, with the splitting plane marked in red. (B) A photograph of the junction between zones 2 and 3 after printing (UW build 3). (C) Laser vector paths of a representative later in EOSprint

2.7.3 Short Feeds

In addition to the cracking occurring in UW Builds 1-3, localized powder short-feeds were observed during the build process, an example of which is shown in Figure 2.14. These short-feeds are thought to be caused by the significant amount of part cross-section along the X axis direction in these areas. Laser exposure causes the metal powder to melt and densify, leading to the melted surface areas retracting slightly below the surrounding powder bed. During the subsequent powder spreading, these melted areas require more powder to fill than the unmelted areas. Significant lengths of part cross-section in the X axis direction could exhaust the powder being spread by the recoater, leading to localized short-feeding. This process may additionally be exacerbated by argon flow, which is highest in the back left corner of the build area [65]. High argon flow can push powder towards the front of the build chamber, especially during recoating.

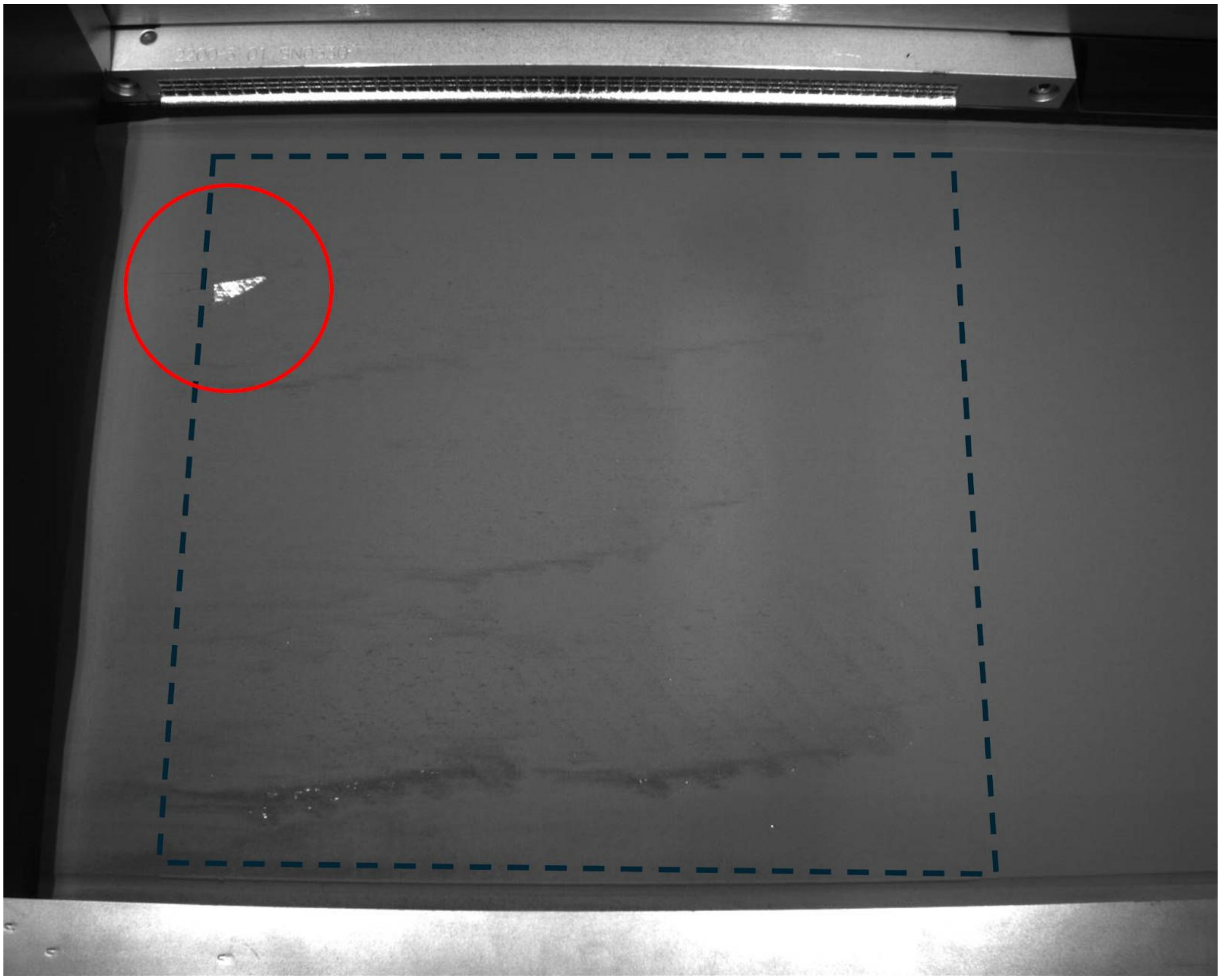

Figure 2.14: Powder bed image from UW Build 1, showing local short-feeding exposing metal in the back left corner, highlighted by the red circle. The dashed black line indicates the approximate build plate perimeter

2.7.4 UW Build 4 and Onward

The continued difficulties with cracking and shortfeeding forced a reevaluation of the build design. In consultation with the Boeing simulation team, it was decided that the overlap between the zones was causing too many issues. Although they could likely be solved eventually, the easiest solution would be to change the orientation of the parts to remove the overlap entirely. A rotated zone configuration was adopted, shown in Figure 2.6, which both removed the overlap between all zones, and performed better at distributing stress in the build plate, according to simulations. It was also decided to remove the block support still present in the horizontal coupon stack in favor of a more intentionally designed support structure that would better distribute the thermal stresses of the build. After completing and validating the new build design, the UW proceeded with their fourth and final build using this final build design. UW build 4 completed without issue and with no observed cracks developing. This final build design was distributed to all partners to print for all four of their builds.

2.8 Build Sequence

UWRR Phase I build sequence involved reduced zone configurations for Builds 2-5, as shown in Figure 2.15. That strategy was adopted to reduce the total number of coupons produced for testing, and to reduce the volume of powder consumed over the program. However, it unfortunately impacted the statistical power of the study and limited ability to resolve spatial trends with reuse. Therefore, to increase the statistical power of the study in Phase II, all partners produce four identical builds, each containing coupons in all five zones, . Ultimately, while all partners did produce builds with full zone complements, the UW build sequence differed slightly in configuration from the other partners. The completed build sequences for the UW and other partners are shown in Figure 2.16. While the differences between builds complicates one-to-one comparisons between partners, this can be easily compensated for by mapping coupon performance to location within the build volume and comparing trends in spatial variation instead. In this way, comparing coupons between different build configurations only requires a simple transformation of coupon coordinates between the two builds.

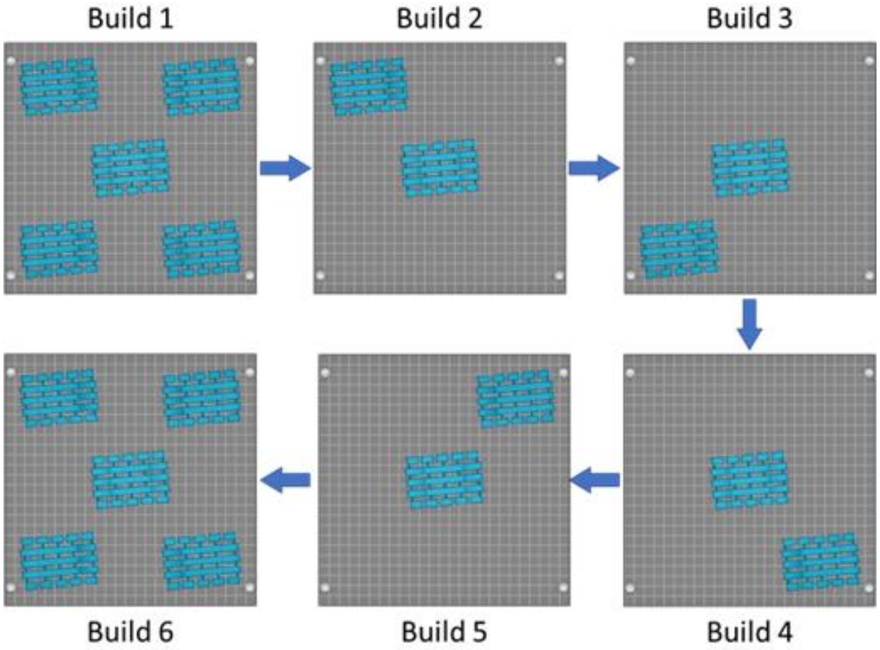

Figure 2.15: Top views of the Phase I build sequence showing the rotating reduced zone configurations

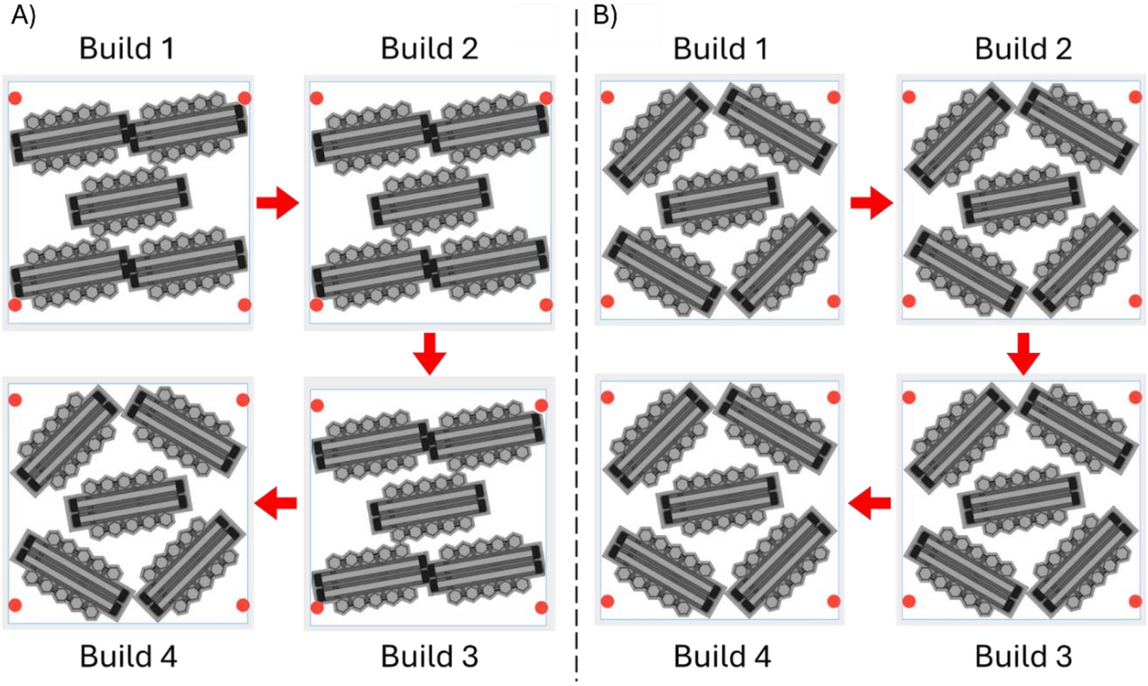

Figure 2.16: Top down views of the sequence of builds printed by (A) UW and (B) all other partners

2.9 Design Lessons Learned

Many lessons were learned in the design and qualification of the build design for the fatigue study. The larger coupons needed for fatigue testing resulted in higher internal stresses in the parts during the printing process, as compared to the Phase I tensile prints. This led to instances of cracking of the support structures, often leading to interruptions in the build process due to protruding metal interfering with the recoater blade. Considerable effort was made by the UW in collaboration with Boeing to minimize the risk of build interruption through the build design optimization.

2.9.1 Support Structure

One of the most difficult challenges encountered in the build design was the balance between support and internal stresses. The horizontal coupons presented a particular challenge due to their long cross-section creating high shrinkage stresses, along with the stacked geometry of the coupons, which led to a gradual buildup in stresses as the build progressed. The stacked coupons act like levers, pulling the supporting structures together with increasing force. In some cases, this force was enough to rip the metal from the build plate, or to cause separation between layers in the build. An example of this occurring in a test build is shown in Figure 2.13. To address this, a tapered support frame was designed, which provides better rigidity against the gradually increasing stresses than a straight sided frame would. A model of the tapered frame is shown in Figure 2.18. Additionally, the block support structure used extensively in Phase I was found to be inadequate in dealing with the forces developed in the builds of Phase II. The block supports offered very little out-of-plane strength, and would often zipper apart, allowing cracks to propagate almost entirely across the length of the support structure. Eventually, a perforated plate structure was employed to bridge the gap between the A and B levels in the clusters. Likewise, pillar-like supports were used between the horizontal coupons in each level. Both the perforated plate and pillar supports can be seen in Figure 2.18. These support structures provide the necessary functions of overhang support and heat dissipation for the horizontal coupons, while minimizing the additional stresses developed by the solidification of the metal during printing.

Figure 2.17: Demonstration of the importance of support structures. The left image shows a delamination of layers due to the compressive stress created by the solidification and cooling of the horizontal coupon melt pool. The right image shows a model of the horizontal coupon assembly, with a tapered support frame to provide rigidity and resist the compressive stresses, and intentionally designed support between horizontal coupons to provide support without increasing the compressive stresses.

2.9.2 Balance of support and stress

Complicating the issues with internal stresses of the horizontal coupons was the need to section the parts off the build plate prior to heat treatment. Conventional wisdom dictates that parts should be stress-relieved on the build plate to prevent warping when they are sectioned off. However, due to learnings in Phase I, all metal of Phase II was required to be heat treated at the same facility, which mandates that the parts are sectioned off the build plate in the as-printed condition. The supporting structures in the build were designed to help prevent warping of the horizontal coupons when they are sectioned off the build plate. Additional solid metal was placed at the bottom of the assembly to tie the legs of the frame together, and a thin solid plate was placed in plane with the coupons to help distribute stress. Initially the metal plate was designed to be fully solid, however it was realized that this too was contributing to the compressive stress acting on the support frame. Any uninterrupted cross-sectional distance contributes to the accumulation of internal stresses. One method to mitigate the stresses is to include perforations in the part where possible to break up the cross section into smaller segments. This approach was used in the vertical plate. While the perforations reduce the thermal stress build up in the part, they may act as stress concentrators if designed incorrectly. Hence, a finite element analysis (FEA) of four different perforation geometries (Figure 2.18) was performed using Autodesk Fusion 360 to evaluate the stress concentration of the geometry. Four small plates were modeled with different perforation geometries (vertical slots, slanted slots, diamonds, and hexagons), and the plates were subjected to a uniaxial tensile force to simulate the force imparted when the parts are sectioned off the build plate. The size of the plates and the magnitude of the force were arbitrary as it was intended to be a direct comparison of the perforation geometries under similar conditions. It was found that the "diamond" perforation geometry had the lowest peak stress, and the hexagon geometry exhibited the highest (likely due to the higher volume of material removed). The vertical and tilted slot geometries had slightly higher peak stresses compared to the diamond geometry. Despite having the lowest peak stress, the diamond geometry appeared to concentrate the stress at the corners of the diamond perforation, which was concerning since the most common failure mode for AM metal is delamination between layers. Hence, the vertical slot geometry was selected to be used in the build design, as it had the second lowest peak stress and did not concentrate stress at layer interfaces.

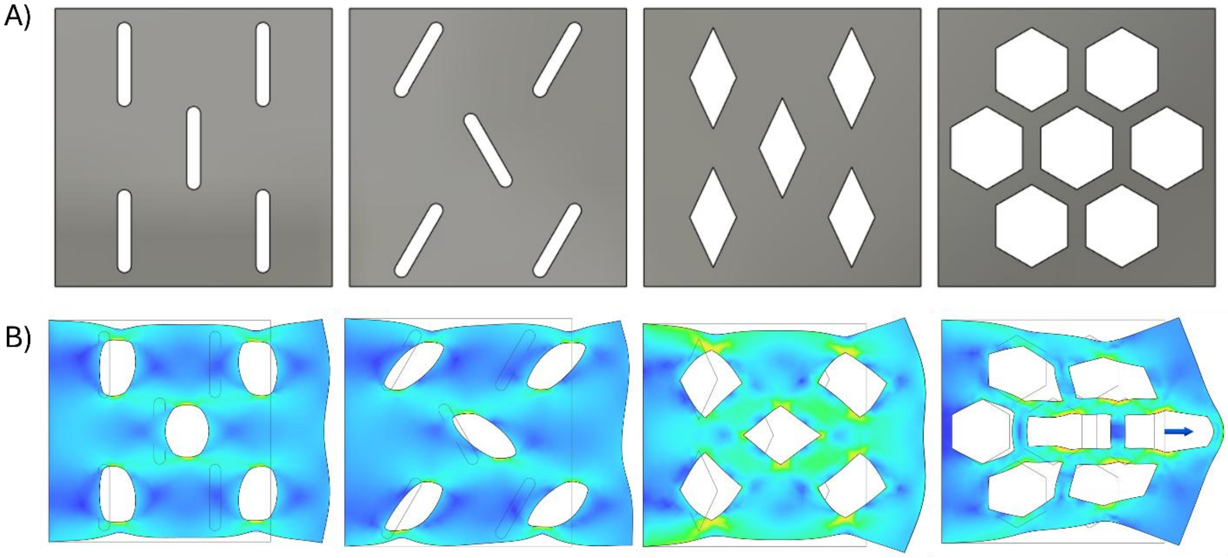

Figure 2.18: (A) Four perforation geometries (left to right: A, B, C, D) evaluated using finite element analysis for stress concentration. (B) Results of the finite element analysis showing a normalized stress heat map and exaggerated deformation displacement.

2.9.3 Registration Marks

While the μCT evaluations of metal in Phase I for static properties produced excellent, high resolution μCT reconstructions, it was not possible to directly relate the observed porosity to failure locations. Specifically, there was no way to relate the geometry in the μCT reconstructions to physical indications on the coupons, i.e., registration was not possible. As fatigue is expected to be more dependent on the location and severity of individual pores, there is a greater call for the ability to correlate failure location to possible indications in the μCT reconstruction. To accomplish registration in Phase II, it was decided to introduce fiducial marks on and in the coupons, which will be easily visible in the μCT reconstruction. These geometries can act as features to register the reconstruction to a physical model and enable the locations of individual indications to be mapped to model coordinates. This registration also makes it theoretically possible to map the μCT data to layer data obtained by optical tomography (OT) and melt pool monitoring via mapping to model coordinates. Ideally, all layer-wise build monitoring data could be correlated to as-built μCT data, and further to a failure origin in the tested samples. With success, moving forward indications in the monitoring data could be used to predict porosity and failure origins. However, this workflow is complicated by the fact that the coupons need to be machined prior to testing. Any external registration marks would need to be machined off to prevent them acting as fatigue crack initiation sites. As such, after machining it would not be possible to map an identified failure location back to the original geometry. Thus, it is necessary to include both internal and external fiducial marks, which can be used to register the post-fracture samples back to the as-built geometries and the model geometries.

2.9.4 External Registration

The key feature of the registration marks is their lack of symmetry in relation to the coupon overall. The µCT datasets have the potential to be rotated, mirrored, or even inverted during processing. If the registration marks shared any of these symmetry operations, the registration would be ambiguous. To prevent this issue from being a problem, it was ensured that the overall geometry did not contain any rotational, mirror, or inversion symmetry. The external registration marks were designed as truncated ellipsoidal notches, 8.4 mm long, 2 mm wide and 0.5 mm deep. Each notch is rotated 10º from the long axis of the coupon to break mirror symmetry. Two of these marks were placed on the faces of the hexagonal coupon, 60º apart, for redundancy. A drawing of the external registration marks is shown in Figure 2.19.

2.9.5 Internal Registration

Internal registration was used enable registration of post-tensile features to the as-built µCT scan. It is crucial that the internal marks do not interfere with the fatigue test by acting as crack initiation points. Thus, in addition to the requirements of the external marks, the internal marks must be small and positioned far enough from the test section to prevent related cracking. It is also important that the internal marks not be too far from the test section that they get machined off or are not visible in the µCT scan. A small right triangular prism was used as the internal geometry. The dimensions of the prism are shown in a drawing in Figure 2.20. The bottom face of the prism is aligned with the XY plane of the build, which gives a distinct reference for the build layer at which the mark starts. The angles of the sides of the prism are all greater than 30º, allowing them to be printed without internal support. While loose powder will inevitably be trapped within the mark during printing, there should be enough porosity for the mark to be visible by µCT.

Figure 2.21 shows the location of the external and internal registration marks in the hexagonal coupon in relation to the appropriate final dimensions of the fatigue coupon. The external registration mark is centered with respect to the test section of the fatigue coupon, which ensures that the µCT scan can be performed on the as-built metal that will be tested in the fatigue test. The internal registration mark is centered with respect to the bottom grip section of the fatigue coupon. This location accommodates several millimeters of deviation in the actual location of the fatigue coupon without the mark coming too close to the end of the coupon or to the test section. It is important to highlight that the registration mark and their placement were guided by discussion with Robert Grube and Cory Cunningham of Boeing. Both of these individuals were instrumental in providing suggestions and guidance based on their extensive expertise.

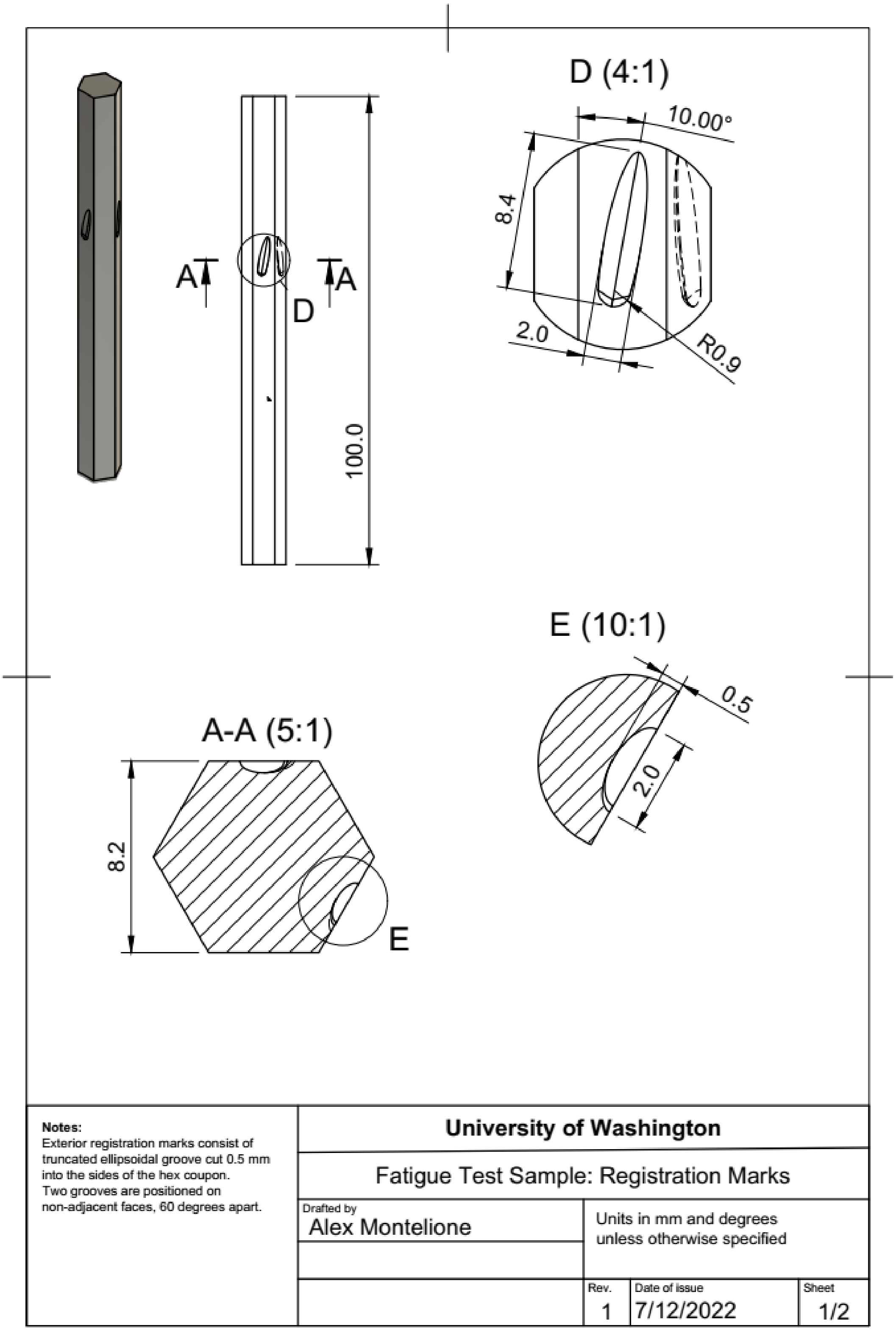

Notes:
Exterior registration marks consist of truncated ellipsoidal groove cut 0.5 mm into the sides of the hex coupon.
Two grooves are positioned on non-adjacent faces, 60 degrees apart.

University of Washington

Fatigue Test Sample: Registration Marks

Drafted by
Alex Montelione

Units in mm and degrees unless otherwise specified

Rev. 1
Date of issue 7/12/2022
Sheet 1/2

Figure 2.19: Drawing showing dimensions and positioning of the external registration marks

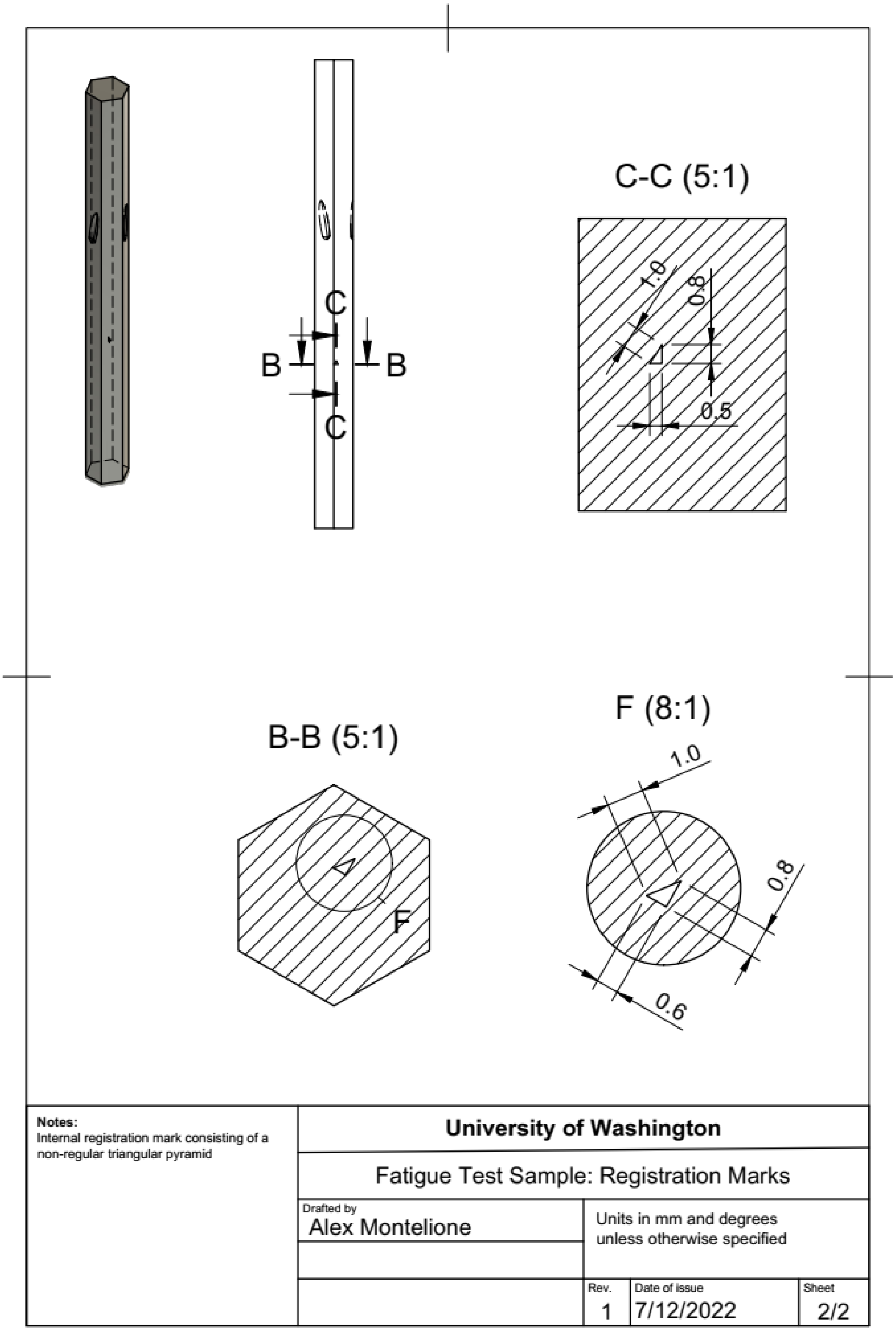

Notes:
Internal registration mark consisting of a non-regular triangular pyramid

University of Washington

Fatigue Test Sample: Registration Marks

Drafted by
Alex Montelione

Units in mm and degrees unless otherwise specified

Rev.	Date of issue	Sheet
1	7/12/2022	2/2

Figure 2.20: Drawing showing dimensions and positioning of the internal registration marks

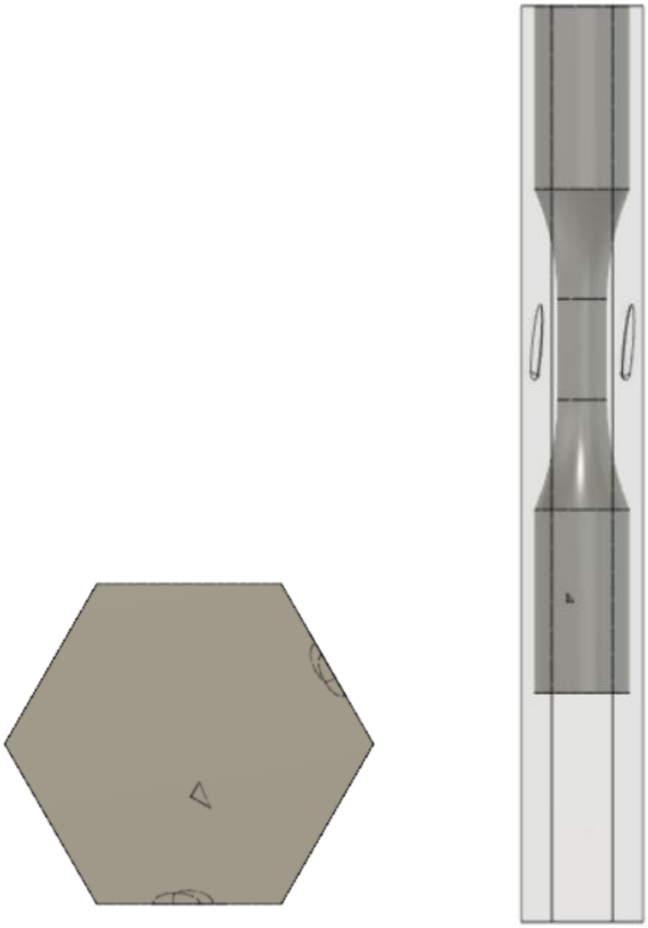

Figure 2.21: Relative positioning of the registration marks within the hex coupon blank to the anticipated machined coupon geometry.

Chapter 3 Variability in Metal AM Powder

The content of this chapter draws upon material first presented in: A. Montelione, R. Schur, R. Schleusener, M. Ramulu, D. Arola, Powder reuse and variability in laser powder bed fusion additive manufacturing of Ti6Al4V: A round robin study, Journal of Materials Research and Technology 35 (2025) 4231–4248. https://doi.org/10.1016/j.jmrt.2025.02.073.

3.1 Introduction

As discussed in Chapter 2, the quality of the powder used in the metal AM process was treated as an important source of variability in the L-PBF process. Characteristics such as particles size, flowability, and oxygen content can be influential on the performance of the final metal parts. Therefore, powder quality was monitored throughout the RR study to assess the impact of powder reuse on both the powder and printed metal. Powder samples were collected prior to each build in both Phase I and Phase II. This chapter describes the evaluation and characterization of the collected powder samples and compares the trends to the performance of the metal. For the sake of preserving data confidentiality on behalf of the participating parties, all results from the study are blinded. Participants were assigned random numbers and are referred to using these numbers as P1-P6.

3.2 Materials

The details of the build design for Phases I and II are laid out in Chapter 2. To reduce the number of factors contributing to variability in the study, all six participants started Phase I with powder from the same lot of plasma atomized Grade 5 Ti-6Al-4V provided by EOS. The characteristics of both powder lots are listed in Table 2.1 and additional powder characteristics can be found in the supplied Certificates of Analysis in Appendix A. Throughout the study, the participants were instructed to follow a replacement powder reuse strategy such as that described in Chapter 1. In this strategy, recovered powder is mixed with virgin powder to replenish the mass lost in the preceding build.

3.2.1 Powder Spread Test

Along with the builds outlined in Chapter 2, a separate build was designed and performed to evaluate the variability of particle sizes across the build area. Hollow ampules were designed to capture powder in-situ during the build. The design of the ampules is shown in Figure 3.1 and the layout of the ampules in the build is shown in Figure 3.2. Additional parts were included in the build for other studies but are not shown in the diagram. The ampules were designed to capture approximately 10 g of powder for chemistry and size analyses. Larger ampules designed to capture approximately 75 g of powder for flowability testing were positioned in the corners of the build plate. All the ampules were positioned 5 mm above the top surface of the build plate to give clearance for sectioning, and to allow time for steady-state conditions to develop in the build process. After completion of the build, the parts were sectioned from the plate without a stress-relief heat treatment to avoid sintering of the particles captured in the ampules. The tops of the ampules were retrieved and the powder inside was recovered for analysis.

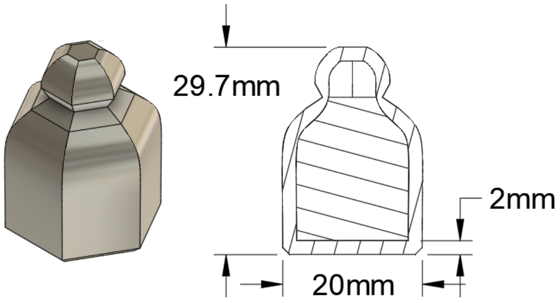

Figure 3.1: Oblique rendering and cross-section diagrams of the 10 g powder capsule used to capture powder in-situ during a build.

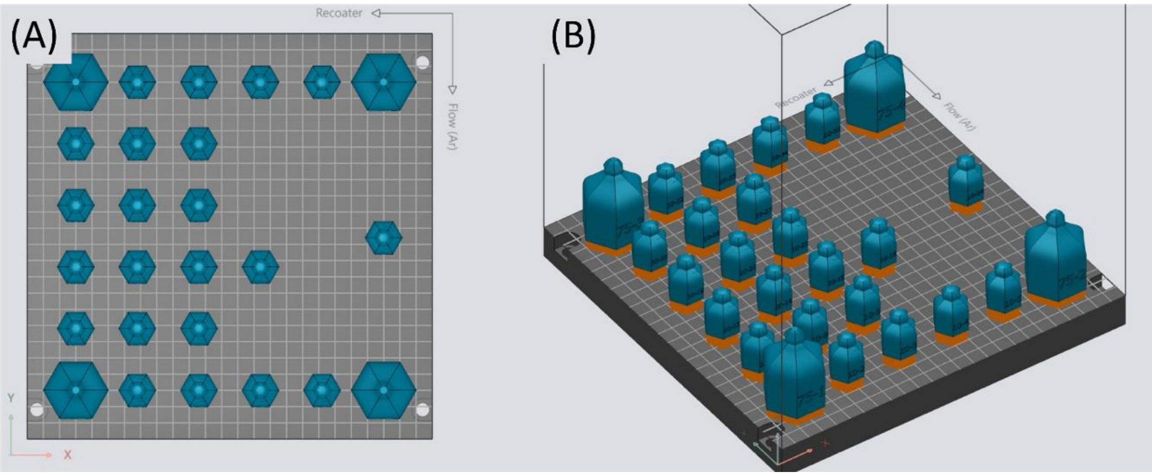

Figure 3.2: Powder capture build layout (A) top view and (B) oblique view showing locations of the powder capsules in the build.

3.3 Methods

3.3.1 SEM

The powder particle morphology was evaluated using a Scanning Electron Microscope (SEM; Phillips, Model XL30 Sirion FEI) in secondary electron imaging mode at low to moderate accelerating voltages ranging from 2 to 5 keV. Powder was dispersed onto conductive carbon tape for analysis. Images were taken at three random locations on the carbon tape at various magnifications to examine the powder size distribution, circularity, and surface texture.

3.3.2 Dynamic Light Scattering

The size characteristics of the powder samples were determined using Dynamic Light Scattering Particle Size Analysis (DLS; Horiba Partica LA950-V2, Kyoto, Japan). Approximately 0.5 g of each powder sample was dispersed in an ethanol/water mixture with a small quantity of Triton X-100 as a dispersant. The aqueous samples were diluted further in deionized water in the DLS instrument during measurement. Five measurements were taken of each sample, with agitation and circulation parameters set between 2 and 8. Ultrasonication was used for 8-10 seconds before each measurement. The Powder Size Distribution (PSD) graphs were averaged together and evaluated to obtain the 10th, 50th (median), and 90th percentiles of the PSD (D10, D50, and D90, respectively) for each build.

3.3.3 Inert Gas Fusion and Combustion

Light element chemistry was measured for the powder samples from each participant using Inert Gas Fusion (IGF; LECO 836 series elemental analyzer, St. Joseph, MI, USA) and combustion analysis (LECO 844 Series combustion analyzer, St. Joseph, MI, USA). The IGF and combustion analyses were performed by Fort Wayne Metals Materials Testing Laboratory (Fort Wayne, Indiana). IGF provides accurate measurement of oxygen, nitrogen, and hydrogen. Combustion analysis was adopted to evaluate carbon content in the powder. Due to a limitation in resources available at the time of carbon analysis, it was only conducted on material from four of the study participants. Samples were measured in accordance with ASTM E1409 for oxygen and nitrogen, ASTM E1447 for hydrogen, and ASTM E1941 for carbon. Each sample was measured three times, with the average chemical value reported. A laboratory variance was estimated by repeating the measurement process on one sample five separate times. This lab variance was used in estimating the sample variance for each measured powder sample.

3.3.4 X-Ray Fluorescence

Metallic element analysis was performed on the powder samples using X-Ray Fluorescence (XRF; Bruker M4 Tornado, Billerica, MA, U.S.). This is a semi-quantitative technique for evaluating trends in elemental composition between builds. Powder samples were dispersed on carbon tape to create a thin, uniform layer of powder for analysis. Each sample was measured in 10 random locations, with each scan performed at 50 kV and 600 μA. Each scan lasted 180 seconds. An elemental library was established for calculating weight percent using a NIST

SRM Ti-V sample (SRM 654b). Using this library, the relative composition of the powder samples could be calculated from the x-ray emission spectra.

3.3.5 Hall Flow and Apparent Density

Currently, there is no standard for measuring powder "spreadability", or the ability of a powder to be spread across a surface (e.g. a build plate or powder bed). Flowability is often used to describe powder quality in AM, since better flowing powders are expected to spread more consistently. Powder packing can be represented by apparent density and/or tap density measurements. The former measures the density of powder allowed to flow freely into a vessel of known size, while the latter utilizes mechanical agitation to shift the powder into a more optimal packing state. Yet, neither of these measures describes exactly how the powder will behave in-situ, and tap density has been criticized as a poor representation of powder packing behavior [34,35,66].

Powder flow characteristics were measured in accordance with ASTM B213 and B212. Briefly, 80 g samples were taken from each collected powder sample for measurement. From that 80 g sample, 50.0 g were weighed out and placed in a Hall Flowmeter funnel, with the funnel end blocked. An apparent density cup was placed approximately an inch below the bottom of the funnel. The powder was then allowed to flow freely through the funnel into the density cup. The flow of the powder was recorded using a smartphone camera for time analysis. After the funnel had fully emptied, an additional 30 g of powder was added to the funnel, to allow the density cup to completely fill and overflow. Excess powder was scraped off so the powder was level with the top of the density cup. The weight of the density cup was weighed both empty and full of powder. The volume of the density cup was measured according to ASTM B873 – 21 and found to be 25.05 cm^3. From the weight of the powder and the volume of the density cup, an apparent density was calculated. Hall Flow times were measured using the captured video footage and a video editing software (VSDC Free Video Editor, FLASH-INTEGRO LLC) to evaluate the powder flow start and stop times with 1/30 s accuracy.

3.3.6 Tensile Properties

Four vertically oriented and four horizontally oriented coupons were selected from every zone of each of the 36 builds for tensile testing. Prior to this aspect of evaluation, the coupons were heat treated under vacuum or argon with a 2 hour soak at 745°C and furnace cooled according to SAE AM-H-81200D [67]. Participants were allowed to conduct their own heat treatment before sending the builds to the University of Washington for processing and testing but were required to follow the prescribed temperature and time history. Following heat treatment, the coupons were machined to net-shape with dimensions per ASTM E8 [68]. Tensile testing was performed with a commercial universal testing system (Instron, Model 5585H; Norwood, MA) under displacement control actuation at 1.27 mm/min. The axial strain was measured with a clip-on extensometer.

3.4 Results

3.4.1 Morphology and Size

Evaluation of the powder morphology by SEM revealed that the particles were spherical with limited evidence of distortion or deformation resulting from the prior builds. Representative images of the powder over a range of magnifications are shown in Figure 3.3. In general, the particles appear to fall in the size range of 10-100 μm. A slight texturing of the surface is visible on most particles as a rough or wrinkled "skin", as seen on the particle in Figure 3.3(A). Occasionally, small "satellite" particles are visible and attached to larger particles; isolated protuberances can be observed on some particles. No visible changes in powder morphology were observed between participants or between builds. Interestingly, the satellite particles, which often are knocked loose during powder handling, are still visible in samples from Build 6.

A few irregular particles were observed in the reused powder samples, which are assumed to be spatter particles arising from the laser-powder interaction that redeposited on the powder bed. While large spatter particles are expected to be removed during the sieving process, spatter particles smaller than the sieve mesh size (63 µm) are passed through and retained in the reused powder mass. Representative images of the powder from Build 6 of all participants are shown in Figure 3.4, where occasional spatter particles are evident in some of the images. Figure 3.5 shows the sequence of powder images from Build 1 to 6 of one participant as a representation of the typical changes observed across all participants.

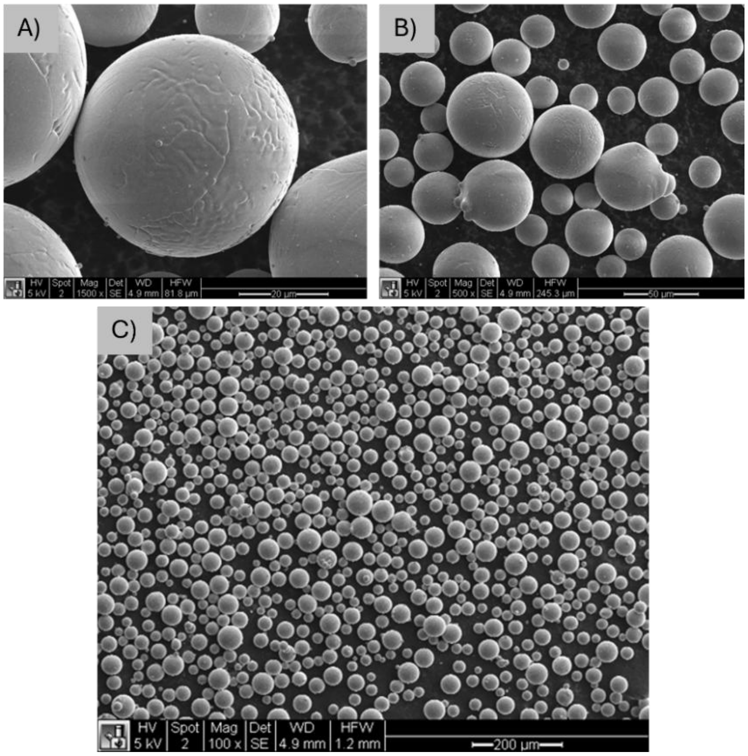

Figure 3.3: Secondary electron images of powder from Partner 1, Build 2 at (A) high, (B) medium, and (C) low magnifications, showing surface texture, morphology, and size distribution.

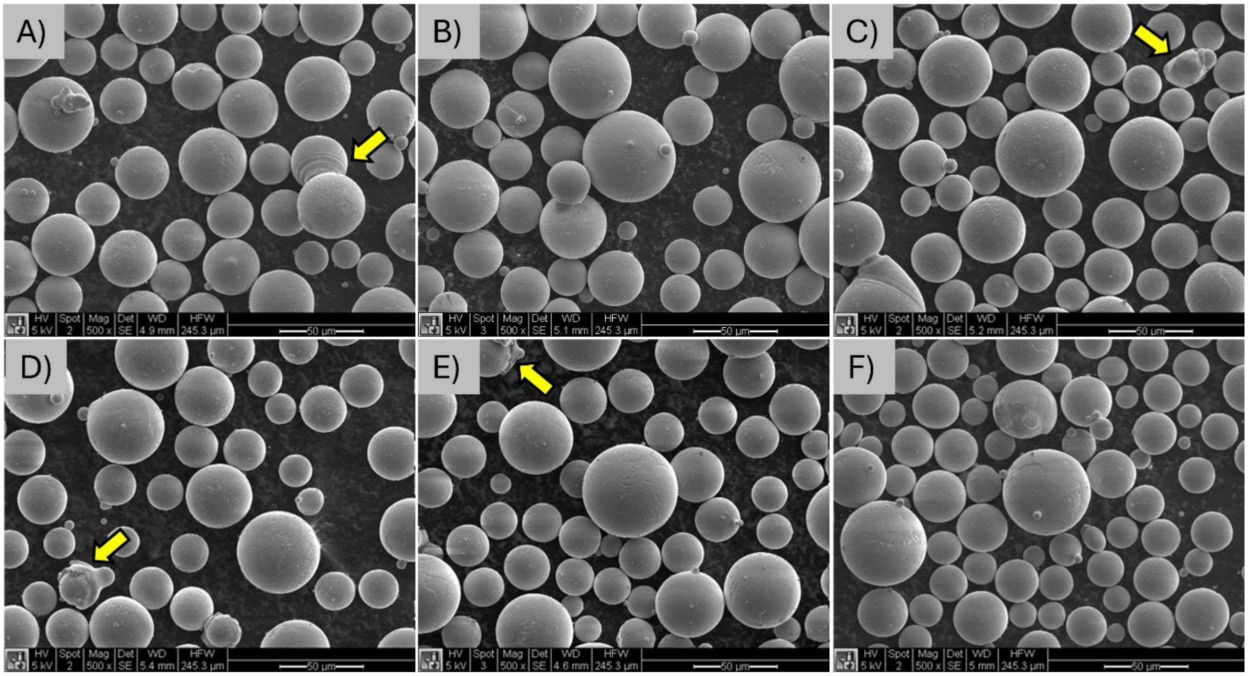

Figure 3.4: Secondary electron images of powder from Build 6 of Partners 1 to 6 are shown in A-F, respectively. The arrows point to irregular particles presumed to be spatter particles.

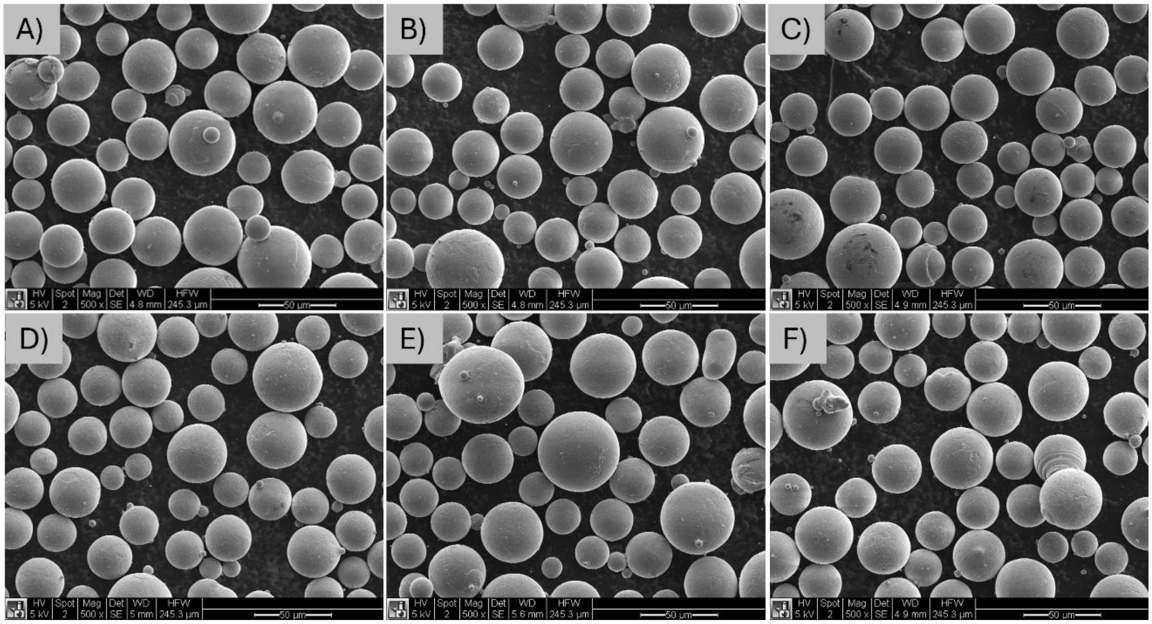

Figure 3.5: Secondary electron images of powder from Builds 1-6 (A-F) of Partner 1.

PSD curves measured for all 36 builds are shown in Figure 3.6. Admittedly, differences between measurements could be due to sampling inconsistencies, given the small amount of material needed for the test. Based on results from the DLS analysis of the powder samples, the PSD ranges from approximately 20-100 µm, with a slight negative skew to the smaller values. The 10-90 percentile range for all builds was roughly 28 µm to 55 µm, with mean particle sizes around 40 µm. Figure 3.6 shows the histograms for each build. The 10th, 50th (mean), and 90th percentiles of the PSD (D10, D50, and D90, respectively) were calculated for each PSD and are plotted in Figure 3.7. The mean (D50) values were fit using a linear regression model and the fit line is drawn in the figures. Overall, a slight increase in the D50 values was observed, with increase from 39 ± 3 µm to 42 ± 2 µm for Build 1 to Build 6, which was significant ($\Delta = 3$ µm, $t = 4.96$, $p < .001$). A larger increase was observed in the average D90 values, from 53 ± 4 in Build 1 to 58 ± 2 in Build 6, also significant ($\Delta = 5$ µm, $t = 6.04$, $p < .001$). The average D10 values of Builds 1 to 6 are identical within errors, although approaching significance ($t = 1.71$, $p = .093$). The average D10, D50, and D90 values for each build are given in Table 3.1.

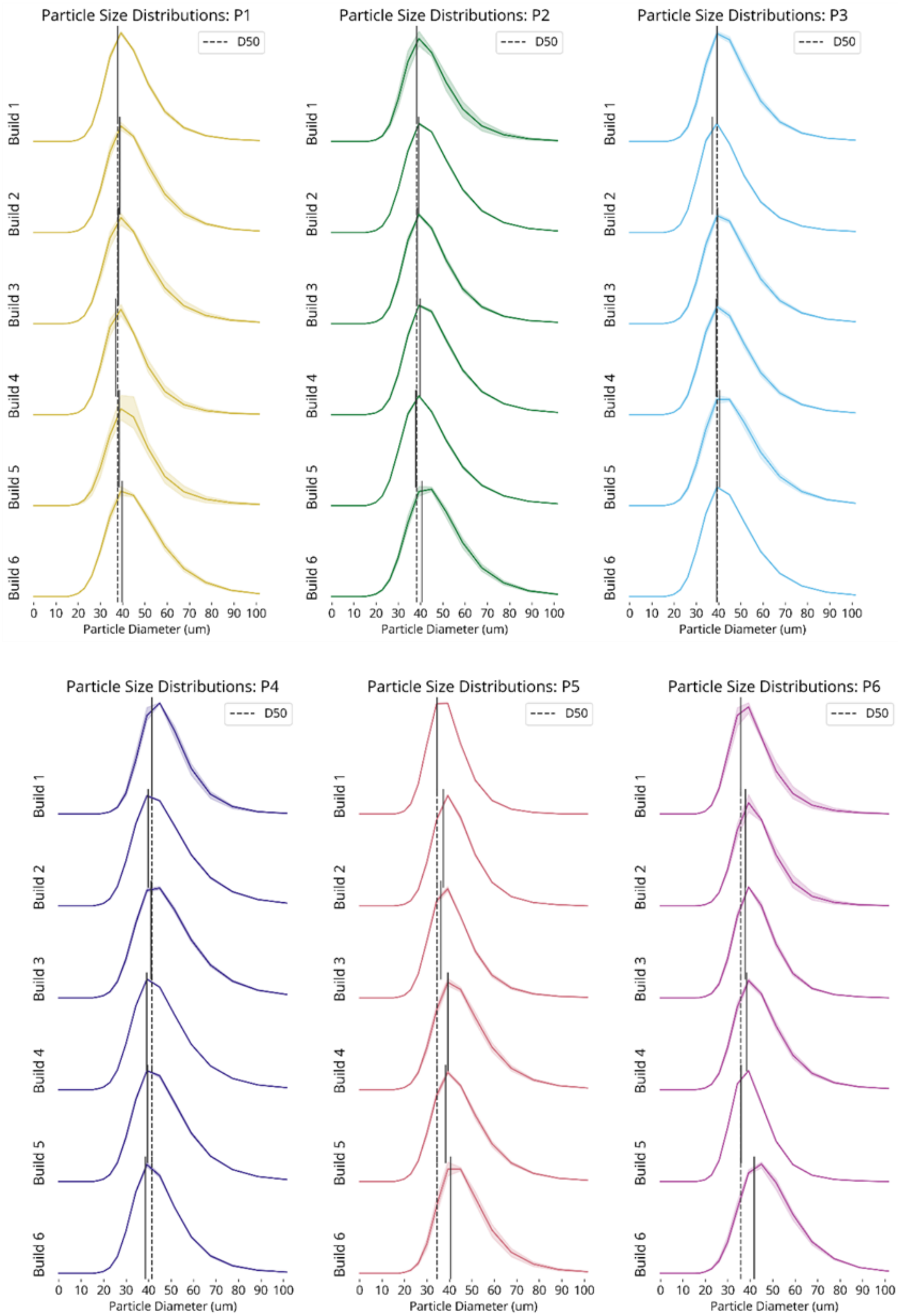

Figure 3.6: Powder size distribution histograms of Builds 1-6 for each study participant, averaged over five measurements. The mean particle size (D50) for each build is denoted by a solid line. The mean particle size of Build 1 for each participant marked in subsequent builds by a dashed line.

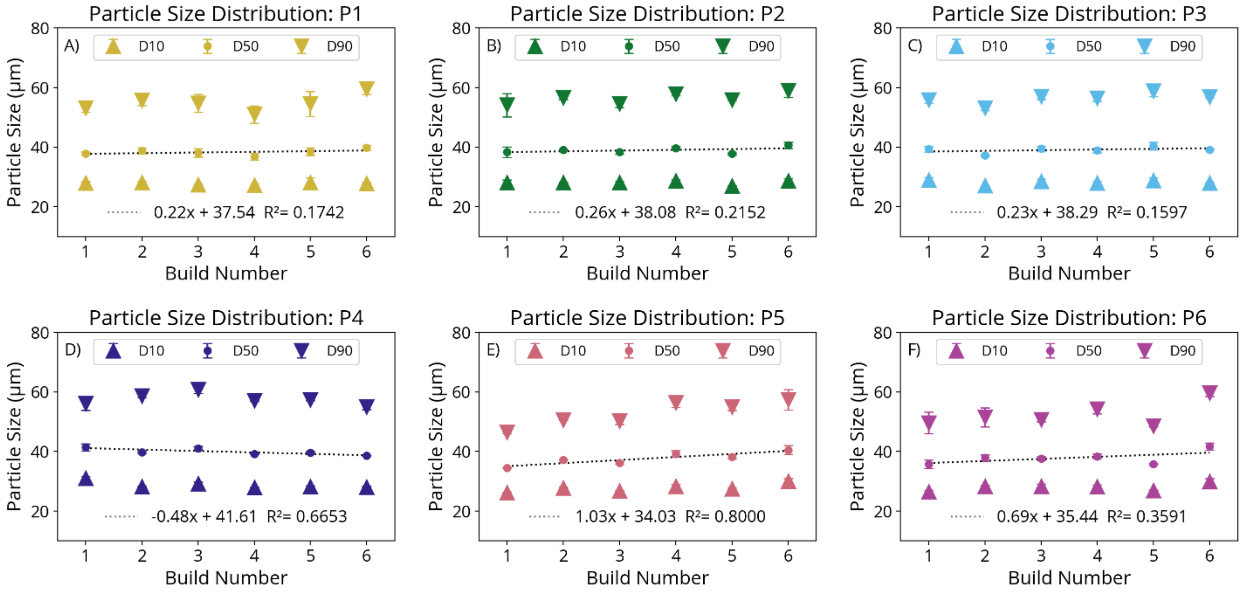

Figure 3.7: Powder size distribution graphs for each participant (P1 through P6) showing D10, D50, and D90 values for each build. Linear trend lines are fit to the D50 estimates.

Table 3.1: D10, D50, and D90 values averaged across all participants for Builds 1-6, with mean (μ), standard deviation (σ) and variance (σ^2) reported.

Build #	**D10**			**D50**			**D90**		
	μ	σ	σ^2	μ	σ	σ^2	μ	σ	σ^2
1	28.18	1.73	3.00	39.14	2.74	7.51	52.55	4.19	17.53
2	27.98	0.48	0.23	40.13	1.51	2.29	54.34	3.22	10.39
3	28.10	0.92	0.85	40.36	2.16	4.66	54.68	3.94	15.50
4	28.11	0.60	0.36	40.78	1.60	2.57	55.51	2.74	7.51
5	27.78	0.89	0.80	40.27	1.82	3.32	54.92	3.50	12.24
6	28.82	1.09	1.19	42.30	1.65	2.72	57.88	2.41	5.83

Mean particle size measurements from the powder captured in-situ within the capsules were plotted against location of the capsules in the build. A 2D contour surface was fit to the data points, as shown in Figure 3.8. The results show that particle size generally increased along the recoater path from the right side of the build area to the left. Particle size appears to decrease along the gas flow direction, from the back of the chamber to the front. The region with the largest median particle size was in the back left corner of the build area, whereas the smallest median particle size was noted in the front right corner of the build plate.

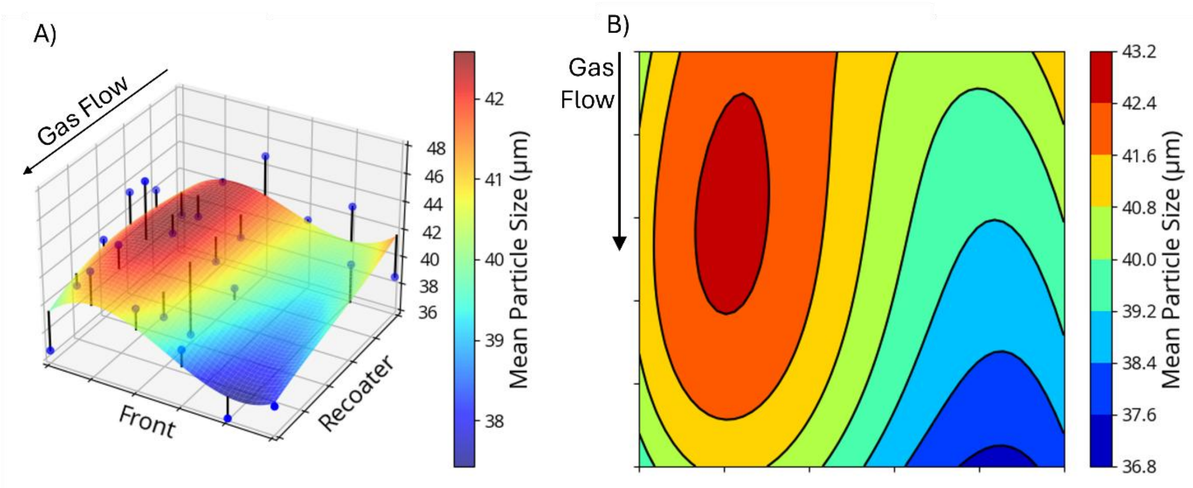

Figure 3.8: Particle size distribution measurements across the build plate. A) 3D surface plot fit to the mean particle size measured at each location in the build area. B) shows the topographic map of the fitted surface representing the build area, with the gas flow being from top to bottom in the image.

3.4.2 Chemistry

The evolution in powder chemistry with reuse is presented in Figure 3.9. Overall, there was no significant change in the light element chemistry between builds or between participants. The light element composition remained below the specification limits given by ASTM F2924-14, and generally close to the values given in the powder CoA. An ANOVA performed between the builds did not reveal a statistically significant result, indicating that no build exhibited significantly different powder chemistry than the others. An ANOVA analysis between participants was not performed due to the limited number of data points available for this analysis.

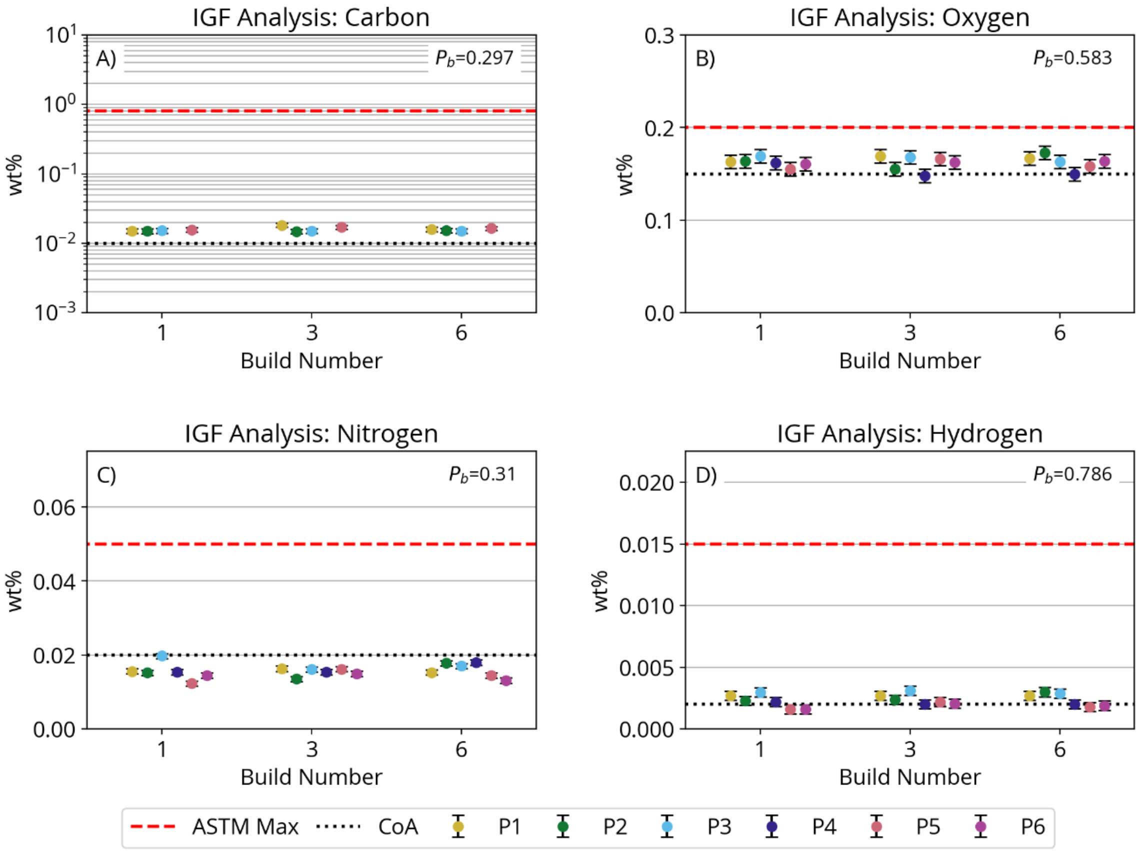

Figure 3.9: Inert gas fusion (O, N, H) and combustion (C) measurements for Builds 1, 3 and 6 for Partners 1-6. Maximum limits given by ASTM F2924 for Ti-6Al-4V are marked with a red dashed line. Certificate of Analysis values for each element are marked with a black dotted line. The P-value derived from ANOVA analysis of the three builds (P_b) is given in the upper right corner of each graph.

Measurements of the metallic element chemistry are presented in Figure 3.10. The trends in Ti, Al, V, and Fe, showed a similar trend to the light elements, with no significant difference observed overall between the builds. The aluminum and iron content did not change appreciably between builds, as confirmed by ANOVA analysis ($P > 0.05$) and remained consistent with the values reported on the CoA. Similarly, the vanadium content did not change from build to build, but was significantly lower than the reported values, and in some cases below the specification minimum outlined by ASTM F2924-14. It is unclear where the discrepancy in the vanadium values originates, but the trend in the measurements is consistent with the other metals. While the ANOVA tests did not show a significant difference in aluminum content between builds ($P > 0.05$), it did exhibit a significant difference between participants for Build 6 ($P << 0.01$) as shown in Figure 3.11. Differences in vanadium content were also observed between participants for all measured builds, although there were more frequent and larger differences in later builds. The iron content was found to differ between builds, but not between participants.

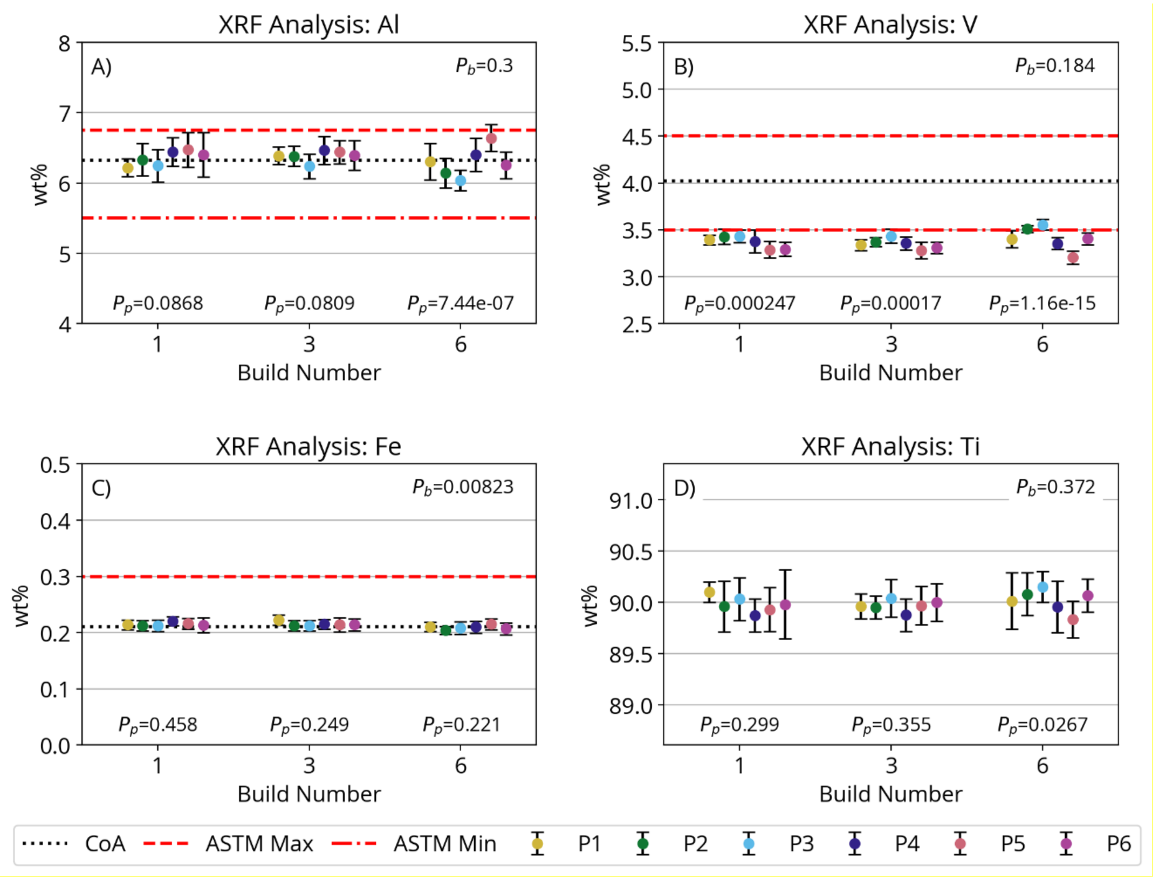

Figure 3.10: XRF measurements for the metallic elements from powder of Builds 1, 3 and 6 for Partners 1-6. Minimum and maximum limits given by ASTM F2924 for Ti-6Al-4V are marked with red dashed lines. Certificate of Analysis values provided by the manufacturer are marked with a black dotted line. The P-value derived from ANOVA analysis of the three builds (P_b) is given in the upper right corner of each graph. P-values derived from ANOVA analysis between participants for each build (P_p) are given below the data points for that build.

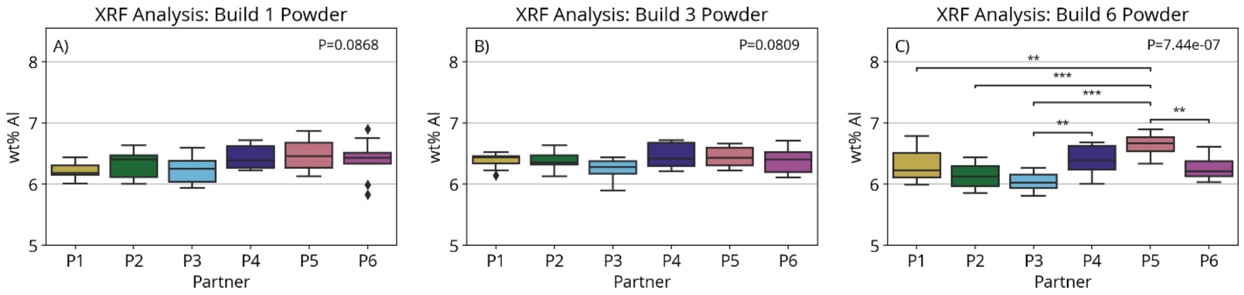

Figure 3.11: Statistical analysis of measured aluminum content of powder samples from Builds 1, 3 and 6. The P-value derived from ANOVA analysis of the six participants is given in the upper right corner of each graph. Statistically significant pairings, determined by Tukey analysis, are shown as annotated brackets.

3.4.3 Hall Flow

The measured Hall flow times for the powder samples did not change significantly over the build program. A small but statistically insignificant ($P > 0.05$) change was observed from 27.8 s at the first build of Phase I to 28.0 s, as shown in Figure 3.12. However, when singling out individual participants there was more variability in the trend. Most participants exhibited an increase in the flow times between Builds 1 and 6, suggesting that the reused powder had lower flowability. The flow times of powder increased steadily over the program for some participants, while it showed a larger increase between Builds 1 and 3 for others, and little to no change between Builds 3 and 6. Results for one participant (P5) actually exhibited an increase in the powder flowability between Builds 1 and 6, highlighting the importance of environment or handling conditions. The hall flow and apparent density measurements are shown individually for the six participants in Figure 3.13. Apparent density tended to follow the opposite trend to flowability, with higher apparent density measurements corresponding to lower flow times, as expected. The overall apparent density showed a slight decrease over the course of the program, and the powder of most of the participants underwent a decrease in apparent density between Builds 1 and 6, except for Partner 5, where the apparent density increased.

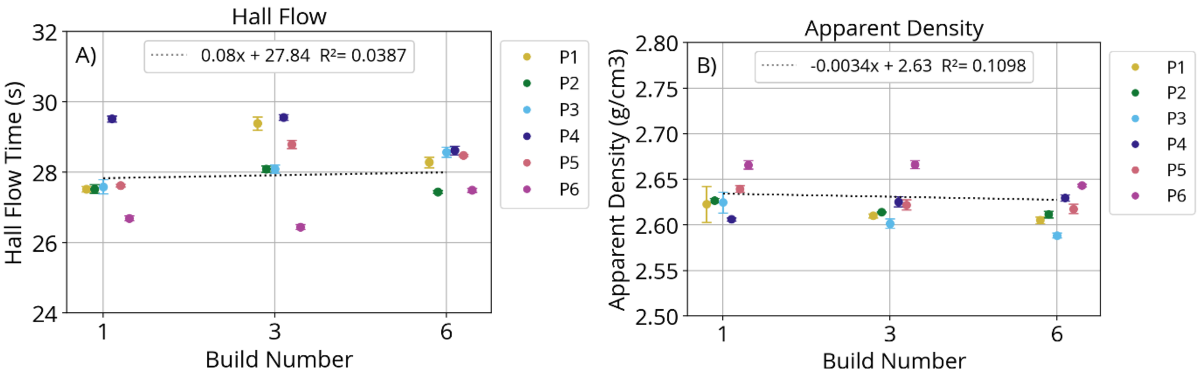

Figure 3.12: Hall flow times compared to apparent density for each of the six participants with trend assessed by linear regression

.

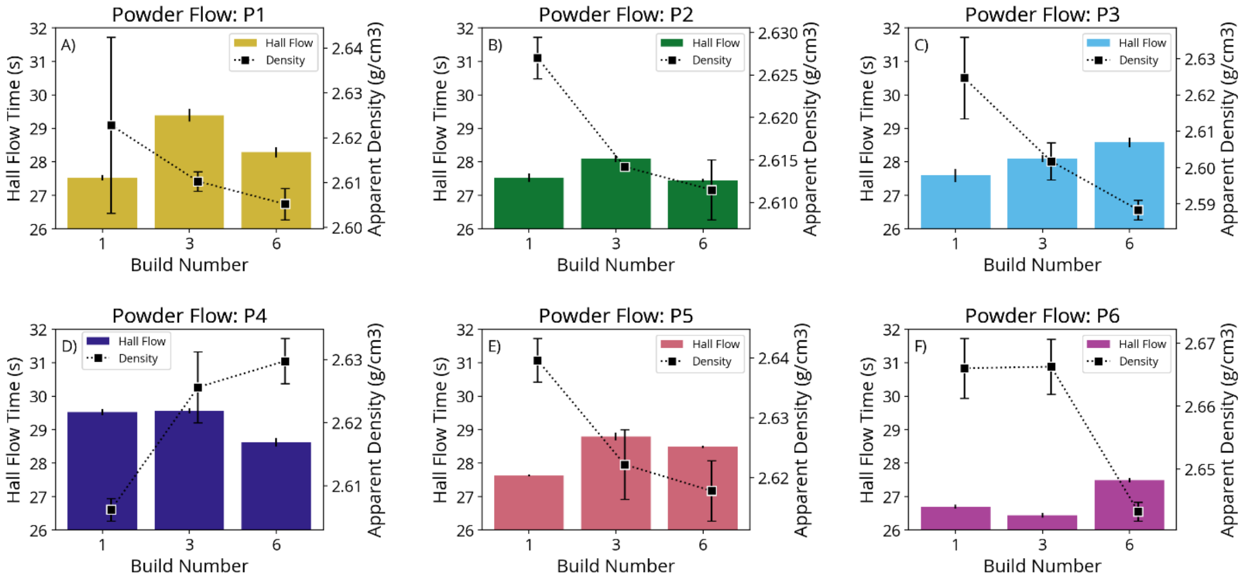

Figure 3.13: Hall flow and apparent density measurements for powder from the six participants for Builds 1, 3 and 6.

3.4.4 Tensile Properties

The average yield strength (YS), ultimate tensile strength (UTS), elongation (EL), and strength at failure (FS) for the metal of each participant are presented in Figure 3.14 with respect to build number. Results of the ANOVA between the builds showed highly significant differences

(P << 0.01) in YS and FS between builds, as well as significant (P < 0.05) differences in the UTS between builds. This implies that at least one build was significantly different from the mean of the groups. No significant difference in the EL was observed between builds. The intra-build analysis also showed significant differences between participants in all measured properties for all builds, which could be attributed to slight differences in heat treatment programs between the participants. A full discussion of the differences in heat treatment and resulting property variability for this study has been published [64]. Notably, the variability in metal properties between participants does not appear to increase with reuse.

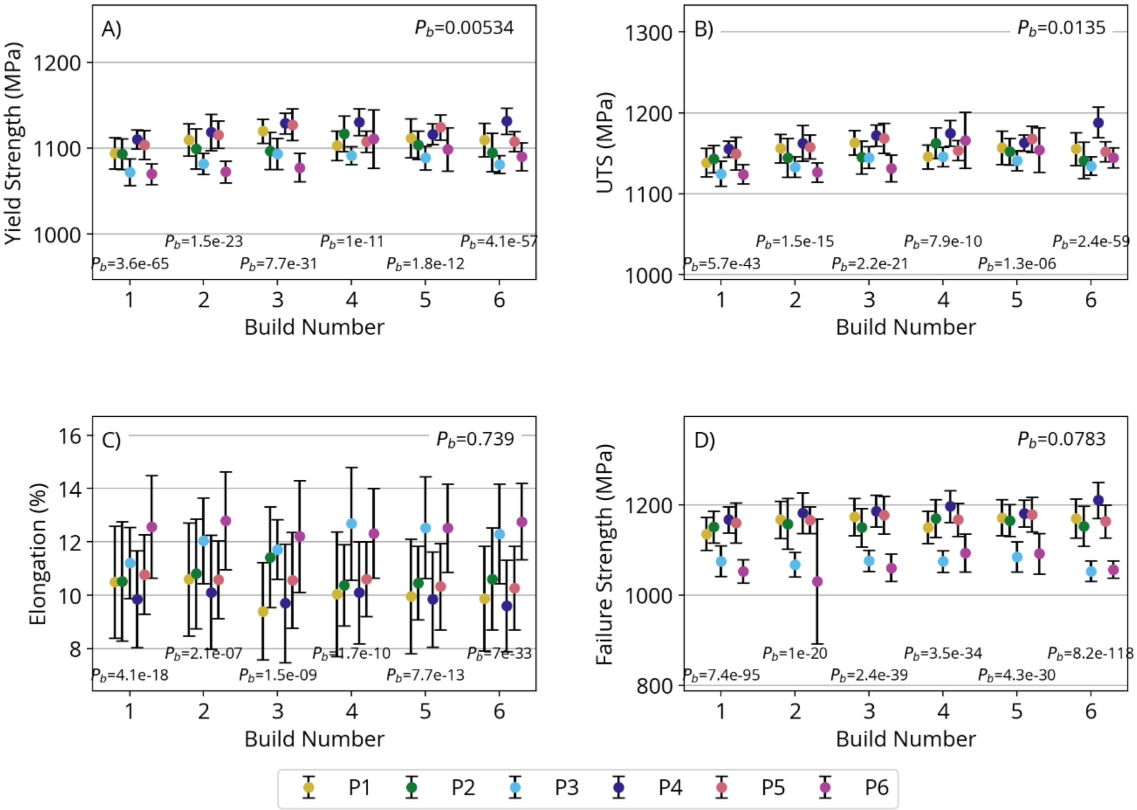

Figure 3.14: YS, UTS, EL, and FS for the six participants for each build. The P-value derived from ANOVA analysis of the six builds (P_b) is given in the upper right corner of each graph. P-values derived from ANOVA analysis between participants for each build (P_p) are given below the data points for that build.

3.5 Discussion

In general, there were limited changes observed in the measured powder properties over the course of the study when results of the powder samples collected from all participants were pooled. Overall, the mean particle size increased by 8% and the Hall flow times of the powder samples increased by 2%, whereas the apparent density decreased by 1%. These results agree with the bulk of previous reports on L-PBF powder reuse [28,29,31–33,36–43].

One aspect of the investigation to highlight is that the light element content of the powder, specifically oxygen and hydrogen, did not change significantly over the course of the study. While most reported studies on powder reuse in L-PBF systems have noted an increase in oxygen content with reuse, most of these studies evaluated changes over a longer reuse program, involving far more than six cycles. Some reuse studies have also reported no change in oxygen with reuse, suggesting that the uptake may be dependent on variables other than the number of build cycles, such as powder handling [32,39,41]. While changes in powder properties with reuse have been reported, the rate of change in properties per build for L-PBF systems is generally small. Substantial changes accumulate rather slowly and generally become important only after over dozens of reuse cycles. This trend appears in part due to the relatively benign environmental conditions in most L-PBF build chambers, as compared to other AM technologies. Typical L-PBF systems maintain near ambient chamber temperatures and pressures. The EOS M290, for instance, operates with a build plate temperature of ~50°C. In comparison, electron beam PBF (E-PBF) systems, which often maintain build chamber temperatures of >700°C, incur rapid degradation of the powder quality over relatively few reuse cycles [15,25,50]. Despite the small magnitude of the changes observed in the present study, their potential contributions to material variability and corresponding build quality cannot be dismissed.

Particle size measurements showed that the median particle size increased from 39 to 42 µm between Builds 1 and 6, which represents an increase of 8%. By contrast, the D90 values of the PSD increased by 10%, while the D10 values did not change significantly from Build 1 to Build 6. The increase in particle size with powder reuse can be attributed to either i) smaller particles filtering into the semi-porous powder bed during recoating, thereby reducing their presence in the bulk powder volume, or ii) to the accumulation of larger spatter particles from the laser melting process. Emminghaus et al. also reported an increase in particle size with powder reuse, and concluded that the effect was driven by the removal of the small and satellite particles [26]. Unlike the results reported by Emminghaus et al. there was no change in the D10 values in the present study with reuse, as would be expected with the loss of small particles. As such, the observed trends suggest that the change in the PSD is driven primarily by an increase in the size and frequency of large particles, rather than a loss of smaller particles in this case. Other studies have reported no changes in powder PSD with reuse [36,37,39], or a shift towards finer particles [38,40–43]. The differences in results reported in the open literature suggest that more research may be needed to better understand the interaction between reuse and particle size. Clearly, differences between machine layout, the sieving process, or powder lot could contribute to the unique evolution in PSD with reuse.

Large irregular particles are often observed in reused powder and are typically attributed to spatter particles generated in prior builds. Definitively determining the origin of any individual particle is difficult due to the chemical and morphological similarities between spatter particles and virgin plasma atomized particles. Young et al. effectively quantified the size ranges of various types of spatter in a typical L-PBF system, showing that spatter particles can vary widely in size, with some spatter sources producing particles of similar size to the base powder, and other sources producing spatter particles as much as ten times larger [69]. While the largest of these particles will be removed in the sieving step of the reuse protocol, the majority will fall under the sieve mesh size and will be retained in the reused powder.

Along with bulk powder characteristics, it is important to consider spatial variations in the process physics within the build space as a source of mechanical property variability. Dynamic recoater motion and gas flow may influence powder settling and packing characteristics. Samples taken from various locations of the build area showed that the average particle size may increase from the right to the left side of the build chamber and decrease from back to front (Figure 3.8). This trend can be interpreted to result from the argon gas flow, which is directed from the back to the front of the build chamber. Furthermore, there is a substantial gas flow gradient from the back to the front of the machine, which could contribute to preferential movement of smaller particles towards the front [70,71]. Smaller, lighter powder particles are undoubtedly more susceptible to the forces exerted by the gas flow and could be displaced by the gas stream towards the front of the build, leading to an accumulation of small particles towards the front of the build area and a reflective coarsening of the powder distribution at the back of the chamber. Although the effects of gas flow on particle movement and size distributions are plausible, a more detailed understanding of the gas flow dynamics and the gas-powder interaction mechanics is needed before conclusions can be drawn.

Another important consideration beyond the direction and magnitude of the changes in powder properties is the variability of those properties. While the powder chemistry did not change significantly throughout the program, a higher variability in chemistry was noted between the participants, and in Build 6, particularly in Al and V. That observation suggests that the powder chemistry was evolving with reuse and becoming more variable, even though there was not a single specific or strong driving force. Many existing studies focus on trends in powder quality with reuse, but few, if any, examine the potential causes of build-to-build variability that may exacerbate or contradict the direction of changes brought on by reuse. Some potential contributors to variability may be spatter and metal-vapor-condensate byproducts of the laser melting process, gas flow irregularities, or foreign object contamination of the powder from environmental sources. For instance, Liu et al. have shown though Computational Fluid Dynamics and Discrete Element Method (CFD-DEM) simulations that spatter-gas interactions can lead to redeposition of spatter on the build area, rather than it being cleared from the chamber [72]. These contributions to powder variability are important to consider since inconsistencies in powder quality could contribute to inconsistences in the parts produced from that powder. Further research is needed in these areas to determine the extent that these factors contribute to part variability, or to identify other factors contributing to variability in L-PBF.

An evaluation of correlations in the tensile properties of the metal from each build was performed with respect to the measured chemistry of the powder. Specifically, results for the YS, UTS, EL, and FS are presented with respect to the oxygen, carbon, and aluminum contents in Figures 3.15, 3.16 and 3.17, respectively. All three of these elements are alpha phase stabilizers in titanium and are known to increase the strength of the alloy [16]. However, there was no correlation between the oxygen content and tensile properties, which is not unexpected as the oxygen content of the powder did not increase significantly with reuse. There were weak correlations between the tensile properties and the carbon and aluminum content of the powder, as shown in Figure 3.16 and Figure 3.17, respectively. Both C and Al are expected to influence tensile properties based on their role in titanium metallurgy [16] and the observed trend is consistent with theory. However, this correlation is partly unexpected given that no overall trend in powder chemistry was observed with reuse. Further research is needed to determine if this correlation is related to gas flow or redeposited spatter or condensate.

When the tensile properties of the metal are evaluated in totality, there is variability in the mechanical properties between builds and between participants. Nevertheless, the extent of variability remained consistent across builds, that is to say the variability in aluminum content observed in the powder of Build 6 did not translate to higher variability in the mechanical properties of the metal from that build. The data for carbon content was not sufficient to perform statistical analysis between participants on a per-build level, so its contribution to mechanical property variability could not be determined.

Overall, the mechanical properties exhibited higher variation between participants (inter-machine) than they did between builds (inter-build), which suggests that differences between builds (e.g. powder chemistry) are less consequential than differences between participant locations. Most relevant to the strain at failure, two of the participants conducted heat treatments using their internal procedures and equipment, which resulted in different heating profiles. The heat treatment would be expected to be a more significant factor in determining mechanical properties, and it could have overwhelmed the effect of powder chemistry on the mechanical properties.

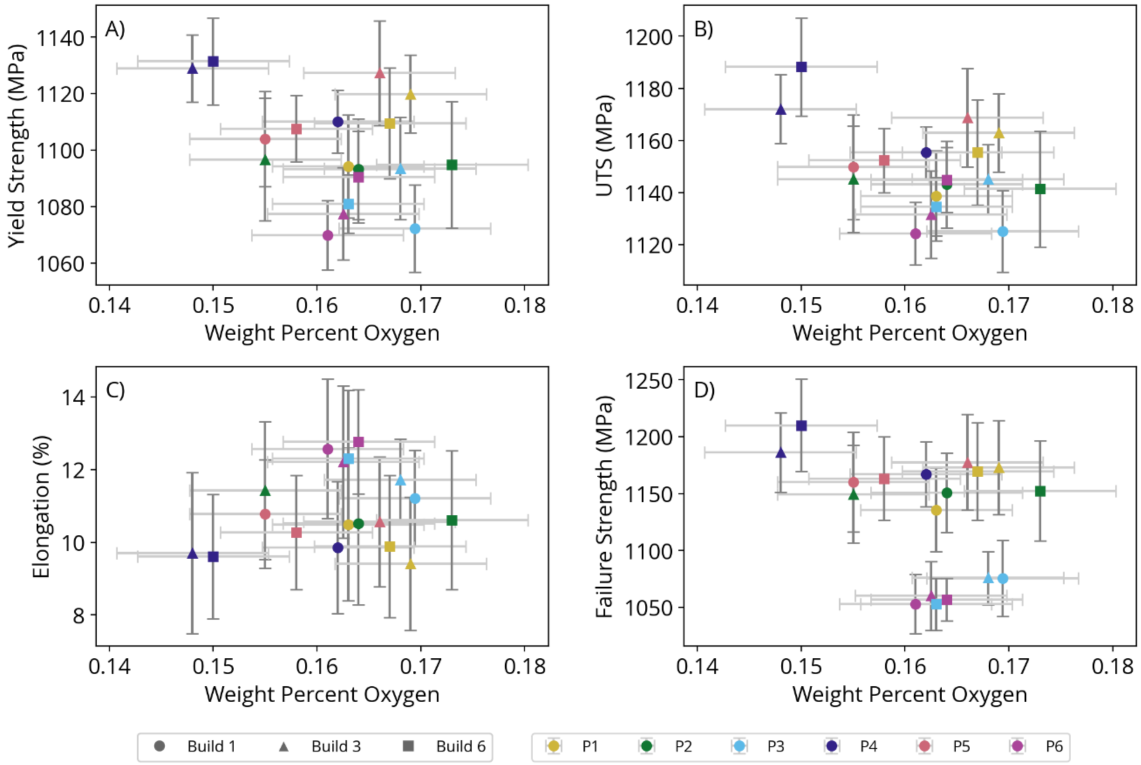

Figure 3.15: YS, UTS, EL, and FS of the metal from Builds 1, 3 and 6 of each participant compared to the measured oxygen content of the powder used for that build.

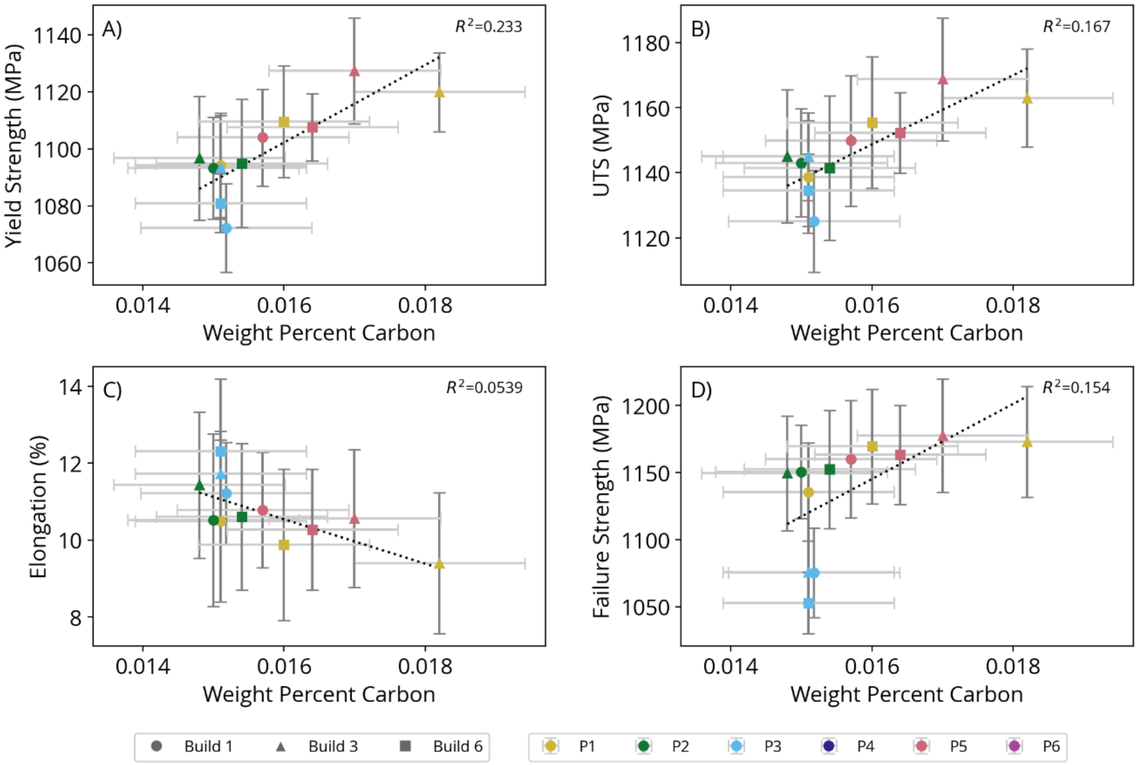

Figure 3.16: YS, UTS, EL, and FS of the metal from Builds 1, 3 and 6 of each participant compared to the measured carbon content of the powder used for that build.

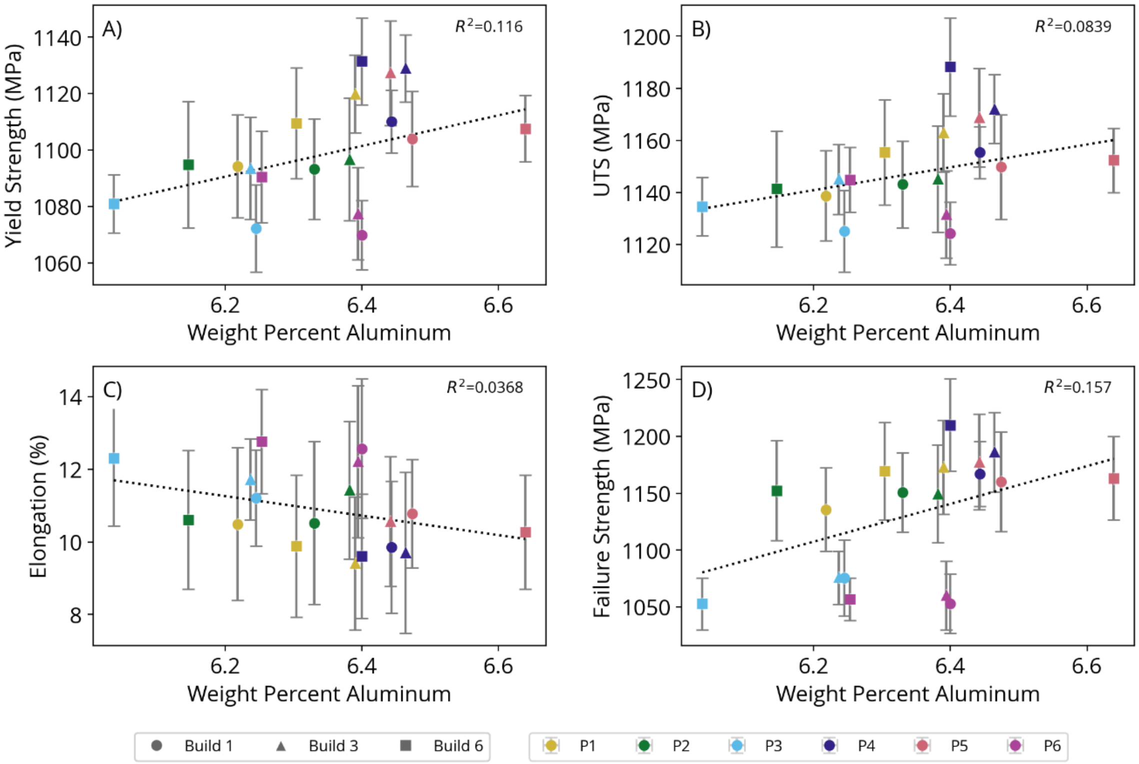

Figure 3.17: YS, UTS, EL, and FS of the metal from Builds 1, 3 and 6 of each participant compared to the measured aluminum content of the powder used for that build.

Recognizing that powder degradation occurs more slowly (i.e. over many build cycles) in L-PBF as compared to other AM processes, the trend of variability with reuse may become more apparent at higher reuse cycles [25]. The relatively low number of builds (N=6) conducted in this study was dictated by the quantity of powder available from the starting lot, and the willingness of the industry participants to engage in larger-scale build sequences. Further investigation with multiple participants and longer reuse programs could clarify the effect of reuse on powder quality variability.

According to results of this experimental investigation, it appears necessary to consider site-specific (i.e. inter-machine) variances in powder properties when defining powder reuse limits for production parts. Results from present investigation show that powder reuse and aging data from one site/manufacturer may not reflect the behavior at other sites, as the trends can vary from one site to another. More research is needed to identify the key factors contributing to how powder undergoes aging with reuse, although environmental factors appear to be a contributing factor. Nonetheless, this study provides new insight into the behavior of powder across different AM providers controlling for machine and powder source. This knowledge is critical to the commercialization and certification of AM technologies and is key to the industrialization of L-PBF for safety-critical applications.

3.6 Conclusions

A powder reuse study was performed as part of a round robin investigation that involved six different EOS M290 L-PBF machines using a single lot of plasma atomized grade 5 Ti-6Al-4V powder. An identical sequence of six builds was performed on each machine, which were operated by a different manufacturer and at a unique site. Powder samples taken prior to each build were analyzed to determine particle size distribution, morphology, bulk chemistry, and flowability. Based on the findings, the following conclusions were drawn:

- The mean particle size of the powder was found to increase by 8% with reuse. Powder flowability did not change significantly.
- Powder chemistry did not change significantly over the six builds conducted. It is expected that continued reuse of the powder will lead to an increase in the oxygen content.
- While there was no overall trend observed in the aluminum and vanadium content of the powder between builds, there were significant difference between participants for later builds. That suggests that powder degradation is influenced by location specific details such as environmental or procedural factors.

- The mean particle size varied across the build area with trend distinguishing an increase in particle size at the left and back of the build chamber. The spatial variation in powder properties could contribute to special variability in part properties or performance.
- Particle morphology did not change noticeably between builds or locations.
- Mechanical properties were correlated to carbon and aluminum content in the powder but were not correlated to build number.
- The mechanical properties exhibited higher variation between participants than they did between builds. Therefore, differences between builds (e.g. powder chemistry) are less consequential than differences between participant locations (e.g. procedures like heat treatment).

Chapter 4 Phase II Powder analysis

4.1 **Introduction**

Phase I of the UW Round Robin project evaluated variability in tensile properties of the Ti6Al4V metal produced by L-PBF, and the effect of powder reuse and consequent condition. Phase II of the UWRR continues the evaluation of variability of this metal from a perspective of fatigue performance and extended powder reuse. This portion of the project was designed as a more focused version of Phase I, with fewer partners and a reduced build program, but with more attention given to spatial variation within the build chamber. Details of the build design and layout for Phase II were described in detail in Chapter 2.

4.2 **Materials**

All builds in the RR study, including those of Phase II, utilized plasma atomized grade 5 Ti-6Al-4V powder provided by EOS (EOS GmbH, Germany). Samples of powder were collected prior to each build performed in Phase II of the UWRR. Details of the powder collection and build design are provided in Chapter 2. Powder samples of approximately 300 g were taken from the charge of powder loaded into the machine for the build. In Phase I, all the partners started with the same lot of powder (A 482001) and continued to use that lot through the build program, as described in Chapter 2. In Phase II, one of the partners was unable to continue builds with the same lot, and so a new lot of powder was introduced to the study to allow this partner to continue their builds. The new lot of powder (A 242001) was selected by EOS to be as close in properties to the original lot as possible. Metrics of powder quality from the Certificates of Analysis are provided for the original and substitution lots in Table 4.1 for comparison. While this new powder lot matched the original powder lot very closely, some aspects of powder quality were notably different between the two lots, as is discussed further in this chapter. In addition, the effects of powder aging that the original lot underwent were not reflected in this new lot of fresh powder. While the use of a "substitution" lot was necessary for the study, it complicated the evaluation of powder reuse. For the duration of Phase II, partners P1 and P3 used powder lot A 482001 while partner P2 used powder lot A 242001.

Table 4.1: Comparison of nominal powder properties obtained from the Certificates of Analysis for the two lots of powder used in Phase II builds.

Powder Lot	**D10**	**D50**	**D90**	**Wt % Ti**	**Wt % Al**	**Wt % V**	**Wt % Fe**	**Wt % O**
A 482001	30 µm	41 µm	57 µm	Bal.	6.32	4.02	0.21	0.15
A 242001	29 µm	40 µm	57 µm	Bal.	6.38	3.94	0.21	0.13

4.3 **Methods**

For continuity in analysis between Phase I and II, the same methods of analysis were used in Phase II as for Phase I, with the exception of tap density, which was added for Phase II.

4.3.1 SEM

The powder particle morphology was evaluated using a Scanning Electron Microscope (SEM; Phillips, Model XL30 Sirion FEI) in secondary electron imaging mode at low to moderate accelerating voltages ranging from 2 to 5 keV. Small portions of the collected powder was dispersed onto conductive carbon tape for analysis. Images were taken at three random locations on the carbon tape at various magnifications to examine the powder size distribution, circularity, and surface texture.

4.3.2 Dynamic Light Scattering

The size characteristics of the powder samples were determined using Dynamic Light Scattering Particle Size Analysis (DLS; Horiba Partica LA950-V2). Approximately 0.5 g of each powder sample was dispersed in an ethanol/water mixture. The aqueous samples were diluted further in deionized water in the DLS instrument during measurement. Five measurements were taken of each sample, with agitation and circulation parameters set between 2 and 8. Ultrasonication was used for 8-10 seconds before each measurement. The Powder Size Distribution (PSD) graphs were averaged together and evaluated to obtain the 10th, 50th (median), and 90th percentiles of the PSD (D10, D50, and D90, respectively) for each build.

4.3.3 Inert Gas Fusion and Combustion

Light element chemistry was measured for the powder samples from each participant using Inert Gas Fusion (IGF; LECO 836 series elemental analyzer) and combustion analysis (LECO 844 Series combustion analyzer). The IGF and combustion analyses were performed by Fort Wayne Metals Materials Testing Laboratory (Fort Wayne, Indiana). IGF provides accurate measurement of oxygen, nitrogen, and hydrogen. Combustion analysis was adopted to evaluate carbon content in the powder. Due to a limitation in resources available at the time carbon analysis was only conducted on material from four of the study participants. Samples were measured in accordance with ASTM E1409 for oxygen and nitrogen, ASTM E1447 for hydrogen, and ASTM E1941 for carbon. Each sample was measured 3 times, with the average chemical value reported. A laboratory variance was estimated by repeating the measurement process on one sample five separate times. This lab variance was used in estimating the sample variance for each measured powder sample.

4.3.4 X-Ray Fluorescence

Metallic element analysis was performed on the powder samples using X-Ray Fluorescence (XRF; Bruker M4 Tornado). This is a semi-quantitative technique for evaluating trends in elemental composition between builds. Powder samples were dispersed on carbon tape to create a thin, uniform layer of powder for analysis. Each sample was measured in 10 random locations, with all scans performed at 50 kV and 600 µA. Each scan lasted 180 seconds. An elemental library was established for calculating weight percent using a NIST SRM Ti-V sample (SRM 654b). Using this library, the relative composition of the powder samples could be calculated from the x-ray emission spectra.

4.3.5 Hall Flow, Apparent Density and Tap Density

Powder flow characteristics were measured in accordance with ASTM B213 and B212. Briefly, 80 g samples were taken from each powder sample for measurement. From that 80 g sample, 50.0 g were weighed out and placed in a Hall Flowmeter funnel, with the funnel end blocked. An apparent density cup was placed approximately an inch below the bottom of the funnel. The powder was then allowed to flow freely through the funnel into the density cup. The flow of the powder was recorded using a smartphone camera for time analysis. After the funnel had fully emptied, an additional 30 g of powder was added to the funnel, to allow the density cup to completely fill and overflow. Excess powder was scraped off so the powder was level with the top of the density cup. The weight of the density cup was weighed both empty and full of powder. The volume of the density cup was measured according to ASTM B873 – 21 and found to be 25.05 cm^3. From the weight of the powder and the volume of the density cup, an apparent density was calculated. Hall Flow times were measured using the captured video footage and a video editing software (VSDC Free Video Editor, FLASH-INTEGRO LLC) to evaluate the powder flow start and stop times with 1/30 s accuracy.

Tap density measurements were obtained by transferring the powder from the apparent density cup to a graduated cylinder. The weight of powder in the cylinder was recorded and then the cylinder was pressed against a vibratory plate to consolidate the powder. The graduated cylinder was held against the vibratory plate for 10 seconds or until the powder mass visibly settled to a point where the volume was no longer changing. The post-consolidation volume was recorded and the tap density measured as the quotient of the mass of powder in the cylinder to the consolidated volume.

4.4 **Results**

4.4.1 Morphology and size

SEM evaluation of the powder did not reveal major morphological changes from Builds 7 to 10. Powder morphology in Build 7 was consistent with Build 6 of Phase I, as expected, indicating that no major morphological changes occurred during storage of the powder between Phase I and II. Figure 4.1 shows representative images of powder from Build 7 over a range of magnifications to highlight surface texture, particle morphology, and homogeneity of the particles in the powder. As in Phase I, a rough or wrinkled texture is present on the surface of most of the particles. Small, infrequent satellite particles are observed adhering to some of the particles. Also consistent with Phase I, occasional irregular particles are observed, which are assumed to be spatter from previous builds.

Figure 4.2 shows the evolution of the powder from Builds 7 to 10 for the three partners involved in Phase II. For Partners 1 and 3, no notable changes were observed, with Build 10 powder being indistinguishable from Build 7. More satellite particles were observed in the powder from partner, especially for Build 7. By Build 10 the frequency of satellite particles had reduced to levels similar to the other partners. Figure 4.3 shows details of the satellite particles on Builds 7 and 10 for Partner 2.

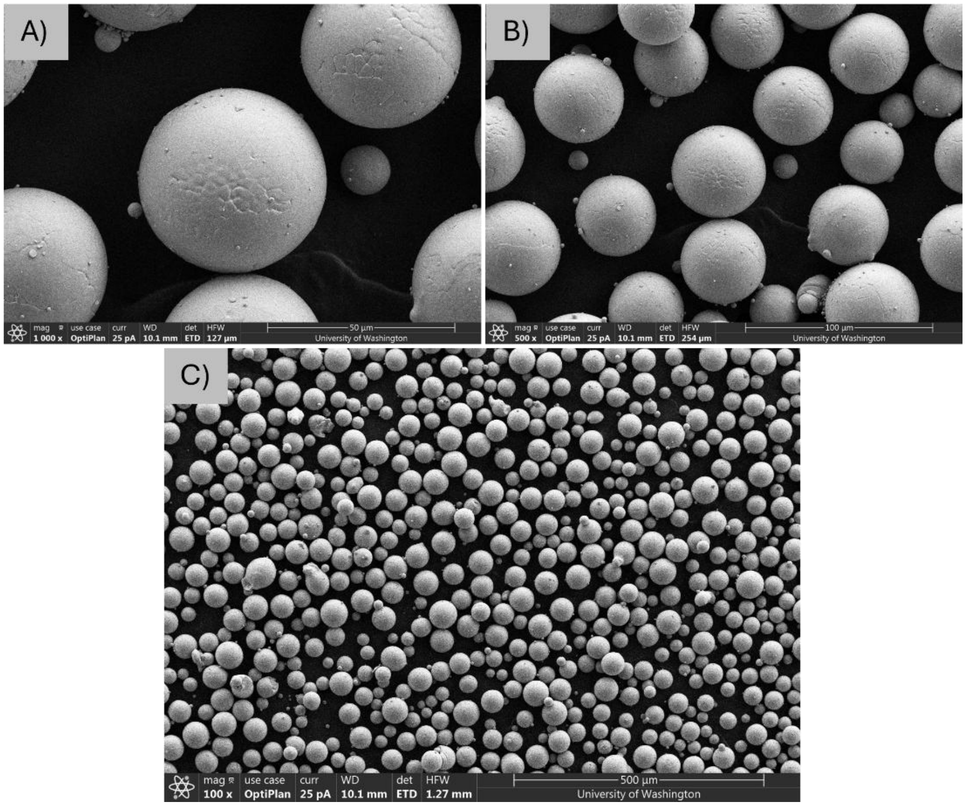

Figure 4.1: Secondary electron images of powder from Partner 1, Build 7 taken at (A) high (1000x), (B) medium (500x) and (C) low (100x) magnification showing representative surface texture, morphology, and distribution.

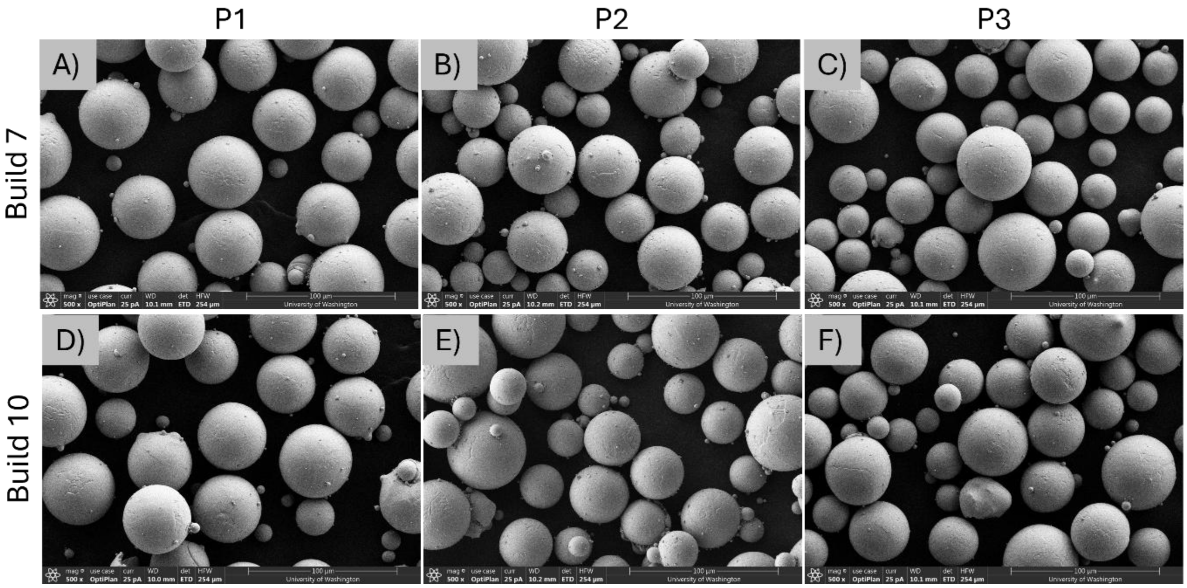

Figure 4.2: Secondar electron images of powder from Builds 7 (A-C) and 10 (D-F) of Partner 1 (A, D), Partner 2 (B, E) and Partner 3 (C, F) comparing morphology of the powder at the start and end of Phase II.

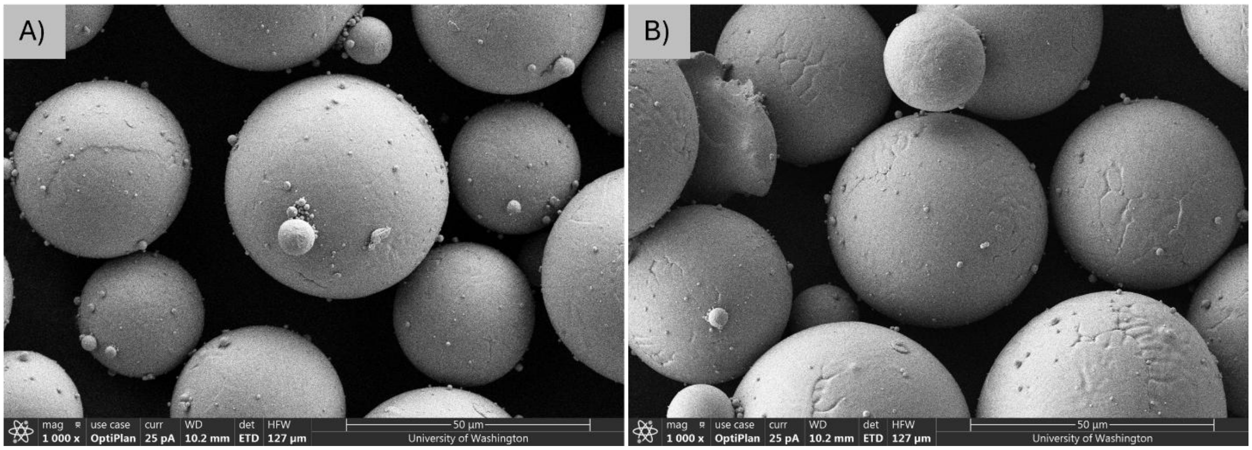

Figure 4.3: Secondary electron images of powder from Partner 2 showing satellite particles

The powder size distributions as measured by DLS for Builds 7-10 of Partners 1-3 in Phase II are shown in Figure 4.4. The 10th, 50th (mean), and 90th percentiles of the PSD (D10, D50, and D90, respectively) were calculated for each PSD and are plotted in Figure 4.5, along with those for Builds 1-6 of Phase I. Figure 4.6 shows the D10, D50, and D90 values plotted just for builds 7-10 for each of the three partners. Particle sizes measured by DLS ranged from about 20-100 µm, with a slight negative skew towards lower values. The 10-90 percentile range for all builds was roughly 28 µm to 55 µm, with a mean around 40 µm. The D10, D50, and D90 values for all 10 builds are reported for Partners 1-3 in Table 4.2. In Phase I, a slight increase in D50 values was observed from Builds 1 to 6. In Phase II, not only did that trend subside, but by Build 10 the trend reversed, resulting in no significant difference in D50 values between Builds 1 and 10 ($P > 0.05$) overall.

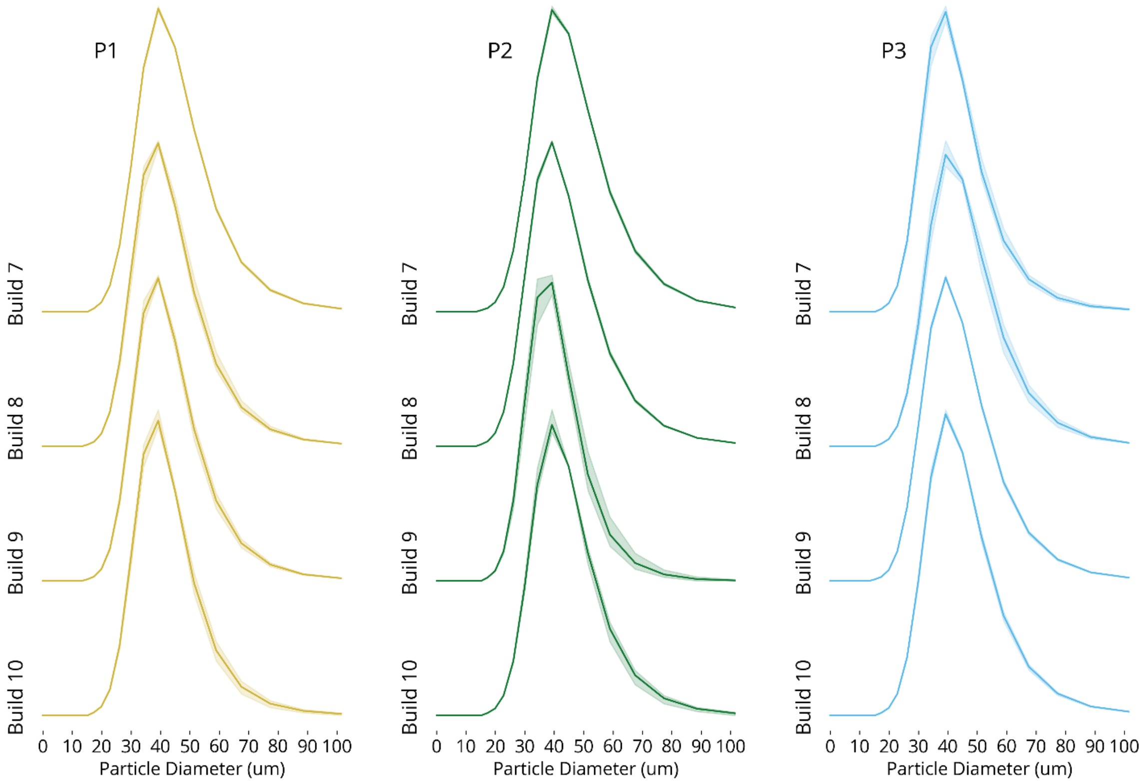

Figure 4.4: Powder size distribution histograms for Builds 7-10 for Partners 1-3 in Phase II.

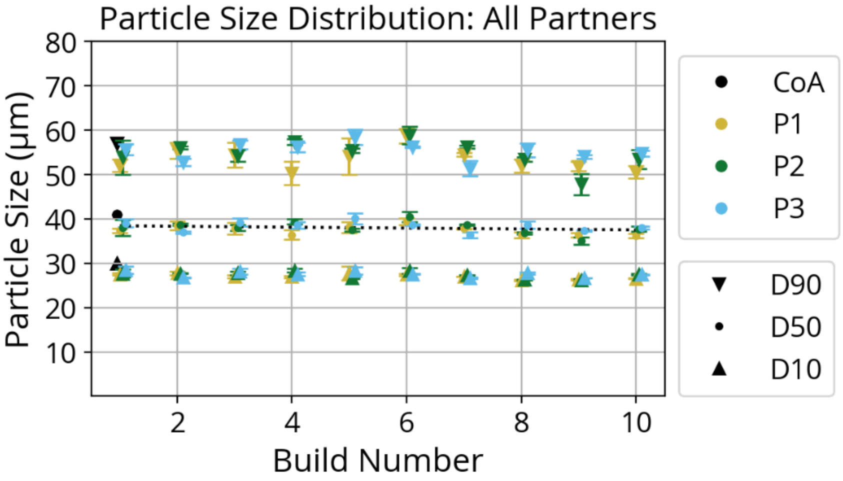

Figure 4.5: Powder size distribution graph for all builds conducted in Phase I (Builds 1-6) and Phase II (Builds 7-10) for the three partners involved in Phase II. D10, D50, and D90 values are given for each build. A linear trend line is fit to the average D50 values.

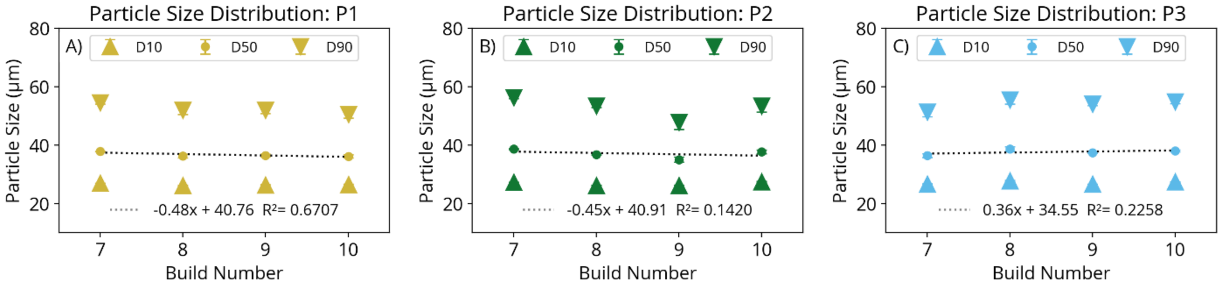

Figure 4.6: Powder size distribution graphs for the individual partners involved in Phase II over the four builds of the program.

Table 4.2: D10, D50, and D90 values averaged across all Phase II participants (P1-3) for Builds 1-10, with mean (μ), standard deviation (σ) and variance (σ^2) reported.

Build #	D10			D50			D90		
	μ	σ	σ^2	μ	σ	σ^2	μ	σ	σ^2
1	27.83	0.69	0.48	37.98	1.21	1.46	53.40	2.59	6.72
2	27.45	0.52	0.27	38.08	0.99	0.98	54.79	1.81	3.26
3	27.65	0.65	0.42	38.38	1.13	1.27	55.15	2.09	4.38
4	27.59	0.72	0.51	38.04	1.54	2.37	54.38	3.68	13.52
5	27.62	1.19	1.42	38.58	1.47	1.15	55.98	3.04	9.26
6	27.80	0.57	0.33	39.58	1.09	1.18	58.08	1.87	3.50
7	27.03	0.31	0.10	37.63	1.05	1.10	54.03	2.32	5.38
8	26.81	0.81	0.65	37.34	1.28	1.64	53.69	2.00	4.00
9	26.39	0.30	0.09	36.28	1.14	1.30	51.25	3.05	9.31
10	27.16	0.44	0.19	37.33	0.96	0.92	52.92	2.27	5.16

4.4.2 Chemistry

Figure 4.7 shows the metallic chemistry measurements for Phase II, independent of the previous phase. Figure 4.8 shows the measurements for Phases 1 and II for comparison. As in Phase I, no clear change in powder chemistry was observed over the course of the Phase II, although some builds or partners showed occasional statistical variance. No statistical difference was observed between Builds 7 and 10 overall when evaluated by pairwise Tukey HSD ($P > 0.05$). No statistical difference was observed between Builds 1 and 10 overall ($P > 0.05$). Numeric values for the measured elements are given in Table 4.3 for Builds 1 and 10 for comparison. There were some significant differences in aluminum and vanadium content between partners observed for particular builds. Specifically, statistically significant differences in aluminum content were observed between Partners 2 and 3 in Build 9 and between Partners 1 and 3 in Build 10, as shown in Figure 4.9. For vanadium, more differences were observed: between Partner 3 and Partners 1 and 2 in Build 7, between Partner 2 and Partners 1 and 3 in Build 9, and between Partners 1 and 3 in Build 10, as shown in Figure 4.10. No statistical differences in iron content were observed between partners in any build. The cause of the occasional variation in powder chemistry is not clear, but may represent inhomogeneity of the powder body. Aluminum, vanadium, and iron all remained at constant values through the 10 builds of Phase I and II, and were within tolerances of ASTM F2924, except for vanadium; the levels of vanadium were at the minimum value for the standard, well below the nominal value provided by the CoA. Akin to Phase I, it is not clear why there is a discrepancy in the vanadium measurement, but the trend continues to be consistent with the other metal elements. Iron measured higher than the reported CoA value, but was below the maximum value required by ASTM F2924.

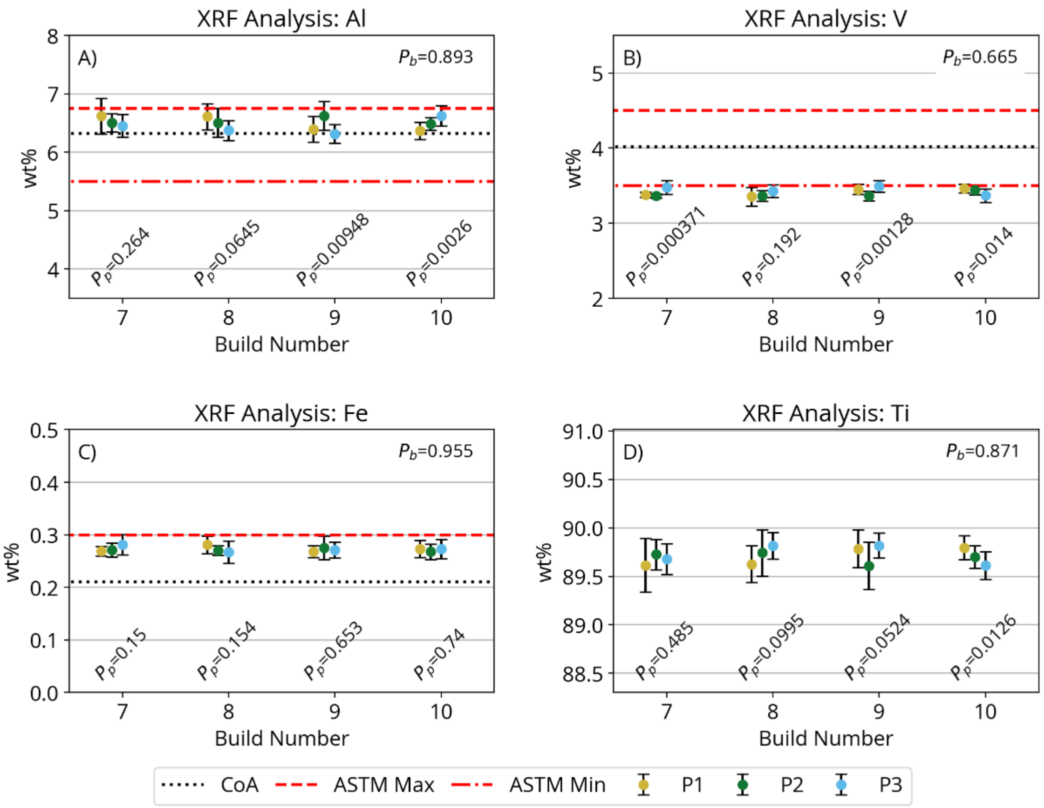

Figure 4.7: XRF measurements for the metallic elements of powder from Builds 7-10 of Phase II, for Partners 1, 2, and 3. Minimum and maximum limits given by ASTM F2924 for Ti-6Al-4V are marked with red dashed lines. Certificate of Analysis (CoA) values provided by the manufacturer are marked with a black dotted line. The P-value derived from ANOVA analysis of the three builds (P_b) is given in the upper right corner of each graph. P-values derived from ANOVA analysis between participants for each build (P_p) are given below the data points for that build.

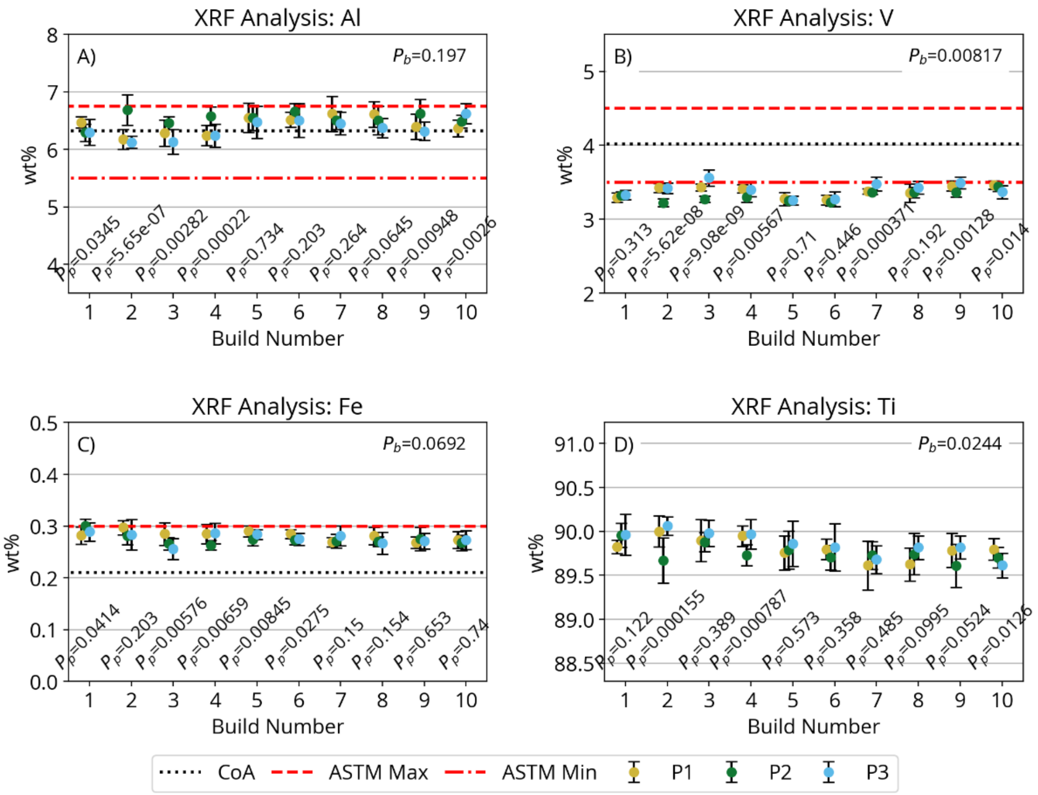

Figure 4.8: XRF measurements for the metallic elements of powder from Phase I and II, Builds 1, 3, 6 and then 7-10 for Partners 1, 2 and 3.

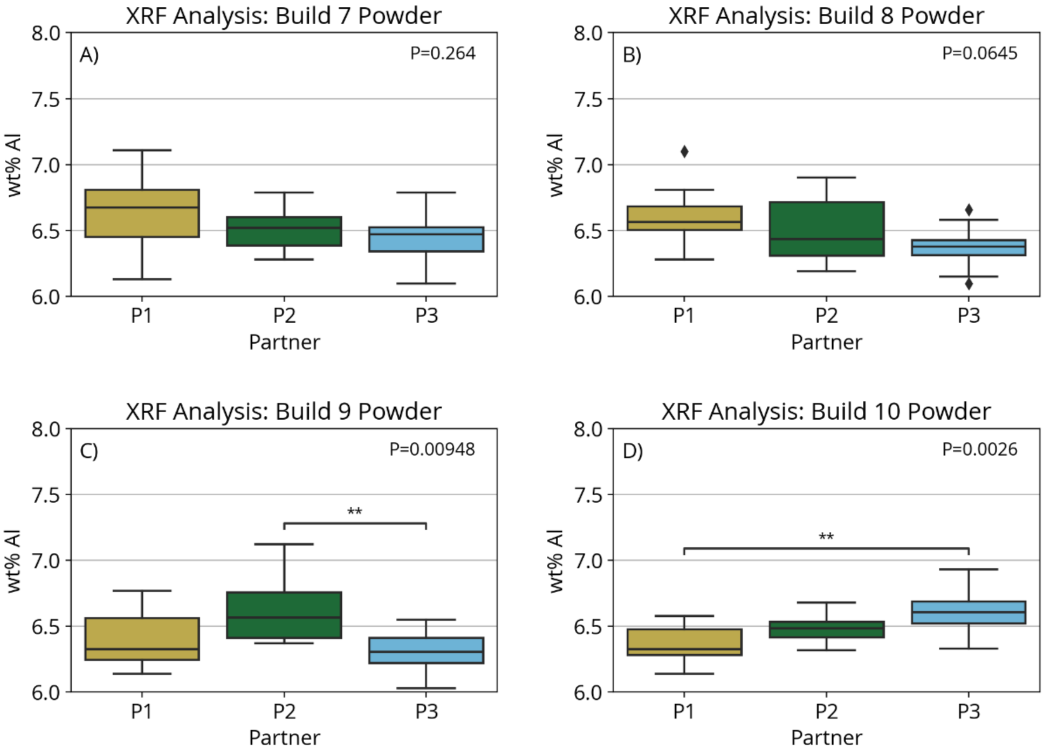

Figure 4.9: Statistical analysis of measures aluminum content of powder samples from Builds 7-10. The P-value derived from ANOVA analysis of the three participants is given in the upper right corner of each graph. Statistically significant pairings, determined by Tukey analysis, are shown as annotated brackets.

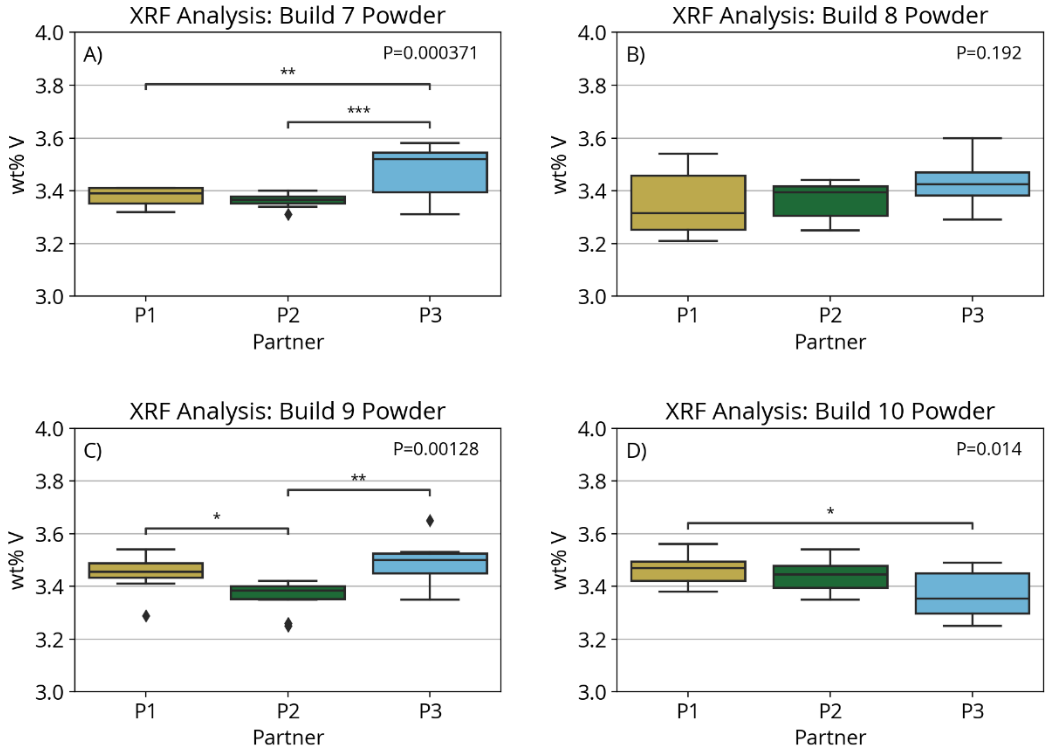

Figure 4.10: Statistical analysis of measures vanadium content of powder samples from Builds 7-10. The P-value derived from ANOVA analysis of the three participants is given in the upper right corner of each graph. Statistically significant pairings, determined by Tukey analysis, are shown as annotated brackets.

Table 4.3: Measured values for metallic components of the powder from Builds 1 and 10 for Partners 1-3.

	Build	**Ti (wt%)**	**Al (wt%)**	**V (wt%)**	**Fe (wt%)**
P1	1	89.82 ± 0.08	6.47 ± 0.10	3.29 ± 0.06	0.28 ± 0.02
	10	89.80 ± 0.12	6.37 ± 0.15	3.46 ± 0.05	0.27 ± 0.02
P2	1	89.96 ± 0.14	6.29 ± 0.15	3.32 ± 0.05	0.30 ± 0.01
	10	89.70 ± 0.12	6.49 ± 0.11	3.44 ± 0.07	0.27 ± 0.01
P3	1	89.96 ± 0.23	6.30 ± 0.22	3.33 ± 0.06	0.29 ± 0.02
	10	89.61 ± 0.14	6.62 ± 0.17	3.37 ± 0.09	0.27 ± 0.02

Figure 4.11 shows the IGF measurements for oxygen, nitrogen, and hydrogen, and the combustion measurements for carbon, for the powder of Phases I and II. Notably, while the measurements are consistent for Phases I (Builds 1, 3, and 6) and 2 (Builds 7-10) individually, there appears to be a significant change in some values from Phase I to Phase II. The measured values of oxygen and nitrogen levels both decrease from Builds 6 to 7. While there was a significant (>2 year) gap between the testing of material from Phase I and Phase II, nothing in the powder storage process would be expected to have a significant effect on oxygen or nitrogen levels in the powder. It is assumed that this discrepancy is due to changes in the sample handling or testing method used by the testing facility. As such, the light element chemistry of the powder was evaluated for Phases I and II separately. Results show that neither Phase I nor Phase II exhibited a significant change in light element chemistry of the powder. All measured values remained close to the nominal values from the CoA across the study.

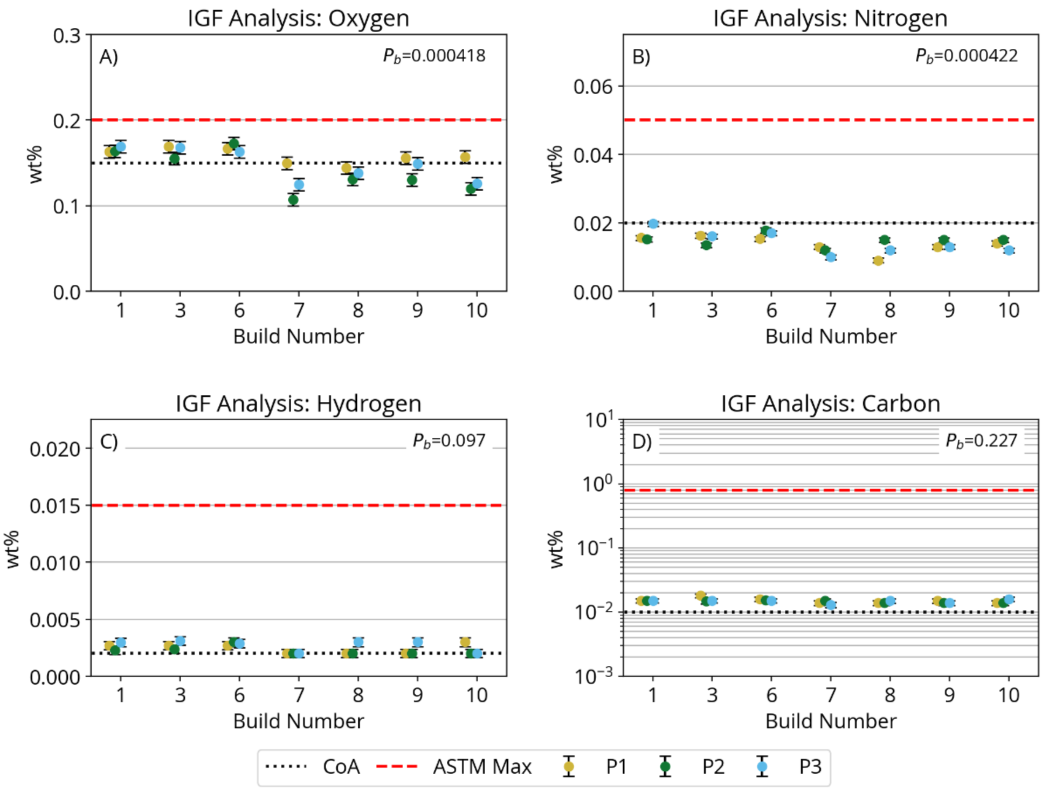

Figure 4.11: Inert gas fusion (O, N, H) and combustion (C) measurements for Phase I and II, Builds 1, 3 and 6, and 7-10 for Partners 1, 2, and 3. Maximum limits given by ASTM F2924 for Ti-6Al-4V are marked with a red dashed line. Certificate of Analysis (CoA) values for each element are marked with a black dotted line. The P-value derived from ANOVA analysis of the three builds (P_b) is given in the upper right corner of each graph.

4.4.3 Hall Flow

Results for the average Hall flow and apparent density measurements for powder from Phase I and II builds are presented in Figure 4.12. The average flow times in Phase II were slightly higher than those measured in Phase I, with average flow times measured as 30.9, 30.0, 29.4, and 29.5 s for Builds 7-10. Average flow times for Phase I were measured as 27.5, 28.6, and 28.1 s for Builds 1, 3, and 6. Hall flow times, apparent density, and tap density measurements for each partner are presented in Figure 4.13. Hall flow times increased considerably for Partner 2 between Builds 6 and 7, from 26.3 s to 37.6 s. This significant jump is most likely due to the change in powder lot used by Partner 2 in Phase II. Excluding Partner 2 from the flow averages gives measurements of 30.0, 28.8, 28.5, and 28.3 s for Builds 7-10. Apparent density, which decreased from Builds 1-6 in Phase I, did not change for Builds 7-10, although it showed much more variability build to build. Tap density, which was not measured in Phase I, decreased slightly from 2.85 to 2.81 g/cm^3.

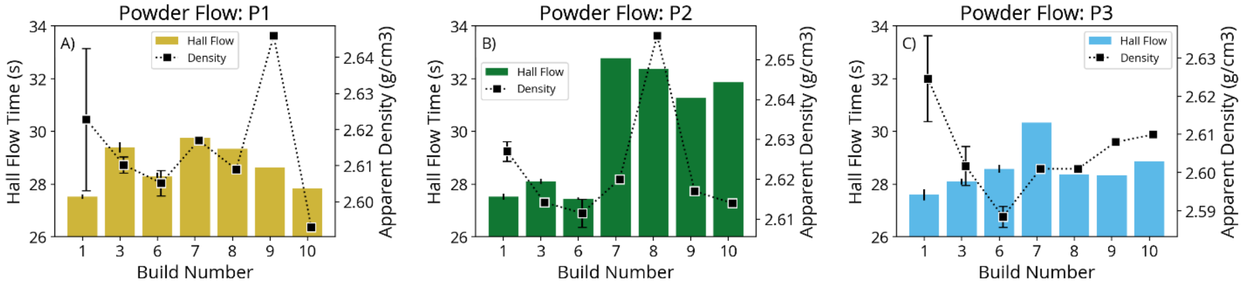

Figure 4.12: Hall flow and apparent density measurements for powder from Phase I and II builds 1, 3, and 6, and 7-10 for Partners 1, 2 and 3.

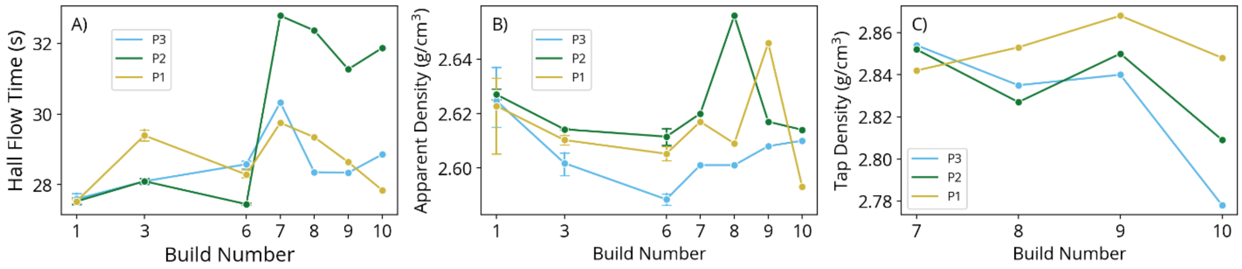

Figure 4.13: Hall flow times, apparent density, and tap density measurements for powder from Phase I and II Builds 1, 3, and 6, and 7-10 for Partners 1, 2 and 3. Tap density measurements include only Builds 7-10 of Phase II.

4.5 **Discussion**

Consistent with results of Phase I (Chapter 3), there were limited changes in powder properties observed in Phase II. Perhaps the most significant change occurred in the powder morphology of Phase I as evidenced by the disappearance of the majority of small satellite particles present on the powder particles at the beginning of the study. By Build 6 of Phase I, all but the most firmly attached satellite particles were removed from the powder particle surfaces. Since this was the same powder that was used at the beginning of Phase II, the already established powder condition did not noticeably change during the additional four builds. The exception to that statement is with Partner 2, who started Phase II with a new lot of virgin powder. As expected, the new lot of powder exhibited the same characteristic properties of virgin powder, including abundant satellite particles. Interestingly, this new powder lot of Partner 2 followed the same general progression in Builds 7-10 that the previous lot of powder did in Builds 1-6. Unfortunately, the quantity of satellite particles was not quantified, due to the complexity in achieving a robust measurement. As such. exact comparisons between the states of the virgin powders and the rate that the satellite were lost cannot be determined.

In examining the particle size distributions of the powder samples from the ten builds across Phases I and II, one of the most interesting observations is that the mean particle sizes increase from Build to Build 6, but then decrease back to the starting values in Builds 7-10. These inconsistent results are similar to the inconsistencies in reported literature for changes to PSD with reuse, with some studies showing an increase [26], a decrease [38,40–43], or no change [36,37,39,45] in PSD. The inconsistent behavior of PSD with reuse could indicate an unaccounted contributing factor in the PSD response. Phase I of the study utilized a powder top-off reuse strategy, as discussed in Chapter 2. The specific protocol called for virgin powder to be added to the recovered powder, equal to the mass of powder lost in the prior print. The nature of this reuse strategy leads to accelerated and heterogeneous aging of the powder mass being cycled in the prints, as both heat-affected powder and spatter are retained in the reused powder mass [15,24]. An accumulation of large spatter and agglomerates could explain the increase in particle size observed in Phase I, as discussed in Chapter 3. The rate of aging of the powder depends in part on the length of laser exposure time in each build, and the volume density of metal in the build. Phase II involved fewer builds but much more total laser exposure time – approximately 420 hours in Phase II versus 160 hours for the six builds in Phase I. Phase II also had a higher volume density of metal in the build – 24% of the build volume versus 11% in Phase I. The interplay between laser exposure time, volume density, and reuse number is poorly studied. On one hand, longer lengths of laser exposure means more spatter generation. However, if a higher volume of metal is being produced, then more of the spatter produced will be consumed via melting into the parts. The balance between spatter generation and consumption may depend on the specific amount and density of metal production in the builds. It is possible that the specific trends in particle size reported in the literature are highly dependent on build design. Further research is warranted in this subject, as particle size is a key factor in powder flowability and packing and therefore highly important to metal quality.

As observed in Phase I, metal chemistry did not change considerably in the powder over the four builds of Phase II. Some variation was observed between partners for select builds but no overall trend was observed. While in Phase I, higher variability was observed between partners in later builds, this trend did not continue in Phase II. Some important considerations in interpreting these results are the reduced number of partners, the reduced build schedule, and the changes in build design for Phase II. With fewer partners participating in Phase II, it is more difficult to quantify the extent of powder variability, owing simply to the reduced sample size. Similarly, the reduced build schedule in Phase II provided less reuse cycles to accumulate changes in powder. Build space utilization is another important factor to consider in powder reuse. The builds in Phase II occupied much more of the build space than those in Phase I, and therefore consumed a larger amount of powder per build. Given that the consumed powder was replaced with virgin powder, this implies that more virgin powder was added after each Phase II build than in Phase I. This higher refreshment rate may have contributed to suppressing accumulating variations in powder chemistry. Build volume usage is not a metric often reported in literature studies on powder reuse, but should be considered as an important contributing factor towards the rate of powder degradation.

Powder flowability for Partners 1 and 3 did not change significantly in Phase II. The average flow times recorded for these two partners were nearly identical between Builds 6 and 10. Admittedly, the valuation of flow characteristics was overall hampered by the reduction in number of partners and the changes in powder lot usage in Phase II. Partner 2 exhibited a significant jump in powder flow time at the start of Phase II, which is attributed to the change in powder lot. While the new powder lot was chosen to be as similar as possible to the previous lot, some properties, such as flow time, were different as a result of specific aspects that arise when beginning with virgin powder. Despite the discontinuity in flow time between Builds 6 and 7, the trend of flow time over Builds 7-10 was the same for Partner 2 as it was for Partners 1 and 3. This observation supports the argument that process induced changes to flowability are minimal. Apparent density showed a slight decrease over Builds 1-10 as discussed in Chapter 3, but no notable trend for Builds 7-10. There was higher build-to build variability in apparent density in the Phase II builds. It is possible that the higher variability could be due to a random distribution of spatter content in the powder samples used for testing. Accurate quantification of spatter content would be needed to verify the effect on the measurement of flow properties. Tap density also decreased over the four builds in Phase II, which could also be attributed to spatter, as irregular particle shapes can disrupt the packing behavior of fine powders. These results are generally consistent with literature, although most studies show a slight increase in flowability, albeit with more reuse cycles [28,29,31–33,36–43].

Despite an absence of any significant degradation in powder quality after 10 builds and nearly 400 hours of build time, it is possible that factors outside the measured characteristics affect powder and metal quality. Fatigue crack initiation, for instance, will tend to originate at any defect that results in a stress concentration. Small quantities of contamination or impurities could significantly degrade fatigue performance while not significantly affecting the bulk properties of the powder. It is important to consider powder quality wholistically and not overly rely on a handful of bulk property measurements.

Powder reuse via the replacement strategy used in this study can have a benefit of slowing the average rate of degradation of the powder compared to reuse with no replacement, as shown in Figure 1.9(A), but it also masks the effects of reuse. Overall, this study was limited by the choice of reuse strategy and the small number of builds performed. While this approach was beneficial for maximizing the quality of metal produced, it made the secondary goal of evaluating powder reuse difficult. For a dedicated study on reuse, powder reuse without replacement should be used to accelerate powder degradation and the accumulation of contamination. Varying the quantity of metal built could also give insight into the relative rates of generation, accumulation, and consumption of the spatter in the powder volume. Combining tensile and fatigue evaluation in every build could allow better evaluation of the effect of powder reuse on mechanical properties.

4.6 **Conclusions**

Based on results from an experimental evaluation of powder reuse within four additional builds in the Round Robin program, the following conclusions are drawn:

- Extended reuse through an additional four builds did not intensify the powder quality trends observed in Phase I of the study. Rather, many of the measurements that increased in Phase I, such as mean powder particle size, returned to nominal values in Phase II.
- Powder chemistry did not change over the course of the RR study, although variability between partners was observed.
- Powder PSD decreased from builds 7-10, returning to values identical to the starting virgin powder values.

Chapter 5 Metal Vapor Condensate

The content of this chapter draws upon material first presented in: A. Montelione, S. Waddel, M. Bokhoor, T.P. Weihs, M. Ramulu, D. Arola, Metal vapor condensate in laser powder bed fusion of Ti6Al4V: Methods of acquisition, characterization and ignition behavior, Additive Manufacturing 121 (2026) 105143. https://doi.org/10.1016/j.addma.2026.105143.

5.1 Introduction

Metal Vapor Condensate (MVC) is an inherent byproduct of the laser melting process in Additive Manufacturing (AM) by Laser Powder Bed Fusion (L-PBF). Due to the small particle size and high reactivity, the MVC that forms during printing of titanium and aluminum alloys poses both physical and health hazards to machine operators during maintenance and operation. The current understanding of MVC and its ignition characteristics is limited. This investigation explores novel methods for collection of MVC in L-PBF of Grade 5 Ti-6Al-4V, methods for characterizing the physical and chemical properties of the material and early results quantifying ignition behavior. Both ex-situ exfoliation techniques and novel in-situ direct substrate deposition methods were applied to collect MVC for analysis by SEM, TEM, EDS, TGA, and hot-filament wire ignition. Results show that the MVC forms complex microscale network structures consisting of 10-60 nm diameter nanoparticles, with very high surface area to volume ratios. Chemical analysis reveals that the material is enriched in aluminum as compared to the base Ti-6Al-4V powder feedstock, with up to 18 wt% Al. Ignition temperatures of 350-450°C were measured, with an estimated activation energy from the Kissinger method of 55 kJ/mol. This novel combination of collection techniques and applied characterization provides a deeper understanding of the physical and chemical characteristics of MVC generated in L-PBF, enroute to the development of better control measures.

5.2 Materials and Methods

5.2.1 Material

The feedstock material used in this study is Grade 5 Ti-6Al-4V powder distributed by EOS (EOS GmbH, Germany). The feedstock material consists of a fine metallic powder produced through plasma atomization of titanium wire. Although different lots of powder were used in the builds included in this study, the typical composition and characteristics of this type of powder are described in Table 5.1. The different powder lots used in the builds varied in extent of reuse history and may have varied slightly in powder characteristics from the nominal values. These variations are not expected to be significant or have influence on the results presented.

Table 5.1: Representative composition and characteristics of Ti-6Al-4V powder used in this study, as given in the certificate of analysis from one of the lots of powder used.

Element	Wt %	Property	Result
Ti	89.27	D10	30 μm
Al	6.32	D50	41 μm
V	4.02	D90	57 μm
Fe	0.21		
O	0.15	Apparent Density	2.59 g/cm^3
C	0.01	Skeletal Density	4.416 g/cm^3
N	0.02		
H	0.002	Water Content	40 ppm

5.2.2 Machine

MVC was collected during and after builds that were performed using an EOS M290 (EOS GmbH, Germany) L-PBF AM machine. The M290 uses a 400 W Yb-fiber laser, with galvanometer scanning mirrors and an F-theta lens for laser focusing and positioning. All builds were performed using standard build parameters from EOSPrint version 2.10 (Ti64_SpeedM291 v1.10), which includes a laser power of 340 W, laser speed of 1250 mm/s, a layer height of 60 µm, and a hatch spacing of 120 µm (energy input of 37.78 J/mm^3). The laser spot size at the build surface is approximately 100 µm, as reported by EOS. The build volume of the M290 is roughly 250 x 250 x 325 mm, including the build plate height. A photograph of the M290 used in the study is shown in Figure 5.1(A). The machine in this study was equiped with a standard HSS recoater blade. This specific machine is only used for printing Ti6Al4V, which made it an ideal resource for this investigation to preclude potential contamination from other feedstock.

Due to the highly reactive nature of many of the materials used in the L-PBF process, the build chamber is designed to operate under an inert atmosphere of argon or nitrogen. During the build process, high purity argon (99.998%) gas is continuously pumped into the chamber by a turbine maintaining a constant 0.8 mbar pressure differential and with volumetric gas flow rate of 120 m^3/hr [65]. Oxygen content in the build chamber is maintained at < 0.1% throughout the build process. The machine conditions were monitored throughout the builds performed and the machine operation settings were identical for all builds. The gas enters the build chamber through a pair of vents in the rear of the build chamber (Figure 5.1(B)). These vents are designed to create a laminar flow of gas over the powder bed to carry the MVC and spatter away from the laser path. A description of the argon gas flow direction as guided by the inlet nozzles within the chamber is shown in Figure 5.1(B).

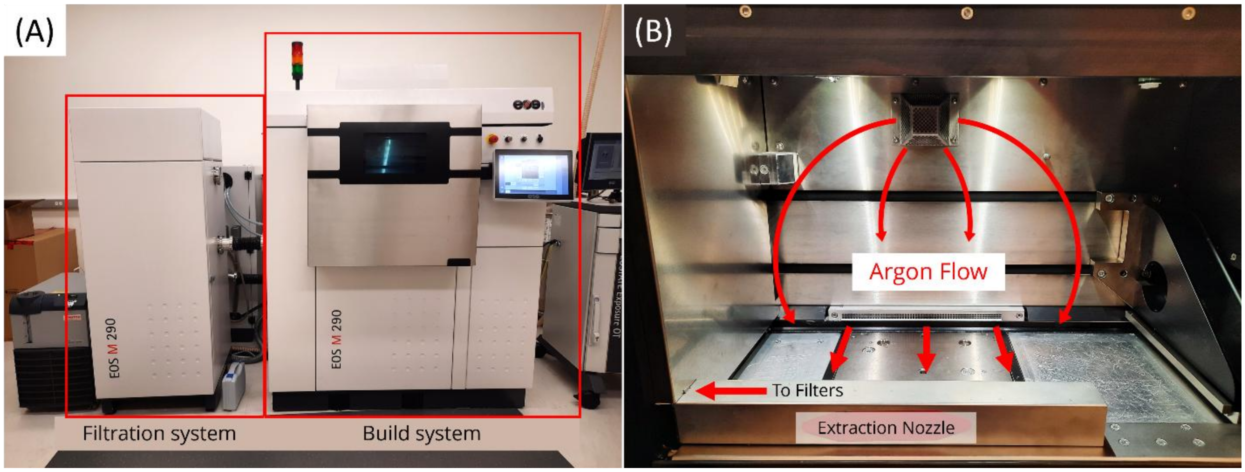

Figure 5.1: The EOS M290 L-PBF AM machine, A) highlighting the filtration system, and B) inside the EOS M290 build chamber, showing the direction of argon gas flow within the chamber during the build process.

An extraction nozzle assembly located at the front of the build chamber enables the inert gas and particles to be exhausted from the build chamber. The gas flow is diverted through this nozzle towards a separate filtration and recirculation unit. Figure 5.2 shows a schematic diagram of the path of the argon gas through the chamber during the build process, as it collects particulate material and is carried to the filtration system. The filtration system (Figure 5.1(A)) has three filtration stages, including a cyclonic separator to remove the powder and large particles, followed by medium (F9) and fine (H13) filters.

5.2.3 Collection

Collection of the MVC was performed using a combination of *in-situ* and *ex-situ* methods. *In-situ* collection, referred to as Direct Substrate Deposition (DSD) method, consisted of placing a collection substrate in the gas stream that remained during the build process and was retrieved after completion. A small metal tab was used to hold the collection substrates by double sided adhesive carbon tape. To enable additional experiments to be performed on the collected MVC and complementary thermal characterization of the collected materials, square plates of Alumina (approx. 0.5x4x4 mm) were prepared from larger sheets. The plates and other substrates used for collection were weighed before and after collection using the internal precision balance on the TGA instrument (Mettler Toledo TGA/DSC 3+) to estimate the mass of material loading

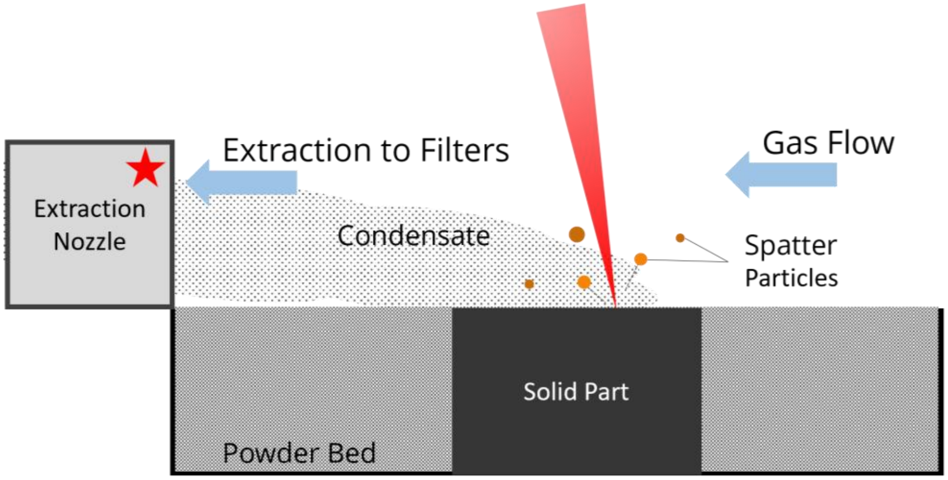

Figure 5.2: Schematic diagram showing the path of gas flow from the back of the build chamber to the front (shown here from right to left). MVC generated by the laser melting process is carried by the gas flow through the extraction nozzle to the filtration system (Figure 5.1). Collection substrates for acquiring condensate are placed in the outgoing gas stream in the extraction nozzle where condensate deposits.

achieved. The collection substrates were secured with metal tabs to the vanes of the extraction nozzle (Figure 5.3(A)). Multiple iterations of preliminary testing showed that facing the tabs inward was advantageous to protect them from spatter thrown off from the melt process, as shown in Figure 5.3(A). The tabs were positioned close to the top wall of the nozzle assembly (as installed) as shown in the diagram in Figure 5.3(C). This position kept them furthest from the powder being swept past the nozzle by the recoater. MVC is generated during the build process and carried by the gas stream past the collection substrates where some of it deposits on the surface of the substrates. The DSD method allows collection of MVC on virtually any substrate without disrupting or interfering with the build process. Using this method, MVC was collected during builds that were performed to support a variety of studies, some of which are shown in Figure 5.4. Images of collection substrates mounted on a metal tab before and after collection from a representative build are shown in Figure 5.5, demonstrating the mechanism of collection.

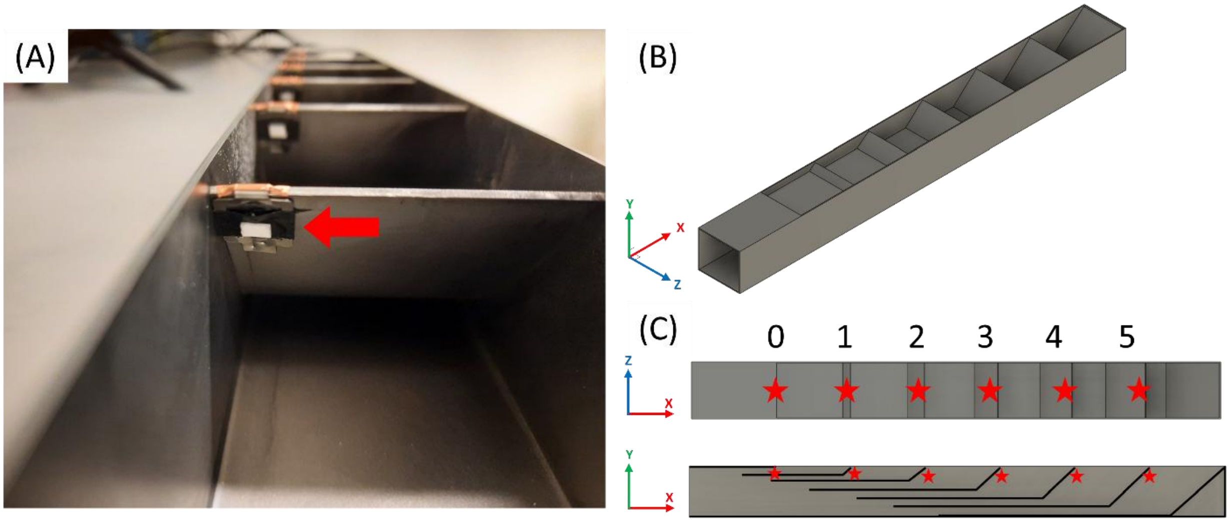

Figure 5.3: Details of the collection materials. A) Photo of tabs mounted on the interior regions of the extraction nozzle to shield them from spatter and powder (red arrow points to tab), (B) Orthographic view of a model of the extraction nozzle with (C) top and side section views of the extraction nozzle with collection tab placement locations indicated by red stars.

Ex-situ collection of MVC was performed by removing material deposited on the surfaces inside the build chamber after the build was complete. The extraction nozzle was the primary location for ex-situ material collection, as MVC was found to deposit on all surfaces of the nozzle. Material was collected by first attaching a piece of double-sided carbon tape to a small aluminum stub and then pressing the carbon tape firmly against the surface of the nozzle (tape collection). The MVC material that was deposited on the surface of the nozzle adhered to the tape and could be removed using this approach for evaluation. The MVC was also collected by scrubbing the surface of the extraction nozzle with a piece of filter material and a solvent (exfoliation). This process loosened the MVC that was adhered to the surface, which could then be rinsed into a collection vial. Various filter materials and solvents were found to work for this method, including PTFE, nylon, and fiberglass filters, using water, acetone, or isopropyl alcohol as solvents. The solvents were chosen based on their prominence in the literature, commercial availability, and ease of access.

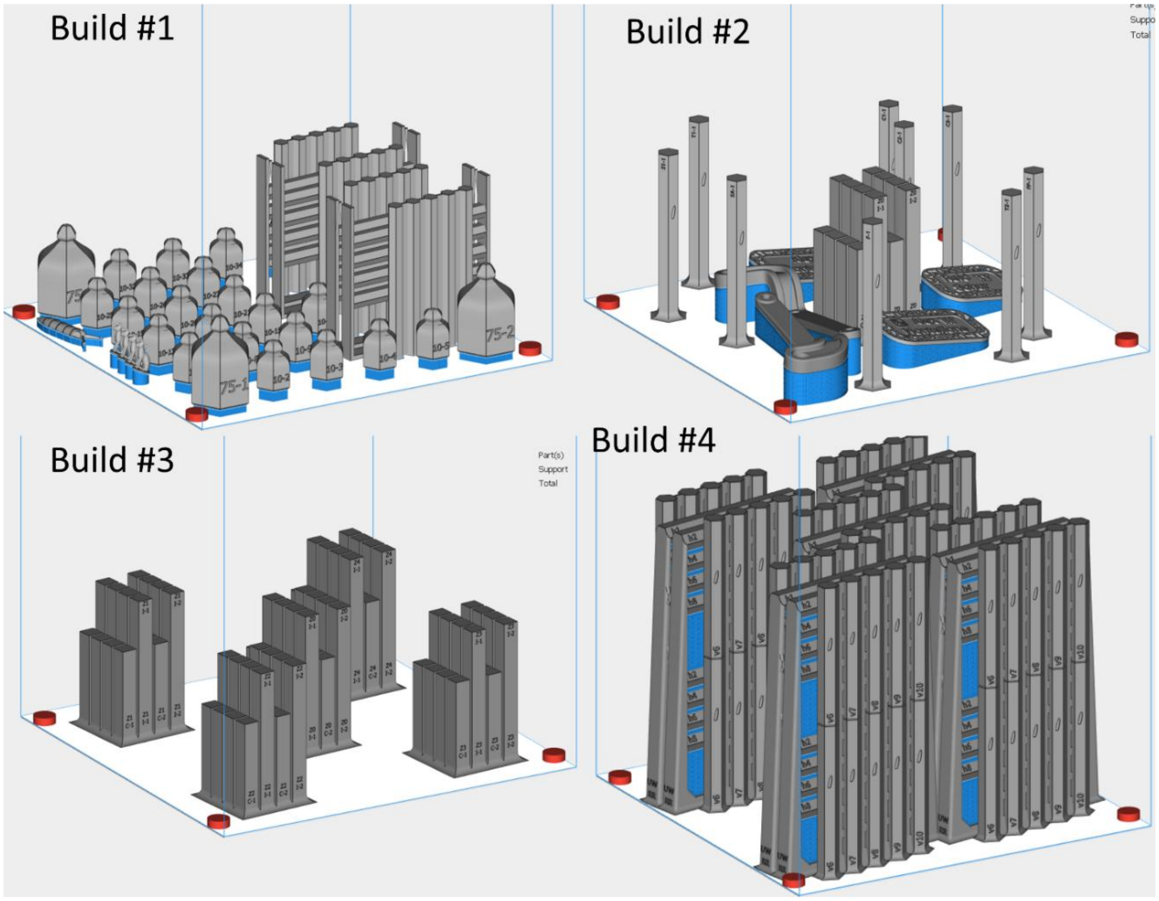

Figure 5.4: Renderings of various builds used for MVC generation and collection.

5.2.4 Characterization

High magnification microscopic evaluation of the MVC was performed using two different scanning electron microscopes (SEM), including a XL30 Sirion FEG Digital SEM (FEI, USA) and an Apreo Variable Pressure SEM (ThermoFisher Scientific, USA). Both machines are equipped with energy-dispersive X-ray (EDS) detectors. Accelerating voltages of 2-5 kV were used for general imaging, while voltages of 15-20 kV were used for EDS analysis. The working distance was kept between 3-5 mm for imaging and 10 mm for EDS. MVC samples were collected directly from the extraction nozzle via tape collection, or by exfoliation using IPA and pipetting material onto copper foil tape. Measurements of the individual MVC particles size were obtained by manual measurement using ImageJ (NIH, Maryland, USA) on the SEM images where individual particles could be easily discerned.

Transmission Electron Microscope (TEM) imaging was used to complement the SEM results in analyzing the particle size and composition, which was effective at reducing signal noise from the background substrate. Imaging was performed using a FEI (Thermo Fisher Scientific) Tecnai TF20 UltraTwin TEM at 200 kV with a Gatan UltraScan CCD camera. The TEM was equipped with an EDAX Elite-T EDS detector for TEM-EDS. To support TEM analysis, the MVC was collected by exfoliation using a PTFE filter material and water. The suspended MVC was then pipetted onto a lacey carbon coated copper grid (Electron Microscopy Sciences, Hatfield, PA) for TEM analysis.

Ignition characteristics were measured via hot-filament ignition pyrometry as described in Polk et al. [73]. MVC collected by *ex-situ* methods from the extraction nozzle area was suspended in n-hexane and applied to a 4 cm length of 28-gauge nichrome wire. Approximately 50 μg of material was used in each test. The wire was heated resistively using current supplied by up to three 12V batteries connected in series. Varying the number of batteries changed the driving voltage and allowed modest control of the heating rate. Current densities were calculated as approximately $2.7\text{x}10^8$, $5.5\text{x}10^8$, and $8.2\text{x}10^8$ A/m^2 for experimental configurations consisting of one, two, or three batteries. Between 10-12 tests were performed for each test configuration. The temperature of the wire was determined using a two-color, low-temperature infrared pyrometer (Kleiber, Model KGA 740-LO). Calibration of the pyrometer was performed using an Omega BB-4A Temperature Calibrator for the 200-982°C temperature range. A high-speed camera (Photron Limited Fastcam SA-Z) set to record at 20,000 fps recorded the moment of ignition. The first moment of particle ignition was identified by a rise in maximum pixel intensity value in the recorded footage. A Python script adapted from the MATLAB script described in the original work determined the ignition temperature from the pyrometer data and the identified ignition frame. The python script additionally calculated the heating rate as the slope of a line fit to the pyrometer data in the region of ignition. The Kissinger method [74,75] was used to determine the activation energy (E) of the ignition reaction using the measured heating rate (β) and ignition temperature (T), and gas constant (R) as follows:

$$E = -R \frac{d \ln\frac{\beta}{T^2}}{d\, T^{-1}} \tag{1}$$

Thermogravimetric analysis (TGA) was used to supplement the ignition characteristics by providing low heating rate reaction data. TGA was performed on a Mettler Toledo TGA/DSC 3+ dual TGA and DSC instrument. The samples were loaded in alumina pans (70 µl, 6 mm x 4.5 mm) and subjected to a heat ramp from room temperature up to 800 °C at a ramp rate of 10 °C min^{-1} under a constant stream of air at a flow rate of 30 mL min^{-1}. The mass of typical samples was around 2 mg. The oxidation onset temperature was defined from the first onset of mass gain for comparison to wire ignition.

5.3 Results

5.3.1 Collection Results

Images of collection substrates before and after a build are shown in Figure 5.5, demonstrating the mechanism of collection and relative effectiveness. There was visible darkening of the collection substrates placed within the extraction nozzle, which confirmed that MVC was depositing on the substrates during the build process. The amount of material that was collected *in-situ* on each alumina plate varied between locations and from build to build, even between identical builds. In general, the mass of MVC collected per build ranged from 20 to 100 µg per square, which equated to approximately 2 $\mu g\ mm^{-2}$ per build and roughly 0.03 $\mu g\ mm^{-2}\ hr^{-1}$. Figure 5.6 presents collection measurement results from four builds performed on the L-PBF machine, including description of the average load per build in Figure 5.6(A) and the sample load normalized by the build volume in Figure 5.6(B). As evident in this figure, the collection rates were generally higher on the vanes near the center of the extraction nozzle. However, some builds exhibited significant outliers in the collection distribution, which is possibly related to the distribution of metal emission that is specific to each individual build. Since the builds varied in duration as well as quantity of metal built overall, some inherently produced more MVC than others, as apparent in Figure 5.6(A). Normalizing the collected MVC per square millimeter of collection surface by the total volume of the parts and supports in the build file resulted in the distribution shown in Figure 5.6(B). Averaging these values for all locations gave an approximate collection rate of 1.36×10^{-9} mg/mm^5; the volume of metal in the build represents the total volume of the parts and supports estimated by the modeling software (Materialise Magics, Belgium). Similar estimates for the collection rates achieved by the *ex-situ* methods were not performed, as the quantity of MVC collected was highly dependent on where the collection was performed, and how often the surfaces were cleaned of accumulated material.

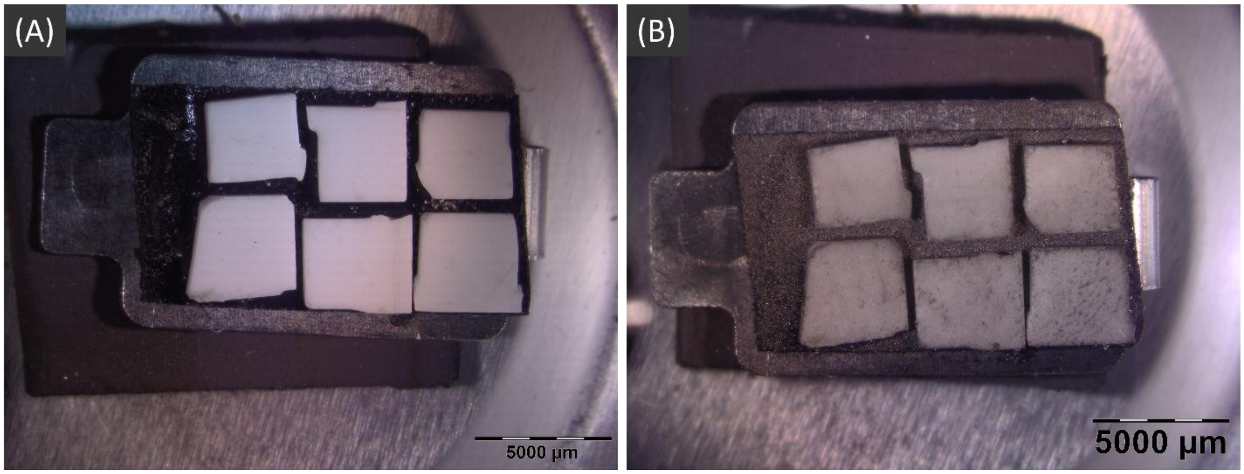

Figure 5.5: Stereomicrographs of a collection tab with six alumina square plates (A) prior to MVC collection and (B) post collection.

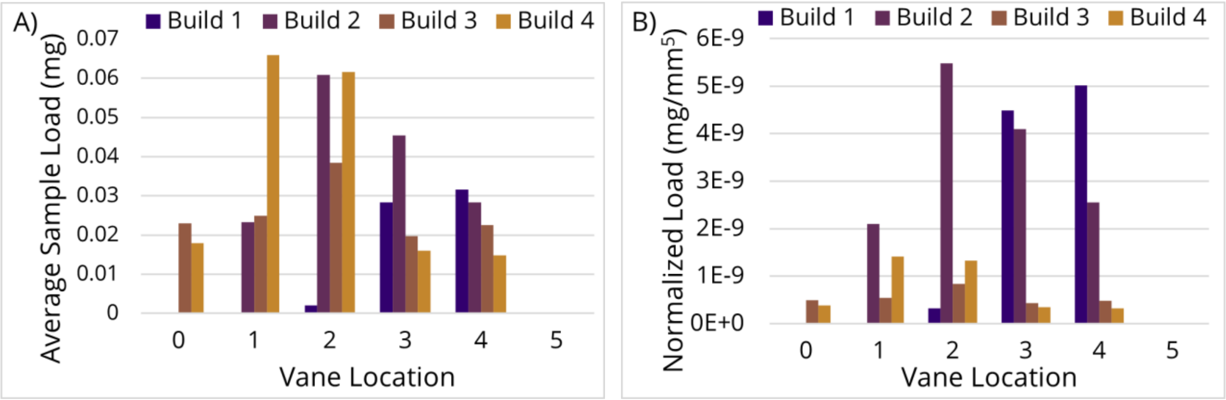

Figure 5.6: Load of MVC collected per 4 mm square from each vane location of the extraction nozzle over multiple builds. A) Average MVC load, and B) MVC load normalized by the volume of build metal and supports. Vane locations are shown in Figure 5.3(C). Certain vanes produced no measurable MVC in some builds.

5.3.2 Morphology

Imaging of the MVC collected *ex-situ* by SEM revealed that the materials consisted of extensive networks or delicate lattices of nanoscale particles. Representative clusters of MVC obtained by *ex-situ* collection are shown in Figure 5.7. The networks were often visible adhered to the sides of larger ejecta particles as shown in this figure. Small groups particles were commonly observed, as well as large mats of agglomerated particles on the filter paper. The networks adhered to ejecta particles were substantially easier to image at higher magnifications.

Details of the subunits of MVC were obtained using both SEM and TEM and are presented in Figure 5.8. Specifically, networks of MVC can be seen in the SEM micrograph in Figure 5.8(A), and more clearly in the TEM micrographs in Figure 5.8(B) and (C). Interestingly, the individual subunits are generally round or globular, and range in size with effective diameter from 10 to 60 nm. The average subunit size is 29 ± 11 nm. The distribution in measured subunit size across the extraction nozzle is shown in Figure 5.9(A) and a histogram for the measurement distribution is shown in Figure 5.9(B). It is important to note that the subunit size did not vary along the extraction nozzle length, as would be expected if the mechanism for generation was consistent across the build area. The subunit size for the collected MVC in Figure 5.9 is consistent with MVC sizes predicted by Shcheglov et al. [76] for laser welding, as well as the MVC observed by Sutton et al. [53] and Noskov et al. [54] for stainless steels. It is also consistent with the measurements reported by Keaveney et al. for L-PBF builds performed with Ti-6Al-4V ELI [59]. As expected, the morphology and subunit size are also consistent with nanoparticles produced by IGC, as the mechanisms of formation are similar [60]. Both SEM and TEM results confirm the ability to capture, isolate, and identify MVC reliably.

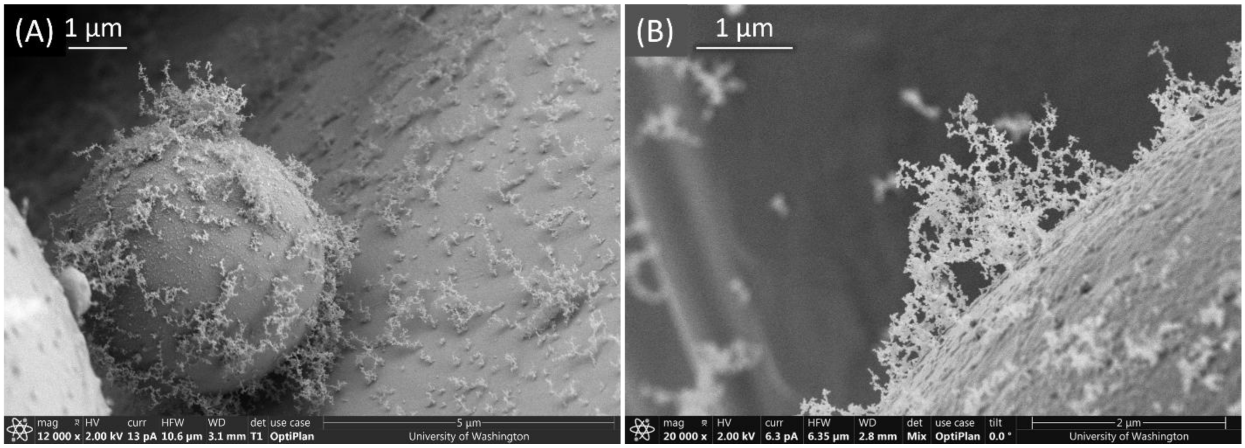

Figure 5.7: Micrographs showing MVC particles adhered to the surface of larger ejected particles of Grade 5 Ti-6Al-4V powder. A) A distribution of smaller networks of particles adorn a larger ejecta particle in the background (right). B) The fine details of the structure are clearly visible silhouetted against an ejecta particle in the background.

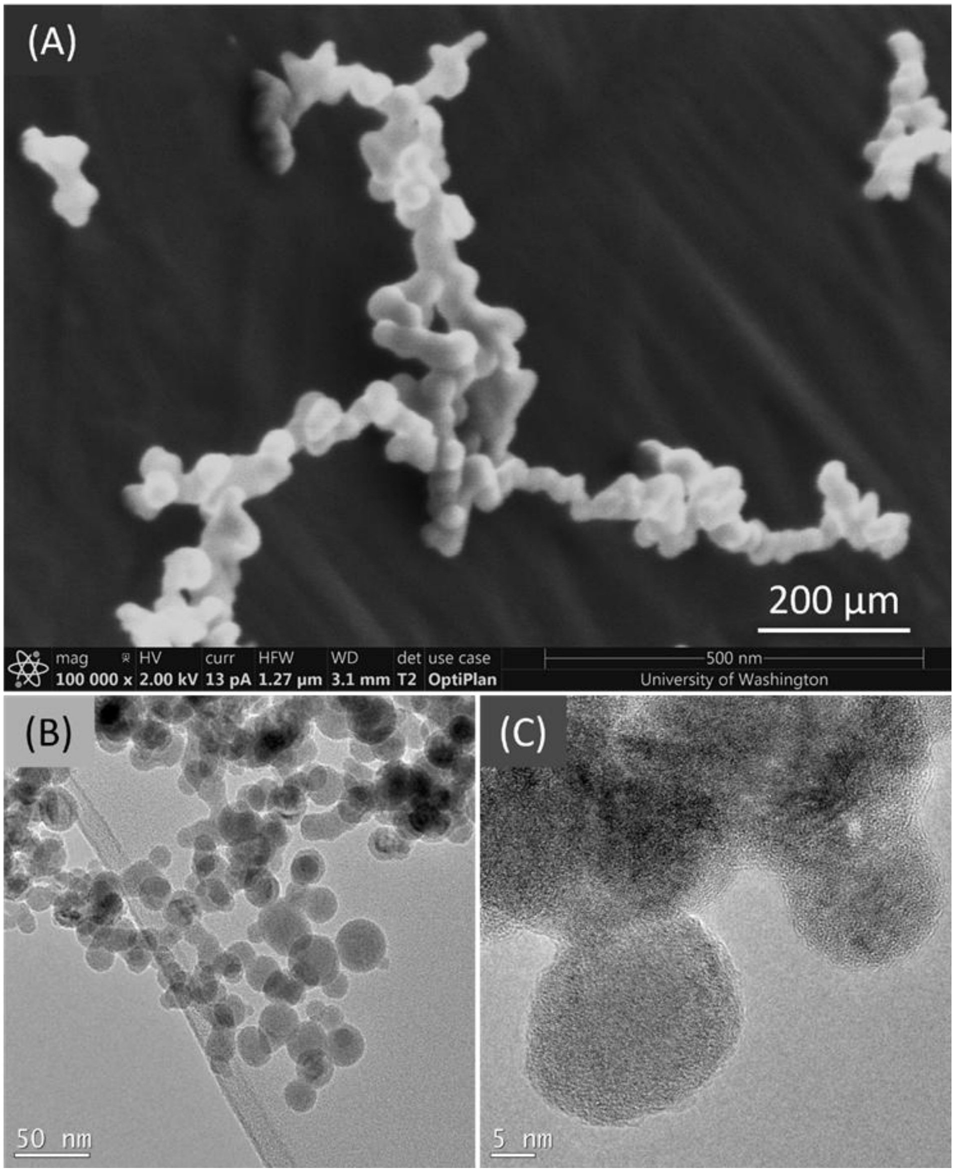

Figure 5.8: A) SEM micrograph showing detail of a small MVC particle consisting of chains of spheroidal nanoparticles. B, C) TEM bright-field micrographs of MVC particles and detail of the MVC subunits.

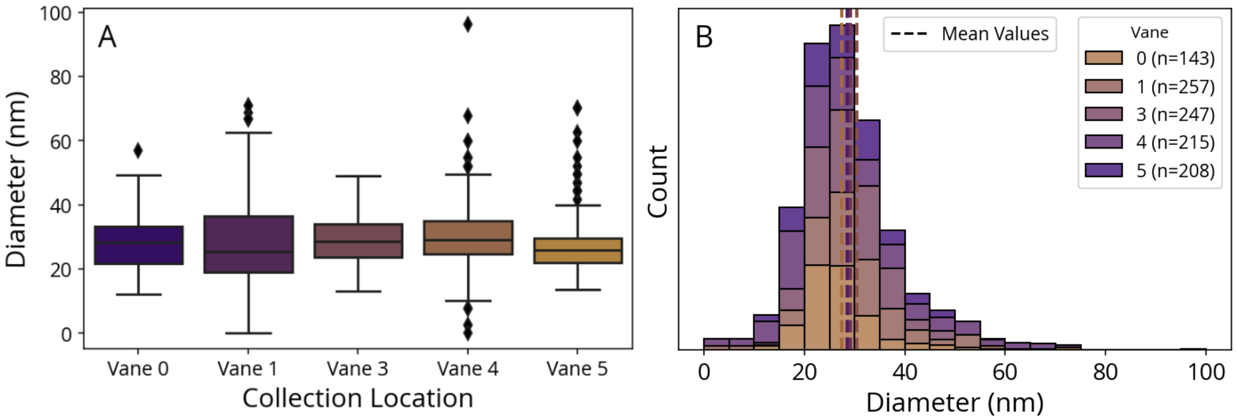

Figure 5.9: The size distribution of individual nanoparticle subunits at different locations on the extraction nozzle. A) Mean diameter and B) histograms of diameter measurements.

5.3.3 Chemical analysis

The chemical composition of the MVC was evaluated by SEM-EDS and TEM-EDS to obtain independent and complementary measures. The small size of the nanoparticles made collecting spectra by EDS difficult due to the high background noise. Beam penetration becomes a significant concern with high accelerating voltages and small sample thicknesses. Nevertheless, a series of small pilot studies showed that accelerating voltages of 10-15 KV were sufficient to identify the target metallic elements Ti and V. For SEM-EDS measurements, the MVC samples were placed on a copper foil substrate to minimize background signal interference, and the spectra were taken on large mats of MVC to provide the best signal rate. Figure 5.10 shows representative large mats and individual clusters of collected MVC nanoparticles on a copper background where SEM-EDS spectra were taken. The characteristic energy of copper is sufficiently distinct from the peak energies of titanium, vanadium, and aluminum, which allowed the copper signal to be disregarded in the spectrum analysis. Oxygen and carbon were identified in the EDS spectrum but excluded from analysis due to their common presence on the mounting substrates. The approximate composition of the particles could be identified semi-quantitatively by removing the background signal from the substrate. By this method, the MVC was identified as being composed mostly of Ti, with ~15-20 wt% Al (Avg. 18.3 ± 1.8 wt%), and trace V (Avg. 2 ± 2.6 wt%). Trace amounts (≤2.0 wt%) of silicon were observed in some samples. Results from the TEM-EDS analysis agreed with this composition, although the measurements showed higher levels of carbon and oxygen. To better compare the metallic components of the material between techniques, the ratio of aluminum to titanium was estimated and results are presented in Table 5.2. Both SEM and TEM showed that the MVC is elevated in aluminum, with Al:Ti ratios of 0.22 and 0.17 by SEM-EDS and TEM-EDS, respectively; the nominal ratio of Al:Ti for the feedstock powder is 0.07. These results suggest that the aluminum is preferentially vaporizing from the meltpool and enriching the MVC that forms.

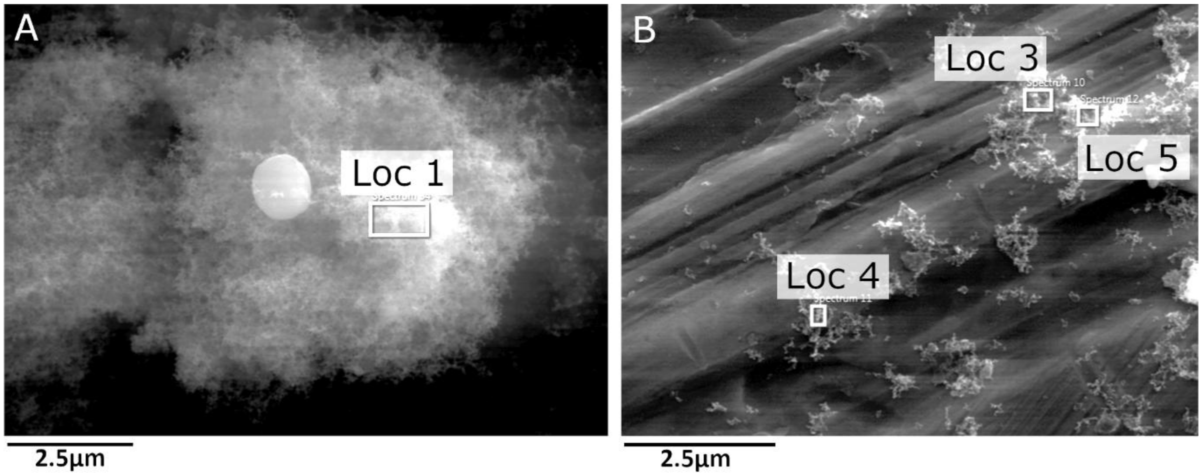

Figure 5.10: SEM micrographs of MVC showing EDS analysis locations. (A) shows a large mat of MVC with an EDS area scan taken at the thickest part (LOC 1). (B) shows smaller MVC agglomerates dispersed on copper foil, with multiple EDS locations noted (LOC 3, 4 and 5).

Table 5.2: Comparison of weight percent ratios of aluminum to titanium for the feedstock powder and the MVC as determined by different methods.

Material	Method	Average wt% Ti	Average wt% Al	wt% Al : wt% Ti
Feedstock powder	Certificate of Analysis	89.27	6.32	0.0708
MVC	SEM-EDS	79.6 ± 1.8	18.3 ± 1.2	0.220
MVC	TEM-EDS	62.0 ± 12.9	10.4 ± 1.7	0.168

5.3.4 Ignition Characteristics

The ignition temperature of the MVC showed a positive trend with heating rate, between 350 and 450°C for heating rates between 2.5×10^3 and 3.1×10^4 K s^{-1}. TGA analysis measured an oxidation onset temperature of 96°C for two trials. TGA trails were limited due to limited material available. Figure 5.11(A) shows the measured ignition temperature (T) vs the heating rate (β) for four trials of hot-filament ignition run with different battery set-ups (i.e. different driving voltages). At low driving voltages (few batteries) the heating rates were very consistent, however at higher voltages the heating rate varied more substantially. A linear fit to the means of the data points for each trial shows a trend of increasing ignition temperatures at higher heating rates. The oxidation onset temperature from TGA was included in the fit to extend the range of heating rates, although it must be recognized the fundamental difference between these techniques. Kissinger analysis of the measured ignition temperatures gives an estimated activation energy of 55 kJ/mol, as shown in the Kissinger plot in Figure 5.11(B). Although the scatter in the data reduces the quality of the fit, the measured activation energy is consistent with literature values for similar nano-sized titanium particles. Zong et al. reported an activation energy of 56 kJ/mol for pure titanium particles of a slightly larger size (146 nm) [77]. Another study reported activation energies of 25-32 kJ/mol for Al particles smaller than 50 nm [78].

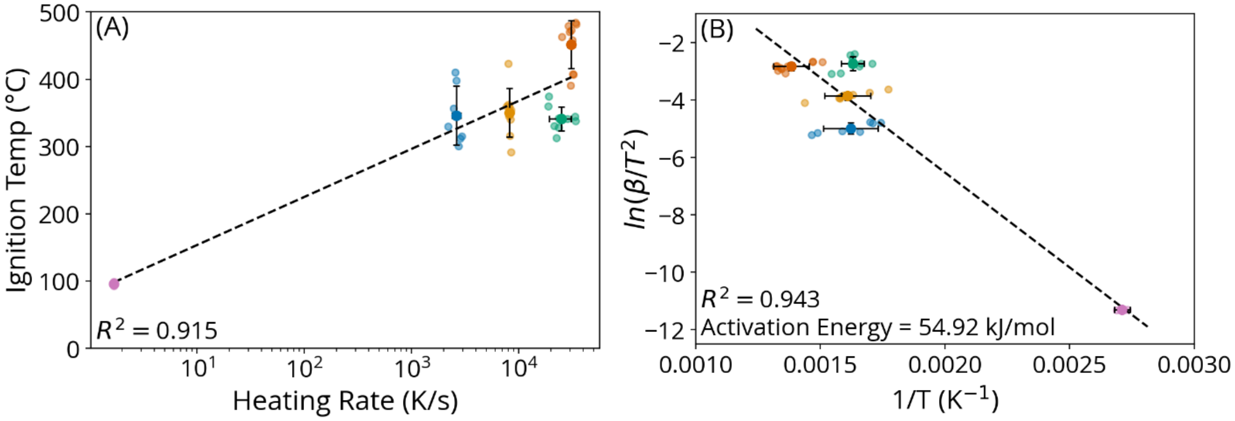

Figure 5.11: Graphs showing (A) ignition temperature of the MVC at various heating rates as determined by hot-filament ignition pyrometry and TGA, and (B) Kissinger analysis based on the heating rate (β) and ignition temperature (T).

5.4 Discussion

Collection of the MVC was highly variable, both in the distribution of quantity of MVC collected at different locations on the extraction nozzle, as well as between builds. This is particularly evident when looking at the distributions of collected MVC in Builds 3 and 4, represented by Figure 5.4 and Figure 5.6. Both of these build layouts were predominately symmetric about the x-axis, yet the distribution of collection along the extraction nozzle was not symmetric, especially for Build 4. The cause of this inconsistency is not clear.

Abeyta et al. have demonstrated variability in the gas flow distribution in the M290 build chamber [65]. These variations would have a direct impact on the manner in which the MVC is carried out of the chamber, and therefore how it interacts with the collection apparatus. The powder dispenser and collection hoppers located to the right and left of the extraction nozzle create large areas of turbulent gas flow [65]. These areas create boundary conditions on the gas flow that may limit the movement of gas through the extraction nozzle at the ends. In the center of the build plate gas flow is less turbulent, and may be more effective at carrying MVC out of the chamber. Another consideration is the spatial variation in laser power due to laser incident angle. At positions near the edge of the build area the laser spot is elongated, reducing the effective energy input, which could result in lower rates of MVC generation. Build duration added a deeper level of variability to the collection. It was expected, and observed, that longer builds produced more MVC. However, the relation between build duration and MVC collection clearly was not linear. It is reasonable to expect that collection rates would change throughout the build, possibly decreasing or plateauing at some point. While not directly observed in this study, flaking or spalling of accumulated MVC layers would cause an apparent decrease in collection rates.

The observed morphology of the MVC is consistent with that reported in both titanium and stainless steel [53,59]. Since the general morphology of the material appear similar between these two alloy systems, it is likely that the morphology is a result of the mechanism of formation, rather than chemistry, although further research would be needed to see if the morphology of MVC is consistent across other material systems. Of note is the high surface area to volume ratio the material exhibits as a result of its fine lattice-like network. The high surface area of sparsely placed nanoparticles is expected to be a key aspect contributing to the reactivity of the material, as it provides more area for reaction.

Characterizing the morphology of the particles is difficult due their complexity. While high magnification images can be obtained relatively easily, direct measurement of the geometry is still difficult. Particle size measurements that rely on light scattering calculate particle size assuming spherical dispersed particles. Clearly that assumption is not correct for MVC, which instead exhibits a complex porous network structure. Light scattering measurement techniques could provide a general idea of the agglomerate size (i.e., an effective diameter) but should not be taken as perfectly accurate for this material. Currently, agglomeration and settling of the particles in solution affect the accuracy of the measurements, leading to large size distributions that span multiple orders of magnitude. Hence, while the manual approach to size measurements is tedious, it is currently the most reliable.

Table 5.3: Melting and boiling points of alloying elements of Ti6Al4V [59].

Element	Melting Point (ºC)	Boiling Point (ºC)
Titanium	1650-1670	3287
Aluminum	660	2519
Vanadium	1735	3407
Ti6Al4V	1604-1660	~2859 [79]

The elevated levels of aluminum observed in the MVC with respect to the feedstock powder are consistent with the lower boiling point of the element compared to those of titanium and vanadium, as evident from Table 5.3. Computational fluid dynamics (CFD) models suggest that the temperature in the melt pool can rise to nearly 3300°C [80], approximately equal to the boiling point of titanium (3287°C, Table 5.3). The lower boiling point of aluminum (2519°C) compared to titanium would result in a higher vapor pressure and preferential vaporization of aluminum from the melt pool. Conversely, the high boiling point of vanadium (3407°C), along with the lower abundance of the material in the feedstock powder, likely contributes to its low abundance in the MVC. Zhang et al. demonstrated via thermodynamic calculations that the activity coefficient (the ratio of activity (effective concentration) to concentration in a mixture of chemical substances) of aluminum in Ti-6Al-4V alloy is much more sensitive to temperature than the titanium and vanadium in the alloy [79]. Above temperatures of around 2700°C the activity coefficient of Al increases rapidly whereas the activity coefficient of titanium remains constant and that of vanadium slightly decreases. Zhang et al. show that the calculation of activity coefficient and saturated vapor pressure predict that Al will have a higher tendency to vaporize at temperatures near the alloy's boiling point. They also calculated that vanadium has near zero saturated vapor pressure. These predictions are consistent with the observed composition of the MVC.

The composition of MVC produced from Ti-6Al-4V alloys could vary with processing parameters. Higher laser power settings would likely produce higher melt pool temperatures and would result in more aluminum vaporization due to the high sensitivity of aluminum vapor pressure to temperature. Lower laser power settings may reduce the overall aluminum content in the MVC, along with likely resulting in less MVC production overall. Oxidation of the MVC is another important consideration. Oxygen levels in the build chamber are controlled, but minor fluctuations during the build process could result in changes to the chemical composition of the MVC as it is produced. Upon exposure to ambient air, it is expected that the MVC oxidizes to form a passive oxide layer. The thickness of this oxide layer would likely depend on the length of exposure and may change the ignition characteristics of the material over time, given that oxide thickness is known to change the pyrophoricity of nano-aluminum particles [81].

Given the high reactivity and flammability of pure aluminum nanoparticles and micro-powders [81], the elevated levels of aluminum and high surface area morphology undoubtedly contribute to the volatility of the condensate relative to that of the powder. This reactivity is reflected in the measured ignition temperatures and activation energy of the ignition reaction. The measured ignition temperatures of 350-450°C were all below the melting point of bulk aluminum (660°C) and well below the melting point of titanium at 1650°C. TGA analysis showed evidence of oxidation at temperatures as low as 100°C, highlighting the high reactivity of the material. The estimated activation energy of 55 kJ/mol agrees with reported literature [77,78] for titanium, despite the particles having a relatively large aluminum content. It has been shown that the physical properties of a particle are size dependent; using simulations, Puri and Yang estimated melting points of aluminum nanoparticles as low as 400 K (127°C) for particles approaching 2 nm [82]. The ignition temperatures measured here are similar to melting points estimated for aluminum nanoparticles of 3-5 nm, although the nanoparticles of MVC are in the range of 20-40 nm. The preceding argument assumes that the mechanism of ignition is dependent on the melting of the metallic portions of the particle. That is not always true, for example, in cases where ignition is correlated with the breakdown of fine oxide scale, such as is described for aluminum nano-powders [83].

It is important to recognize the fundamental difference between the mechanisms of measurement of TGA and hot-wire ignition. TGA is suitable for studying controlled, non self-propagating reactions, while hot-filament ignition experiments are designed to quantify the onset of a self-propagating reaction. Using both experimental methods together in a Kissinger analysis assumes that the kinetics of the reactions are comparable and consistent across the different orders of magnitude of heating rates. Without better understanding of the fundamental underlying kinetic mechanisms, this is a risky assumption to make. Nonetheless, it gives a first order of magnitude estimation of the activation energy and provide useful insight into the behavior of the MVC material when external energy is applied. Additionally, while the Kissinger method is inarguably a useful tool in evaluating the activation energy of thermally driven reactions, it has a tendency to simplify the reaction kinetics of processes [84]. Multi-step reactions have more than one energy barrier and may not be adequately described by the single activation energy ascribed to them by the Kissinger method. It is possible that the ignition of the MVC particles could involve multiple process steps, such as those described by Sundaram et al. for the general oxidation of aluminum particles [83]. These mechanisms would not be identified by the methods available in this study.

By combining *in-situ* and *ex-situ* collection of MVC, a more detailed characterization and evaluation of the material is possible than garnered from either approach alone. These methods are effective and easy to perform in a manufacturing environment since they do not require modifications to the machine. They can be performed as a part of machine monitoring, or as a method of collecting MVC material for research. Current methods of handling and disposal of the material are dangerous and expensive, which is largely attributed to a lack of understanding. Clearly, more nuanced and targeted approaches to mitigating the danger of MVC should be developed. Until the dangers of the waste products can be appropriately delt with, they will continue to be a costly and logistical impediment to the adoption of PBF AM as a principal manufacturing technology.

Despite the successes of both the ex-situ and in-situ collection approaches, as well as the complementary analyses performed, there were limitations to the investigation that are important to note. As the majority of MVC collection was performed on builds intended for other studies, the geometries and layouts of those builds were already defined. The inflexibility in build design made evaluating the effects of build design and part placement on *in-situ* collection difficult. The ex-situ collection provided an effective means for collecting samples on a variety of substrates, but it was impossible to restrict the collection to the MVC without larger ejecta particles. Careful placement of the collection tabs in the extraction nozzle enabled the acquisition of material sans ejecta, which is most appropriate for the thermal analysis. The placement of the tabs on the edge of the baffle fins likely impacted MVC collection, and biased the collection according to the interaction of the MVC and the gas flow through the chamber, as well as the quantity and distribution of metal in the builds. However, one major limitation of the in-situ collection process is the limited quantity of MVC that can be obtained – less than 1 mg was obtained per swab. To measure the thermal energetics of the MVC with greater reliability, quantities on the order of grams are sought, which presents two concerns. The first is how the collection methods can be scaled up to acquire a sufficient volume of material. The second concern is clearly the safety of collecting larger quantities of MVC for analysis. Due to the inherent fire and health hazards of MVC, increasing the quantity of material collected must be performed with proper safety considerations in mind. Alternatively, developing techniques for evaluating the thermal behavior of the material in sub-milligram quantities would alleviate the safety concerns of handling large quantities.

Despite these limitations, the success of the collection techniques demonstrates the viability of their use in future studies aimed at assessing passivation methods of the MVC. The ability to collect MVC on various substrates enables the collection to be tailored to the testing and analysis and provides better and more accurate results. These techniques are applicable to titanium and other alloy systems, and may also be adaptable to other AM processes. Our future work will focus on refining these techniques to increase collection and pursue robust methods for evaluating the energetics of MVC and methods for passivation or digestion. Evaluation techniques could include TEM analysis to estimate 2D surface area and fine line EDS analysis to evaluate the surface oxidation. Surface area to volume ratios of the MVC could be determined using a technique such as Brunaur-Emmett-Teller (BET) analysis. Time resolved hot-stage TEM analysis could reveal more information about the mechanism of ignition, and a more precise calculation of activation energy could be obtained by replacing the car batteries in the wire ignition set up with a polyvalent electric generator to achieve lower driving voltages. These are exciting prospects that are reserved for future studies.

5.5 Conclusions

A novel combination of in-situ and ex-situ collection of MVC from a L-PBF AM machine was performed, which enabled a detailed characterization of the metal vapor condensate. Based on results of the experimental evaluation, the following conclusions are drawn:

- The collected MVC consisted of small to large networks of nanoparticles with intricate structures, often forming large spongy mats. Individual nano-particle sizes were measured to be 10-60 nm.
- SEM-EDS and TEM-EDS show that the material has an elevated aluminum-titanium ratio (0.17-0.22) relative to the base powder, likely due to the preferential vaporization of aluminum from the melt-pool due to its lower vaporization temperature.
- Hot-wire ignition showed the particles to ignite between 350 and 450°C with an estimated activation energy of 55 kJ/mol.
- TGA analysis showed an onset of oxidation at temperatures as low as 100°C

Chapter 6 Spatter

6.1 Introduction

As demonstrated in previous chapters as well as in the literature [15,37] extended powder reuse can cause changes in powder chemistry, morphology, and flowability, possibly to the detriment of metal quality. Recently, more attention has been given to spatter as both a source of powder variability and a direct contributor to metal quality [85,86]. Spatter is an unavoidable result of the laser-powder interactions during the printing process, which results from the ejection of metal droplets from the meltpool; they deposit on the powder bed and on exposed metal surfaces post-exposure. While some studies have examined how laser-spatter interactions can induce porosity in metal [55,87,88], no quantification has been reported on how spatter content in the powder contributes to reductions in metal quality. This chapter evaluates the variability of spatter produced during L-PBF.

6.2 Material and Methods

6.2.1 Material

To achieve a better understanding of spatter emitted in L-PBF of Ti6Al4V, the spatter generated in the M290 at the UW was collected from two sources. The first source, regarded as "Baffle Spatter" was collected from the top of the extraction nozzle within the machine after the completion of selected builds. Spatter ejected from the build area collects on horizontal surfaces within the machine over the course of each build. This spatter is a pure representation of the material ejected from the melt pool, since it does not mingle with the powder in the powder bed. The other source of spatter, regarded as "Sieve Spatter", was collected from the sieve unit after the build and during powder recovery. This spatter, while easier to collect in large quantities, also incorporates some quantity of powder that is not related to ejected material. Figure 6.1 shows the collection locations for these two portions of spatter.

To evaluate the printability of spatter-contaminated powder, small batches of "spatter-enriched" powder were produced using mixtures of virgin grade 5 titanium powder and baffle spatter. The collected spatter was mixed with virgin powder at different weight percent proportions to generate ~50 g batches of spatter-enriched powder. Proportions of spatter and virgin powder were adjusted to create 0%, 20%, 50% and 100% spatter samples, by weight.

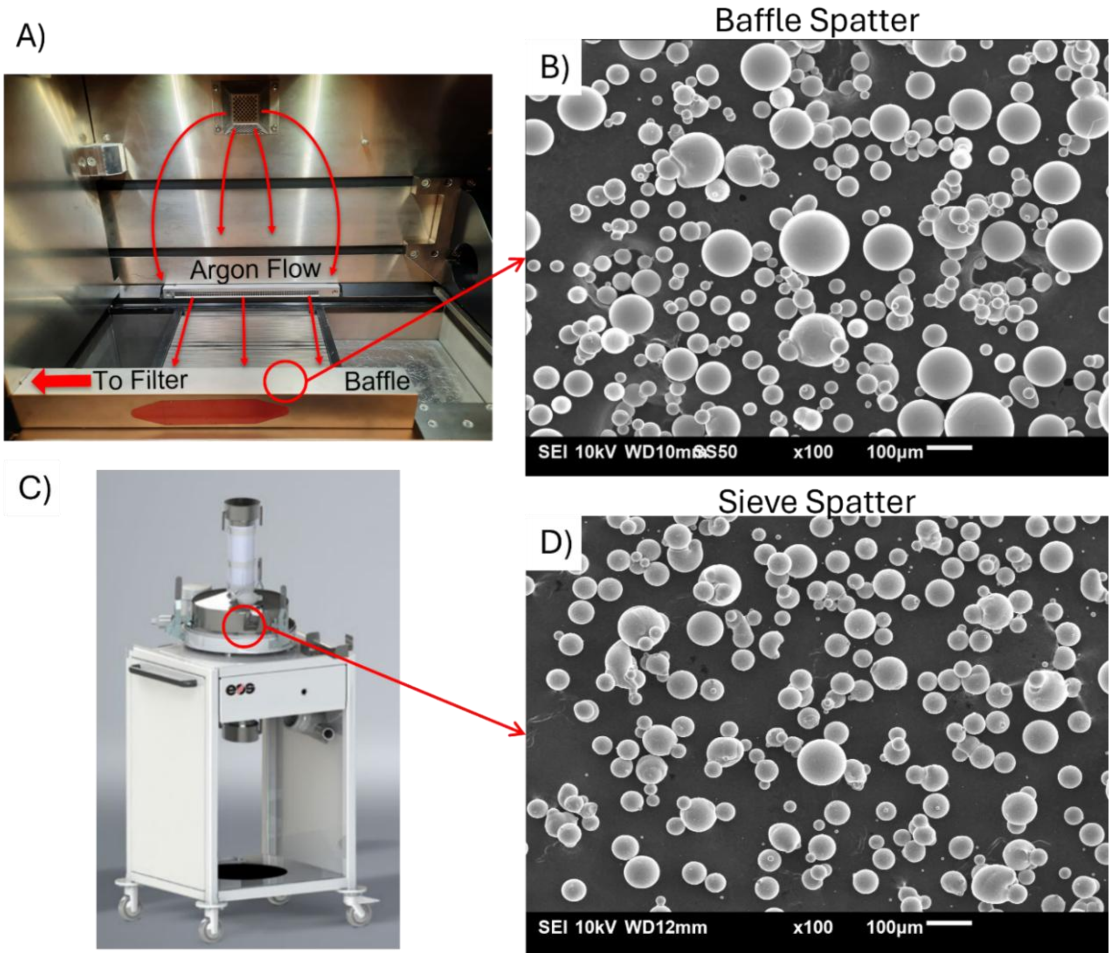

Figure 6.1: Locations and representative micrographs of spatter collected from the UW M290. (A) Annotated photograph of the build chamber of the EOS M290. (B) Representative SEM micrograph of spatter collected from the top of the baffle. (C) Stock image of an EOS sieve unit. (D) Representative SEM micrograph of spatter collected from the sieve unit.

6.2.2 Machine Setup

A support frame was fabricated from a ¼” ground low-carbon steel sheet cut to the dimensions of the build plate (252x252 mm), with bolt holes introduced for fastening and a cutout in the center to hold test coupons. The test coupons (i.e. weld coupons) were cut from ¼” rolled high-strength grade 5 titanium bar stock using an abrasive waterjet. A rendering of the tooling setup is shown in Figure 6.2(A). The coupons were surface milled with a 0.5” endmill to produce a surface finish similar to the base plate used in a typical build process. Likewise, the support frame was surface milled to achieve a flat surface in the area around the test coupon. Due to the slight cupping of the stock material used for the coupons, only the center of the support frame was surfaced. The outer area of the support frame was lower relative to the center and left untouched to avoid thinning the center area excessively. The support frame was installed in the build chamber on top of a standard steel build plate (P/N 2200-4374, EOS GmbH, Germany). Low profile bolts were used to secure both the support frame and the build plate to the build platform piston, as shown in Figure 6.2(B).

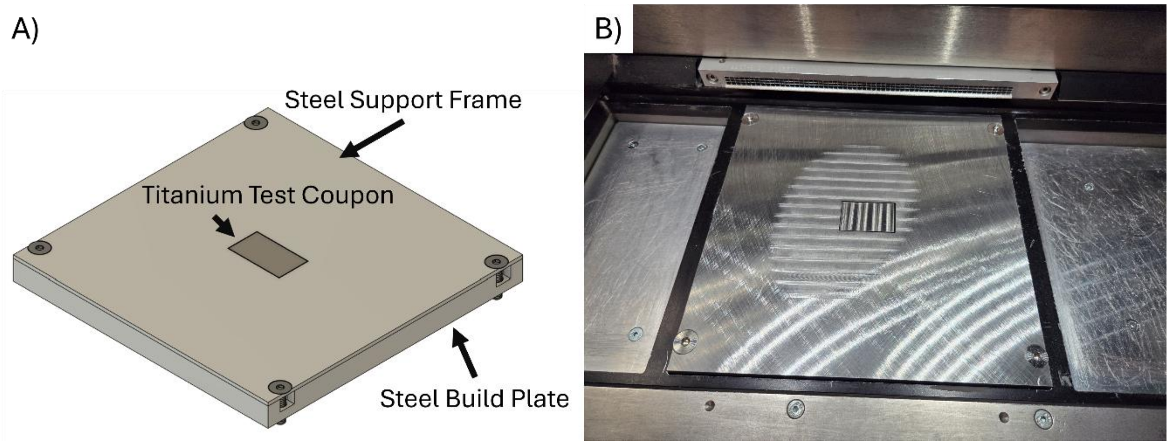

Figure 6.2: Details of the experimental arrangement for spatter generation and capture. (A) Schematic showing the build plate tooling setup for the weld test coupons and (B) photo of the tooling setup installed in the M290.

A volume of powder sufficient to completely cover the surface of the weld coupon was used for each exposure test. Approximately 10 g of mixed powder with selected spatter mixture was poured into a pile on the right side of the weld coupon. Using the machine controls, the recoater was moved across the build plate at full operational speed to spread the powder in a single, even layer over the weld coupon. Due to slight inconsistencies in the thickness of the weld coupons after machining, the thickness of the powder layer was found to be inconsistent between runs. To mitigate this discrepancy, the height of the build platform was adjusted until the opacity of the powder layer was just enough to see the machining marks on the coupon surface below. While imprecise, this procedure is consistent with standard practice for leveling and setting the height of the build platform for the first layer during builds. The condition of the first layer can be seen in the photos in Figure 6.3 for varying spatter content. The prevalence of large particles in the spatter made streaking a major issue even with the 20 wt% spatter sample, which could have contributed to further variation in the powder layer thickness, beyond that from initial setup.

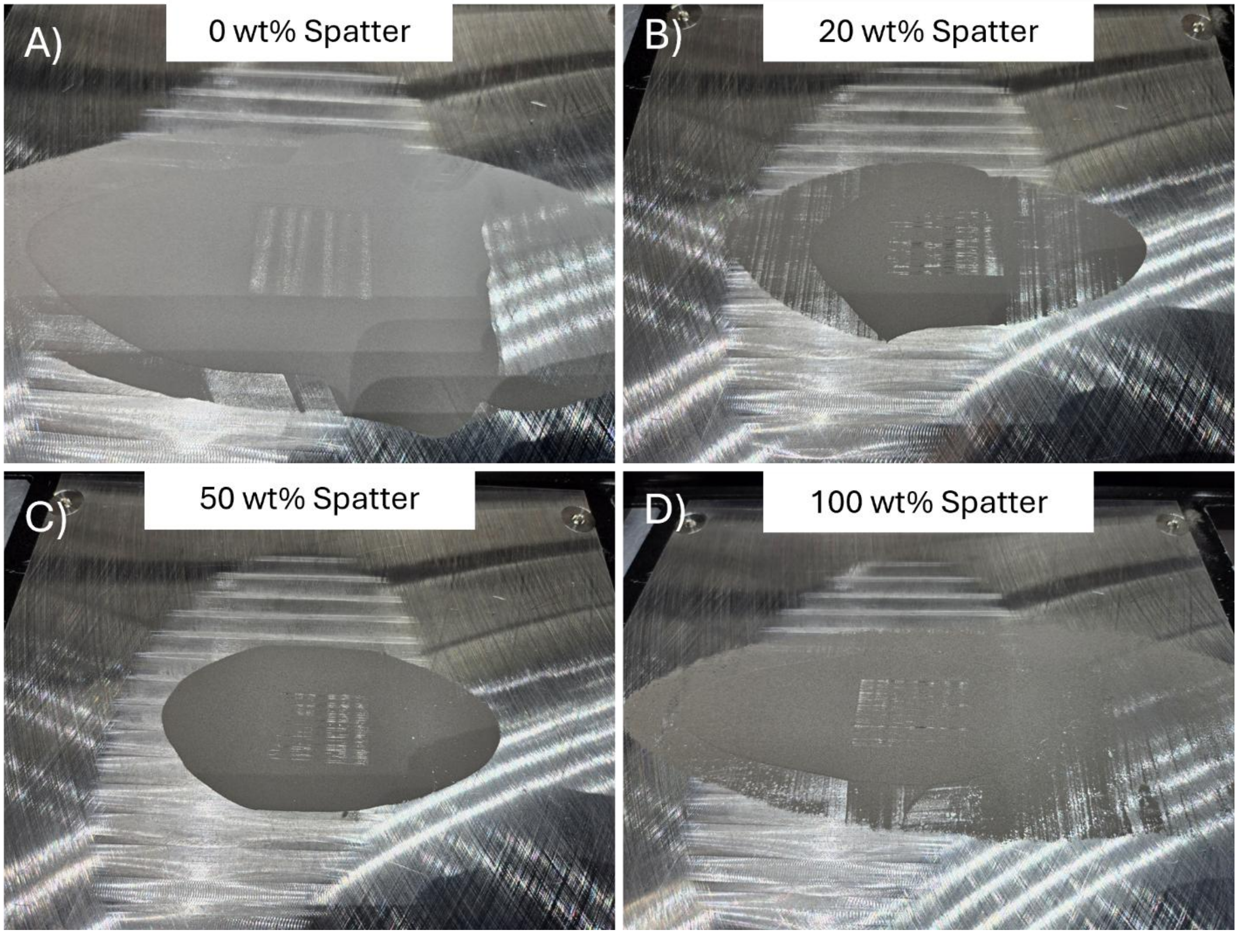

Figure 6.3: Photos of the powder layer before exposure for the weld coupon tests with (A) 0 wt% spatter, (B) 20 wt% spatter, (C) 50 wt% spatter, and (D) 100 wt% spatter.

To enable printing of single layers with specified laser scan angle, a 25×25×50 mm box positioned at the center of the build plate was created using Magics software, which was then exported to EOSprint, sliced, and exported to the M290 machine. Specific laser scan angles were targeted by identifying layers corresponding to that scan angle for the build in EOSprint. Print jobs were initiated on the M290 from the exported build file with custom layer ranges encompassing the single layer with the desired laser scan angle. By repeating this process, custom sequences of layers with specific laser scan angles could be specified.

Direct observation of emitted spatter particles and their trajectories was accomplished by placing a remote operated action camera (Insta360 Go3, Arashi Vision Inc., Shenzhen, China) in the chamber to capture video of the ejection events during the melting process. A shortpass filter (#62-625, Edmond Optics, Barrington, NJ, USA) was fitted to the front of the action camera lens to block infra-red reflections from the EOS M290 Yt-fiber laser. In addition to taking video, the horizontal spatter travel distance was measured by capturing emitted particles over prescribed paths from the weld coupon. Specifically, four 100 × 6 mm aluminum plates were positioned adjacent to the weld plate on cardinal directions. A strip of double sided carbon tape was placed on top of the aluminum plates to capture any spatter that landed on the plate. Placement of the collection plates was performed after spreading the powder layer. A photo of the experimental setup is shown in Figure 6.4. Single layer exposures were performed with laser scan angles of 0° and 90° to evaluate the effect of gas flow on spatter generation and distribution.

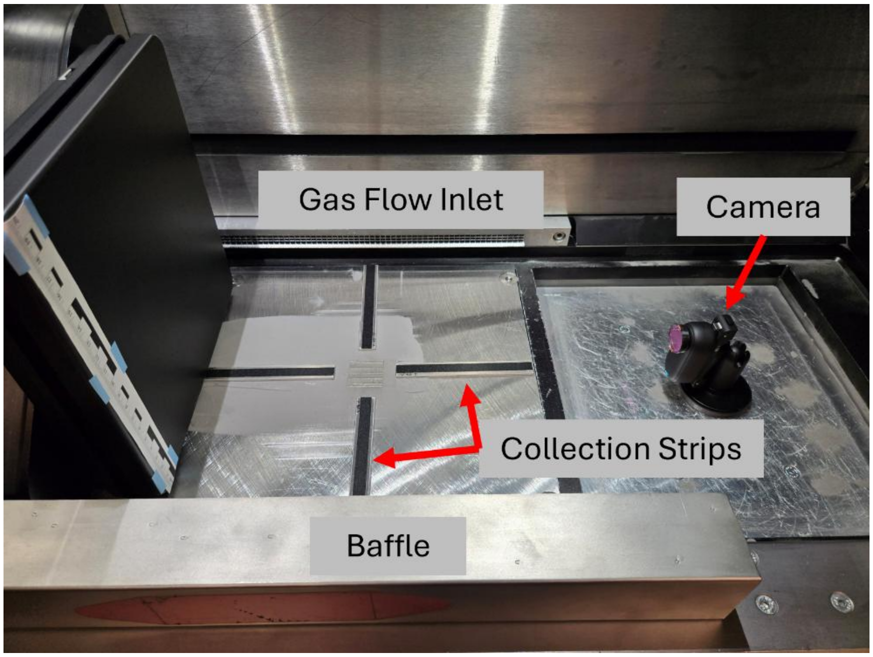

Figure 6.4: Photograph of the spatter evaluation and collection setup in the M290 chamber, with four spatter collection strips and the action camera in position.

6.2.3 Evaluation of Spatter

Spatter samples from the baffle spatter and sieve spatter were measured by light scanning particle size analysis (LSPSA) to determine the particle size distributions of the two materials. This was performed prior to mixing the selected spatter with virgin powder for the spatter emission efforts.

After completion of the lasing routine, the surface roughness of the weld coupons was evaluated using an optical profilometer (Keyence VR-3100, Keyence Corporation, Itasca, IL). Surface profiles were taken parallel to the stripe direction (i.e. perpendicular to the laser scan direction) down the center of each stripe as shown in Figure 6.5. For each profile, the average roughness (Ra), 10-point roughness (Rz), reduced peak height (Rpk), and reduced valley depth (Rvk) were calculated according to the ISO 4288 standard. As defined by this standard, for a measured Ra of ≤10 μm, a cutoff length of 2.5 mm and traverse length of 15 mm were used. Rpk and Rvk represent the mean height and depth of peaks and valleys beyond the core roughness. Following the roughness measurements, the samples were imaged at high resolution using SEM. Images were taken at the back left (BL), front left (FL), front right (FR) and back right (BR) corners and were evaluated using semi-automatic image processing via custom python scripts to determine spatter particle size, count, and percent area coverage.

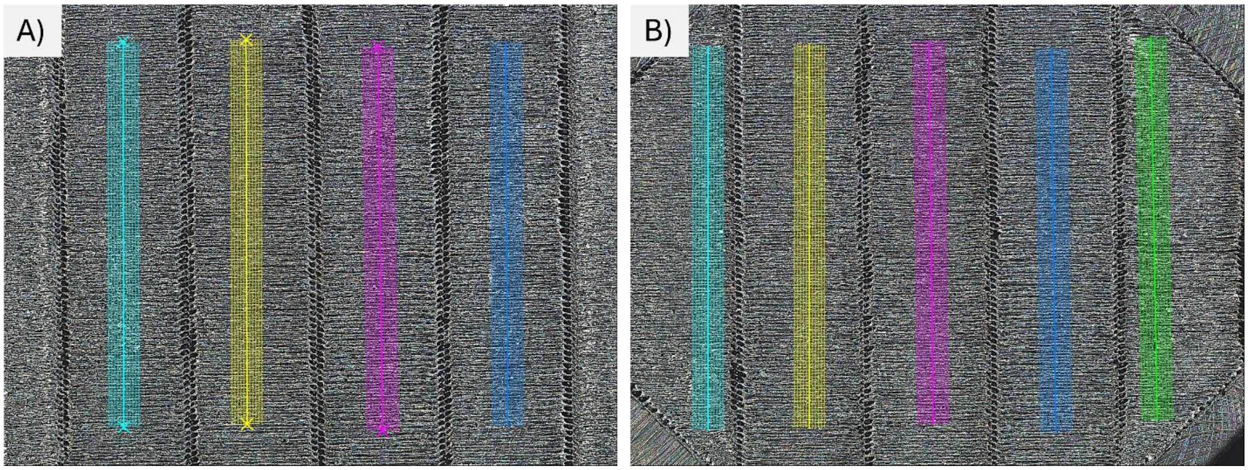

Figure 6.5: Line scan locations for (A) 0° and 90° coupons and (B) 45° coupons.

Similar to the weld coupons, the spatter collection strips were evaluated using optical microscopy and image analysis to count the number of spatter particles at multiple locations along the length of the strips. A commercial software (ImageJ) was used to identify and count particles from the optical images by first gray scaling and thresholding the images, then using the internal particle analysis routine to identify and count particles. While this approach is quick to employ it is susceptible to misidentification of non-metallic particles on the sample surface. Therefore, the samples were covered as a precautionary measure to keep them free of contamination. This method also struggles to differentiate groups of particles, often treating them as a single misshaped particle. However, for samples that are similar in particle composition and density, this approach is an effective method for comparing relative quantities and densities of particles.

6.3 **Results**

6.3.1 Spatter PSD

The PSD measurements for the collected spatter obtained from LSPSA are shown in **Figure 6.6**. The sieve spatter exhibited a narrow distribution with a single peak at 77 µm. The baffle spatter had a generally bimodal distribution with peaks at around 39 and 110 µm. Despite the sieve spatter having a more visually clean distribution, it is assumed that the baffle spatter better represents the true nature of spatter as it is ejected from the melt pool. Due to the nature of the collection process, it is likely that the sieve spatter samples contain a high percentage of unmelted powder particles from the powder bed.

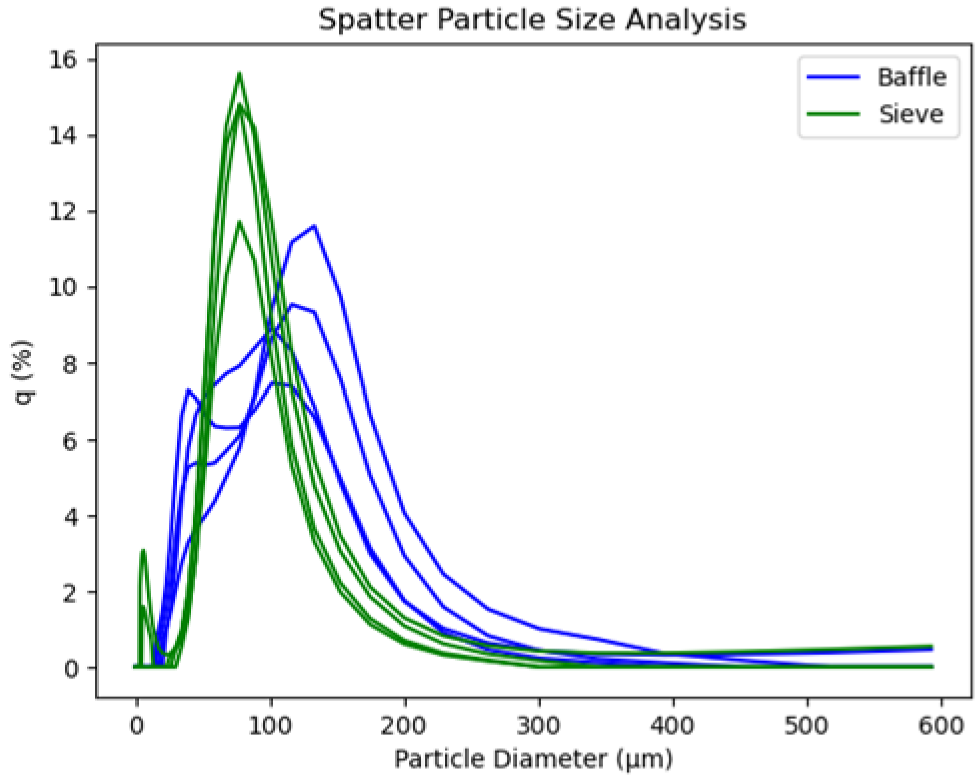

Figure 6.6: PSD results from the Baffle and Sieve spatter samples.

6.3.2 Weld Coupon Results

A photo of the six weld coupons after single layer exposure is shown in Figure 6.7(A). All test conditions successfully produced clean, even layers with clear laser tracks and stripe patterns with surface finishes typical of the L-PBF process. No abnormalities or major defects were observed in the printing process. Figure 6.7(B) shows the 0% spatter, 0° scan angle coupon in more detail, with the four locations used to count adhered spatter particles (Back Left - BL, Front Left -

FL, Front Right - FR, Back Right - BR). Then, Figure 6.7(C) shows a schematic diagram of the coupon, including the laser stripe boundaries, with a red line showing the order of exposure of the stripe pattern.

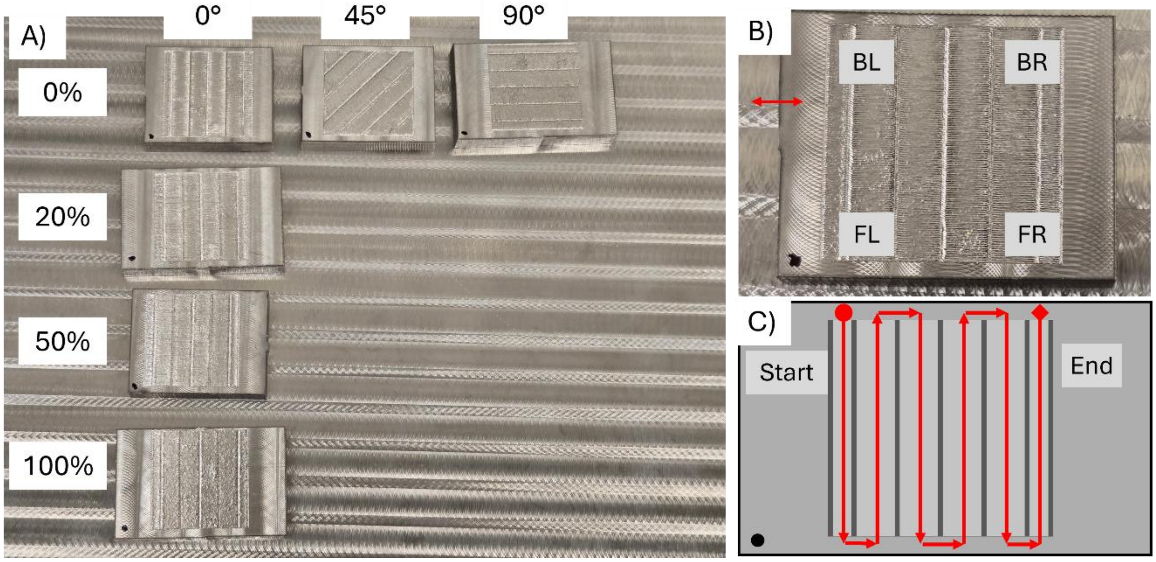

Figure 6.7: A) Annotated photograph of the six weld coupons produced by the L-PBF passes. Each row of coupons corresponds to the indicated wt% of spatter in the powder mix, and each column of coupon corresponds to the indicated laser scan angle. The black dot on each coupon indicates the bottom left corner, relative to the machine build area. (B) Detail view of 0%-90° coupon with locations of SEM analysis labeled. (C) Diagram of laser stripe melt pattern during printing.

Surface roughness measurements were obtained from optical profilometry scans performed on the exposed regions of the weld test coupons. Several roughness parameters were estimated and are tabulated in Table 6.1, including the Ra, Rz, Rpk and Rvk. The roughness was found to trend with spatter content in the powder mix with higher enrichment of spatter correlated with higher surface roughness. In all cases, the Rpk was higher than Rvk, indicating a positively skewed roughness with larger peaks than valleys. Laser scan angle did not appear to contribute significantly to the roughness, although the 90° sample had slightly higher roughness than the 0° and 45° samples. Representative line scan profiles for each coupon are shown in Figure 6.8.

SEM imaging of the exposed regions of the coupons revealed redeposited spatter on the melt surface, as shown in Figure 6.9. These redeposited particles are expected to contribute to the positive skew of the surfaces, as they would contribute to greater “peakedness”. The underlying melt surface is relatively consistent in roughness, with visible overlapping weld tracks. The redeposited particles appear to vary in size and frequency with the spatter content. Specifically, the powder mixes of higher spatter content had fewer, but larger redeposited spatter particles.

Table 6.1: Surface roughness measurement values for weld test coupons

Spatter Content	**Laser Scan angle**	**Overall Averages ± STDEV (µm)**			
		Ra	**Rz**	**Rpk**	**Rvk**
Virgin	0°	2.2 ± 0.3	13.1 ± 2.1	3.5 ± 0.9	2.9 ± 0.7
	45°	2.1 ± 0.7	12.4 ± 4.3	3.0 ± 1.0	2.4 ± 1.1
	90°	3.1 ± 0.5	19.2 ± 3.7	6.4 ± 1.7	6.5 ± 3.1
20% Spatter	0°	3.4 ± 0.3	19.5 ± 1.8	5.2 ± 0.6	3.5 ± 0.5
50% Spatter	0°	3.5 ± 0.1	20.3 ± 0.3	5.4 ± 0.2	3.9 ± 0.7
100% Spatter	0°	4.0 ± 0.7	25.3 ± 4.9	8.0 ± 0.2	5.0 ± 1.4

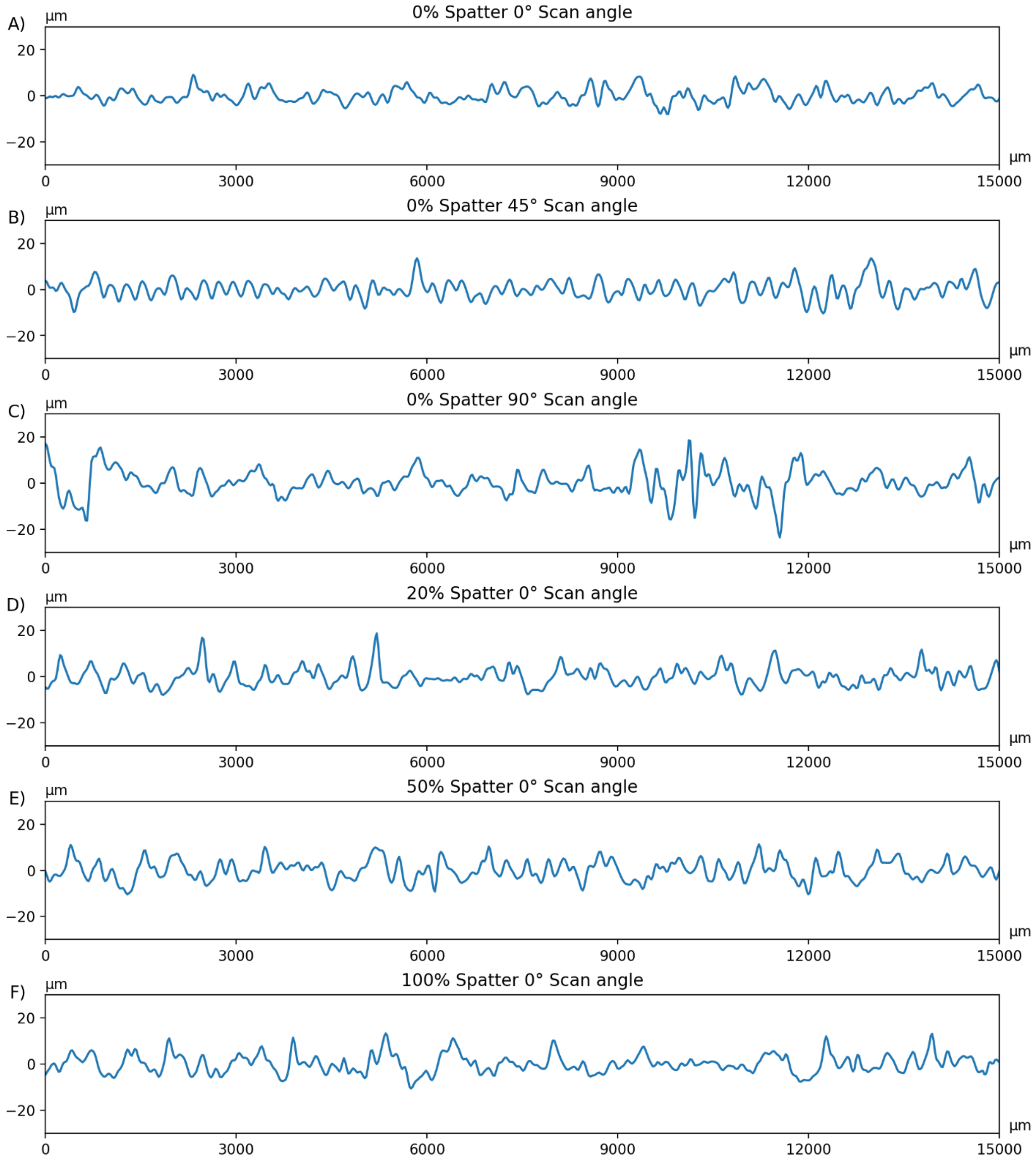

Figure 6.8: Representative surface roughness profiles from each test coupon. (A) 0% spatter (virgin) 0° scan angle, (B) 0% spatter 45° scan angle, (C) 0% spatter 90° scan angle, (D) 20% spatter 0° scan angle, (E) 50% spatter 0° scan angle, (F) 100% spatter 0° scan angle.

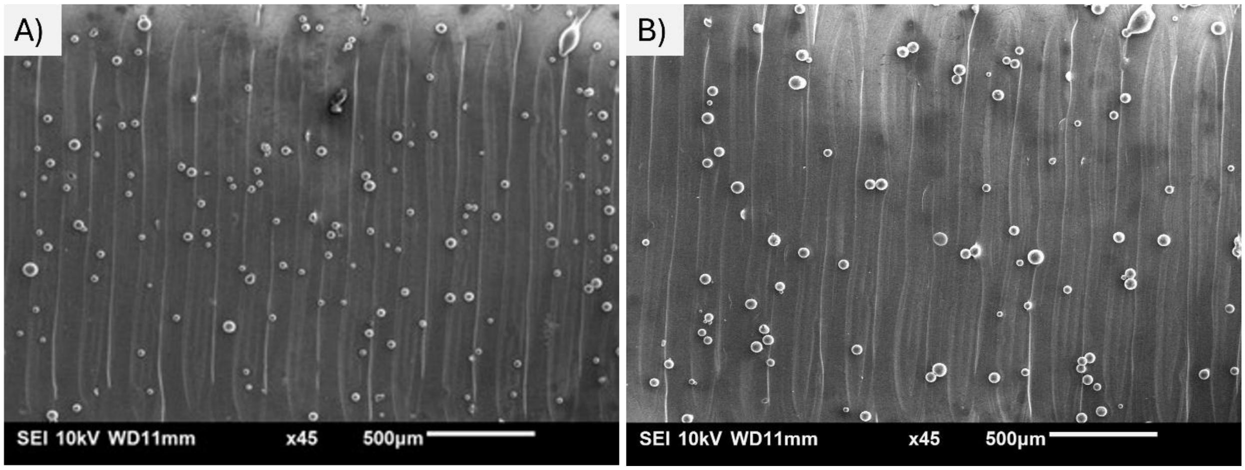

Figure 6.9: Representative SEM micrographs of the surface condition of the exposed areas of the weld coupons using (A) 0 wt% spatter (virgin) powder and (B) 100 wt% spatter powder.

Image analysis of the SEM images of redeposited spatter on the weld coupons showed that the average particle size did not vary across the surface of the coupons, from front to back and from right to left. Conversely, the number of particles did seem to have a front/back dependence, although the trend was not consistent. The 0% spatter (virgin) powder mix had more redeposited spatter at the back of the coupons, while the 100% spatter coupons had more redeposited particles towards the front of the coupons. The number of spatter particles was consistent between the left and right sides of both coupons. The average particle diameters, percent area coverage, and number of redeposited spatter particles for the 0% and 100% spatter 0° scan angle coupons are tabulated in Table 6.2. The average spatter particle size was 37.5 μm for the 0% spatter coupon and 51.2 μm for the 100% spatter coupon, for a total difference of 13.7 μm. Histograms of the redeposited spatter particle sizes at different locations are shown for the 0% and 100% spatter coupons in Figure 6.10, and Figure 6.11 shows the cumulative histogram for all measured locations. The histograms support the mean particle size results, showing that the mean particle size increased from 37.97 μm for the 0% spatter coupon, to 49.66 μm for the 100% spatter coupon.

Table 6.2: Redeposited spatter particle count and size according to location on coupon for 0° laser scan angle coupons. Locations on the coupon are shown in Figure 6.7.

	Average Particle Diameter (µm)		Spatter Area Percent		Number of Particles	
Location on Coupon	**0% Spatter**	**100% Spatter**	**0% Spatter**	**100% Spatter**	**0% Spatter**	**100% Spatter**
BL	38.1	50.7	2.52 %	3.02 %	142	95
FL	40.7	51.9	2.27 %	4.48 %	107	142
BR	34.7	51.7	1.95 %	3.12 %	134	101
FR	36.9	50.6	1.83 %	5.43 %	110	182
Entire Coupon	37.5	51.2	2.14%	4.01%	493	520

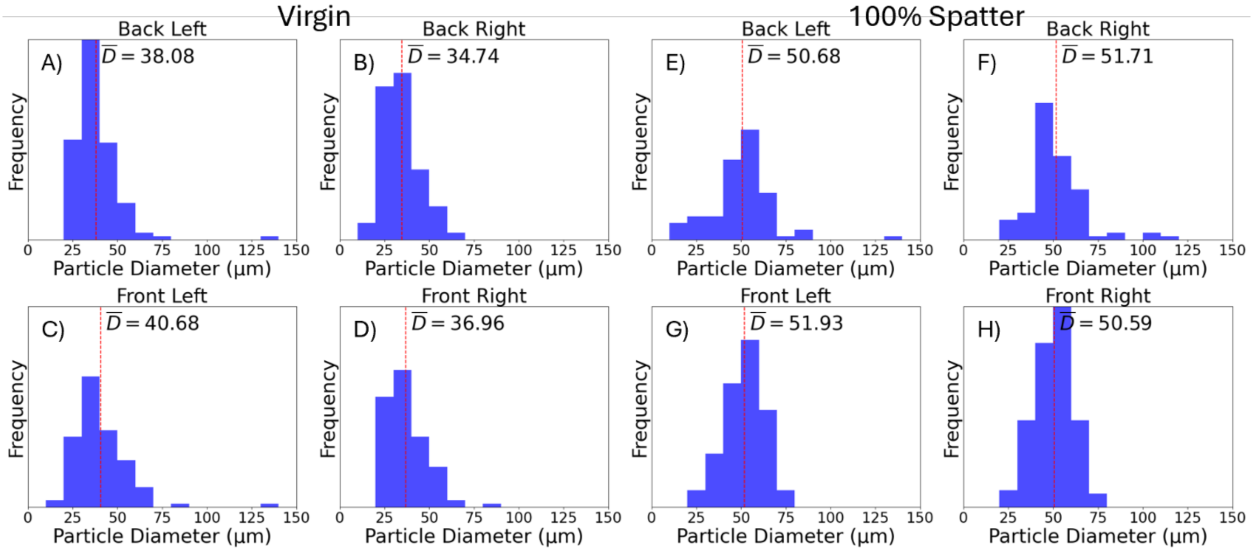

Figure 6.10: Histograms of surface spatter particle size per location for (A-D) 0 wt% spatter (virgin) and (E-H) 100 wt% spatter coupons (0° scan angle). Red lines indicate the average particle diameter (D̄) for the location.

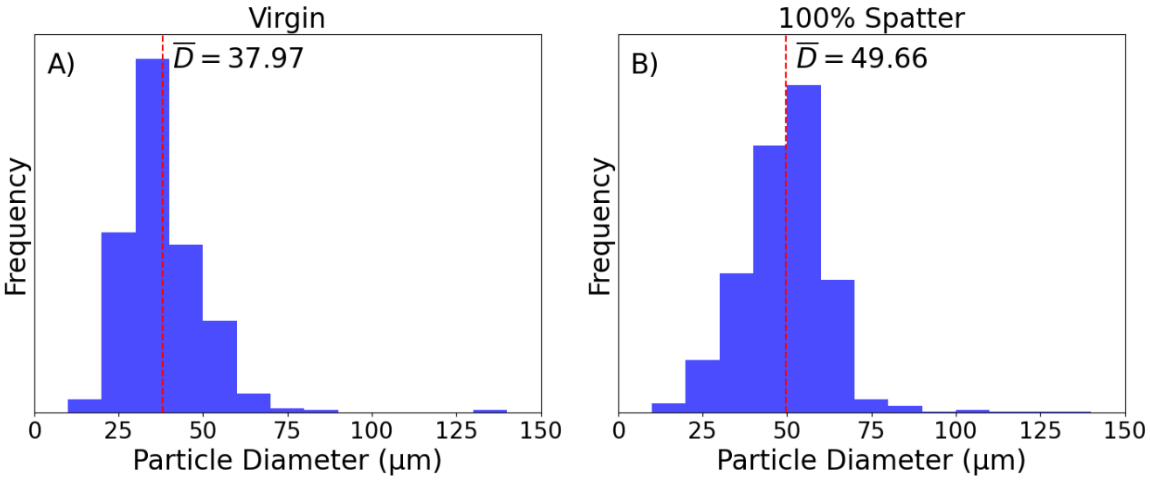

Figure 6.11: Histograms of surface spatter particle size per location for (A-D) 0 wt% spatter (virgin) and (E-H) 100 wt% spatter coupons (0° scan angle). Red lines indicate the average particle diameter ($\bar{D}$) for the location.

6.3.3 Spatter Strip Collection

An example video still of the interaction between the laser and powder during lasing of the weld sample is shown in Figure 6.12. Analysis of the in-chamber video captures revealed a surprising result. As shown in the still frame in this figure, spatter visible as glowing streaks can travel a substantial distance from the central meltpool. The streaks are attributed to the high temperature and speed of the spatter relative to the camera frame rate (30 Hz). The spatter disappears when the particles cool to a temperature that no longer emits visible light. It is not clear whether the spatter visible in these images is molten or solid. Additional stills are presented in Figure 6.13. Careful analysis of the still images shows evidence of laser-gas-spatter interactions; some of the spatter trajectories appear to be visibly altered by the flow of gas, as shown in Figure 6.13A. Some sparks and streaks appear above the melt pool traveling in the path of the laser beam and do not appear to originate from the melt pool, such as those shown in Figure 6.13B. These are assumed to be airborne particulate that are re-energized by the laser beam.

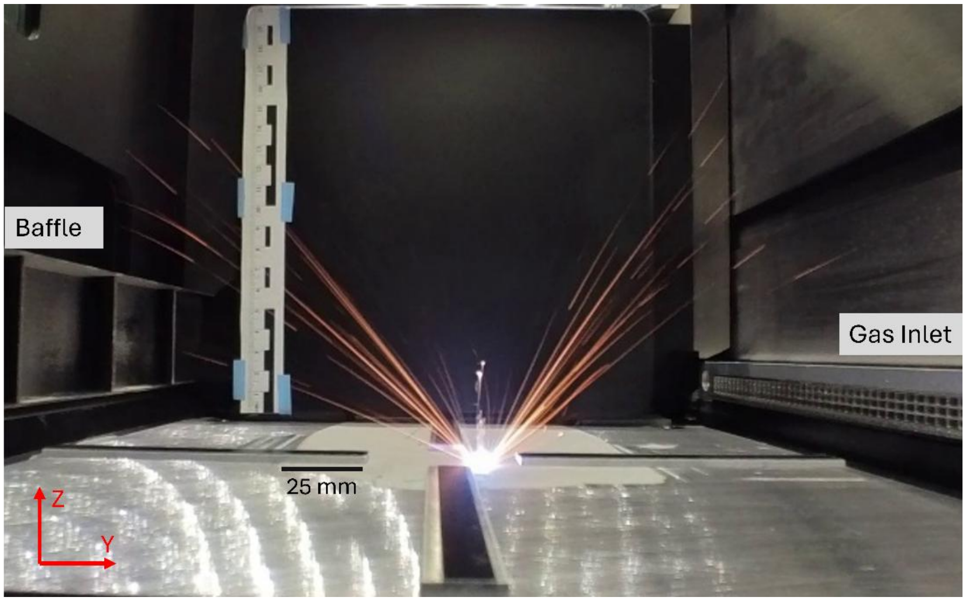

Figure 6.12: Annotated still frame from video captured by an action camera placed in-chamber during a single layer exposure. Spatter is visible as glowing streaks ejected from the melt area.

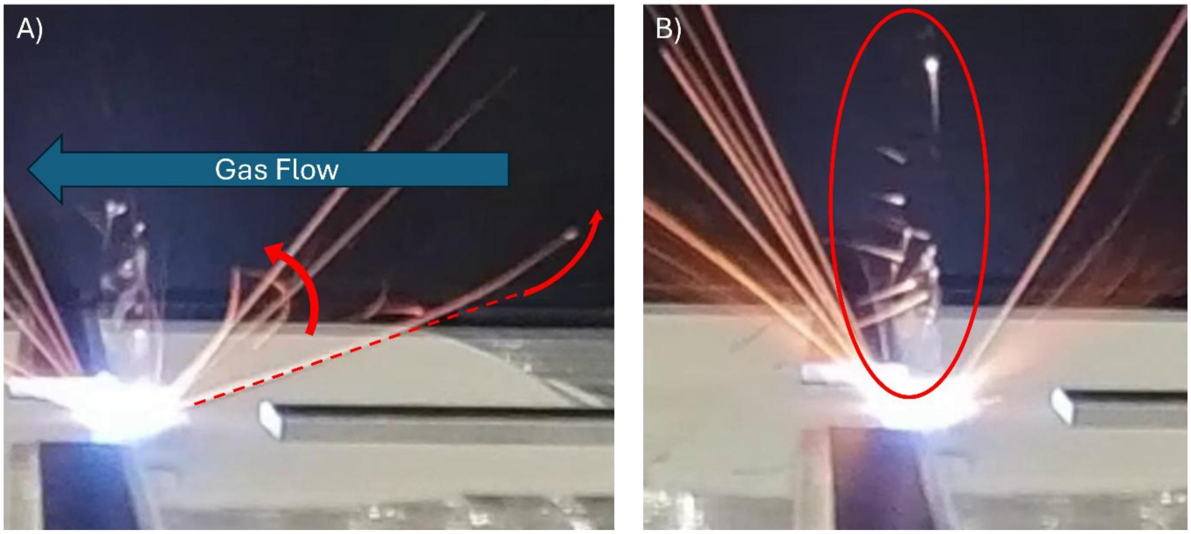

Figure 6.13: Annotated still frames from video captured in-chamber showing (A) spatter streaks redirected in the direction of the gas flow and (B) sparks/streaking occurring in the path of the laser beam above the melt pool.

Evaluation of the spatter collection strips showed notable differences in spatter quantity with location and travel distance. Histograms of particle counts vs distance from the part boundary are shown in Figure 6.14 (A) and (B) shows for coupons with 90° and 0° laser scan angles, respectively. For each coupon the particle counts are presented in four directions including above (+Y), below (-Y), and to the right (+X) and left (-X) of the part as defined from the operator perspective. Notably, the coupon printed with a 90° scan angle produced much greater quantities of spatter particles in all directions than the coupon with a 0° scan angle. In general, more spatter was collected on the strip located below the coupon, i.e. downwind, which would be expected if spatter trajectories are influenced by the gas flow. Spatter is typically ejected from the melt pool opposite to the direction of laser travel, so it would be expected that the majority of spatter would be ejected at angles of 90° (+Y) and 270° (-Y) for the 90° sample and at 0° (+X) and 180° (-X) for the 0° sample. Surprisingly, however, more spatter was collected to the right and left of the 90° coupon than in the same locations for the 0° coupon.

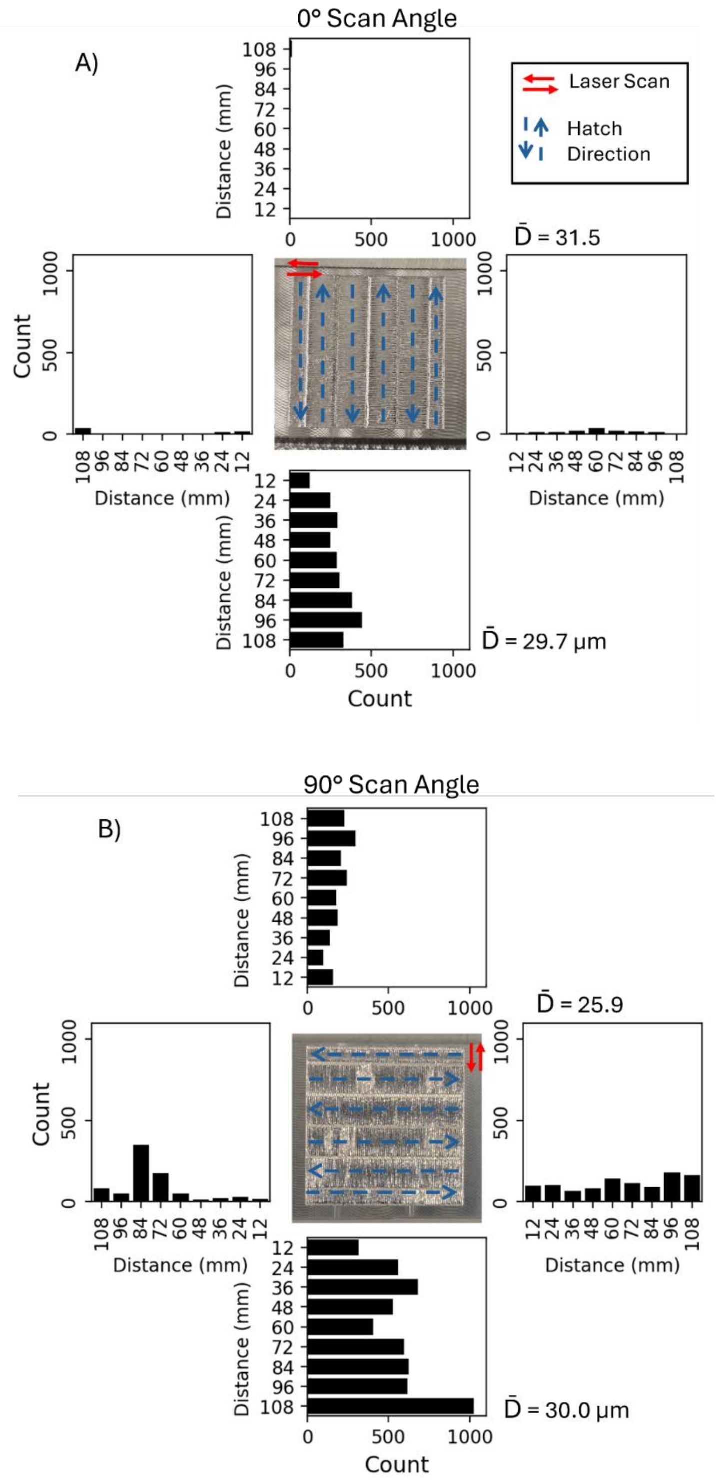

Figure 6.14: Spatter count histograms vs distance from the part boundary in the cardinal directions for coupons produced with (A) 0° laser scan angle and (B) 90° laser scan angle. measures are for builds performed with 0% spatter powder (virgin). Average particle size (D̄) of spatter as measured by SEM are given for the right and bottom collection areas.

6.4 **Discussion**

While SEM evaluation of the Baffle and Sieve spatter shows that the two materials look visually similar, LSPSA analysis showed that there are key differences. The Baffle spatter has a much broader particle size distribution with a semi-bimodal size distribution that suggests two separate populations of particles. It is possible that the peak denoting the smaller size particles could represent powder that was ejected from the powder bed from the recoil pressure of the metal vaporization. The peak and breadth of the 39 μm peak is consistent with the PSD of the precursor powder (Chapter 3, Figure 3.6). It is also possible that multiple mechanisms of spatter generation could cause different morphologies and particle sizes ranges. For instance, if the spatter solidifies before colliding with the surface would cause much different shape than if it impacts in a still molten or partially molten state.

Notably, the peak at 39 μm is not present in the Sieve spatter particle distribution. Particles of this size would be expected to fall through the sieve and thus would not remain in the portion of powder collected from the sieve. While the Sieve spatter does have a distribution that tends toward larger particle sizes, the lower size cutoff is not as distinct as would be expected for sieved powder. Some of the powder falls in the <63 μm size range, which could indicate that some powder particles are being retained in the Sieve spatter. Nonetheless, the Sieve spatter is similar enough in size and morphology to baffle spatter for it to be considered a reasonable representation of the spatter produced by L-PBF for use in this study.

The surface roughness of the weld coupon surface increased with spatter concentration in the powder mix. Laser-powder interactions are known to depend on particle size and morphology, so the interactions are not surprising. SEM analysis suggests that the cause of the differences in surface roughness is mainly driven by the size of the redeposited spatter particles on the surface. It is not clear if the laser-powder interactions are the cause of the different size of redeposited particles, or if they are more directly related to the size distribution of the precursor powder. It is also possible that the roughness trends are related to discrepancies in the powder layer thickness, which was not well controlled due to inconsistencies in weld coupon thickness.

What was responsible for the difference in the number of redeposited spatter particles between the front and back areas of the coupons? If we assume spatter is deposited at a steady rate throughout the exposure time, based on the order of melting (left to right) it would be expected to find more spatter deposited on the left side of the exposed surface, which was melted and resolidified first and thus had more time to accumulate spatter. However, the SEM evaluation found no substantial difference in quantity of spatter observed between the right (+x) and left (-x) sides of the coupons. Alternatively, if we assume that spatter is predominantly carried by the gas flow, then we would expect the majority of the spatter to be deposited on the front end (-y) of the exposed area. While the 100% spatter coupon did have more spatter on the front end, the 0% spatter coupon had the opposite trend, with less spatter observed at the front end of the coupon. The inconsistency of the result suggests that the process is more complicated than previously thought. It is possible that the contour pass performed after hatch melting could contribute to spatter deposition, which may explain the even side to side coverage. Interactions between the laser and the spatter in the powder layer may be causing changes to the melt pool dynamics that affect spatter ejection behavior. Laser-spatter interactions may also be the cause of the 100% spatter coupon having larger adhered spatter particles, despite having the same overall number of particles as the 0% coupon. Overall, more work is needed to determine if the observed trends are repeatable or random and whether they are related to spatter content or powder layer thickness.

Similarly, the differences in spatter collection between different laser scan angles raised as many questions as it answered. For the 0° scan angle coupon, very little spatter was captured above and to the sides of the coupon. Since spatter is typically ejected from the melt pool approximately 180° from the direction of laser movement, it would be expected that spatter would be primarily ejected to the right and left of the coupon. While some spatter was captured at the right and left locations, significantly more was captured below the coupon, suggesting that gas flow could play a large role in carrying spatter downwind during the melting process. This is supported by the observation of bright streaks in the laser path during the melting process, which are suspected to be small particles of spatter and MVC being re-ignited by the laser beam as they are carried by the argon flow.

Following the logic of spatter being carried by the gas flow, it would be expected that most of the spatter would be collected below during the printing of the 90° scan angle coupon, and to a lesser extent above the coupon. Indeed, the majority of spatter for the 90° scan angle coupon was collected below and above the coupon. However, a substantial amount was collected to the right and left. In fact, more spatter overall was collected to the right and left of the 90° scan angle coupon than the 0° coupon, despite the dynamics of spatter not favoring those directions. This result could suggest that certain scan angles are more prone to production of spatter than others. Alternatively, it could suggest that spatter that travels in -y is deflected by the gas flow, interferes with the laser and reignites, and causes more spatter. Further study is needed to confirm the propensity of spatter generation for different scan angles. The results could guide L-PBF performance improvement. If certain ranges of laser scan angles produce more spatter, then those scan angles should be skipped in the laser scan angle rotation, or the laser parameters could be adjusted for those scan angles to compensate for the increased spatter generation.

The in-chamber video capture gave enlightening insight into the spatter production process. Spatter traveled much farther in the chamber than expected, with many of the observed streaks traveling on trajectories that would carry them significantly farther than the confines of the chamber. As such, spatter can be deposited at any location within the build area regardless of the location of the parts being built, which precludes the option of spacing parts out to avoid spatter deposition. Occlusion or interference of the laser beam by spatter and/or metal vapor condensate could be one potential source of laser power fluctuation that can contribute to metal defects.

6.5 **Limitations**

Despite the development of new understanding regarding the contributions of processing and spatter content in the feedstock to the generation of spatter, there are some limitations to the effort. The major limitation in this evaluation was the inconsistencies in powder layer thickness between weld coupons. Discrepancies in test coupon thickness affected the recoater blade spacing, which caused the initial layer thickness to vary. Layer thickness directly influences laser energy density and melt pool temperature, which almost certainly affects spatter generation. Precise control over powder layer thickness is necessary for improving this research. The EOS M290 does not come with a native mechanism for measuring the initial powder layer thickness and instead relies on subjective tests and operator experience. For accurate comparison of spatter generation, control of the powder layer thickness to micrometer levels of accuracy would be needed. The standard layer height (60 μm) being comparable to the powder particle size compounds the difficulty. Thicker layers, while not representative of production procedure, might be better for studies comparing spatter generation.

The evaluation of spatter by direct evaluation of emission was limited by both the refresh rate and the camera resolution. Spatter is ejected at such high speed that standard 30 Hz frame rates result in long streaks in the video frames. Moreover, once the spatter cools below visible emission temperatures the particles are impossible to visualize at the current resolution. High-speed in-chamber video capture would be useful in tracking spatter trajectories and evaluating the interactions between spatter and gas flow. High resolution cameras could be more useful in tracking spatter particles after they have cooled below visible emission temperatures as well.

6.6 **Conclusions**

Results from the spatter collection evaluation show that the majority of spatter redeposition occurs downwind of the exposed area, and that deposition rates do not decrease appreciably for at least 100 mm from the edge of the part. Deposition rates to the sides and upwind of the part are substantially lower. It was also revealed that a 90° scan angle produced more spatter overall compared to a 0° scan angle.

The interactions between laser melting, spatter generation, and defect formation in L-PBF are still poorly understood. Individually these topics have received attention in the literature, and interest in their understanding is growing. The work presented here provides some new insights and shows that powder reuse, which is expected to harbor more spatter, is more likely to create spatter. Yet, ultimately, more research is needed to establish how gas flow, laser scan angle, and laser incidence angle affect the generation of spatter and how its distribution over the build area impacts defect distribution in parts.

Chapter 7 An Application of Machine Learning to Powder Reuse

7.1 Introduction

Chapters 3 and 4 discuss the key findings of the Round Robin study with respect to powder reuse. Due to the highly multivariate nature of the study, it is highly plausible that correlations exist between variables that were not previously identified using the traditional approaches. The high number of variables makes manually checking pairwise relationships difficult, so it is desirable to utilize analytical algorithms to evaluate the data in a wholistic and synchronous manner. This chapter discusses the use of machine learning methods to search for correlations between variables in the Round Robin dataset.

7.2 Background

The rise of advanced computing technologies has allowed the development of highly complex statistical computer models that can be used to identify, predict, and quantify patterns in data. As opposed to hard-coded programs that follow a rigorous set of instructions, these advanced algorithms can modify their internal model to optimize their performance for a specific task. Collectively, this approach to data processing is called Machine Learning (ML) [89]. Broadly, ML can be split into two categories, including supervised and unsupervised approaches. Supervised ML typically uses a portion of the dataset to train a model with the specific goal of predicting or categorizing an outcome based on input data [90,91]. Supervised ML relies on large datasets split into input and output variables, where the input variables are used to predict the outputs. In contrast, unsupervised ML aims to identify patterns and describe associations within a dataset. Contrary to the requirements of supervised ML, unsupervised ML does not rely on the dataset having predictor and outcome variables and is more suitable for datasets with large numbers of variables [90].

Self-Organizing Maps (SOMs) are a form of unsupervised ML that can be used to visualize high dimensional data by converting it to simple geometric relationships [92]. While other forms of unsupervised ML can be useful for determining correlations mathematically, they often do so at the expense of physical meaning [93]. SOMs excel at presenting the distributions in high-dimensional data in ways that support human-intuitive visualization. SOM methods leverage clustering algorithms to map a two-dimensional grid into the higher dimensional space of the dataset [90]. The nodes of the 2D grid are fit to the data to minimize variance. The multi-dimensional data points can then be mapped back to 2D space based on their proximity to nodes on the SOM. This method allows visualization of the features while largely preserving their topography.

The clustering behavior inherent to the SOM method enables the application of other complimentary clustering methods. For instance, K-means clustering is a method for separating or segregating data into a determined number of groups or clusters based on numerical similarity [90]. The K-means method applies an iterative procedure to minimize total variance of each cluster's datapoints from the center of that cluster. Starting from randomly chosen starting points, each cluster is defined by the subset of datapoints closest to each starting point. The means of each cluster subset are calculated and taken as the new centers. New clusters and centers are iteratively calculated until the clusters converge on a stable distribution or array.

The combination of SOMs and K-means clustering allows quick and effective identification of trends and groupings in highly dimensional datasets. These techniques were applied to the data generated by the UW Round Robin (UWRR) program to identify relationships between variables of powder reuse and metal quality.

7.3 Data

Machine Learning analysis was performed on data pertaining to the powder reuse acquired in Phases I and II of the UWRR study. Included in the analysis were measurements of powder quality described in Chapters 3 and 4, mechanical properties measured by uniaxial tension testing, and metal porosity measured by micro-computed tomography (μCT) on stress-relieved metal, in both the as-printed and machined conditions. Spatial variability based on the build space discretization described in Figure 2.2 of Chapter 2 was included in the dataset.

Powder particle size distributions were measured by Dynamic Light Scattering Particle Size Analysis (DLS; Horiba Partica LA950-V2, Kyoto, Japan) and are described by 10th, 50th (median), and 90th percentiles of the PSD (D10, D50, and D90, respectively). Light element chemistry was measured by Inert Gas Fusion (IGF; LECO 836 series elemental analyzer, St. Joseph, MI, USA) and combustion analysis (LECO 844 Series combustion analyzer, St. Joseph, MI, USA). The IGF and combustion analyses were performed by Fort Wayne Metals Materials Testing Lab (Fort Wayne, IN) in accordance with ASTM E1409 for oxygen and nitrogen, ASTM E1447 for hydrogen, and ASTM E1941 for carbon. Metallic chemistry was measured by X-Ray Fluorescence (XRF; Bruker M4 Tornado, Billerica, MA, U.S.) using an instrument at the UW. Hall Flow analysis and apparent density were used to assess the powder flowability and the measurements were performed in accordance with ASTM B213 and B212.

Evaluation of the internal void distribution within the metal specimens was performed using μCT on a North Star Imaging X5000 (Rogers, MN, USA). Continuous scans were performed with a voltage of 200 kV, current of 50 μA, and 127 μm brass filter, yielding a resolution of just over 8 μm. Radiographs were reconstructed and segmented into image slices for post-processing in VGStudio Max using the VGDefX/Only Threshold porosity analysis calculation with a 2% probability threshold applied to define pores. Summaries of average pore diameter, pore volume, and pore surface area were calculated from the data exported from the scans for each specimen. The sphericity of each pore was calculated, which is defined by the ratio of the void surface area to the surface area of a sphere with an equivalent diameter (*D*) identical to the void; a value of 1 would indicate a perfectly spherical void. Pore depth was defined as the shortest distance from the center of the pore to the nearest surface. Linear and 2D projections of the pore were used to calculate the projected size and area along each major dimension. Importantly, since the μCT scans were not registered to the machine coordinate system, the X and Y axes reported for the samples are somewhat arbitrary and do not directly correlate to the X and Y axes of the machine coordinate system. The long axis of the coupon was used to define the Z axis in the μCT scans, and does correspond to the machine axes, with +Z being the build direction. As such, voids identified in the XY plane of the μCT scans are in the XY plane of the metal specimens.

Tensile testing was performed with a commercial universal testing system (Instron, Model 5585H; Norwood, MA) under displacement control actuation at 1.27 mm/min. The axial strain was measured with a clip-on extensometer.

The data acquired from the analyses performed on the powder and metal from each build, and each partner, was compiled into a single dataset using Python (version 3.13.7). A customized version of the open source Python package for Self-Organizing Maps (SOMPY) was used to produce visualizations [94]. Map dimensions and cluster sizes were chosen to provide an optimized visual for the reader. The number of k-means clusters used in the analysis was chosen based on the number of clusters observed in the U-matrix for the SOM. The U-matric illustrates distances between neurons in the SOM, providing insights into cluster boundaries [95]. Each SOM was trained through competitive learning to minimize topographic error and quantization error. Topographic error indicates the quality of the projection and quantizatiozzzn error indicates the quality of the learning, with smaller error values indicating higher quality. Data processing was performed on a local laptop with a 2.10 GHz AMD Ryzen 5 5500U processor.

The heat maps produced by this version of SOMPY provide visual patterns of similarity and difference between the numerical datasets. Heat maps that present visually similar patterns indicate a correlation between the properties that those maps represent. Correlations can be positive (noted by similar colors) or negative (as noted by opposite colors). A more in depth description of the process by which these SOMs are developed can be found in the literature [91,93].

In total, 29 measurement dimensions were considered for evaluation by SOMs. Including all these measurement dimensions in a single SOM could lead to problems with sparsity of the data set, both due to the high number of dimensions (see "curse of dimensionality", Donoho 2020 [96]) as well as "density" of measurements. Another concern, powder characteristics were measured on a per-build basis, while tensile and µCT properties were measured on a per-coupon basis. Due to the difference in measurement density, coupon measurements were averaged across each build for comparison to powder characteristics for that build. But reducing the coupon performance to an average for each build discards any information on spatial variance within the build. To account for these concerns and not overlook spatial variability, the dataset was divided into three studies, each looking at a subset of the total dataset. Data subsets were chosen to best reflect the question posed by the study. First, powder properties and mechanical properties were evaluated over Phase I to evaluate the effect of powder reuse. Next, spatial variability in mechanical properties and porosity in Phase I was considered. Lastly, the effects of extended reuse between Phase I and Phase II was evaluated for powder properties only. The details and results of these studies are given in the following sections.

7.4 SOM Results

7.4.1 Study 1: Phase I Powder and Mechanical Properties

The data utilized in SOM Study 1 included three builds (i.e. Builds 1, 3 and 6) of all six partners in Phase I. The measurements included in this study were: particle size analysis (D10, D50, D90), chemical analysis (wt% Ti, Al, V, Fe), powder flow measurements (Hall flow time, apparent density), μCT measurements (pore diameter, pore sphericity, pore volume, edge distance, and projected sizes and areas), and tensile properties (yield strength, elastic modulus, elongation (engineering strain), and toughness). As previously described, the tensile and μCT properties were averaged across each build in this study to have a comparable number of data points to the other measurements. The SOM model was trained with a map size of 14x14, with 4 k-means clusters. Map dimensions were chosen based on the size of the data set to achieve optimal visualization for the reader. The SOM was trained through competitive learning to minimize topographic error and quantization error. Topographic error measures the efficacy of preserving spatial relationships in the SOM, with a lower value indicating greater efficacy in arranging similar patterns in close proximity [95]. The final topographic error and quantization error were 0.016 and 0.02859, respectively. Figure 7.1 shows the heatmap visualization of the SOM, representing low (blue) to high (red) values for each of the measurement dimensions included in the study.

A subset of the maps with more clear correlations are shown in Figure 7.2. Visual pattern similarities in the maps suggest strong positive correlations between aluminum content, flowability, and yield strength, and a negative correlation of those properties with elongation, as shown by the regions highlighted in the SOM maps. The same heat maps in Figure 7.2 highlights regions of negative correlation for median particle size (D50) and pore diameter; regions of high median particle size correspond to low pore diameter, and low median particle size with high pore diameter.

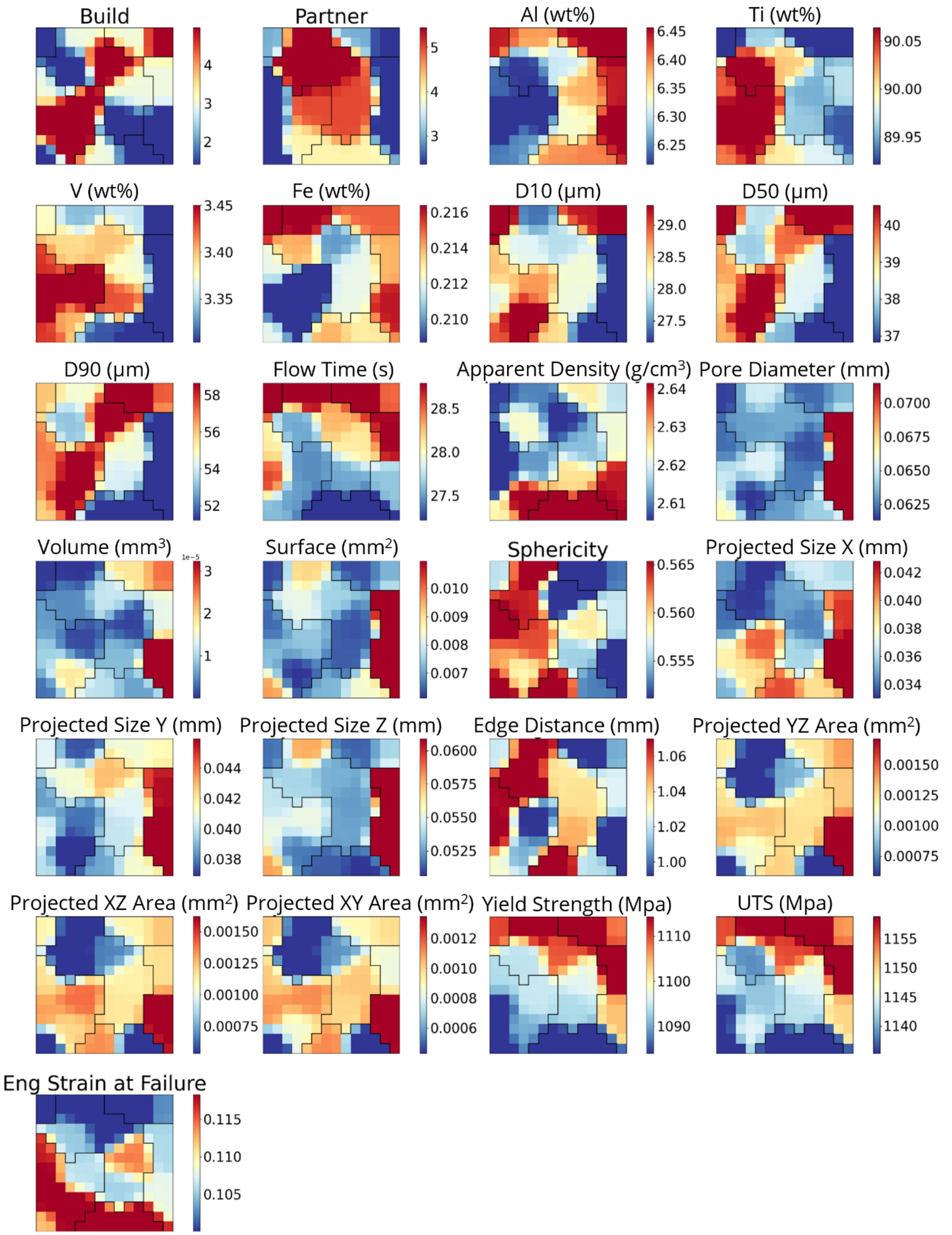

Figure 7.1: SOM heat maps for Study 1. The x and y-axes for each plot are the 14x14 2D grid of the trained SOM. Colors represent low (blue) to high (red) values for each measurement dimension, mapped onto the trained SOM. Black lines outline the five k-means clusters.

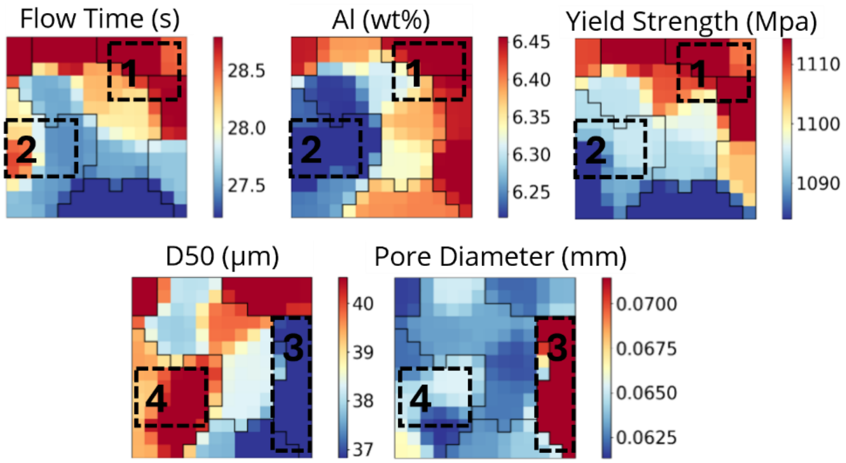

Figure 7.2: Selected SOM heatmaps from Figure 7.1 showing regions of similarity indicated positive and negative correlations. Note the positive correlation between flow time, Al weight percent and yield strength, and negative correlations between the D50 measurement and pore diameter. Highlighted regions 1 to 4 are described in the text.

7.4.2 Study 2: Porosity and Tensile Properties

Study 2 involved more detailed evaluation of the relationships between the mechanical properties and the microstructure evaluated by µCT. Still focusing on results of Phase I, this ML study included the results of all six builds for all six partners. The µCT measures of porosity include pore diameter, pore diameter, pore sphericity, pore volume, edge distance, and projected sizes and areas. Tensile properties included yield strength, ultimate tensile strength (UTS), and engineering strain at failure. Since tensile and µCT measurements were performed on a per sample basis, spatial variables of level, zone, and location (coupon number) could also be included. The SOM model was trained with a map size of 30x30, with 8 k-means clusters. The final topographic error and quantization error were 0.032 and 1.0802, respectively. Figure 7.3 shows the heatmap visualization of the SOM.

While there was visual similarity within the tensile measurement variables as well as within the µCT measurement variables, no obvious correlation patterns were observed between tensile properties and μCT properties. The heat maps for the tensile properties shows the values forming a vertical gradient from top to bottom in the graphs, while the heat maps for the μCT properties appear to reflect horizontal gradients. The difference in these distributions indicates that those properties are independent of each other. There may be slight agreement between the patterns in the engineering strain at failure heat map and the sphericity and pore edge distance heat maps. Heatmaps for these three variables are presented in Figure 7.4 with two regions of similarity highlighted. Region 1 contains samples that exhibited low elongation and low sphericity pores close to the surface. Region 2 contains samples that exhibited high elongation metal with highly spherical pores located far from the surface.

Spatial factors did not appear to contribute to variability in porosity or tensile properties, as indicated by the random distribution of values for the level, zone, and location variables. Likewise, partner and build number did not appear to be correlated with other variables, indicating that inter-build and inter-machine variability was low in this study.

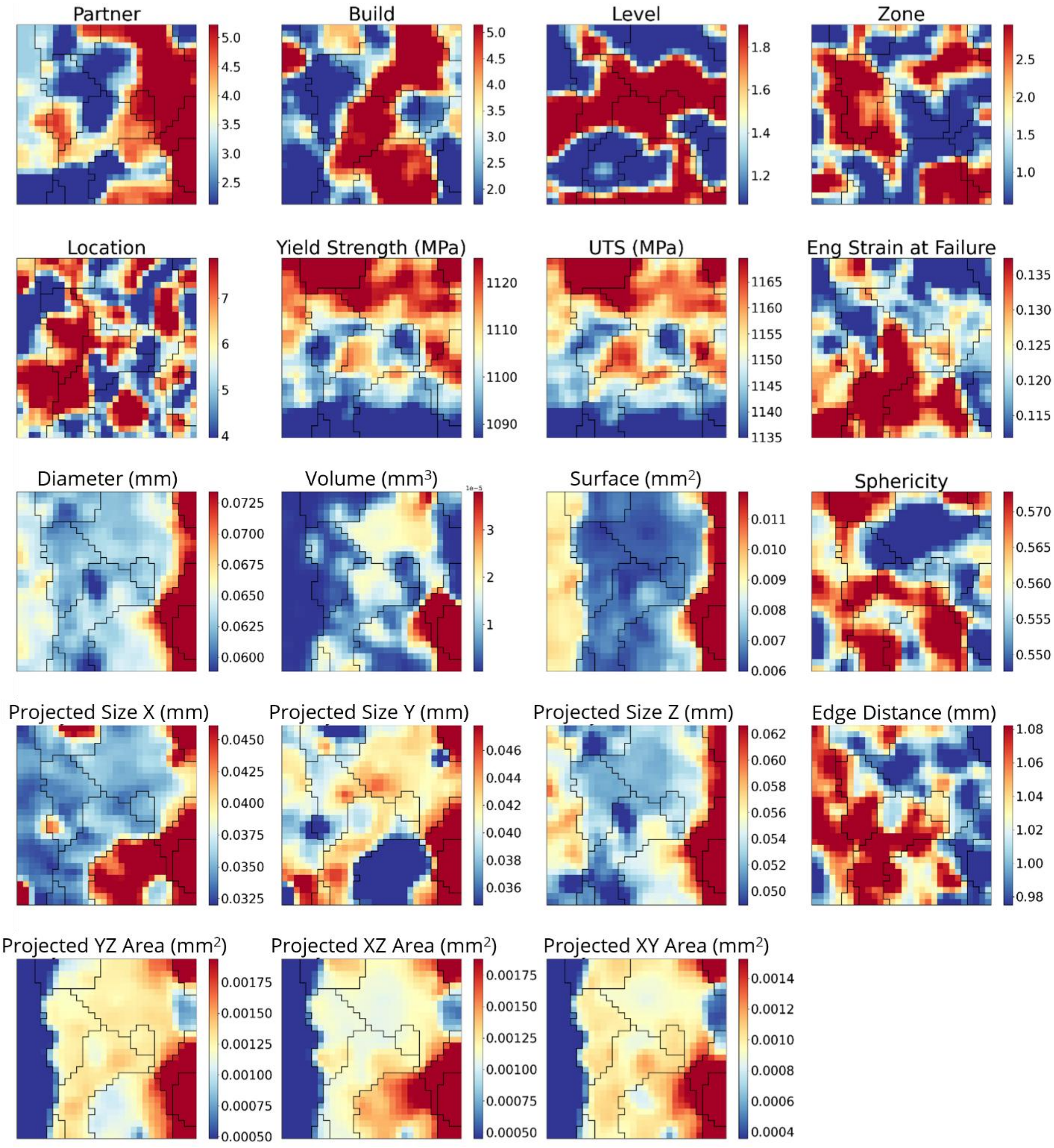

Figure 7.3: SOM heat maps for Study 2. The x and y-axes for each plot are the 20x20 2D grid of the trained SOM. Colors represent low (blue) to high (red) values for each measurement dimension, mapped onto the trained SOM. Black lines outline the eight k-means clusters.

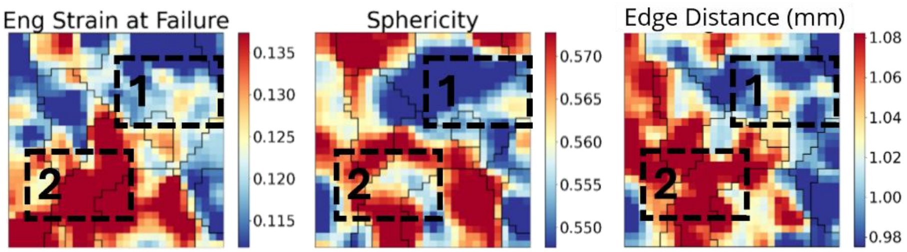

Figure 7.4: Selected SOM heatmaps from Figure 7.3, showing two regions of similarity discussed in the text.

7.4.3 Study 3: Phase I and Phase II Powder Properties

While the efforts in the first two studies were concentrated on Phase I of the UWRR, Study 3 focused on the continued effect of powder reuse from Phase I to Phase II. Powder properties, including particle size analysis (D10, D50, D90), chemical analysis (wt% Ti, Al, V, Fe), and powder flow measurements (Hall flow time, apparent density). This study included three partners and seven builds of the study (Builds 1, 3, 6, 7-10). Tensile properties and µCt measures were excluded as these measurements were not performed for Phase II in the same way they were in Phase I. The SOM model was trained with a map size of 12x12, with 4 k-means clusters. The final topographic error and quantization error were 0.014 and 0.1654, respectively. Figure 7.5 shows the heatmap visualization of the SOM.

This study involved the smallest of the three data sets developed for analysis. As such the conclusions drawn from the SOM are similarly limited. Consistent with the results of Study 1, the aluminum content distribution exhibits a possible positive correlation with flow time, as was observed in the SOMs of Study 1, supporting the connection between those properties. The particle size properties (D10, D50, D90) also show a correlation with flow time, which is an inverse relationship in Study 3, which was not specifically observed in the SOMs of Study 1. While build number appears to have a negative correlation with oxygen content, this data was called into question, as discussed in Chapter 4, and so inferences regarding this measurement are reserved.

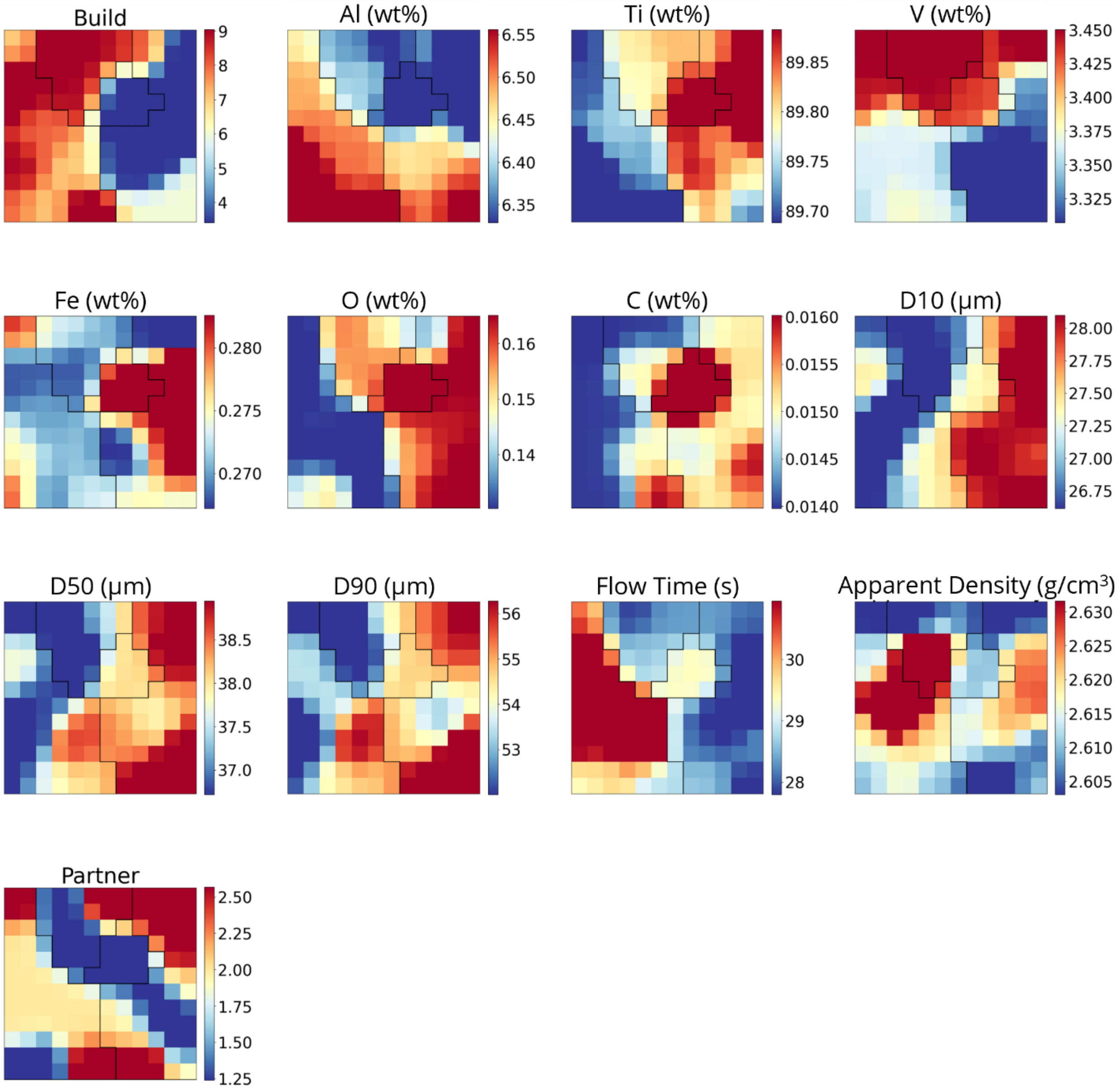

Figure 7.5: SOM heat maps for Study 3. The x and y-axes for each plot are the 12x12 2D grid of the trained SOM. Colors represent low (blue) to high (red) values for each measurement dimension, mapped onto the trained SOM. Black lines outline the three k-means clusters.

7.5 Discussion

Results of the SOMs prepared in Study 1 for Phase I of the UWRR clearly identified the correlation between aluminum content in the powder and yield strength of the metal. The visual similarities between the heatmaps are strong and consistent, reflecting the strong correlation observed in the data. As mentioned previously, this relationship is expected, since aluminum is known to act as an interstitial hardening element in titanium. However, the source of the aluminum is unclear, as it does not appear to be correlated with build number. As discussed in Chapter 4, metal vapor condensate was found to be enriched in aluminum and could act as a source of aluminum contamination if it deposits on the powder bed during the build process. No strong evidence has been yet observed of such redeposition in practice. The aluminum content also showed a positive correlation with flow time. This could also be explained by MVC redeposition affecting the relative friction and cohesion between particles. Further investigation into the behavior of MVC redeposition could benefit the understanding of powder reuse.

The observed relation between the median particle size and pore diameter could indicate a causal relationship between particle size and porosity, possibly mediated through effects of particle size on packing factor. This relationship is not clearly demonstrated and would require further investigation to rule out other compounding factors.

The low correlation between porosity and tensile properties portrayed by the SOMs in Study 2 has already been reported for this study [64]. As such, the lack of pattern similarities between these properties in the SOM analysis is not surprising. The insensitivity of the tensile properties to porosity has been attributed to multiple factors. First, the small size and distribution of the pores in the metal, and second, the limitation of μCT in identifying pores exposed close to the surface, which would contribute more to ductility than pores within the metal are primary factors. Nonetheless, a tenuous trend between ductility, pore sphericity, and edge distance was noted in Study 1, as shown in Figure 7.4. Low sphericity pores located near to the surface would be expected to contribute more to lowering ductility, as indicated by this relation. Overall, this study showed high consistency between the machines and builds involved.

The data distributions reflected in the SOMs of Study 3 unfortunately suffered from a sparse dataset, which made finding correlations difficult. Since Phase I evaluated tensile properties and Phase II evaluated fatigue properties, neither behavior could be included in the SOM model combining these results. Some powder properties, such as oxygen and carbon content, exhibited discontinuities between Phase I and Phase II, though the cause is unclear. The impact on the SOM model causes correlations to appear between powder properties and build number. However, it is unclear if these are genuine relationships or if they are artifactual. The SOM study does seem to support the correlation between aluminum content and number of builds or reuse cycles that was observed in Study 1. Flow time also appears to be negatively correlated with the particle size measures (D10, D50, D90), which may be related to the overall distribution of the PSD. More targeted evaluations are needed to confirm these relationships, which is reserved for future work.

As with any machine learning evaluation, caution must be taken against drawing conclusions that are not supported by physical evidence. The application of SOMs, in particular, are subjective evaluations that are best used for guiding future investigations or in screening of important factors from those that are less or not important.. Nonetheless, leveraging human pattern recognition is a powerful tool for identifying relationships that would otherwise elude discovery.

7.6 Conclusions

Based on an evaluation of the UW Round Robin data by the SOMs method of machine learning the following conclusions are drawn:

- Evaluation of the UWRR data by SOMs supports the previous conclusions drawn regarding the trends observed in the data regarding composition of the powder and strength. Specifically, ML supports the observed positive correlation between aluminum content and tensile strength.
- The SOMs prepared for Phase I of the UWRR suggest correlations between aluminum content and flowability of the powder, and between median particle size and porosity. That is expected to result from the deposition of aluminum-rich condensate onto the powder bed and increase in the inter-particle pore size.
- Tensile properties of the metal and porosity evaluated by μCT from Phase I were not strongly correlated. That reinforces findings presented in Chapter 3 and is expected due to the limited effects of pores on the strength and ductility, as well as considering the limited range in pore size.

Chapter 8 Conclusions and Future Work

8.1 Conclusions

The research presented in this dissertation characterizes the variability in powder reuse in L-PBF and its effects on property variability. The study utilized a unique round robin approach leveraging multiple machines executing a controlled build process to minimize the sources of variability. Unique to this study was the establishment of a highly defined starting condition whereby six different organizations printed the same set of six builds from the same lot of powder, following the same nominal process condition. The use of a single powder lot starting condition allowed changes observed in powder quality to be attributed directly to differences in machine condition or procedures at the participating organizations.

The evaluation of powder through the round robin study in Chapters 3 and 4 revealed that changes to powder quality occur slowly and inconsistently when comparing results across partners, but that powder reuse does contribute to variability in powder quality. Most measured powder properties did not change substantially over the course of the study, including powder size, metallic chemistry, and light element chemistry. None of those properties exceeded the limits designated by relevant standards. However, variability in these properties between participants did increase in both phases of the study. Moreover, measurable effects of powder quality on metal performance were observed. These results highlight the inconsistent effect of powder reuse on powder properties and the importance of continued powder monitoring when producing parts commercially by L-PBF.

Along with powder quality, spatter induced by the laser melting process can have an impact on both powder and part quality. Results described in Chapter 6 shows that spatter produced at the center of the build area can be deposited though out the build chamber, potentially affecting parts in all locations of the build. Moreover, the results suggest that spatter content in the powder can in-turn increase the size of new spatter particles produced during the laser melting process. These results demonstrate the importance of spatter as a contributor to metal property variability, and they highlight the need for further study of this topic. In addition, gas flow was found to have a significant impact on spatter deposition (Chapter 6), regardless of laser scan direction. Most of the spatter accumulated downstream of the melt location. Nevertheless, spatter ejection distance was found to be much greater than the length of the powder bed, indicting that there is no "safe" spacing of parts to avoid spatter deposition. Spatter was observed to be ejected in all directions from the melt area

Another potential contributor to powder and metal variability is the metal vapor condensate produced during the laser melting process. Presented in Chapter 5, the development of novel collection methods allowed detailed characterization of MVC, including estimating the ignition temperatures and activation energy of ignition. Results showed that the ignition of MVC occurs at relatively low temperatures (~400°C) and with a estimated activation temperature of 55 kJ/mol. Oxidation of the MVC was observed at temperatures around 100°C. These findings highlight the tremendous volatility of this material that contributes to the health and fire safety risks associated with its handling and disposal. In addition to ignition behavior, the MVC was found to have elevated levels of aluminum compared to the base powder due to the preferential vaporization of aluminum from the melt pool. As such, the MVC could behave as a source of contamination in the powder if it deposits on the powder bed in significant quantities.

Finally, machine learning methods were used in Chapter 7 to reinforce the correlations observed in the earlier sections and identify other possible correlations. Powder quality data from

Phases I and II was combined with tensile and μCT data in self-organizing maps to compare similarities and differences in the datasets across partners and builds. Results from the ML supported the correlations observed between aluminum content and tensile properties. ML also suggested new correlations, specifically between aluminum content and flowability, and between median particle size and porosity. Overall, these findings show that variability in powder quality may not be limited to just the bulk powder measurements outlined in current standards. L-PBF is a highly dynamic process with many interacting factors that make predicting behavior difficult. Most importantly, These findings highlight the potential for variability to arise in the powder feedstock between two organizations running the same procedure, even on the same machine, after a relatively few number of builds. These findings are crucial for the development of certification procedures for using L-PBF to produce stress-critical components.

8.2 Recommended Future Work

8.2.1 Powder reuse

While this research provided new understanding of powder degradation in reuse through the control of starting conditions and build parameters, it was limited by the number of builds, and the discontinuity of build design from Phase I to Phase II. Ideally a study focused on powder reuse would involve a much higher number of builds and a consistent build design throughout the build program. The present investigation and build design was not developed to optimize the reuse portions of the program. Of importance in these future studies, high ratios of printed metal to build volume are not recommended due to the high powder consumption rates of the builds and need for replenishing the consumed powder with virgin feedstock. Likewise, very sparse builds are not conducive to powder reuse studies, since they limit the exposure of the powder to the byproducts of the laser melting process. Limiting the amount of virgin powder added to the in-use powder would also help expedite powder degradation and the accumulation of contamination.

Several interesting possible associations were identified through the use of the SOMs that could benefit from further research. Powder flow time was seen to have positive pattern matches with aluminum content, but the causal link is unclear. MVC deposition on the powder could alter the surface characteristics of the powder enough to influence flowability and should be investigated more thoroughly. This could potentially be achieved by careful and thorough use of electronic microscopy to identify MVC on reused powder, and AFM to characterize changes in surface roughness.

8.2.2 Contamination

Contamination of the powder is a critical concern that was not addressed in the design of this study. Debris may be introduced to the powder during manufacturing or during handling when the powder is exposed to the environment. The entrained debris could contribute significantly to the mechanical properties of the metal, especially the fatigue performance, even at concentrations too low to detect by bulk chemistry measurements. Evaluation of the powder and metal for contamination that is introduced in the build should be a major priority in evaluating variability in performance. Sources of contamination could include the AM process itself. Of note, the MVC was found to have different chemistry from the base powder and was shown to accumulate on surfaces in the build chamber. Based on results of this investigation, it is not unlikely that MVC deposition could alter the local chemistry of a part significantly enough to affect its mechanical performance. Evaluation of MVC contamination of the powder bed during reuse should therefore be a consideration for further research in this field.

8.2.3 Spatter

The interactions between laser melting, spatter generation, and defect formation in L-PBF are still poorly understood. Individually these topics have received attention in the literature, and interest in understanding their contribution to build quality is growing. Complicating this interaction is the possibility that spatter redeposited in the powder bed may alter the conditions of the melt pool, leading to further changes in spatter generation. The work presented in Chapter ? suggests that spatter rich reused powder, may in turn generate spatter at a higher rate than virgin powder. Feedback loops of spatter-induced spatter generation could hasten powder degradation or impart higher rates of porosity in the metal. Ultimately, more research is needed to establish how gas flow, laser scan angle, and laser incidence angle affect the generation of spatter and how its distribution over the build area impacts defect distribution in parts.

8.2.4 Metal Vapor Condensate

As described in relation to the effects of spatter, effects from the generation and deposition of MVC on the powder bed to metal quality requires further research. Some studies [52] have suggested that MVC deposits directly on the powder bed downstream of the melt areas. However, the rate and extent of MVC deposition is not clear. Downstream deposition may impact the quality of parts in those areas, degrading the part variability in a build. Safety is another factor in considering MVC. It would be advantageous to all L-PBF system operators to have better methods of handling and disposing of MVC. Ideally, methods would be developed to passivate the MVC collected within the system, making it easier to dispose of. Chemical digestion is another possible avenue for addressing MVC waste, which warrants further research. While these research topics pose significant challenges and hurdles, they are crucial to improving and refining the PBF AM process and will prove invaluable to the future of the field.

References

[1] ISO/ASTM. ISO/ASTM 52900:2015(E) Standard Terminology for Additive Manufacturing – General Principles – Terminology. ASTM International 2015:1–9. https://doi.org/10.1520/F2792-12A.2.

[2] Bourell DL, Frazier W, Kuhn H, Seifi M, editors. ASM Handbook, Volume 24, Additive Manufacturing Processes. vol. 24. ASM International; 2020.

[3] Kruth JP, Levy G, Klocke F, Childs THC. Consolidation phenomena in laser and powder-bed based layered manufacturing. CIRP Annals - Manufacturing Technology 2007;56:730–59. https://doi.org/10.1016/j.cirp.2007.10.004.

[4] Thijs L, Verhaeghe F, Craeghs T, Humbeeck JV, Kruth JP. A study of the microstructural evolution during selective laser melting of Ti-6Al-4V. Acta Materialia 2010;58:3303–12. https://doi.org/10.1016/j.actamat.2010.02.004.

[5] Agius D, Kourousis KI, Wallbrink C. A review of the as-built SLM Ti-6Al-4V mechanical properties towards achieving fatigue resistant designs. Metals 2018;8. https://doi.org/10.3390/met8010075.

[6] Watson JK, Taminger KMB. A decision-support model for selecting additive manufacturing versus subtractive manufacturing based on energy consumption. Journal of Cleaner Production 2018;176:1316–22. https://doi.org/10.1016/j.jclepro.2015.12.009.

[7] Renishaw. Investigating the effects of multiple re-use of Ti6Al4V powder in additive manufacturing. Renishaw 2016:1–10.

[8] Badiru AB, Valencia VV, Liu D. Additive manufacturing: Handbook product development for the defense industry. CRC Press; 2017. https://doi.org/10.1201/9781315119106.

[9] Bourell DL. Perspectives on Additive Manufacturing. Annual Review of Materials Research 2016;46:1–18. https://doi.org/10.1146/annurev-matsci-070115-031606.

[10] DebRoy T, Wei HL, Zuback JS, Mukherjee T, Elmer JW, Milewski JO, et al. Additive manufacturing of metallic components – Process, structure and properties. Progress in Materials Science 2018;92:112–224. https://doi.org/10.1016/j.pmatsci.2017.10.001.

[11] Herzog D, Seyda V, Wycisk E, Emmelmann C. Additive manufacturing of metals. Acta Materialia 2016;117:371–92. https://doi.org/10.1016/j.actamat.2016.07.019.

[12] Frazier WE. Metal additive manufacturing: A review. Journal of Materials Engineering and Performance 2014;23:1917–28. https://doi.org/10.1007/s11665-014-0958-z.

[13] Vrancken B, Thijs L, Kruth JP, Van Humbeeck J. Heat treatment of Ti6Al4V produced by Selective Laser Melting: Microstructure and mechanical properties. Journal of Alloys and Compounds 2012;541:177–85. https://doi.org/10.1016/j.jallcom.2012.07.022.

[14] Zhao X, Li S, Zhang M, Liu Y, Sercombe TB, Wang S, et al. Comparison of the microstructures and mechanical properties of Ti-6Al-4V fabricated by selective laser melting and electron beam melting. Materials and Design 2016;95:21–31. https://doi.org/10.1016/j.matdes.2015.12.135.

[15] Montelione A, Ghods S, Schur R, Wisdom C, Arola D, Ramulu M. Powder Reuse in Electron Beam Melting Additive Manufacturing of Ti6Al4V: Particle Microstructure, Oxygen Content and Mechanical Properties. Additive Manufacturing 2020;35:101216. https://doi.org/10.1016/j.addma.2020.101216.

[16] Donachie MJ. Titanium: A Technical Guide. ASM International; 2000.

[17] Mower TM, Long MJ. Mechanical behavior of additive manufactured, powder-bed laser-fused materials. Materials Science and Engineering A 2016;651:198–213. https://doi.org/10.1016/j.msea.2015.10.068.

[18] Svensson M, Ackelid U. Titanium Alloys Manufactured with Electron Beam Melting Mechanical and Chemical Properties. Materials & Processes for Medical Devices Conference 2009, Minneapolis, Minnesota, USA: ASM International; 2009, p. 189–94.

[19] Lewandowski JJ, Seifi M. Metal Additive Manufacturing: A Review of Mechanical Properties. Annual Review of Materials Research 2016;46:151–86. https://doi.org/10.1146/annurev-matsci-070115-032024.

[20] Gil Mur FX, Rodríguez D, Planell JA. Influence of tempering temperature and time on the α′-Ti-6Al-4V martensite. Journal of Alloys and Compounds 1996;234:287–9. https://doi.org/10.1016/0925-8388(95)02057-8.

[21] Murray JL, Wriedt HA. The O-Ti (Oxygen-Titanium) System 1987;8:148–65.

[22] Gil FJ, Ginebra MP, Manero JM, Planell JA. Formation of α-Widmanstätten structure: Effects of grain size and cooling rate on the Widmanstätten morphologies and on the mechanical properties in Ti6Al4V alloy. Journal of Alloys and Compounds 2001;329:142–52. https://doi.org/10.1016/S0925-8388(01)01571-7.

[23] Baumers M, Dickens P, Tuck C, Hague R. The cost of additive manufacturing: Machine productivity, economies of scale and technology-push. Technological Forecasting and Social Change 2016;102:193–201. https://doi.org/10.1016/j.techfore.2015.02.015.

[24] Lutter-Gunther M. Powder Recycling in Laser Beam Melting: Strategies, consumption modeling and influence on resource efficiency. Production Engineering 2018;12:377–89.

[25] Moghimian P, Poirié T, Habibnejad-Korayem M, Zavala JA, Kroeger J, Marion F, et al. Metal powders in additive manufacturing: A review on reusability and recyclability of common titanium, nickel and aluminum alloys. Additive Manufacturing 2021;43:102017. https://doi.org/10.1016/j.addma.2021.102017.

[26] Emminghaus N, Bernhard R, Hermsdorf J, Kaierle S. Residual oxygen content and powder recycling: effects on microstructure and mechanical properties of additively manufactured Ti-6Al-4V parts. Int J Adv Manuf Technol 2022;121:3685–701. https://doi.org/10.1007/s00170-022-09503-7.

[27] Bajt Leban M, Hren M, Kosec T. The microstructure, mechanical and electrochemical properties of 3D printed alloys with reusing powders. Sci Rep 2023;13. https://doi.org/10.1038/s41598-023-28971-9.

[28] Nandwana P, Peter WH, Dehoff RR, Lowe LE, Kirka MM, Medina F, et al. Recyclability Study on Inconel 718 and Ti-6Al-4V Powders for Use in Electron Beam Melting. Metallurgical and Materials Transactions B 2016;47:754–62. https://doi.org/10.1007/s11663-015-0477-9.

[29] Rousseau JN, Bois-Brochu A, Blais C. Effect of oxygen content in new and reused powder on microstructural and mechanical properties of Ti6Al4V parts produced by directed energy deposition. Additive Manufacturing 2018;23:197–205. https://doi.org/10.1016/j.addma.2018.08.011.

[30] Soltani-Tehrani A, Isaac JP, Tippur HV, Silva DF, Shao S, Shamsaei N. Ti-6Al-4V powder reuse in laser powder bed fusion (L-PBF): The effect on porosity, microstructure, and mechanical behavior. International Journal of Fatigue 2023;167:107343. https://doi.org/10.1016/j.ijfatigue.2022.107343.

[31] Tang HP, Qian M, Liu N, Zhang XZ, Yang GY, Wang J. Effect of Powder Reuse Times on Additive Manufacturing of Ti-6Al-4V by Selective Electron Beam Melting. JOM 2015;67:555–63. https://doi.org/10.1007/s11837-015-1300-4.

[32] O'Leary R, Setchi R, Prickett P, Hankins G, Jones N. An Investigation into the Recycling of Ti-6Al-4V Powder Used Within SLM to Improve Sustainability. SDM'2015: 2nd International Conference on Sustainable Design and Manufacturing , (2015) 2015:14–7.

[33] Seyda V, Kaufmann N, Emmelmann C. Investigation of Aging Processes of Ti-6Al-4V Powder Material in Laser Melting. Physics Procedia, vol. 39, Elsevier B.V.; 2012, p. 425–31. https://doi.org/10.1016/j.phpro.2012.10.057.

[34] Powell D, Rennie AEW, Geekie L, Burns N. Understanding powder degradation in metal additive manufacturing to allow the upcycling of recycled powders. Journal of Cleaner Production 2020;268:122077. https://doi.org/10.1016/j.jclepro.2020.122077.

[35] Sassaman D, Phillips T, Milroy C, Ide M, Beaman J. A Method for Predicting Powder Flowability for Selective Laser Sintering. JOM 2022;74:1102–10. https://doi.org/10.1007/s11837-021-05050-w.

[36] Harkin R, Wu H, Nikam S, Quinn J, McFadden S. Reuse of Grade 23 Ti6Al4V Powder during the Laser-Based Powder Bed Fusion Process. Metals 2020;10:1700. https://doi.org/10.3390/met10121700.

[37] Meier B, Warchomicka F, Ehgartner D, Schuetz D, Angerer P, Wosik J, et al. Toward a sustainable laser powder bed fusion of Ti 6Al 4 V: Powder reuse and its effects on material properties during a single batch regime. Sustainable Materials and Technologies 2023;36:e00626. https://doi.org/10.1016/j.susmat.2023.e00626.

[38] Carrion PE, Soltani-Tehrani A, Phan N, Shamsaei N. Powder Recycling Effects on the Tensile and Fatigue Behavior of Additively Manufactured Ti-6Al-4V Parts. Jom 2019;71:963–73. https://doi.org/10.1007/s11837-018-3248-7.

[39] Cordova L, Campos M, Tinga T. Revealing the Effects of Powder Reuse for Selective Laser Melting by Powder Characterization. JOM 2019;71:1062–72. https://doi.org/10.1007/s11837-018-3305-2.

[40] Denti L, Sola A, Defanti S, Sciancalepore C, Bondioli F. Effect of Powder Recycling in Laser-based Powder Bed Fusion of Ti-6Al-4V. Manufacturing Technology 2019;19:190–6. https://doi.org/10.21062/ujep/268.2019/a/1213-2489/MT/19/2/190.

[41] Thejane K, Chikosha S, du Preez WB. Characterisation and monitoring of TI6AL4V (ELI) powder used in different selective laser melting systems. South African Journal of Industrial Engineering 2017;28:161–71. https://doi.org/10.7166/28-3-1853.

[42] Quintana OA, Alvarez J, Mcmillan R, Tong W, Tomonto C. Effects of Reusing Ti-6Al-4V Powder in a Selective Laser Melting Additive System Operated in an Industrial Setting. Jom 2018;70:1863–9. https://doi.org/10.1007/s11837-018-3011-0.

[43] Skalon M, Meier B, Leitner T, Arneitz S, Amancio-Filho ST, Sommitsch C. Reuse of Ti6al4V powder and its impact on surface tension, melt pool behavior and mechanical properties of additively manufactured components. Materials 2021;14:1–22. https://doi.org/10.3390/ma14051251.

[44] Harkin R, Wu H, Nikam S, Yin S, Lupoi R, McKay W, et al. Powder Reuse in Laser-Based Powder Bed Fusion of Ti6Al4V—Changes in Mechanical Properties during a Powder Top-Up Regime. Materials 2022;15:2238. https://doi.org/10.3390/ma15062238.

[45] Sun X, Chen M, Liu T, Zhang K, Wei H, Zhu Z, et al. Characterization, preparation, and reuse of metallic powders for laser powder bed fusion: a review. Int J Extrem Manuf 2024;6:012003. https://doi.org/10.1088/2631-7990/acfbc3.

[46] Petrovic V, Niñerola R. Powder recyclability in electron beam melting for aeronautical use. Aircraft Engineering and Aerospace Technology 2015;87:147–55. https://doi.org/10.1108/AEAT-11-2013-0212.

[47] Bellini C, Berto F, Cocco VD, Franchitti S, Iacoviello F, Mocanu LP, et al. Effect of recycling on internal and external defects of Ti-6Al-4V powder particles for electron beam melting process. Procedia Structural Integrity 2022;41:175–82. https://doi.org/10.1016/j.prostr.2022.05.019.

[48] Popov VV, Katz-Demyanetz A, Garkun A, Bamberger M. The effect of powder recycling on the mechanical properties and microstructure of electron beam melted Ti-6Al-4 V specimens. Additive Manufacturing 2018;22:834–43. https://doi.org/10.1016/j.addma.2018.06.003.

[49] Sun Y, Aindow M, Hebert RJ. The effect of recycling on the oxygen distribution in Ti-6Al-4V powder for additive manufacturing. Materials at High Temperatures 2017;35:217–24. https://doi.org/10.1080/09603409.2017.1389133.

[50] Ghods S, Schultz E, Wisdom C, Schur R, Pahuja R, Montelione A, et al. Electron Beam Additive Manufacturing of Ti6Al4V: Evolution of Powder Morphology and Part Microstructure with Powder Reuse. Materialia 2020;9:100631. https://doi.org/10.1016/j.mtla.2020.100631.

[51] Liu J, Wen P. Metal vaporization and its influence during laser powder bed fusion process. Materials and Design 2022;215. https://doi.org/10.1016/j.matdes.2022.110505.

[52] Ladewig A, Schlick G, Fisser M, Schulze V, Glatzel U. Influence of the shielding gas flow on the removal of process by-products in the selective laser melting process. Additive Manufacturing 2016;10:1–9. https://doi.org/10.1016/j.addma.2016.01.004.

[53] Sutton A, Karnati S, Leu M, Kriewall C, Newkirk J. Characterization of AISI 304L stainless steel powder recycled in the laser powder-bed fusion process. J 2020;32. https://doi.org/10.1016/j.addma.2019.100981.

[54] Noskov A, Ervik TK, Tsivilskiy I, Gilmutdinov A, Thomassen Y. Characterization of ultrafine particles emitted during laser-based additive manufacturing of metal parts. Scientific Reports 2020;10:1–13. https://doi.org/10.1038/s41598-020-78073-z.

[55] Wang D, Wu S, Fu F, Mai S, Yang Y, Liu Y, et al. Mechanisms and characteristics of spatter generation in SLM processing and its effect on the properties. Materials and Design 2017;117:121–30. https://doi.org/10.1016/j.matdes.2016.12.060.

[56] Bidare P, Bitharas I, Ward RM, Attallah MM, Moore AJ. Fluid and particle dynamics in laser powder bed fusion. Acta Materialia 2018;142:107–20. https://doi.org/10.1016/J.ACTAMAT.2017.09.051.

[57] Yin J, Wang D, Yang L, Wei H, Dong P, Ke L, et al. Correlation between forming quality and spatter dynamics in laser powder bed fusion. Additive Manufacturing 2020;31:100958. https://doi.org/10.1016/J.ADDMA.2019.100958.

[58] Santecchia E, Spigarelli S, Cabibbo M. Material reuse in laser powder bed fusion: Side effects of the laser—metal powder interaction. Metals 2020;10:1–21. https://doi.org/10.3390/met10030341.

[59] Keaveney S, Shmeliov A, Nicolosi V, Dowling DP. Investigation of process by-products during the Selective Laser Melting of Ti6AL4V powder. Additive Manufacturing 2020;36:101514. https://doi.org/10.1016/j.addma.2020.101514.

[60] Simchi A, Ahmadi R, Reihani SMS, Mahdavi A. Kinetics and mechanisms of nanoparticle formation and growth in vapor phase condensation process. Materials and Design 2007;28:850–6. https://doi.org/10.1016/j.matdes.2005.10.017.

[61] Simonelli M, Tuck C, Aboulkhair NT, Maskery I, Ashcroft I, Wildman RD, et al. A Study on the Laser Spatter and the Oxidation Reactions During Selective Laser Melting of 316L Stainless Steel, Al-Si10-Mg, and Ti-6Al-4V. Metall Mater Trans A 2015;46:3842–51. https://doi.org/10.1007/s11661-015-2882-8.

[62] Moylan S, Jurrens K, Donmez MA, Moylan S, Cooke A, Jurrens K. NIST Technical Note 1801 Lessons Learned in Establishing the NIST Metal Additive Manufacturing Laboratory NIST Technical Note 1801 Lessons Learned in Establishing the NIST Metal Additive Manufacturing Laboratory. 2013.

[63] Jensen ACØ, Harboe H, Brostrøm A, Jensen KA, Fonseca AS. Nanoparticle Exposure and Workplace Measurements During Processes Related to 3D Printing of a Metal Object. Frontiers in Public Health 2020;8:1–11. https://doi.org/10.3389/fpubh.2020.608718.

[64] Schur R. Laser Powder Bed Fusion of Ti-6Al-4V: A Round Robin Analysis of Mechanical Property Variability. University of Washington, 2023.

[65] Abeyta A, Nouwens C, Jones AM, Haworth TA, Montelione A, Ramulu M, et al. Characterizing Gas Flow in the Build Chamber of Laser Powder Bed Fusion Systems Utilizing Particle Image Velocimetry: A Path to Improvements 2025. https://doi.org/10.2139/ssrn.5125860.

[66] Spierings AB, Voegtlin M, Bauer T, Wegener K. Powder flowability characterisation methodology for powder-bed-based metal additive manufacturing. Progress in Additive Manufacturing 2016;1:9–20. https://doi.org/10.1007/s40964-015-0001-4.

[67] SAE International. SAE AMS-H-81200 Heat Treatment of Titanium and Titanium Alloys 2014.

[68] ASTM. ASTM E8/E8M-16a Standard Test Methods for Tension Testing of Metallic Materials 2016. https://doi.org/10.1520/E0008.

[69] Young ZA, Guo Q, Parab ND, Zhao C, Qu M, Escano LI, et al. Types of spatter and their features and formation mechanisms in laser powder bed fusion additive manufacturing process. Additive Manufacturing 2020;36:101438. https://doi.org/10.1016/j.addma.2020.101438.

[70] Elkins CJ, Mireles J, Estrada HH, Morgan DW, Taylor HC, Wicker RB. Resolving the three-dimensional flow field within commercial metal additive manufacturing machines: Application of experimental Magnetic Resonance Velocimetry. Additive Manufacturing 2023;73:103651. https://doi.org/10.1016/j.addma.2023.103651.

[71] Weaver JS, Schlenoff A, Deisenroth DC, Moylan SP. Inert gas flow speed measurements in laser powder bed fusion additive manufacturing. Gaithersburg, MD: National Institute of Standards and Technology (U.S.); 2021. https://doi.org/10.6028/NIST.AMS.100-43.

[72] Liu Y, Shi X, Wang Y, Gan W, Cen W. Spatter-flow interaction behavior under protective gas flow parameters and scanning directions. Materials Today Communications 2024;39:109028. https://doi.org/10.1016/j.mtcomm.2024.109028.

[73] Polk AL, Chintersingh KA, Flickinger MR, Valdes ER, Gardner WL, Weihs TP. Effect of composition and process control agents on the microstructure and ignition properties of

ball-milled Al-Zr powders. Powder Technology 2023;427:118729. https://doi.org/10.1016/j.powtec.2023.118729.

[74] Kissinger HE. Variation of peak temperature with heating rate in differential thermal analysis. J RES NATL BUR STAN 1956;57:217. https://doi.org/10.6028/jres.057.026.

[75] Kissinger HE. Reaction Kinetics in Differential Thermal Analysis. Anal Chem 1957;29:1702–6. https://doi.org/10.1021/ac60131a045.

[76] Shcheglov PYu, Gumenyuk AV, Gornushkin IB, Rethmeier M, Petrovskiy VN. Vapor-plasma plume investigation during high-power laser laser welding. Laser Physics 2013;23:7.

[77] Zong Y, Jacob RJ, Li S, Zachariah MR. Size Resolved High Temperature Oxidation Kinetics of Nano-Sized Titanium and Zirconium Particles. J Phys Chem A 2015;119:6171–8. https://doi.org/10.1021/acs.jpca.5b02590.

[78] Park K, Lee D, Rai A, Mukherjee D, Zachariah MR. Size-Resolved Kinetic Measurements of Aluminum Nanoparticle Oxidation with Single Particle Mass Spectrometry. J Phys Chem B 2005;109:7290–9. https://doi.org/10.1021/jp048041v.

[79] Zhang G, Chen J, Zheng M, Yan Z, Lu X, Lin X, et al. Element Vaporization of Ti-6Al-4V Alloy during Selective Laser Melting. Metals 2020;10:435. https://doi.org/10.3390/met10040435.

[80] Ur Rehman A, Mahmood MA, Pitir F, Salamci MU, Popescu AC, Mihailescu IN. Keyhole Formation by Laser Drilling in Laser Powder Bed Fusion of Ti6Al4V Biomedical Alloy: Mesoscopic Computational Fluid Dynamics Simulation versus Mathematical Modelling Using Empirical Validation. Nanomaterials 2021;11:3284. https://doi.org/10.3390/nano11123284.

[81] Sundaram DS, Puri P, Yang V. Pyrophoricity of nascent and passivated aluminum particles at nano-scales. Combustion and Flame 2013;160:1870–5. https://doi.org/10.1016/j.combustflame.2013.03.031.

[82] Puri P, Yang V. Effect of Particle Size on Melting of Aluminum at Nano Scales. J Phys Chem C 2007;111:11776–83. https://doi.org/10.1021/jp0724774.

[83] Sundaram DS, Puri P, Yang V. A general theory of ignition and combustion of nano- and micron-sized aluminum particles. Combustion and Flame 2016;169:94–109. https://doi.org/10.1016/j.combustflame.2016.04.005.

[84] Vyazovkin S. Kissinger Method in Kinetics of Materials: Things to Beware and Be Aware of. Molecules 2020;25:2813. https://doi.org/10.3390/molecules25122813.

[85] Ali U, Esmaeilizadeh R, Ahmed F, Sarker D, Muhammad W, Keshavarzkermani A, et al. Identification and characterization of spatter particles and their effect on surface roughness, density and mechanical response of 17-4 PH stainless steel laser powder-bed fusion parts. Materials Science and Engineering: A 2019;756:98–107. https://doi.org/10.1016/j.msea.2019.04.026.

[86] Li Z, Li H, Yin J, Li Y, Nie Z, Li X, et al. A Review of Spatter in Laser Powder Bed Fusion Additive Manufacturing: In Situ Detection, Generation, Effects, and Countermeasures. Micromachines 2022;13:1366. https://doi.org/10.3390/mi13081366.

[87] Schwerz C, Raza A, Lei X, Nyborg L, Hryha E, Wirdelius H. In-situ detection of redeposited spatter and its influence on the formation of internal flaws in laser powder bed fusion. Additive Manufacturing 2021;47:102370. https://doi.org/10.1016/j.addma.2021.102370.

[88] Snow Z, Scime L, Ziabari A, Fisher B, Paquit V. Observation of spatter-induced stochastic lack-of-fusion in laser powder bed fusion using in situ process monitoring. Additive Manufacturing 2023;61:103298. https://doi.org/10.1016/j.addma.2022.103298.

[89] Bergmann D. What is Machine Learning? | IBM 2025. https://www.ibm.com/think/topics/machine-learning (accessed March 3, 2026).

[90] Hastie T, Tibshirani R, Friedman J. The Elements of Statistical Learning. New York, NY: Springer New York; 2009. https://doi.org/10.1007/978-0-387-84858-7.

[91] Qian J, Nguyen NP, Oya Y, Kikugawa G, Okabe T, Huang Y, et al. Introducing self-organized maps (SOM) as a visualization tool for materials research and education. Results in Materials 2019;4:100020. https://doi.org/10.1016/j.rinma.2019.100020.

[92] Kohonen T, Oja E, Simula O, Visa A, Kangas J. Engineering applications of the self-organizing map. Proc IEEE 1996;84:1358–84. https://doi.org/10.1109/5.537105.

[93] Huang Y, Zhang J, Jiang ES, Oya Y, Saeki A, Kikugawa G, et al. Structure–Property Correlation Study for Organic Photovoltaic Polymer Materials Using Data Science Approach. J Phys Chem C 2020;124:12871–82. https://doi.org/10.1021/acs.jpcc.0c00517.

[94] Moosavi V, Packmann S, Vallés I. SOMPY: A Python Library for Self Organizing Map (SOM) 2026.

[95] Zamri N, Abu Bakar NA, Abd Aziz AZ, Madi EN, Ramli RA, Sukono, et al. Tuning Data Preprocessing Techniques in Enhancing the Accuracy of Self-Organizing MAP (SOM) for Prostate Genomic Cancer. Procedia Computer Science 2025;263:892–9. https://doi.org/10.1016/j.procs.2025.07.107.

[96] Donoho DL. High-Dimensional Data Analysis: The Curses and Blessings of Dimensionality 2000;1:32.

Appendix A –Certificates of Analysis of Powder Lots

(1): EOS lot A 482001

Inspection Certificate

EOS Titanium Ti64

Inspection certificate according to EN 10204, type 3.1

Trade name	EOS Titanium Ti64	Manufacturing method	Plasma atomized
EOS product no.	9011-0039	Date of manufacturing	11.12.2020
Lot number	A 482001		
Manufacturer	Electro Optical Systems Finland Oy Lemminkäisenkatu 36 FI-20520 Turku Finland Tel.: +358 (0)20 765 91 40 Quality_Control_FINLAND@eos.info	Supplier	EOS GmbH Electro Optical Systems Robert-Stirling-Ring 1 D-82152 Krailling Germany Tel.: +49 89 893 36 0

Declaration of conformance

As part of EOS quality assurance, the powder lot has been analyzed for powder properties and has been tested to work in EOS M machine. Parts built with this lot have been tested against EOS criteria and standard requirements.

Powder lot conforms to EOS requirements for powder, machine behavior, and solid part properties. The chemical composition and mechanical properties are in accordance with standards ISO 5832-3, ASTM F1472, ASTM F2924 and ASTM F3302.

Date: 11.12.2020

Approved by:

Marjaana Hovi

QA Specialist

Electro Optical Systems Finland Oy

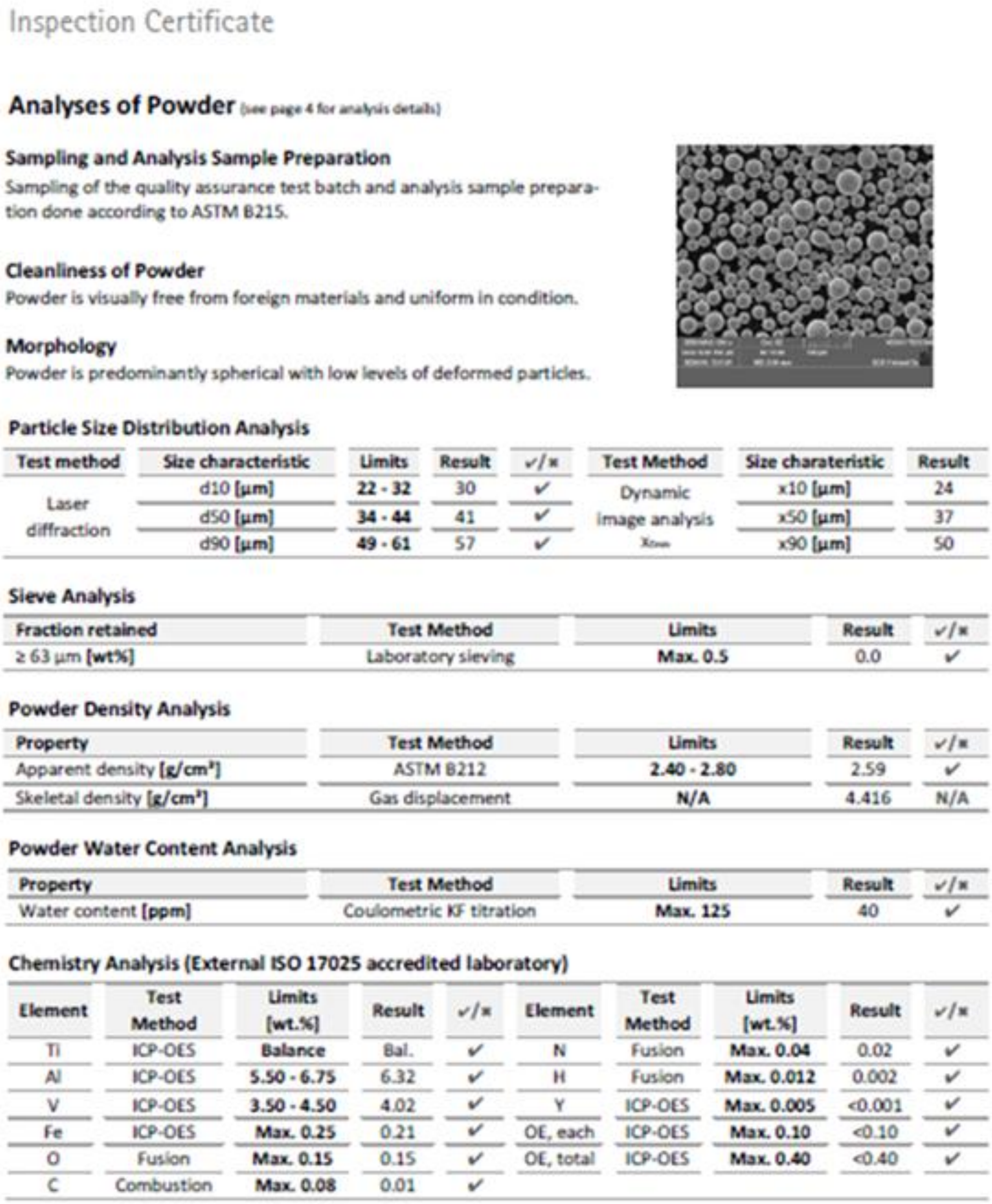

Inspection Certificate

Analyses of Powder (see page 4 for analysis details)

Sampling and Analysis Sample Preparation

Sampling of the quality assurance test batch and analysis sample preparation done according to ASTM B215.

Cleanliness of Powder

Powder is visually free from foreign materials and uniform in condition.

Morphology

Powder is predominantly spherical with low levels of deformed particles.

Particle Size Distribution Analysis

Test method	Size characteristic	Limits	Result	✓/✗	Test Method	Size charateristic	Result
Laser diffraction	d10 [µm]	**22 - 32**	30	✓	Dynamic image analysis $x_{c\,min}$	x10 [µm]	24
	d50 [µm]	**34 - 44**	41	✓		x50 [µm]	37
	d90 [µm]	**49 - 61**	57	✓		x90 [µm]	50

Sieve Analysis

Fraction retained	Test Method	Limits	Result	✓/✗
≥ 63 µm [wt%]	Laboratory sieving	**Max. 0.5**	0.0	✓

Powder Density Analysis

Property	Test Method	Limits	Result	✓/✗
Apparent density [g/cm³]	ASTM B212	**2.40 - 2.80**	2.59	✓
Skeletal density [g/cm³]	Gas displacement	**N/A**	4.416	N/A

Powder Water Content Analysis

Property	Test Method	Limits	Result	✓/✗
Water content [ppm]	Coulometric KF titration	**Max. 125**	40	✓

Chemistry Analysis (External ISO 17025 accredited laboratory)

Element	Test Method	Limits [wt.%]	Result	✓/✗	Element	Test Method	Limits [wt.%]	Result	✓/✗
Ti	ICP-OES	**Balance**	Bal.	✓	N	Fusion	**Max. 0.04**	0.02	✓
Al	ICP-OES	**5.50 - 6.75**	6.32	✓	H	Fusion	**Max. 0.012**	0.002	✓
V	ICP-OES	**3.50 - 4.50**	4.02	✓	Y	ICP-OES	**Max. 0.005**	<0.001	✓
Fe	ICP-OES	**Max. 0.25**	0.21	✓	OE, each	ICP-OES	**Max. 0.10**	<0.10	✓
O	Fusion	**Max. 0.15**	0.15	✓	OE, total	ICP-OES	**Max. 0.40**	<0.40	✓
C	Combustion	**Max. 0.08**	0.01	✓					

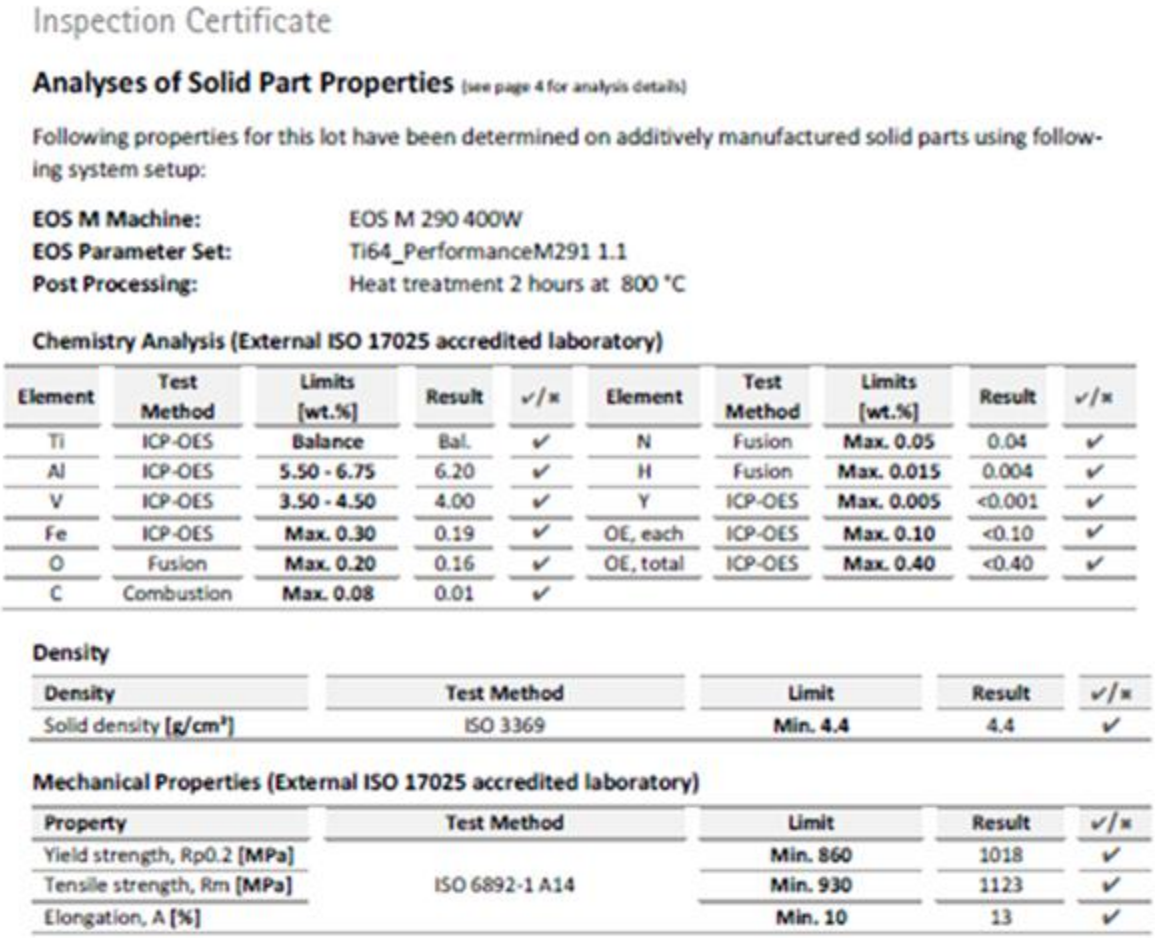

Inspection Certificate

Analyses of Solid Part Properties (see page 4 for analysis details)

Following properties for this lot have been determined on additively manufactured solid parts using following system setup:

EOS M Machine:	EOS M 290 400W
EOS Parameter Set:	Ti64_PerformanceM291 1.1
Post Processing:	Heat treatment 2 hours at 800 °C

Chemistry Analysis (External ISO 17025 accredited laboratory)

Element	Test Method	Limits [wt.%]	Result	✓/✗	Element	Test Method	Limits [wt.%]	Result	✓/✗
Ti	ICP-OES	**Balance**	Bal.	✓	N	Fusion	**Max. 0.05**	0.04	✓
Al	ICP-OES	**5.50 - 6.75**	6.20	✓	H	Fusion	**Max. 0.015**	0.004	✓
V	ICP-OES	**3.50 - 4.50**	4.00	✓	Y	ICP-OES	**Max. 0.005**	<0.001	✓
Fe	ICP-OES	**Max. 0.30**	0.19	✓	OE, each	ICP-OES	**Max. 0.10**	<0.10	✓
O	Fusion	**Max. 0.20**	0.16	✓	OE, total	ICP-OES	**Max. 0.40**	<0.40	✓
C	Combustion	**Max. 0.08**	0.01	✓					

Density

Density	Test Method	Limit	Result	✓/✗
Solid density **[g/cm³]**	ISO 3369	**Min. 4.4**	4.4	✓

Mechanical Properties (External ISO 17025 accredited laboratory)

Property	Test Method	Limit	Result	✓/✗
Yield strength, Rp0.2 **[MPa]**	ISO 6892-1 A14	**Min. 860**	1018	✓
Tensile strength, Rm **[MPa]**		**Min. 930**	1123	✓
Elongation, A **[%]**		**Min. 10**	13	✓

(2): EOS lot A 242001

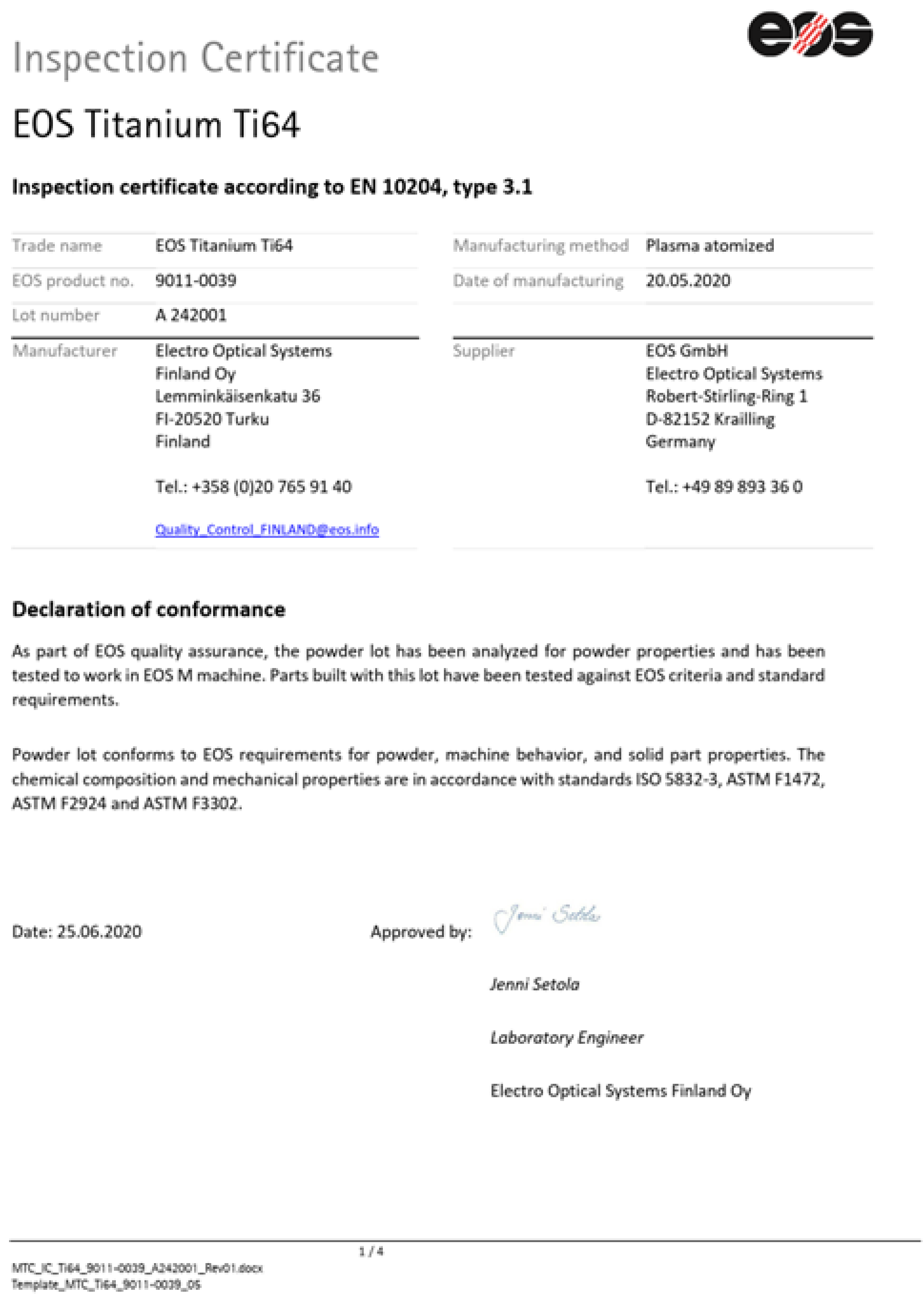

Inspection Certificate

EOS Titanium Ti64

Inspection certificate according to EN 10204, type 3.1

Trade name	EOS Titanium Ti64	Manufacturing method	Plasma atomized
EOS product no.	9011-0039	Date of manufacturing	20.05.2020
Lot number	A 242001		
Manufacturer	Electro Optical Systems Finland Oy Lemminkäisenkatu 36 FI-20520 Turku Finland Tel.: +358 (0)20 765 91 40 Quality_Control_FINLAND@eos.info	Supplier	EOS GmbH Electro Optical Systems Robert-Stirling-Ring 1 D-82152 Krailling Germany Tel.: +49 89 893 36 0

Declaration of conformance

As part of EOS quality assurance, the powder lot has been analyzed for powder properties and has been tested to work in EOS M machine. Parts built with this lot have been tested against EOS criteria and standard requirements.

Powder lot conforms to EOS requirements for powder, machine behavior, and solid part properties. The chemical composition and mechanical properties are in accordance with standards ISO 5832-3, ASTM F1472, ASTM F2924 and ASTM F3302.

Date: 25.06.2020

Approved by: Jenni Setola

Jenni Setola

Laboratory Engineer

Electro Optical Systems Finland Oy

1 / 4

MTC_IC_Ti64_9011-0039_A242001_Rev01.docx
Template_MTC_Ti64_9011-0039_05

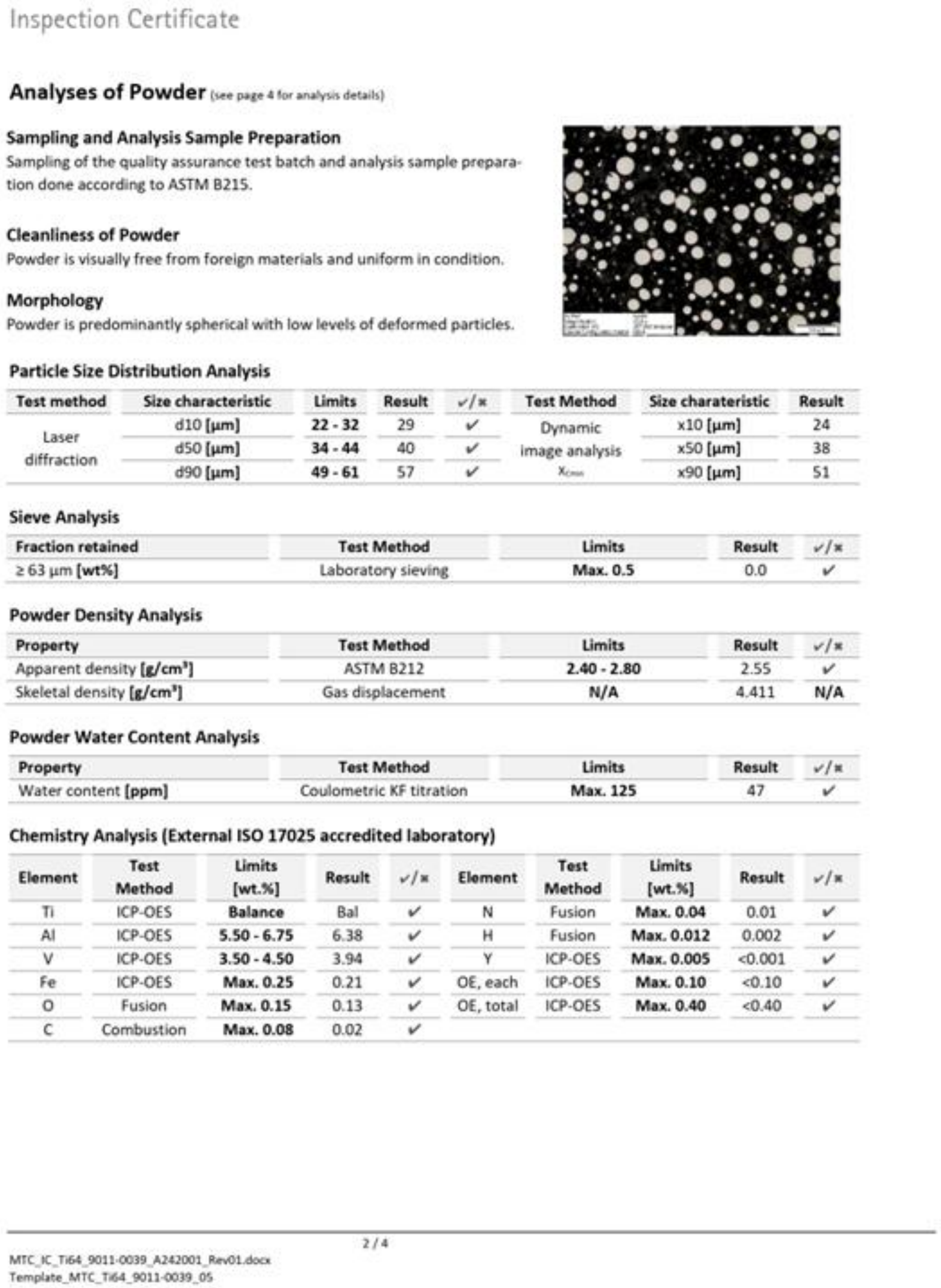

Inspection Certificate

Analyses of Powder (see page 4 for analysis details)

Sampling and Analysis Sample Preparation

Sampling of the quality assurance test batch and analysis sample preparation done according to ASTM B215.

Cleanliness of Powder

Powder is visually free from foreign materials and uniform in condition.

Morphology

Powder is predominantly spherical with low levels of deformed particles.

Particle Size Distribution Analysis

Test method	Size characteristic	Limits	Result	✓/✗	Test Method	Size charateristic	Result
Laser diffraction	d10 [µm]	**22 - 32**	29	✓	Dynamic image analysis x_{Cmin}	x10 [µm]	24
	d50 [µm]	**34 - 44**	40	✓		x50 [µm]	38
	d90 [µm]	**49 - 61**	57	✓		x90 [µm]	51

Sieve Analysis

Fraction retained	Test Method	Limits	Result	✓/✗
≥ 63 µm **[wt%]**	Laboratory sieving	**Max. 0.5**	0.0	✓

Powder Density Analysis

Property	Test Method	Limits	Result	✓/✗
Apparent density **[g/cm³]**	ASTM B212	**2.40 - 2.80**	2.55	✓
Skeletal density **[g/cm³]**	Gas displacement	**N/A**	4.411	**N/A**

Powder Water Content Analysis

Property	Test Method	Limits	Result	✓/✗
Water content **[ppm]**	Coulometric KF titration	**Max. 125**	47	✓

Chemistry Analysis (External ISO 17025 accredited laboratory)

Element	Test Method	Limits [wt.%]	Result	✓/✗	Element	Test Method	Limits [wt.%]	Result	✓/✗
Ti	ICP-OES	**Balance**	Bal	✓	N	Fusion	**Max. 0.04**	0.01	✓
Al	ICP-OES	**5.50 - 6.75**	6.38	✓	H	Fusion	**Max. 0.012**	0.002	✓
V	ICP-OES	**3.50 - 4.50**	3.94	✓	Y	ICP-OES	**Max. 0.005**	<0.001	✓
Fe	ICP-OES	**Max. 0.25**	0.21	✓	OE, each	ICP-OES	**Max. 0.10**	<0.10	✓
O	Fusion	**Max. 0.15**	0.13	✓	OE, total	ICP-OES	**Max. 0.40**	<0.40	✓
C	Combustion	**Max. 0.08**	0.02	✓					

2 / 4

MTC_IC_Ti64_9011-0039_A242001_Rev01.docx
Template_MTC_Ti64_9011-0039_05

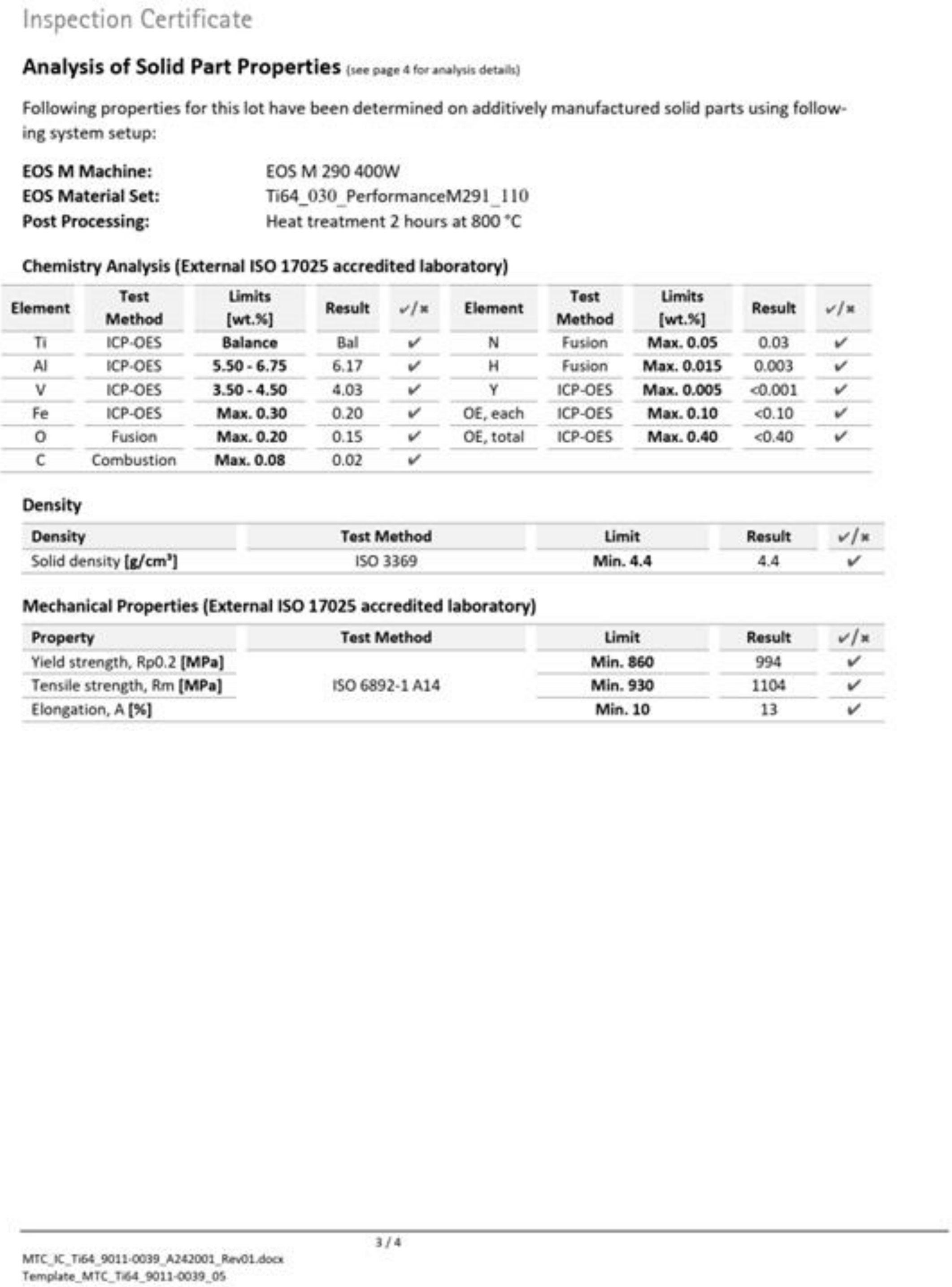

Inspection Certificate

Analysis of Solid Part Properties (see page 4 for analysis details)

Following properties for this lot have been determined on additively manufactured solid parts using following system setup:

EOS M Machine:	EOS M 290 400W
EOS Material Set:	Ti64_030_PerformanceM291_110
Post Processing:	Heat treatment 2 hours at 800 °C

Chemistry Analysis (External ISO 17025 accredited laboratory)

Element	Test Method	Limits [wt.%]	Result	✓/✗	Element	Test Method	Limits [wt.%]	Result	✓/✗
Ti	ICP-OES	**Balance**	Bal	✓	N	Fusion	**Max. 0.05**	0.03	✓
Al	ICP-OES	**5.50 - 6.75**	6.17	✓	H	Fusion	**Max. 0.015**	0.003	✓
V	ICP-OES	**3.50 - 4.50**	4.03	✓	Y	ICP-OES	**Max. 0.005**	<0.001	✓
Fe	ICP-OES	**Max. 0.30**	0.20	✓	OE, each	ICP-OES	**Max. 0.10**	<0.10	✓
O	Fusion	**Max. 0.20**	0.15	✓	OE, total	ICP-OES	**Max. 0.40**	<0.40	✓
C	Combustion	**Max. 0.08**	0.02	✓					

Density

Density	Test Method	Limit	Result	✓/✗
Solid density **[g/cm³]**	ISO 3369	**Min. 4.4**	4.4	✓

Mechanical Properties (External ISO 17025 accredited laboratory)

Property	Test Method	Limit	Result	✓/✗
Yield strength, Rp0.2 **[MPa]**	ISO 6892-1 A14	**Min. 860**	994	✓
Tensile strength, Rm **[MPa]**		**Min. 930**	1104	✓
Elongation, A **[%]**		**Min. 10**	13	✓

3 / 4

MTC_IC_Ti64_9011-0039_A242001_Rev01.docx
Template_MTC_Ti64_9011-0039_05

Inspection Certificate

You've got a question(s) or request(s) on the content of this document?
Don't hesitate to email us at Quality_Control_FINLAND@eos.info

Information on Analysis Methods

Internal powder and solid part analyses done using qualified and calibrated (where applicable) analysis equipment. Calibration/operational check performed on predetermined intervals according to internal procedures and/or procedures recommended by the manufacturer. Daily operational checks for equipment where applicable using traceable reference materials (if available) or internal reference materials.

Sampling and sample preparation: According to ASTM B215. Analysis sample(s) for sieve analysis, laser diffraction analysis and powder densities prepared using spinning rifflers.

Cleanliness of powder and powder morphology: Visual examination of powder according to internal procedure using optical microscope Olympus BX41 or GX51 to investigate powder monolayer and mounted, polished samples. Terminology in accordance with ASTM B243.

Particle size distribution: Laser diffraction analysis and sample preparation according to ASTM B822 and ISO 13320 with Microtrac S3500 or with Sympatec HelosRodos according to ISO 13320. Dynamic image analysis according to ISO 13322-2 with CAMSIZER XT.

Sieve analysis: Sieve analysis based on ASTM B 214. Retsch AS200 Digit sieving system is used. Sieves according ASTM E11.

Powder density: Apparent density analysis according to ASTM B212 or ASTMB417 or ASTM B329. Skeletal density determination by Quantachrome UltraPyc 1200e gas pycnometrer (He) according to ASTM B923.

Powder water content: Water content determination according to internal procedure using coulometric Karl Fischer titrator C30s with InMotion KF Flex oven autosampler.

Powder chemistry: Elemental composition determined in ISO 17025 certified laboratory according to ASTM E2371 (ICP-OES), ASTM E1409 (Fusion: Oxygen, Nitrogen), ASTM E1447 (Fusion: Hydrogen) and ASTM E1941 (Combustion: Carbon). All methods ISO 17025 accredited. The chemical composition is in accordance with standards ISO 5832-3, ASTM F1472, ASTM F2924 and ASTM F3302. Powder analyses without surface removal. Bal. = balance. OE= Other Elements.

Density: Weighing of part in air and water according to ISO 3369 with Kern PLT 650-3M balance.

Mechanical properties: Mechanical properties determined in ISO 17025 accredited laboratory according to ISO 6892-1 A14 or ASTM E8 for samples in heat treated condition. Method ISO 17025 accredited. Specimen machining according to ISO 6892-1 (Annex D), cylindrical samples with d=5 mm in neck region. Samples build in horizontal orientation. Mechanical properties are in accordance with ISO 5832-3, ASTM F1472, ASTM F2924 and ASTM F3302.

Solid chemistry: Elemental composition of solid material determined in ISO 17025 accredited laboratory according to ASTM E2371 (ICP-OES), ASTM E1409 (Fusion: Oxygen, Nitrogen), ASTM E1447 (Fusion: Hydrogen) and ASTM E1941 (Combustion: Carbon). The chemical composition is in accordance with standards ISO 5832-3, ASTM F1472, ASTM F2924 and ASTM F3302. Bal. = balance. OE= Other Elements.

The data correspond to our knowledge and experience at the time of publication. They do not on their own represent a sufficient basis for any part design, neither do they provide any agreement about or guarantee the specific properties of a product or part or the suitability of a product or part for a specific application. It is the responsibility of the producer or customer of a part to check its properties as well as its suitability for a particular purpose. This also applies to consideration of possible intellectual property rights as well as laws and regulations. The data are subject to change without notice as part of EOS' continuous development and improvement processes. EOS has not FDA cleared this product for medical device manufacturers to use this material in FDA sensitive applications.

4 / 4

MTC_IC_Ti64_9011-0039_A242001_Rev01.docx
Template_MTC_Ti64_9011-0039_05

Appendix B – Process Control Document

University of Washington Round Robin (UWRR): Property Variability in AM of Ti6Al4V by SLM

Process Control Document

Updated for Phase II

Prepared by:

Alex Montelione, Rick Schleusener, Reid Schur, Sean Ghods

Dwayne Arola*

Material Science and Engineering, UW

Roberts Hall, 333, Box 352120,

Seattle, WA 98195

*Email: darola@uw.edu
*Phone: (206) 685-8158

06/14/2024

Prepared for all Participants

University of Washington (lead)

The Boeing Company

EOS

Toray Precision Company

1. Overview

    1.1. This document outlines the operating procedures and supporting details that will be followed throughout the second phase (Phase II) of this round robin study focused on stress-life fatigue properties. For convenience, we use the designation University of Washington Round Robin (UWRR) for this effort. The following procedures explain important aspects of the study and provide guidelines that we expect each study participant will adhere to. Overall, they conform to the guidelines for Laser Powder Bed Fusion (LPBF) processes outlined in AMS 7003 [1] for aerospace materials. The operating procedures described in this document are critical to achieving consistency in data between the participants of this study and in maximizing the utility of the data. If at any point a participant has questions regarding the program or operational issues, please contact:

Dwayne Arola: darola@uw.edu, or

Alex Montelione: afm57@uw.edu

1.2. **Contributing Members**: Points of Contact

University of Washington: Dwayne Arola, darola@uw.edu, 443-854-9437

The Boeing Company: Patrick Buffington, Patrick.D.Buffington@boeing.com, or

Stacey Huang, hsien-lin.huang@boeing.com

EOS: Spencer Thompson, spencer.Thompson@eos-na.com, or

Dr. Ankit Saharan, Ankit.Saharan@eos-na.com or

Toray Precision Company: Masaharu Toyama, masaharu.toyama.z9@mail.toray

1.3. Acquiring Powder

1.3.1. A total volume of 900 kg was reserved for the UWRR and was used by all partners in Phase I. A portion of that volume remains and will be used in Phase II. Participants shall continue to print with powder from this lot (A 482001) for this UWRR study if they have powder remaining from Phase I. New participants entering the study, or those without sufficient powder to complete the four planned builds may acquire powder from additional approved lots provided by EOS. Each contributor shall acquire powder directly from EOS per the details in 1.3.1.1. In Phase I, each participant acquired approximately 100 kg of powder. Phase II will require approximately 120 kg of powder to complete the four planned builds. Each Participant should ensure that they have 120 kg of powder from one of the approved lots of powder at the beginning of the study. The powder certifications of the approved powder lots are located in Appendix A.

1.3.1.1.POC for ordering powder from EOS: P.J. Nehil, pj.nehil@eos-na.com

1.3.1.2.Approved powder lots

1.3.1.2.1. A 482001

1.3.1.2.2. A 242001

1.3.2. Upon receipt from EOS, the powder should be placed in a controlled storage location and left sealed until preparing to perform the first build.

1.3.2.1. The storage location should be the same as where powder is normally stored for the partner (normal conditions) and documented. It is recommended that the powder be stored in a hazard free location, within a flammables/explosives cabinet.

1.3.2.2. The environmental conditions should be 68-72°F at less than 60% humidity, in accordance with EOS recommendations and UW operating procedures. Deviation from these conditions shall be reported to the UW for review.

1.3.2.3. Each participant shall provide a description of their powder storage condition, including temperature and humidity.

1.3.2.4. Participants should review Section 3.1.7 of AMS 7003 [1] concerning “Moisture and Contamination Control Plan”. Any questions concerning this advisement should be discussed with the UW team.

1.3.2.5. Participants shall never mix the allocated powder batch with any other batches of powder.

1.3.2.6. Participants shall not use the powder for any other purposes except those permitted by this document until the end of the study.

2. Machine Pedigree

2.1. Participants shall use a single EOS M290 for the duration of the study. The EOSSYSTEM software version shall be recorded.

2.2. Participants should use EOSPRINT operating software v.2.6 or later. The version shall be documented.

2.3. Participants shall control ambient conditions around the machine to maintain a temperature of 68-72F and the relative humidity below 60%. Inability to maintain these settings must be reported to the University of Washington team for review of environmental conditions.

2.4. Participants shall monitor and document the machine operating environment, indicating the temperature and humidity. This should be recorded at the start and end of every build.

2.5. Participants shall document all powder chemistries that have been used in their machine prior to the UWRR, as well as what powder chemistries were used just prior to each build including all appropriate powder information, if applicable.

2.6. If participants use materials other than Ti-6Al-4V on their machine, they shall document their procedure used for cleaning the machine after switching materials and send to the UW for approval.

Note: If changing the type of metal, it is recommended to follow Section 6.8 of the EOS M290 Manual [2] to avoid potentially hazardous situations and minimize contamination.

2.7. Participants shall document any machine maintenance that occurs during the study. This shall include the date of service, or which builds it occurred between, who performed the work (i.e. internal or by EOS technicians), what specifically was performed, and any documentation available (including but not limited to: laser caustic, laser power curve, and scanner calibrations).

3. Qualified Process Parameter Sets
    3.1. All participants shall use the modified Ti64_SpeedM291 1.10 parameter set as provided in the build file. All necessary changes shall be included in the build file and shall not be changed. Details of this parameter set can be provided upon request.
4. Build Plate Material Specification, Preparation Requirements, and Re-Use Preparation Procedure
    4.1. All participants shall build using a Ti-6Al-4V build plate. The build plate shall be of EOS origin or match their plate geometry (see Appendix B.5). Plates with either 6 or 8mm bolt holes are acceptable. This includes a starting thickness of 25 mm. The plate shall be replaced if the thickness drops below 19 mm.
    4.2. Participants shall document the plate thickness before each build.
5. Monitored Process Conditions
    5.1. Contributors shall export and report the full Job Quality Report.
    5.2. Contributors with EOSCONNECT shall also export and report the logs from the following sensors as recorded during the build:
        5.2.1. EOS.Machine.Sensors.BuildingPlatform.Temperature
        5.2.2. Machine.Sensors.Environment.HumidityRelative
        5.2.3. EOS.Machine.Sensors.Environment.Temperature
        5.2.4. EOS.Machine.Sensors.ExposureUnits.ExposureUnit1.Temperature (as well as units 2-4)
        5.2.5. EOS.Machine.Sensors.Filter.O2Concentration
        5.2.6. EOS.Machine.Sensors.Filter.Pressure

        - 5.2.7. EOS.Machine.Sensors.ProcessChamber.O2Concentration.Bottom
        - 5.2.8. EOS.Machine.Sensors.ProcessChamber.O2Concentration.Top
        - 5.2.9. EOS.Machine.Sensors.ProcessChamber.Temperature
        - 5.2.10. EOS.Machine.Sensors.Turbine.Pressure
    - 5.3. Participants may be asked for additional logs if deemed necessary.

6. Build Chamber Purge Gas Type, Specification, Certificates, and Gas Traceability Plan
    - 6.1. Participants shall use a minimum of 99.996% pure argon (argon 4.6) per EOS recommendations. Participants should document the specific purity of argon used in the machine.
    - 6.2. Participants shall acquire and provide supplier certification of gas purity.
    - 6.3. Contributors shall document their argon delivery system to the machine. This can be a simple drawing or explanation of how argon is stored and transferred to the machine.

7. L-PBF Machine Hardware or Software Modifications
    - 7.1. A "grid nozzle " (2200-5501) shall be used for all builds, and shall be documented.
    - 7.2. A high-speed steel type recoater blade shall be used for all builds in the study. All contributors shall document the type of recoater blade installed on the machine used in the UWRR.
    - 7.3. Any other software or hardware modifications made to the machine must be recorded and sent to the University of Washington team for review prior to the start of the study.

8. Operator Instructions: Standard Procedures and Work Instructions for General Machine Operation and Process Control
    - 8.1. Participants shall ensure enough argon is on hand to complete the build.
    - 8.2. The operator shall document if a material other than Ti-6Al-4V was used in the previous build on the M290.
    - 8.3. The "laser emission on-time hours" shall be recorded on the provided "Build Documentation Document" prior to each build.
    - 8.4. The ambient temperature and humidity shall be recorded on the "Build Documentation Document" that will be provided.
    - 8.5. The machine operator shall clean the build chamber thoroughly to ensure there is no contaminating powder, in addition to the powder supply chamber. Other powder lots outside this study should be considered foreign material, even if the chemistry is similar, and as such the machine should be cleaned according to Section 6.8 of the EOS M290 Manual [2].

8.6. Check that a grid-nozzle is installed. Install one if not already present.

8.7. Check and confirm that a steel recoater blade is installed and does not show damage. Replace the recoater blade if damage is present.

8.8. Check that the lens and optics system is clean and free of damage. An visual inspection of the f-theta lens and glass cover plate will be adequate. Look for chips or apparent lens damage.

8.9. The powder shall be sampled prior to each build. Sampling shall take place during the dispenser filling procedure as outlined below.

8.10. The operator shall add approximately 20 kg of powder to the dispenser. Using a stainless steel scoop, 75 g of powder shall be scraped off the top of the freshly deposited powder from the center of the dispenser. The powder in the dispenser shall then be compacted using a powder spatula. This shall be repeated until 74 kg of powder has been added to the dispenser, or until the dispenser is full. If 74 kg of powder could not be added to the dispenser, the excess powder, being the difference between 74 kg and the mass of powder added to the dispenser, shall be weighed and the weight recorded on the build documentation document. The excess powder shall then be stored and used to replenish the depleted powder after the build, compensating with virgin powder as described in Section 8.22. A total of 300 g of powder should be collected and stored in the provided vial.

8.11. The 300 grams of powder from each build shall be delivered to the University of Washington in the sealed container for evaluation and testing. Please ship samples attn Rick Schleusener at the University of Washington, along with the fabricated parts of that build (section 8.29).

8.12. The machine operator shall load the build file provided by the University of Washington for the build and complete the build setup using the Ti64_PerformanceM291 1.10 parameter set as defined in the build file. This parameter set contains modifications from the standard Ti64_PerformanceM291 1.10 parameter set and shall not be modified in any way.

Note: All details concerning the printing conditions and part configurations shall be provided for each build by the UW team.

A preview of the builds for Phase II is provided in Appendix B.2. The machine operator shall perform the printing preparations according to EOS SOPs as outlined in Section 6 of the EOS M290 Operating Manual [2]. Operator should also check the chiller is on and the monitoring suites are GREEN.

8.13. The operator shall record the “cartridge filter clogging %” once the build has started.

8.14. Dosing may be adjusted by the operator during the build to ensure print completion while preventing powder short feeds. **It is recommended that the dosing be increased to at least 150% for the first 10 layers, then decreased to 100% for the remainder of the build. The build design is prone to localized short feeds in the back left corner of the build area. If this is observed, it is recommended to increasing the dosing slightly to compensate.**

8.15. The operator shall use the layer camera (if available) to capture the 1st build layer from each build and provide this to the University of Washington.

8.16. Record the “laser emission on-time hours” after the build is complete.

8.17. After the build has completed, wait to open the chamber until the chamber has reached room temperature.

8.18. The operator shall remove the loose powder from the build chamber, dispenser and collector. It is recommended this be done using an IPCM Extra to conform to the University of Washington’s procedures. If this is not possible, powder extraction can be done according to standard practice at your organization. The method used by each participant is expected to conform to EOS and should be documented. Additionally, the operator shall remove as much powder from the perforated supports as possible and combine with the rest of the recovered powder.

8.19. Powder shall be removed in such a way as to avoid contamination from the manufacturing environment or from other powder since this powder will be reused.

8.20. The recovered powder shall be sieved using a 63 µm mesh size.

8.21. The recovered powder shall be weighed and the weight recorded.

8.22. The operator shall mix the sieved recovered powder collected from the build chamber with an amount of reserved, virgin powder calculated as follows:

$$\begin{aligned} &Virgin\ Powder\ to\ Add\ (kg) \\ &\quad = 74 - Sieved\ Powder\ Mass\ (section\ 8.21) \\ &\quad - Excess\ Powder\ (section\ 8.10) \end{aligned}$$

8.23. Powder shall only be added to replace powder consumed during the manufacturing process, as determined by the powder mass after sieving (8.21). Added powder shall come from the reserved powder from the allocated study powder lot.

8.24. The mixing procedure shall be performed as follows:

8.24.1. The operator shall add half of the used powder to a powder keg, then add half of the calculated quantity of virgin powder to the keg. The keg should then be closed. Using an EOS lift truck (or similar), the keg shall be lifted to allow it to freely rotate. The powder keg shall be carefully spun 10 times forwards (towards the operator), 10 times backwards, and 10 more times forwards. See Appendix B.6 for a schematic.

8.24.2. The previous method shall be applied to the other half of the used and virgin powder in an empty powder keg.

Note: This process should take place on an ESD mat or be grounded with a grounding wire to avoid potential hazards.

8.24.3. The UW shall be consulted on any deviations from this process prior to the start of the study.

8.25. Mixed powder shall be stored in airtight containers until the next build.

8.26. The operator shall separate the parts from the build plate. The method used for this process must be documented. Sectioning should be performed to separate the parts from the build plate. The cut should be made less than 5 mm from the surface of the build plate to preserve the labeling of the parts. A schematic of the cut locations is shown in Appendix B.4 Figure D1.

8.27. **In Phase II, all heat treatment of metal will be performed by the University of Washington.** The heat treatment performed in Phase II will be identical to that used in Phase I. The furnace that is used shall meet the following conditions:

8.27.1. Utilize argon or vacuum environment to minimize oxidation.

8.27.2. Maintain temperature uniformity requirement of ±10 C within the work zone.

8.27.3. Thermocouples used shall adhere to AMS2750, including but not limited to the thermocouple type and calibration frequency.

8.28. Stress relief utilized shall adhere to the following procedure:

8.28.1. Two thermocouples should be placed within the furnace. If the heat treatment is performed on build plate, one thermocouple shall be in contact with the center of the build plate. The other thermocouple shall be in contact with a tensile coupon. If the specimens are separated from the build plate at the time of heat treatment, both thermocouples shall be in contact with tensile coupons.

8.28.2. Charge shall be placed in cold furnace and backfilled with argon or brought to vacuum level per participant organization's SOP.

8.28.3. Furnace temperature shall be raised to 745 ± 10C over approximately 60 minutes.

8.28.4. Soak at 745°C for 120 minutes. The soak time shall begin when the lowest temperature thermocouple reaches 745C.

8.28.5. Furnace cool to 500°C, then rapid cool. The furnace shall be under argon or vacuum for the duration of the cool.

8.29. No other work shall be performed on the parts. Participants should not attempt to remove additional support material or perform any surface finishing.

Note: All necessary post processing shall be performed at The University of

Washington, and include the following:

8.29.1. Separation of remaining support structures from samples.

8.29.2. Full stress relief on all samples.

8.29.3. Machining of the specimens to conform with either ASTM E8 [12] (static tensile properties) or ASTM E466 [13] dimensions and surface roughness.

8.30. Participants shall ship parts along with the vials of collected powder (section 8.6) to The University of Washington for testing and analysis. Parts and powder should be packaged with appropriate packing materials to prevent damage to the contents. Additionally, it is requested that the parts be wrapped in plastic to avoid powder escaping from the support structures. Contents shall be labelled with the following: Company-Build File Name-Build Number. It is advised they be shipped by standard ground shipping. Parts are individually labelled within the build files, and as such labelling of the parts is unnecessary.

Shipping address for all materials:

Mr. Rick Schleusener

2110 NE Mason Road,

302 Roberts Hall, 352120

Seattle, WA 98195-2120

8.31. The build file for the subsequent build shall be supplied upon receival by the UW of printed parts, powder sample, and digital documentation.

9. Build Failures

   9.1. Any interruptions to the build process shall be documented and reported to the UW. Reasons for interruptions may include, but are not limited to, power loss to the machine, recoater blade impact, and powder shortage.

   9.2. Participants may attempt to continue the build after an interruption event. The operators shall document the layer of the build that the interruption occurred, the cause of the interruption, and what steps were taken to recover and continue the build.

   9.3. For build interruptions that occur in the first layer of the parts or earlier, the build may be aborted and restarted. Any powder on the build plate and in the collector hopper shall be recovered and sieved. The build can be restarted with a resurfaced plate.

   9.4. For build interruptions that occur after the first layer of the parts, the operator may attempt to continue the build using their organization's SOP for build interruption recovery.

   9.5. In the event of a build interruption caused by insufficient powder, the operator may attempt to continue the build process by moving powder from the collection hopper to the dispenser hopper. The operator should perform this procedure according to their organization's SOPs. A recommended process of moving powder in the machine without breaking the inert gas atmosphere is provided below.

      9.5.1. Lower dispenser platform by 20 mm to give space for the powder to fall, and preventing it from accumulating along the right side wall, which prevents full recoater travel.

      9.5.2. With the reocater in the leftmost position, Raise collector platform using inching run until the powder level is above the build plane.

      9.5.3. Move recoater to the right end to push powder from the collector hopper to the dispenser hopper

      9.5.4. Lower collector platform by 20 mm

      9.5.5. Move recoater to leftmost position

      9.5.6. Raise collector by 20 mm. Raise collector and additional 5 mm as needed to expose more powder

      9.5.7. Raise dispenser platform by 2 mm

      9.5.8. Move recoater to rightmost position

9.5.9. Repeat steps 9.5.4 – 9.5.8 until sufficient powder has been moved to ensure build completion, or until powder in dispenser hopper is level across its width.

9.6. Ensure that the powder in the dispenser hopper is fully level before continuing the build process

9.6.1. Move the recoater to the left side of the dispenser platform

9.6.2. Raise the dispenser platform 2-5 mm

9.6.3. Move the recoater to the left end of the dispenser platform

9.6.4. Repeat until the powder in the dispenser hopper is fully level front to back and side to side.

10. Ancillary In-Situ Monitoring Techniques Used During Deposition

10.1. Participants shall provide details of whether they have melt pool monitoring or optical thermography. The UW team has both of these options and will capture that data during the builds. The team shall pursue documenting data acquired from the other participants with these capabilities.

10.2. Participants shall provide in-situ powder layer pictures.

11. Check of Laser Prior to Each Build

11.1. Contributors are requested to perform laser power measurements before builds. Testing shall be performed with a pocket monitor at 280W for 10 seconds. Readings shall be recorded and reported to the University of Washington. “Acceptable” readings shall be in accordance with the participant’s standard practice.

12. Maintenance and Machine Calibration Data Plan

12.1. Participants shall provide details regarding machine age and date of most recent maintenance/service. If the serial number is provided to the UW, that information can be made available from EOS with your consent.

Note: It is expected that each participant will only use a single machine for this effort and that it remains the same throughout the duration of the investigation. It is also requested that every build in the series be performed by the same operator if possible. Participants will document if a different operator completes a build.

12.2. All participants are requested to have service performed according to the recommended schedule and practice by EOS during the course of the evaluation.

12.3. Participants shall provide a copy of the recent machine maintenance record including any anomalies, replacements or noted concerns.

12.4. Participants shall provide details of the beam spot size, shape, beam quality, and the beam focal plane.

12.5. Participants shall document routine maintenance performed by the machine operator.

Tasks Performed at the University of Washington

12.6. Powder samples shall be placed in a desiccator at the University of Washington preceding testing. Testing by the University of Washington shall include the following:

1. The powder samples shall be tested at UW according to ASTM F3049-14 [4] to evaluate changes in powder feedstock quality over the duration of the study. Some tests may be outsourced by UW to a third party testing facility if the required testing equipment or protocol is not available.
2. Particle size analysis by light scattering shall be measured per ASTM B822 [5] or by image analysis per ASTM F3049-14 [4].
3. Light element chemistry shall be measured by inert gas fusion per ASTM E1447 [6] and ASTM E1409 [7].
4. Metallic chemistry shall be measured by x-ray fluorescence per ASTM E539 [8].
5. Flowability and apparent density shall be measured per ASTM B212 [9] and ASTM B213 [10].
6. Particle morphology and microstructure shall be evaluated by optical microscopy (OM) and scanning electron microscopy (SEM) methods.

Appendix B.1: Relevant Standards and Documents

[1] SAE-International, AMS7003: Laser Powder Bed Fusion Process, (2018) 1–15.

[2] EOS, M290 Operating Manual, Edition 2.19, (2019).

[3] ASTM-International, B215-15: Standard Practices for Sampling Metal Powders, (2015) 1–7. https://doi.org/10.1520/B0215-10.2.

[4] ASTM-International, F3049-14: Standard Guide for Characterizing Properties of Metal Powders Used for Additive Manufacturing Processes, (2014) 1–3. https://doi.org/10.1520/F3049-14.

[5] ASTM-International, B822-17: Standard Test Method for Particle Size Distribution of Metal Powders and Related Compounds by Light Scattering, (2017) 1–4. https://doi.org/10.1520/B0822-17.2.

[6] ASTM-International, E1447−9: Standard Test Method for Determination of Hydrogen in Titanium and Titanium Alloys by the Inert Gas Fusion Thermal Conductivity Method, (2016) 1–4. https://doi.org/10.1520/E1447-09R16.2.

[7] ASTM-International, E1409-13: Standard Test Method for Determination of Oxygen and Nitrogen in Titanium and Titanium Alloys by Inert Gas Fusion, (2013) 1–7. https://doi.org/10.1520/E1409.

[8] ASTM-International, E539-19: Standard Test Method for Analysis of Titanium Alloys by Wavelength Dispersive X-Ray Fluorescence Spectrometry, (2019) 1–10. https://doi.org/10.1520/E0539-11.2.

[9] ASTM-International, B212-17: Standard Test Method for Apparent Density of Free-Flowing Metal Powders Using the Hall Flowmeter Funnel, (2017) 1–4. https://doi.org/10.1520/B0212.

[10] ASTM-International, B213-20: Standard Test Methods for Flow Rate of Metal Powders Using the Hall Flowmeter Funnel, (2020) 1–4. https://doi.org/10.1520/B0213-13.2.

[11] SAE, AMS-H-81200D: Heat Treatment of Titanium and Titanium Alloys, (2014) 1–24.

[12] ASTM-International, E8/E8M-16a: Standard Test Methods for Tension Testing of Metallic Materials, (2018) 1–30.

[13] ASTM-International, E466-21: Standard Practice for Conducting Force Controlled Constant Amplitude Axial Fatigue Tests of Metallic Materials, (2021) 1–7.

Appendix B.2: Build Design

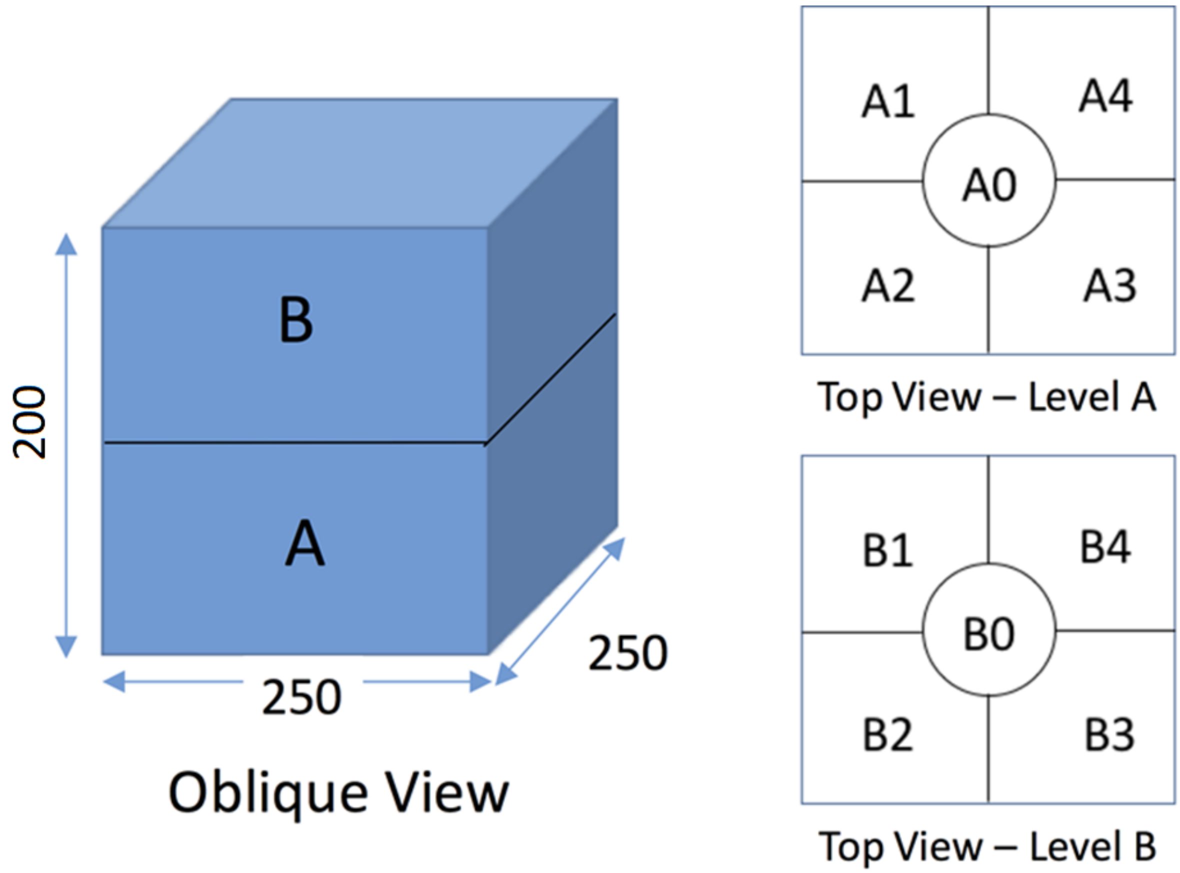

Figure B1: Oblique view of the EOS M290 build volume broken up into a A and B level. Top views of each level broken up into the 5 regions of interest. Region 0 for both levels is in the center and regions 1 through 4 are counterclockwise starting in the back-left corner of the build space.

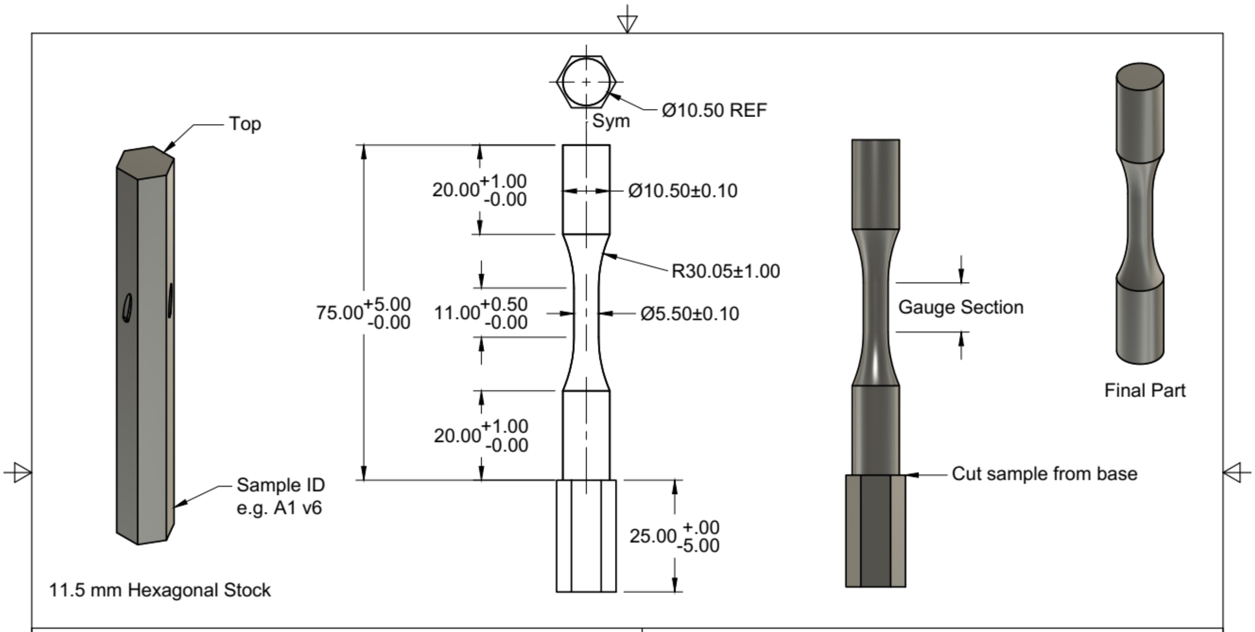

Notes:

- Material is stress relieved Ti-6Al-4V (grade 5)
- Finished parts to comply with ASTM E466-21
- Longitudinal polish gauge section to remove turning marks

- The coupon should be held in the chuck by the end with the sample ID
- Keep sample ID together with machined part

PROJECT
University of Washington

TITLE
UWRR Fatigue Test Sample Dimensions
Additive Manufactured Ti-6Al-4V

APPROVED	SIZE	CODE	DWG NO	REV
CHECKED	A			6
DRAWN Alexander Montelione 5/8/2023	SCALE 1:1	WEIGHT	SHEET 1/1	

Figure B2: Machined fatigue specimen dimensions. Specimen dimensions shall conform to ASTM E466-21 [13] subsize after machining.

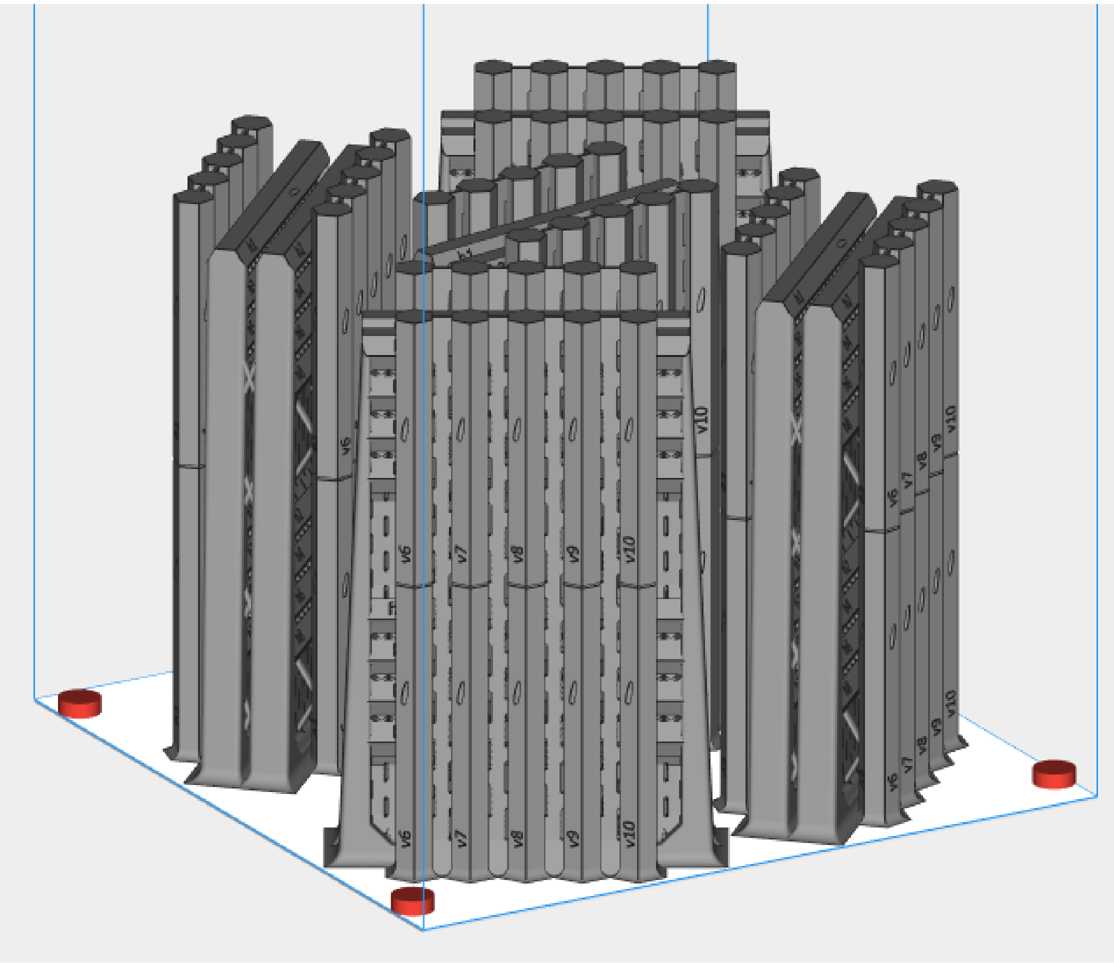

Figure B3: Oblique view of the build. A single configuration is used for Phase II of the Round Robin.

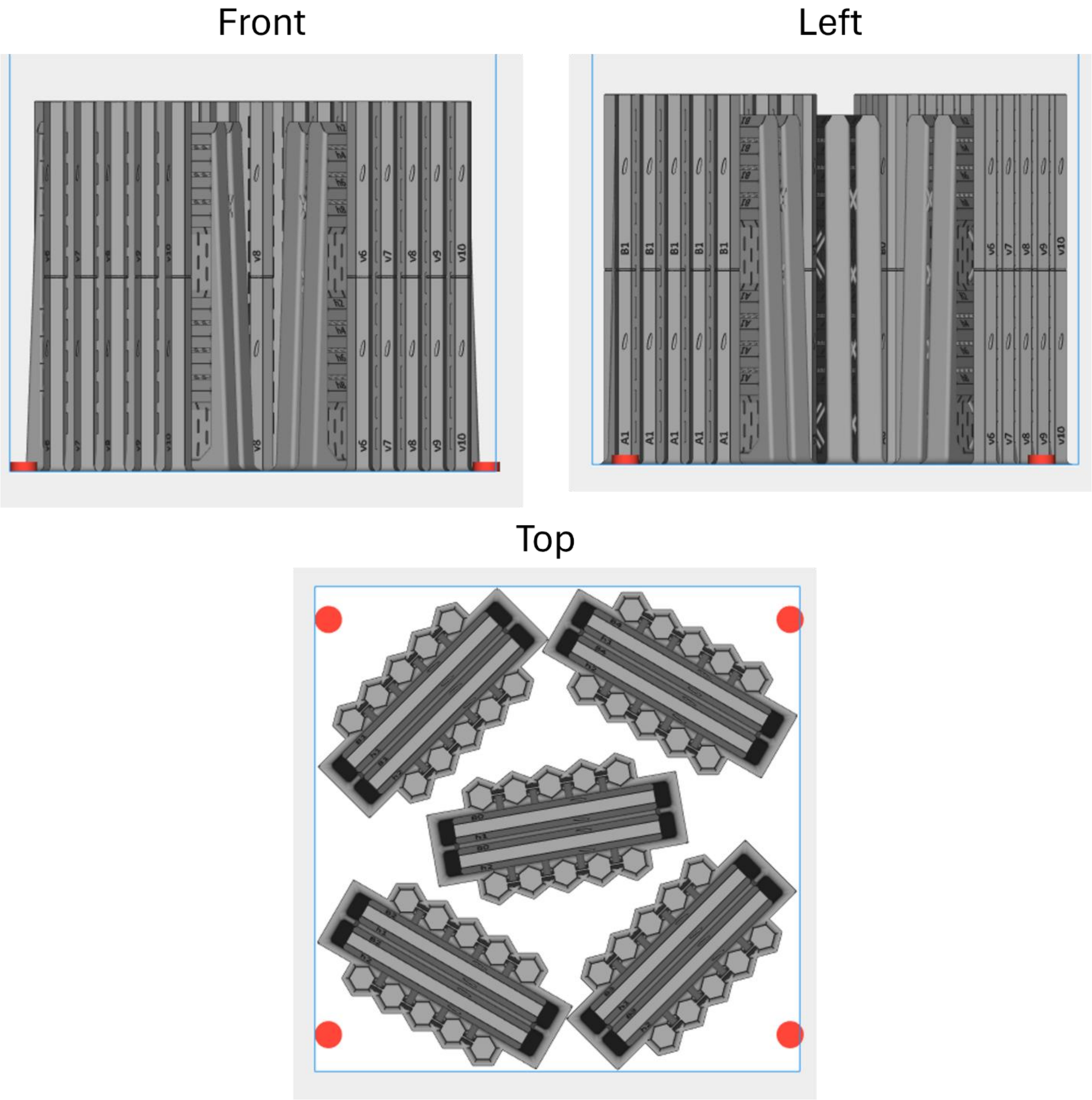

Front

Left

Top

Figure B4: Front, right, and top view of the build design used for Phase II of the Round Robin.

Appendix B.3: Powder Certification(s)

(1): EOS lot A 482001

Inspection Certificate

EOS Titanium Ti64

Inspection certificate according to EN 10204, type 3.1

Trade name	**EOS Titanium Ti64**	Manufacturing method	**Plasma atomized**
EOS product no.	**9011-0039**	Date of manufacturing	**11.12.2020**
Lot number	**A 482001**		
Manufacturer	Electro Optical Systems Finland Oy Lemminkäisenkatu 36 FI-20520 Turku Finland Tel.: +358 (0)20 765 91 40 Quality_Control_FINLAND@eos.info	Supplier	EOS GmbH Electro Optical Systems Robert-Stirling-Ring 1 D-82152 Krailling Germany Tel.: +49 89 893 36 0

Declaration of conformance

As part of EOS quality assurance, the powder lot has been analyzed for powder properties and has been tested to work in EOS M machine. Parts built with this lot have been tested against EOS criteria and standard requirements.

Powder lot conforms to EOS requirements for powder, machine behavior, and solid part properties. The chemical composition and mechanical properties are in accordance with standards ISO 5832-3, ASTM F1472, ASTM F2924 and ASTM F3302.

Date: 11.12.2020

Approved by:

Marjaana Hovi

QA Specialist

Electro Optical Systems Finland Oy

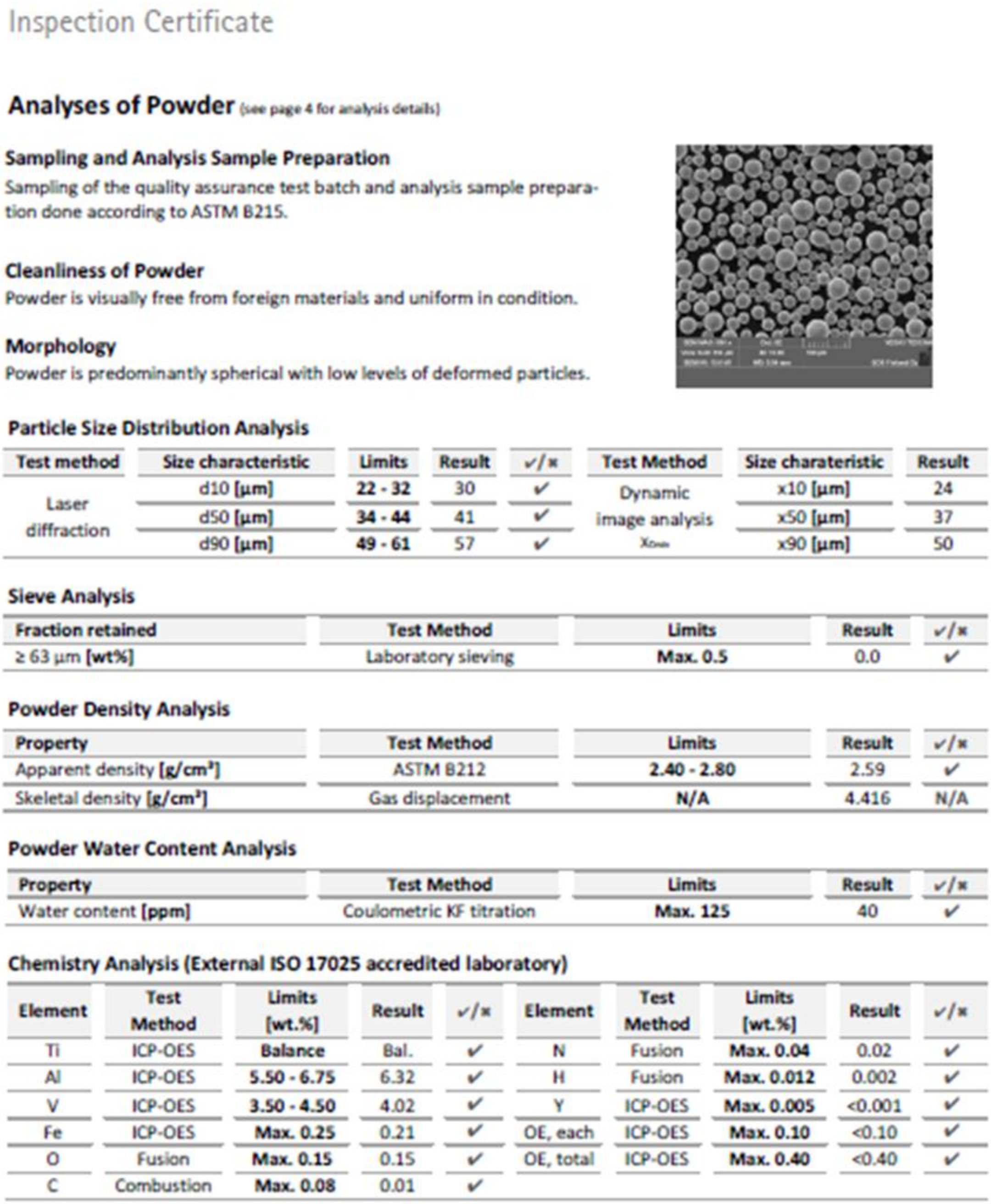

Inspection Certificate

Analyses of Powder (see page 4 for analysis details)

Sampling and Analysis Sample Preparation

Sampling of the quality assurance test batch and analysis sample preparation done according to ASTM B215.

Cleanliness of Powder

Powder is visually free from foreign materials and uniform in condition.

Morphology

Powder is predominantly spherical with low levels of deformed particles.

Particle Size Distribution Analysis

Test method	Size characteristic	Limits	Result	✓/✗	Test Method	Size charateristic	Result
Laser diffraction	d10 **[µm]**	**22 - 32**	30	✓	Dynamic image analysis X_{Cmin}	x10 **[µm]**	24
	d50 **[µm]**	**34 - 44**	41	✓		x50 **[µm]**	37
	d90 **[µm]**	**49 - 61**	57	✓		x90 **[µm]**	50

Sieve Analysis

Fraction retained	Test Method	Limits	Result	✓/✗
≥ 63 µm **[wt%]**	Laboratory sieving	**Max. 0.5**	0.0	✓

Powder Density Analysis

Property	Test Method	Limits	Result	✓/✗
Apparent density **[g/cm³]**	ASTM B212	**2.40 - 2.80**	2.59	✓
Skeletal density **[g/cm³]**	Gas displacement	**N/A**	4.416	N/A

Powder Water Content Analysis

Property	Test Method	Limits	Result	✓/✗
Water content **[ppm]**	Coulometric KF titration	**Max. 125**	40	✓

Chemistry Analysis (External ISO 17025 accredited laboratory)

Element	Test Method	Limits [wt.%]	Result	✓/✗	Element	Test Method	Limits [wt.%]	Result	✓/✗
Ti	ICP-OES	**Balance**	Bal.	✓	N	Fusion	**Max. 0.04**	0.02	✓
Al	ICP-OES	**5.50 - 6.75**	6.32	✓	H	Fusion	**Max. 0.012**	0.002	✓
V	ICP-OES	**3.50 - 4.50**	4.02	✓	Y	ICP-OES	**Max. 0.005**	<0.001	✓
Fe	ICP-OES	**Max. 0.25**	0.21	✓	OE, each	ICP-OES	**Max. 0.10**	<0.10	✓
O	Fusion	**Max. 0.15**	0.15	✓	OE, total	ICP-OES	**Max. 0.40**	<0.40	✓
C	Combustion	**Max. 0.08**	0.01	✓					

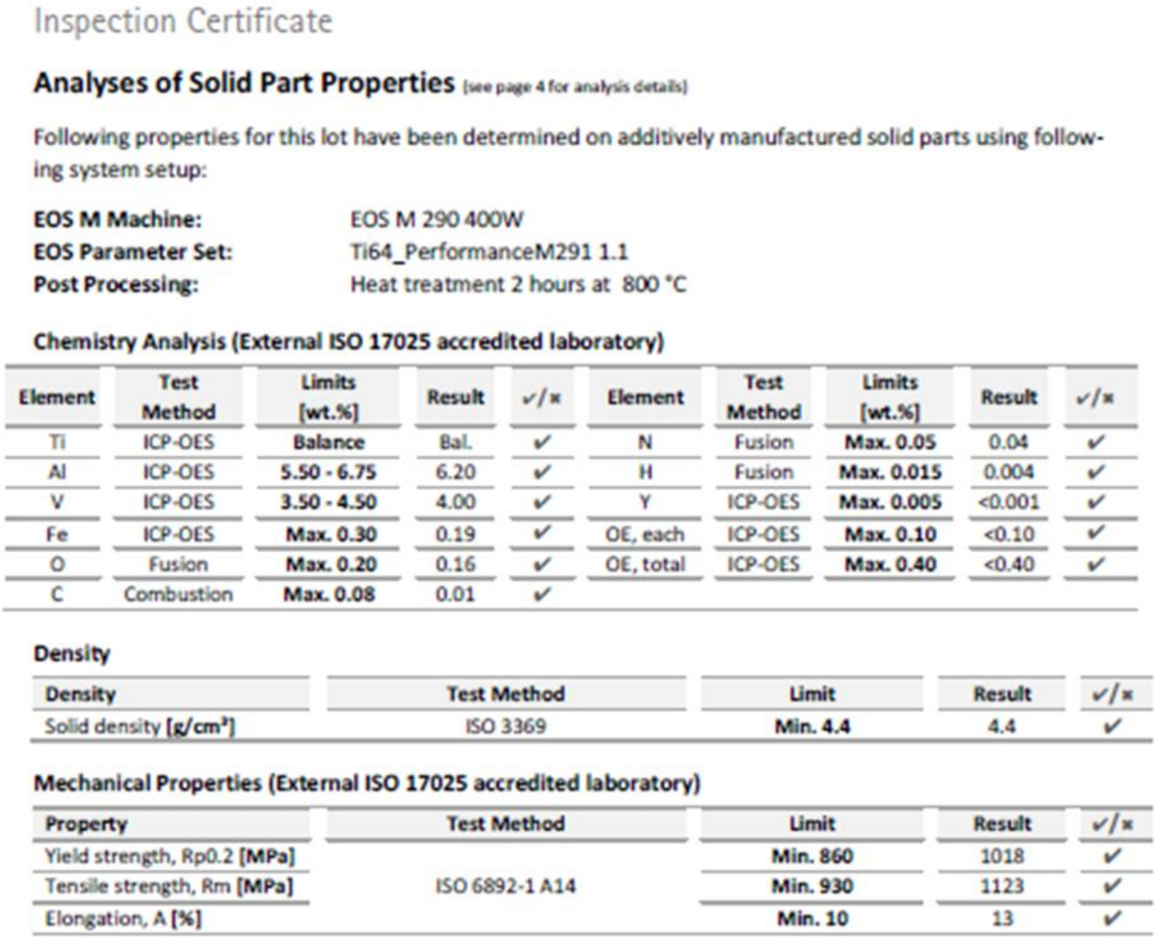

Inspection Certificate

Analyses of Solid Part Properties (see page 4 for analysis details)

Following properties for this lot have been determined on additively manufactured solid parts using following system setup:

EOS M Machine:	EOS M 290 400W
EOS Parameter Set:	Ti64_PerformanceM291 1.1
Post Processing:	Heat treatment 2 hours at 800 °C

Chemistry Analysis (External ISO 17025 accredited laboratory)

Element	Test Method	Limits [wt.%]	Result	✓/✗	Element	Test Method	Limits [wt.%]	Result	✓/✗
Ti	ICP-OES	**Balance**	Bal.	✓	N	Fusion	**Max. 0.05**	0.04	✓
Al	ICP-OES	**5.50 - 6.75**	6.20	✓	H	Fusion	**Max. 0.015**	0.004	✓
V	ICP-OES	**3.50 - 4.50**	4.00	✓	Y	ICP-OES	**Max. 0.005**	<0.001	✓
Fe	ICP-OES	**Max. 0.30**	0.19	✓	OE, each	ICP-OES	**Max. 0.10**	<0.10	✓
O	Fusion	**Max. 0.20**	0.16	✓	OE, total	ICP-OES	**Max. 0.40**	<0.40	✓
C	Combustion	**Max. 0.08**	0.01	✓					

Density

Density	Test Method	Limit	Result	✓/✗
Solid density **[g/cm³]**	ISO 3369	**Min. 4.4**	4.4	✓

Mechanical Properties (External ISO 17025 accredited laboratory)

Property	Test Method	Limit	Result	✓/✗
Yield strength, Rp0.2 **[MPa]**	ISO 6892-1 A14	**Min. 860**	1018	✓
Tensile strength, Rm **[MPa]**		**Min. 930**	1123	✓
Elongation, A **[%]**		**Min. 10**	13	✓

(2): EOS lot A 242001

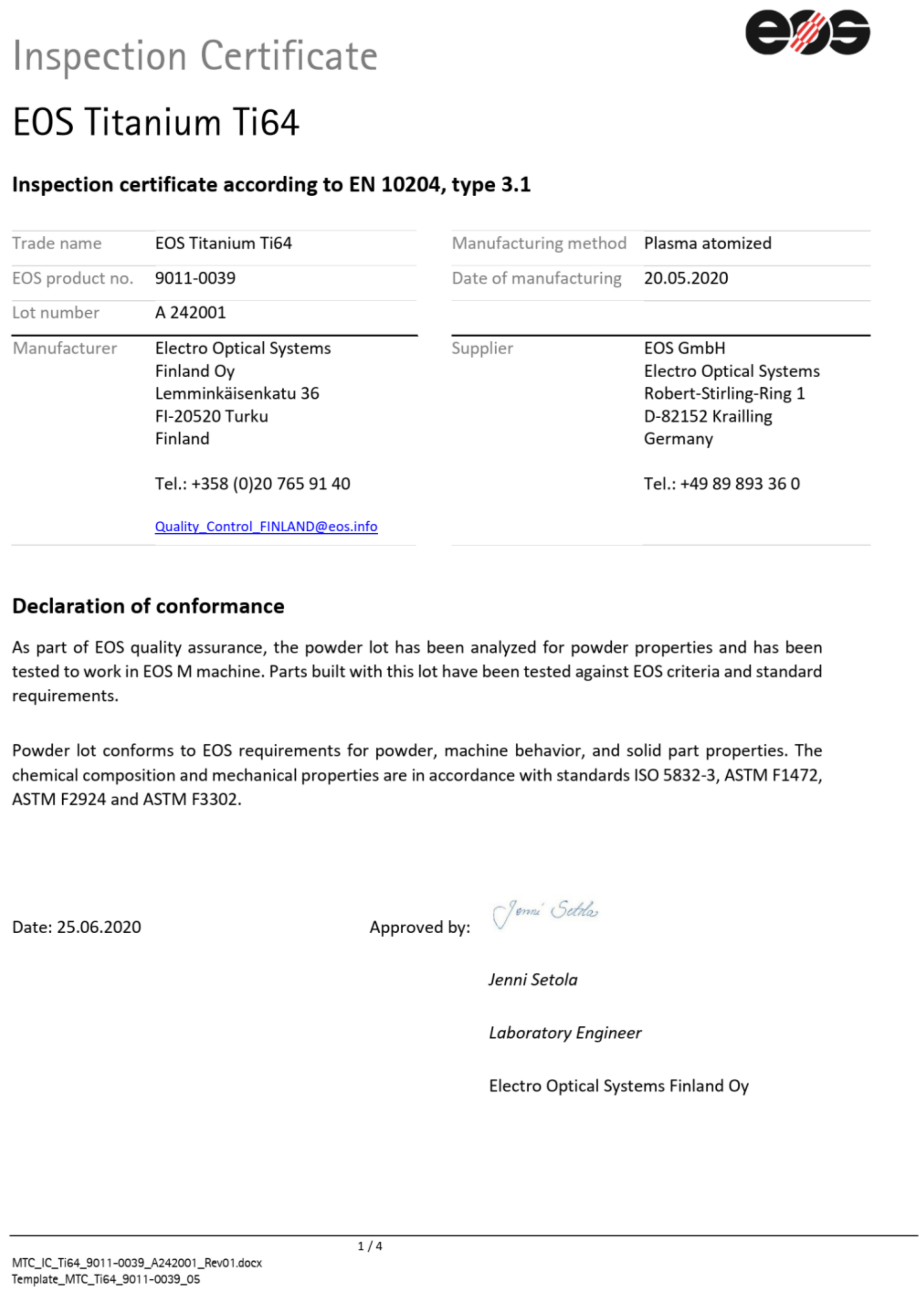

Inspection Certificate

EOS Titanium Ti64

Inspection certificate according to EN 10204, type 3.1

Trade name	EOS Titanium Ti64	Manufacturing method	Plasma atomized
EOS product no.	9011-0039	Date of manufacturing	20.05.2020
Lot number	A 242001		
Manufacturer	Electro Optical Systems Finland Oy Lemminkäisenkatu 36 FI-20520 Turku Finland Tel.: +358 (0)20 765 91 40 Quality_Control_FINLAND@eos.info	Supplier	EOS GmbH Electro Optical Systems Robert-Stirling-Ring 1 D-82152 Krailling Germany Tel.: +49 89 893 36 0

Declaration of conformance

As part of EOS quality assurance, the powder lot has been analyzed for powder properties and has been tested to work in EOS M machine. Parts built with this lot have been tested against EOS criteria and standard requirements.

Powder lot conforms to EOS requirements for powder, machine behavior, and solid part properties. The chemical composition and mechanical properties are in accordance with standards ISO 5832-3, ASTM F1472, ASTM F2924 and ASTM F3302.

Date: 25.06.2020

Approved by: Jenni Setola

Jenni Setola

Laboratory Engineer

Electro Optical Systems Finland Oy

Inspection Certificate

Analyses of Powder (see page 4 for analysis details)

Sampling and Analysis Sample Preparation

Sampling of the quality assurance test batch and analysis sample preparation done according to ASTM B215.

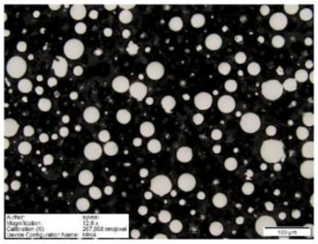

Cleanliness of Powder

Powder is visually free from foreign materials and uniform in condition.

Morphology

Powder is predominantly spherical with low levels of deformed particles.

Particle Size Distribution Analysis

Test method	Size characteristic	Limits	Result	✓/✖	Test Method	Size charateristic	Result
Laser diffraction	d10 **[µm]**	**22 - 32**	29	✓	Dynamic image analysis X_{Cmin}	x10 **[µm]**	24
	d50 **[µm]**	**34 - 44**	40	✓		x50 **[µm]**	38
	d90 **[µm]**	**49 - 61**	57	✓		x90 **[µm]**	51

Sieve Analysis

Fraction retained	Test Method	Limits	Result	✓/✖
≥ 63 µm **[wt%]**	Laboratory sieving	**Max. 0.5**	0.0	✓

Powder Density Analysis

Property	Test Method	Limits	Result	✓/✖
Apparent density **[g/cm³]**	ASTM B212	**2.40 - 2.80**	2.55	✓
Skeletal density **[g/cm³]**	Gas displacement	**N/A**	4.411	**N/A**

Powder Water Content Analysis

Property	Test Method	Limits	Result	✓/✖
Water content **[ppm]**	Coulometric KF titration	**Max. 125**	47	✓

Chemistry Analysis (External ISO 17025 accredited laboratory)

Element	Test Method	Limits [wt.%]	Result	✓/✖	Element	Test Method	Limits [wt.%]	Result	✓/✖
Ti	ICP-OES	**Balance**	Bal	✓	N	Fusion	**Max. 0.04**	0.01	✓
Al	ICP-OES	**5.50 - 6.75**	6.38	✓	H	Fusion	**Max. 0.012**	0.002	✓
V	ICP-OES	**3.50 - 4.50**	3.94	✓	Y	ICP-OES	**Max. 0.005**	<0.001	✓
Fe	ICP-OES	**Max. 0.25**	0.21	✓	OE, each	ICP-OES	**Max. 0.10**	<0.10	✓
O	Fusion	**Max. 0.15**	0.13	✓	OE, total	ICP-OES	**Max. 0.40**	<0.40	✓
C	Combustion	**Max. 0.08**	0.02	✓					

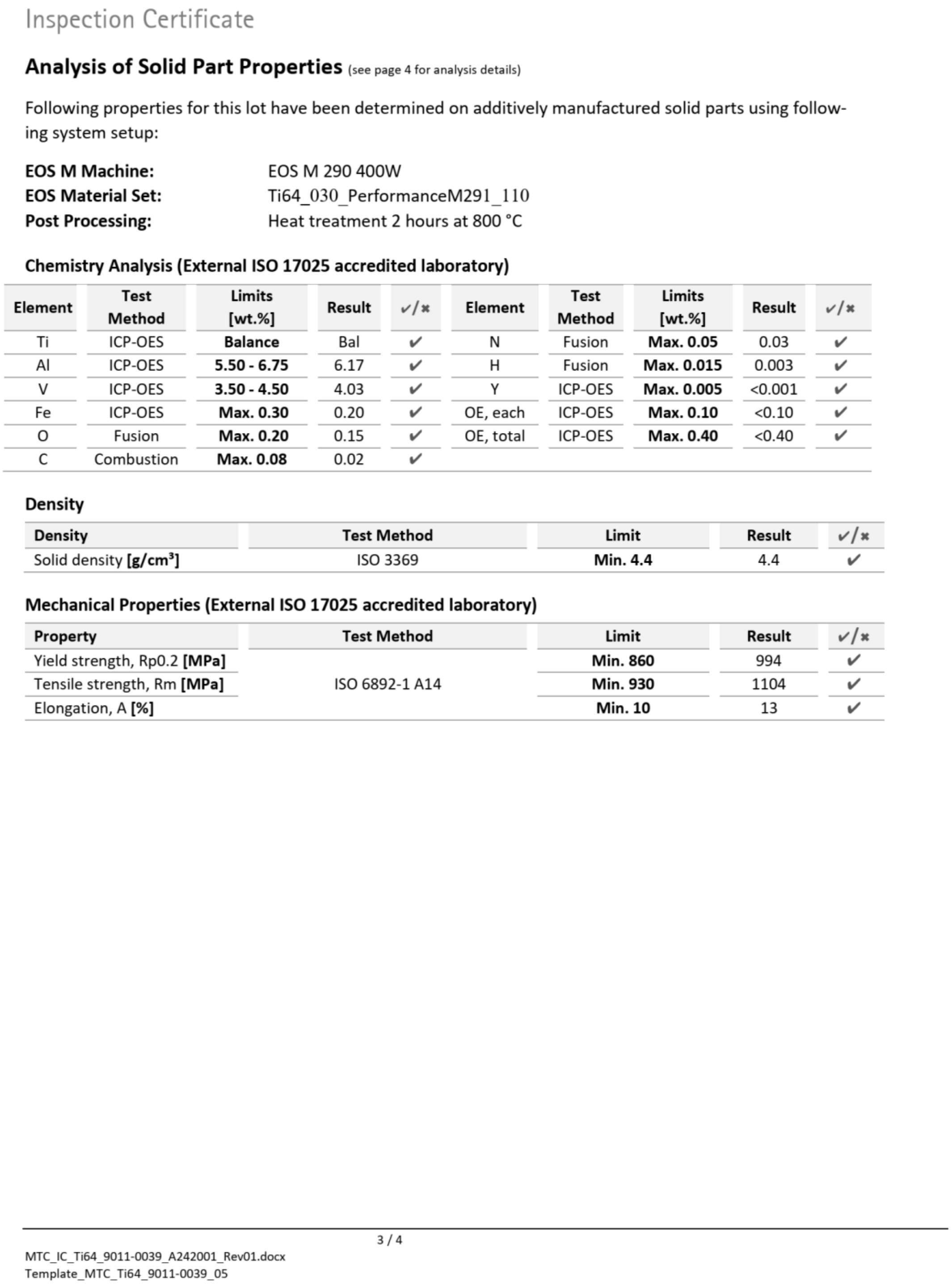

Inspection Certificate

Analysis of Solid Part Properties (see page 4 for analysis details)

Following properties for this lot have been determined on additively manufactured solid parts using following system setup:

EOS M Machine:	EOS M 290 400W
EOS Material Set:	Ti64_030_PerformanceM291_110
Post Processing:	Heat treatment 2 hours at 800 °C

Chemistry Analysis (External ISO 17025 accredited laboratory)

Element	Test Method	Limits [wt.%]	Result	✓/✗	Element	Test Method	Limits [wt.%]	Result	✓/✗
Ti	ICP-OES	**Balance**	Bal	✓	N	Fusion	**Max. 0.05**	0.03	✓
Al	ICP-OES	**5.50 - 6.75**	6.17	✓	H	Fusion	**Max. 0.015**	0.003	✓
V	ICP-OES	**3.50 - 4.50**	4.03	✓	Y	ICP-OES	**Max. 0.005**	<0.001	✓
Fe	ICP-OES	**Max. 0.30**	0.20	✓	OE, each	ICP-OES	**Max. 0.10**	<0.10	✓
O	Fusion	**Max. 0.20**	0.15	✓	OE, total	ICP-OES	**Max. 0.40**	<0.40	✓
C	Combustion	**Max. 0.08**	0.02	✓					

Density

Density	Test Method	Limit	Result	✓/✗
Solid density **[g/cm³]**	ISO 3369	**Min. 4.4**	4.4	✓

Mechanical Properties (External ISO 17025 accredited laboratory)

Property	Test Method	Limit	Result	✓/✗
Yield strength, Rp0.2 **[MPa]**	ISO 6892-1 A14	**Min. 860**	994	✓
Tensile strength, Rm **[MPa]**		**Min. 930**	1104	✓
Elongation, A **[%]**		**Min. 10**	13	✓

You've got a question(s) or request(s) on the content of this document?
Don't hesitate to email us at Quality_Control_FINLAND@eos.info

Information on Analysis Methods

Internal powder and solid part analyses done using qualified and calibrated (where applicable) analysis equipment. Calibration/operational check performed on predetermined intervals according to internal procedures and/or procedures recommended by the manufacturer. Daily operational checks for equipment where applicable using traceable reference materials (if available) or internal reference materials.

Sampling and sample preparation: According to ASTM B215. Analysis sample(s) for sieve analysis, laser diffraction analysis and powder densities prepared using spinning rifflers.

Cleanliness of powder and powder morphology: Visual examination of powder according to internal procedure using optical microscope Olympus BX41 or GX51 to investigate powder monolayer and mounted, polished samples. Terminology in accordance with ASTM B243.

Particle size distribution: Laser diffraction analysis and sample preparation according to ASTM B822 and ISO 13320 with Microtrac S3500 or with Sympatec HelosRodos according to ISO 13320. Dynamic image analysis according to ISO 13322-2 with CAMSIZER XT.

Sieve analysis: Sieve analysis based on ASTM B 214. Retsch AS200 Digit sieving system is used. Sieves according ASTM E11.

Powder density: Apparent density analysis according to ASTM B212 or ASTMB417 or ASTM B329. Skeletal density determination by Quantachrome UltraPyc 1200e gas pycnometrer (He) according to ASTM B923.

Powder water content: Water content determination according to internal procedure using coulometric Karl Fischer titrator C30s with InMotion KF Flex oven autosampler.

Powder chemistry: Elemental composition determined in ISO 17025 certified laboratory according to ASTM E2371 (ICP-OES), ASTM E1409 (Fusion: Oxygen, Nitrogen), ASTM E1447 (Fusion: Hydrogen) and ASTM E1941 (Combustion: Carbon). All methods ISO 17025 accredited. The chemical composition is in accordance with standards ISO 5832-3, ASTM F1472, ASTM F2924 and ASTM F3302. Powder analyses without surface removal. Bal. = balance. OE= Other Elements.

Density: Weighing of part in air and water according to ISO 3369 with Kern PLT 650-3M balance.

Mechanical properties: Mechanical properties determined in ISO 17025 accredited laboratory according to ISO 6892-1 A14 or ASTM E8 for samples in heat treated condition. Method ISO 17025 accredited. Specimen machining according to ISO 6892-1 (Annex D), cylindrical samples with d=5 mm in neck region. Samples build in horizontal orientation. Mechanical properties are in accordance with ISO 5832-3, ASTM F1472, ASTM F2924 and ASTM F3302.

Solid chemistry: Elemental composition of solid material determined in ISO 17025 accredited laboratory according to ASTM E2371 (ICP-OES), ASTM E1409 (Fusion: Oxygen, Nitrogen), ASTM E1447 (Fusion: Hydrogen) and ASTM E1941 (Combustion: Carbon). The chemical composition is in accordance with standards ISO 5832-3, ASTM F1472, ASTM F2924 and ASTM F3302. Bal. = balance. OE= Other Elements.

The data correspond to our knowledge and experience at the time of publication. They do not on their own represent a sufficient basis for any part design, neither do they provide any agreement about or guarantee the specific properties of a product or part or the suitability of a product or part for a specific application. It is the responsibility of the producer or customer of a part to check its properties as well as its suitability for a particular purpose. This also applies to consideration of possible intellectual property rights as well as laws and regulations. The data are subject to change without notice as part of EOS' continuous development and improvement processes. EOS has not FDA cleared this product for medical device manufacturers to use this material in FDA sensitive applications.

Appendix B.4: Support Removal

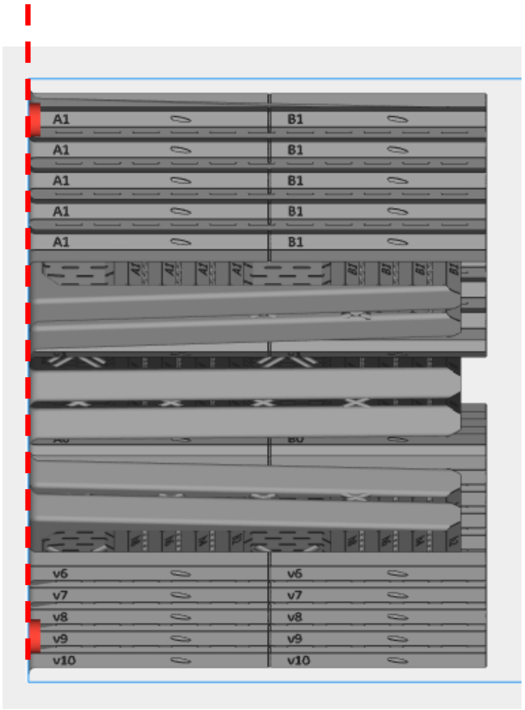

Figure D1: Approximate location of the cut. Each contributor shall make to separate the structures from the build plate.

Appendix B.5: Ti6Al4V Build Plate Drawing

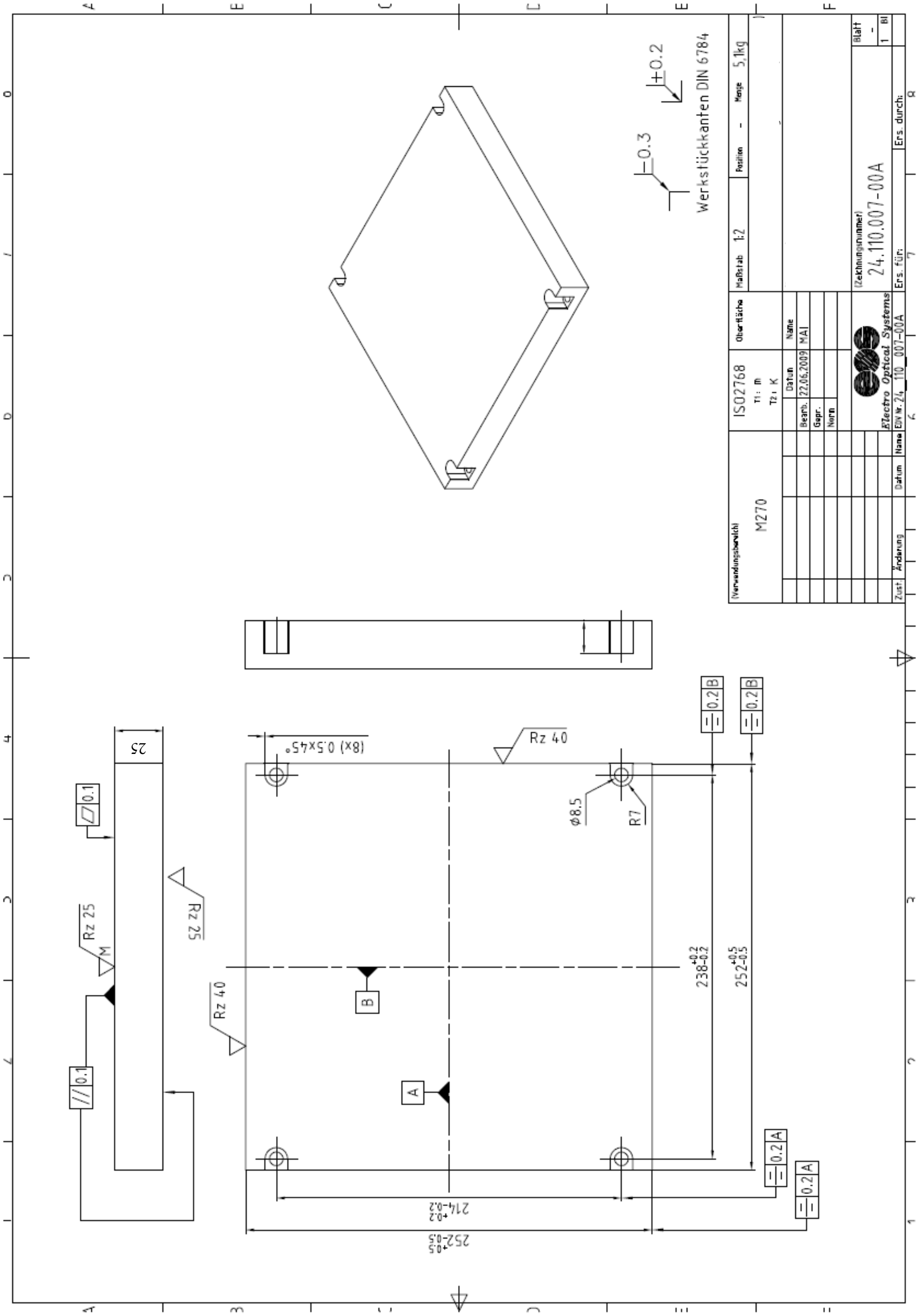

Appendix B.6: Powder Mixing Schematics

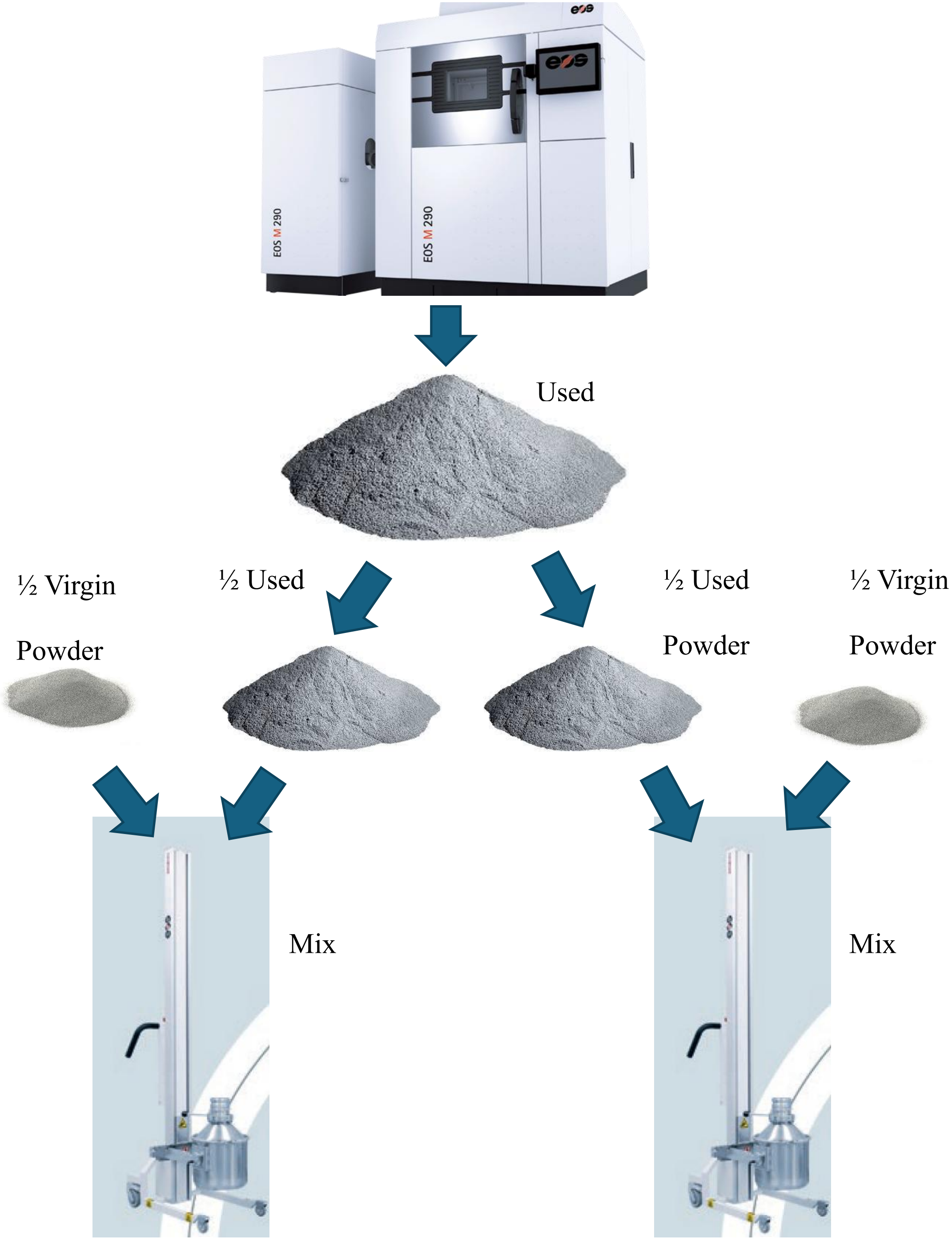

Figure G1: Flow chart outlining the powder collection and mixing process.

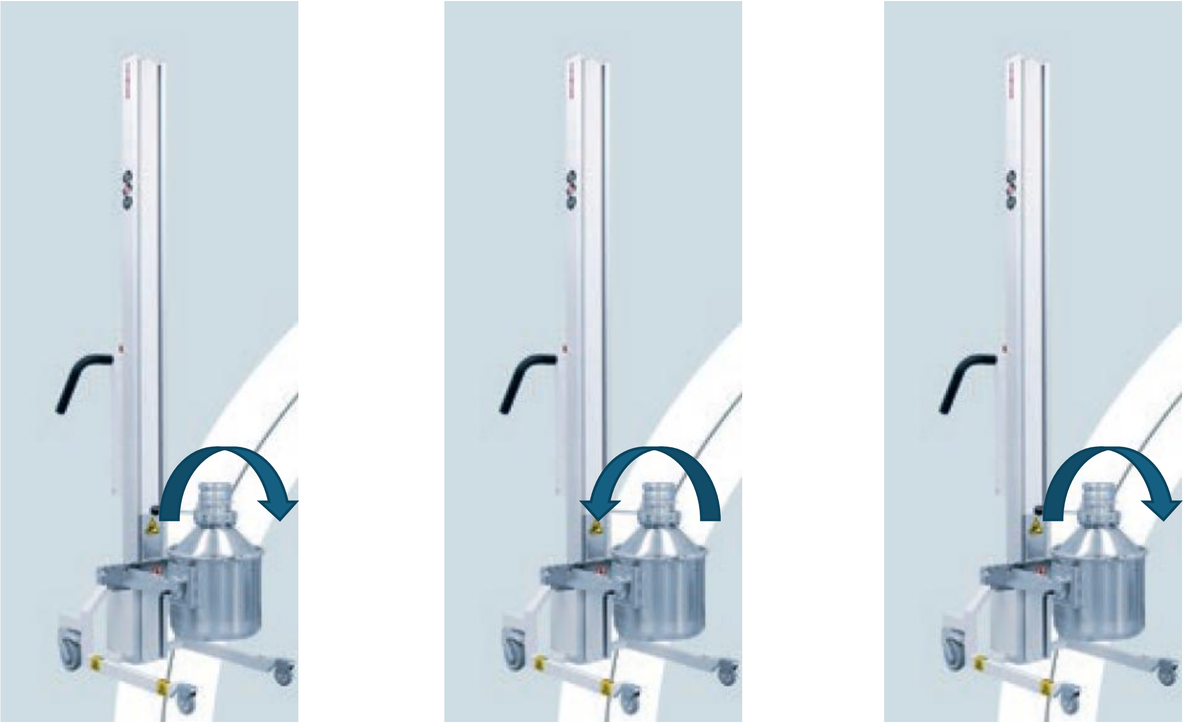

10X 10X 10X

Figure G2: Schematic outlining the powder keg rotation as part of the powder mixing process. Keg is turned 10 times forwards, 10 times backwards, and 10 more times forwards.